

Development of effective green lubricants for industrial drilling systems in
aggressive environments

by
Mohammadjavad Palimi

A thesis submitted in partial fulfillment of the requirements for the degree of

Doctor of Philosophy

in
Materials Engineering

Department of Chemical and Materials Engineering
University of Alberta

© Mohammadjavad Palimi, 2023

Abstract

In drilling systems used in the oil and gas industry, drilling equipment often encounter critical problems which could result in irreparable damage to metallic equipment. Chemical and physical interactions at the contact between different parts, such as drill bits, drill strings with well walls and other hard materials, can cause wear and thus negatively affect the mechanical system's efficiency, sustainability, and safety. Moreover, the drilling operations often proceed in corrosive environments, which can deteriorate the performance of the drilling equipment. The most special concern is the synergistic attack by both wear and corrosion, referred to as tribo-corrosion, which can result in significant material loss, compared to those caused by wear and corrosion separately. Drilling fluids used to facilitate drilling operations are essential, which generate lubricating films to minimize direct contact between moving metal parts and surroundings for reduced friction, corrosion, wear, and synergistic wear-corrosion attack. Various factors, such as temperature, solution chemistry, contact force, sliding speed, and electrochemical potential, all can affect wear, corrosion, and tribo-corrosion in the drilling systems. Thus, comprehending the mechanisms of wear, and corrosion, the wear-corrosion synergy, and their effective preventative measures is essential to improve the drilling effectiveness and mitigate the mentioned issues.

This research attempts to improve the corrosion, wear and tribo-corrosion resistance of carbon steel immersed in the drilling fluids. The study evaluated the effect of different green corrosion inhibitors containing various heteroatoms (O, N, P) on the corrosion, wear, and tribo-corrosion of steel in emulsion-based drilling fluids (WBEs) under static and dynamic conditions. Various concentrations of mineral oil as base oil, surfactant and corrosion inhibitors were added to the 5% KCl base solution to make highly stable WBEs, which were evaluated by dynamic light scattering technique, zeta potential measurements, turbidimetry and inverted light fluorescence microscope.

Then, the CO₂ corrosion-inhibiting effectiveness of inhibitor molecules on carbon steel in a rotating cylinder electrode system was studied using electrochemical tests, including electrochemical impedance spectroscopy (EIS) and potentiodynamic polarization analyses. In the following, a pin-on-disc tribometer incorporated into the electrochemical system under a linear reciprocating sliding module studied the anti-tribo-corrosion behavior of carbon steel immersed in the WBEs containing different corrosion inhibitors. The effectiveness of the different corrosion inhibitors in suppressing corrosive wear performance was thoroughly evaluated by measuring the coefficient of friction (COF), potentiodynamic polarization, current density, and potential evolution with time. In addition, the synergy between wear and corrosion was also measured. The surface morphology, chemical composition, volume loss, wear track profile, and specific wear rate of worn surfaces after tribo-corrosion experiments were examined by scanning electron microscopy and energy dispersive X-ray spectroscopy (SEM-EDX), X-ray photoelectron spectrophotometer (XPS) and 3D optical profilometer. The results showed that the green inhibitors significantly improved the emulsion-based fluids, evidenced by significant reductions in corrosion rate, COF and wear rate and wear-corrosion synergy. Finally, the effect of various controllable parameters such as contact force, sliding speed, electrochemical potential, and the concentration of corrosion inhibitor on the tribo-corrosion properties of steel samples immersed in WBEs were investigated. The study revealed the strong effects of abovementioned parameters on corrosion potential, corrosion current density, COF, volume loss, corrosive wear, and adsorption rate of inhibitor molecules to the iron surface.

Preface

This thesis is an original work by Mohammadjavad Palimi. A version of Chapter 2 from the thesis has been accepted for publication as M.J. Palimi, Y. Tang, V. Alvarez, E. Kuru, D.Y. Li, “*Green corrosion inhibitors for drilling operation: New derivatives of fatty acid-based inhibitors in drilling fluids for 1018 carbon steel in CO₂-saturated KCl environments*,” *Materials Chemistry and Physics* 288 (2022) 126406. A version of Chapter 3 has been published as M.j. Palimi, Y. Tang, M. Wu, V. Alvarez, M. Ghavidel, E. Kuru, Q.Y. Li, Wei Li, D.Y. Li, “*Improve the tribo-corrosion behavior of oil-in-water emulsion-based drilling fluids by new derivatives of fatty acid-based green inhibitors*,” *Tribology International* 174 (2022) 107723. Chapter 4 of this thesis has been accepted for publication as M.J. Palimi, V. Alvarez, E. Kuru, D.Y. Li, “*Effects of sliding speed on corrosion and tribo-corrosion of carbon steel in emulsion- based drilling fluids with green corrosion inhibitors*,” *Journal of bio- and tribo-corrosion* (2022). In addition, A version of chapter 5 has also been published as M.J. Palimi, Y. Tang, S. E. Mousavi, Wengang Chen, V. Alvarez, E. Kuru, D.Y. Li, “*Tribo-corrosion behavior of C-steel in water-based emulsion drilling fluids containing green corrosion inhibitors: experimental and computational studies*,” *Tribology International* (2023). Finally, chapter 6 of this thesis will be submitted as M.J. Palimi, S. Y. Mousavi, Y. Tang, V. Alvarez, E. Kuru, D.Y. Li, “*Influence of sliding forces and electrochemical potential on tribo-corrosion protection of 1018 carbon steel in the drilling fluids by in-situ electrochemical techniques*,” *Electrochemical Acta* (2023).

I was responsible for data collection and analysis, as well as the manuscript composition. Profs. Dongyang Li and Ergun Kuru are the supervisory authors.

Dedicated to My love and Family

Acknowledgement

Since September 2019, I have been given the privilege of studying PhD program at the University of Alberta. I would like to thank my supervisors, **Prof. Dongyang Li and Ergun Kuru**, who gave me the chance to study at the University of Alberta, which began a new chapter in my life. Hereby, I want to convey my heartfelt and sincere gratitude towards the vision, patience, guidance, unconditional support, and wealth of knowledge they provided through my studies.

I would like to thank **Prof. Weixing Chen and Jing Liu** as well for all their supports, their kind guidance, and instructive comments during this study.

Additional thanks to the technical staff of the Department of Chemical and Materials Engineering for all their assistance. A big thanks to my colleagues Seyed Elias Mousavi, Yunqing Tang, Zhen Xu, Dong Zhang, Elias Mousavi, Akash Kumar, Guijang Diao and Mingyu wu.

I would also like to thank Dr. Hamid Niazi for her kind advice for improving the illustrations in this study.

I would like to appreciate for financial support from the Natural Science and Engineering Research Council of Canada (NSERC CRDPJ 530161-18 Li), Compute Canada (CCI uzm-481), and Camber Technology Corporation (CRSL CRD 530161 Li).

At the end, I would like to express my immense gratitude to my love, my parents, and siblings for all their boundless love, the sacrifices they made, and their unconditional supports.

Mohammad Palimi

Table of contents

Abstract.....	II
Preface	IV
Acknowledgement	VI
List of tables.....	XIII
List of Figures	XV
Chapter 1 Introduction.....	1
1. 1 Introduction	1
1. 2 Thesis Outline	9
Chapter 2 Green corrosion inhibitors for drilling operation: New derivatives of fatty acid-based inhibitors in drilling fluids for 1018 carbon steel in CO ₂ -saturated KCl environment	12
2. 1 Introduction	12
2. 2 Experimental.....	17
2. 2. 1 Material.....	17
2. 2. 2 Emulsion-based drilling fluids.....	19
2. 2. 3 Characterization.....	19
2. 2. 3. 1 FTIR characterization.....	19
2. 2. 3. 2 CHNS-O analysis.....	19
2. 2. 3. 3 Turbidity measurement.....	19
2. 2. 3. 4 Zeta potential study.....	20
2. 2. 3. 5 Electrochemical measurements.....	20
2. 2. 3. 6 Surface analysis.....	21

2. 3 Results and discussion.....	21
2. 3. 1 FTIR measurement.....	21
2. 3. 2 CHNS-O analysis.....	24
2. 3. 3 Stability results.....	25
2. 3. 3. 1 Turbidity results.....	25
2. 3. 3. 2 Zeta potential measurement.....	26
2. 3. 4 Corrosion performance studies.....	28
2. 3. 4. 1 OCP measurements.....	28
2. 3. 4. 2 EIS measurements.....	29
2. 3. 4. 3 Polarization tests.....	35
2. 3. 5 Surface characterization.....	37
2. 3. 5. 1 SEM analysis.....	37
2. 3. 5. 2 XPS analysis.....	40
2. 3. 6 Corrosion inhibition mechanism of fatty acid-based green inhibitors.....	44
2. 4 Conclusion.....	46
Chapter 3 Improve the tribo-corrosion behavior of oil-in-water emulsion-based drilling fluids by new derivatives of fatty acid-based green inhibitors.....	47
3. 1 Introduction	47
3. 2 Experimental.....	50
3. 2. 1 Materials.....	50
3. 2. 2 Preparation of emulsion-based drilling fluids (WBEs).....	51
3. 2. 3 Characterization.....	51
3. 2. 3. 1 Particle size distribution.....	51

3. 2. 3. 2	Inverted light fluorescence microscope.....	52
3. 2. 3. 3	Turbidity evaluation.....	52
3. 2. 3. 4	Tribo-corrosion evaluation.....	52
3. 2. 3. 5	Surface characterization.....	53
3. 3	Results and discussion.....	54
3. 3. 1	Stability analysis of the prepared WBEs.....	54
3. 3. 1. 1	Droplet size measurement.....	54
3. 3. 2	Tribo-corrosion study.....	57
3. 3. 2. 1	Surface characterization of worn surfaces with an optical profilometer.....	61
3. 3. 2. 2	Surface characterization of worn surfaces by SEM-EDX.....	64
3. 3. 3	Tribo-corrosion mechanisms of samples immersed in various solutions.....	70
3. 3. 4	Stability of WBEs consisting of PEG-2 oleamide at various concentrations.....	72
3. 3. 4. 1	Visual observation.....	72
3. 3. 4. 2	Turbidity measurement.....	74
3. 3. 4. 3	Particle size distribution.....	75
3. 3. 4. 4	Zeta potential measurements.....	76
3. 3. 4. 5	Observation with inverted light fluorescence microscope.....	77
3. 4	Conclusions.....	78
Chapter 4	Effect of sliding speed on corrosion and tribo-corrosion of carbon steel in emulsion-based drilling fluids with green corrosion inhibitors.....	80
4. 1	Introduction	80
4. 2	Experimental procedures.....	83
4. 2. 1	Material and water-based emulsions (WBEs) preparation.....	83

4. 2. 2	Tribo-corrosion and corrosion tests.....	83
4. 2. 3	Surface characterization.....	84
4. 3	Results and discussion.....	85
4. 3. 1	Corrosion of steel under static and dynamic conditions	85
4. 3. 2	Tribo-corrosion.....	90
4. 3. 2. 1	Effect of sliding speed on corrosion during tribo-corrosion tests.....	90
4. 3. 2. 2	Effect of sliding speed on polarization curves.....	92
4. 3. 2. 3	Effect of sliding speed on friction.....	95
4. 3. 3	Wear and worn surface analysis.....	97
4. 3. 4	Further surface characterization by SEM-EDX.....	100
4. 3. 4. 1	Corrosion.....	100
4. 3. 4. 2	Tribo-corrosion.....	102
4. 4	Discussion.....	106
4. 4. 1	Friction.....	106
4. 4. 2	Tribo-corrosion.....	107
4. 4. 3	Effect of speed on corrosion.....	110
4. 5	Conclusions.....	111
Chapter 5	Phosphate-derived green corrosion inhibitors: enhancing anti-tribo-corrosion properties of carbon steel in emulsion-based drilling fluids.....	113
5. 1	Introduction	113
5. 2	Experimental.....	115
5. 2. 1	Raw material and WBEs preparation	115
5. 2. 2	Characterization.....	116

5. 2. 2. 1	Tribo-corrosion study.....	116
5. 2. 2. 2	Surface analysis.....	117
5. 3	Experimental Results.....	117
5. 3. 1	FTIR analysis.....	117
5. 3. 2	Stability evaluation.....	118
5. 3. 2. 1	Turbidity measurement.....	110
5. 3. 2. 2	Zeta potential.....	120
5. 3. 3	Corrosion and tribo-corrosion study.....	122
5. 3. 3. 1	Effect of corrosion inhibitors on tribo-corrosion.....	122
5. 3. 3. 2	Effect of sliding speed on corrosion during tribo-corrosion test.....	129
5. 3. 3. 3	The effect of speed on Tribological behavior during tribo-corrosion tests.....	133
5. 3. 3. 4	Wear-corrosion synergy.....	135
5. 3. 3. 5	Adsorption isotherm.....	137
5. 3. 3. 6	Surface characterization of worn samples.....	140
5. 3. 4	Tribo-corrosion mechanisms of the carbon steel immersed in different solutions.....	147
5. 4	Conclusions.....	150
Chapter 6	Influence of sliding forces and electrochemical potential on tribo-corrosion protection of carbon steel in the drilling fluids by in-situ electrochemical techniques.....	152
6. 1	Introduction	152
6. 2	Materials and Experimental.....	154
6. 2. 1	Materials and emulsion-based drilling fluids preparation	154
6. 2. 2	Experiments.....	155
6. 3	Results and discussion.....	157

6. 3. 1	Tribo-corrosion behavior under different sliding forces.....	157
6. 3. 1. 1	Potentiostatic tribo-corrosion tests.....	157
6. 3. 1. 2	Electrochemical impedance spectroscopy characterization.....	159
6. 3. 1. 3	Friction and wear study.....	162
6. 3. 1. 4	Wear-corrosion synergy.....	165
6. 3. 1. 5	Surface morphology and elemental composition analysis of wear track.....	167
6. 3. 1. 6	Tribo-corrosion mechanism under different forces.....	173
6. 3. 2	Tribo-corrosion behavior under different applied potentials.....	175
6. 3. 2. 1	Potentiodynamic measurements.....	175
6. 3. 2. 2	Potentiostatic measurements.....	177
6. 3. 2. 3	EIS study.....	179
6. 3. 2. 4	The effect of electrochemical potential on wear and Friction behavior.....	181
6. 3. 2. 5	Synergistic effects.....	184
6. 3. 2. 6	Morphologies and component analysis of worn surfaces.....	186
6. 3. 2. 7	Tribo-corrosion mechanism under different potentials.....	192
6. 4	Conclusions.....	194
Chapter 7	Conclusion and Recommendations.....	196
7. 1	Concluding remarks	196
7. 2	Recommendations for future studies.....	198
References	200

List of Tables

Table 2.1. Representative inhibitors and their inhibition efficiencies for oilfield applications.....	16
Table 2.2. Composition of carbon steel 1018 specimens.....	19
Table 2.3. Prominent adsorption peaks obtained from FTIR spectra of the three fatty acid-based corrosion inhibitors and corresponding functional groups	23
Table 2.4. values of CHNS-O elemental analysis for the corrosion inhibitors and theoretical values based on their structures	24
Table 2.5. Formulated water-based emulsions (WBEs) as drilling fluid.....	25
Table 2.6. Formulated water-based emulsions (WBEs) as drilling fluid.....	28
Table 2.7. Electrochemical parameters from impedance data for the carbon steel samples exposed to the brine solution and different water-based emulsion fluids involving CO ₂ corrosion.....	32
Table 2.8. Values of corrosion current density, corrosion potential, cathodic and anodic Tafel slopes, corrosion rates of carbon steel samples immersed to the brine solution and different water-oil emulsions involving CO ₂ corrosion.....	36
Table 2.9. EDS data (percent concentrations of elements, wt.%) obtained from surfaces of steel samples exposed to different solutions involving CO ₂ corrosion	39
Table 2.10. Binding energies and concentrations of various elements on the steel surfaces exposed to the brine solution and WBE 2, 4, 5 involving CO ₂ corrosion, respectively.....	41
Table 2.11. Data obtained from deconvoluted XPS spectra of steel surface immersed in WBE 4 after CO ₂ corrosion.....	44
Table 3.1. Mechanical properties of 1018 carbon steel based on AISI/SAE.....	51
Table 3.2. Water-based emulsions (WBEs) for the present study.....	56

Table 4.1. Values of corrosion current density, corrosion potential, cathodic and anodic Tafel slopes, corrosion rate of steel sample immersed in the brine solution, and WBE 4 under the static condition and linear motion condition at different speeds 2, 3.5, 5, and 10 mm/s.....	89
Table 4.2. Values of corrosion current density, corrosion potential, cathodic and anodic Tafel slopes, corrosion rate of steel sample immersed in the brine solution, and WBE 4 at various sliding speeds.....	93
Table 5.1. Prepared water-based emulsions (WBEs).....	119
Table 5.2. Water-based emulsions (WBEs) for the current research.....	122
Table 5.3. Electrochemical parameters calculated via the Tafel extrapolation method for samples immersed in the brine solution, WBE (A2) and WBE (A3) at four different sliding speeds.....	132
Table 5.4. Langmuir adsorption isotherm parameters for WBE (A2) and WBE (A3) at different sliding speed.....	140
Table 6.1. Water-based emulsions (WBEs) for the current research.....	155
Table 6.2. Electrochemical parameters extracted from impedance data for the carbon steel samples immersed in the brine solution and various WBEs at different sliding forces.....	161
Table 6.3. Summary of various volume loss components for 1018 carbon steel at applied forces of 2, 4, 8 and 10 N on multiple solutions after the tribo-corrosion test.....	165
Table 6.4. Fitted results of EIS spectra for the carbon steel samples exposed to the brine solution and various WBEs at different applied potentials, force 10 N and sliding speed 2 mm/s.....	180
Table 6.5. Summary of different volume loss components for 1018 carbon steel at applied potentials of -0.3, 0, 0.1, and 0.3 V vs OCP after tribo-corrosion test in various solutions.....	184

List of Figures

Figure 2.1. Molecular structure of (a) PEG-2 oleamide, (b) Glycerol myristate (GM), and (c) Glycerol linoleate (GL).....	18
Figure 2.2. FTIR spectrum of (a) PEG-2 oleamide, (b) GM, and (c) GL used in WBEs preparation.....	23
Figure 2.3. Turbidity values of the prepared WBEs measured at different time intervals.....	26
Figure 2.4. Zeta potentials of the formulated WBEs listed in Table 5.....	27
Figure 2.5. Variations in OCP versus immersion time for the 1018 carbon steel samples immersed in the brine solution and various WBEs under the influence of CO ₂ corrosion.....	29
Figure 2.6. The EIS results as Bode (a) and Nyquist (b) diagrams for carbon steel coupons immersed in the brine solution and WBEs for 2 h involving CO ₂ corrosion. The measured data point is depicted as certain marker styles, while the fitted curves are shown by solid curves.....	30
Figure 2.7. Equivalent circuits used to model impedance data for brine solution (right) and various WBEs (left).....	31
Figure 2.8. The values of (a) phase angle at high frequency and (b) polarization resistance of steel samples immersed in the brine solution and various WBEs under CO ₂ corrosion after 2 h.....	34
Figure 2.9. Polarization curves of carbon steel samples in the brine solution and different WBEs for 2 h involving CO ₂ corrosion.....	36
Figure 2.10. SEM micrographs of carbon steel sample surfaces exposed to (a) brine solution, (b) WBE 1, (c) WBE 2, (d) WBE 3, (e) WBE 4 and (f) WBE 5, involving CO ₂ corrosion.....	38
Figure 2.11. XPS survey spectra of carbon steel surfaces respectively exposed to (a) the brine solution, (b) WBE 2, (c) WBE 4, and (d) WBE 5, involving CO ₂ corrosion.....	41

Figure 2.12. High resolution XPS spectra of detected elements on the steel surface immersed in WBE 4 and their deconvolution after CO ₂ corrosion.....	43
Figure 2.13. Mechanism of PEG-2 oleamide adsorption on 1018 carbon steel in CO ₂ -saturated 5% KCl environment.....	45
Figure 3.1. A schematic view of the experimental set-up used for tribo-corrosion tests.....	53
Figure 3.2. Particle size distribution (a ₁ to a ₇) and average particle size (b) of the prepared WBEs including mineral oil + TERGITOL NP-9 as a surfactant + PEG-2 oleamide.....	55
Figure 3.3. (a) Variations in current and (b) COF versus the sliding time; (c) average COF values for the brine solution and WBEs including mineral oil, TERGITOL NP-9 and three corrosion inhibitors of PEG 2-oleamide, GM and GL.....	58
Figure 3.4. Evolution of potential versus time for 1018 carbon steels immersed in brine solution and various WBEs.....	60
Figure 3.5. Volume losses caused by corrosion and tribo-corrosion tests performed in the brine and WBE 4-1, respectively. Determined values are given in the attached table.....	61
Figure 3.6. Optical images of wear tracks on steel samples after tribo-corrosion test in (a) the brine, (b) WBE 1, (c) WBE 2, (d) WBE 3, (e) WBE 4-1, and (f) WBE 5. Load: 10 N.....	62
Figure 3.7. Cross-sectional wear track profiles (a) and volume losses (b) measured by optical profilometer for carbon steels immersed tested in the brine solution and various WBEs.....	64
Figure 3.8. SEM micrographs and EDS analysis of worn surfaces after tribo-corrosion tests in (a) brine solution, (b) WBE 2, (c) WBE 4-1, and (d) WBE 5.....	65
Figure 3.9. Current-time curves for steel samples in WBE 4 with the combination (mineral oil + surfactant + inhibitor of PEG 2-oleamide) at various concentrations (0.1, 0.5 and 1 g)	67

Figure 3.10. Optical microscopic images of wear tracks on steel samples after tribo-corrosion tests in (a) WBE 4-1, (b) WBE 4-5, (c) WBE 4-10, and (d) corresponding volume losses.....	69
Figure 3.11. SEM-EDS worn surfaces of steel samples after tribo-corrosion testing in (a) WBE 4-1, (b) WBE 4-5, (c) WBE 4-10.....	70
Figure 3.12. Schematic illustration of the mechanism for tribo-corrosion of steel samples immersed in (a) the brine solution and (b) WBEs containing PEG-2 oleamide.....	71
Figure 3.13. Visual observation regarding the stability of formulated WBEs containing the combination (mineral oil + surfactant + PEG 2-oleamide) at various concentrations (0.1, 0.5, 1 and 2 g in the brine solution, forming WBEs of 100 g, respectively): (a) after mixing; (b) 5 minutes after mixing, (c) 2 h after mixing and (d) 6 h after mixing.....	73
Figure 3.14. Turbidity values of WBE 4 containing different amounts (0.1, 0.5, 1 and 2 g) of the combination (65% mineral oil + 3% TERGITOL NP-9 + 32% PEG-2 oleamide) in the brine solution versus time.....	74
Figure 3.15. Particle size distribution (a) and average particle size (b) of prepared WBEs with mineral oil + TERGITOL NP-9 + PEG-2 oleamide at various concentrations (0.1, 0.5, 1, 2 g)....	75
Figure 3.16. The zeta potential of formulated WBE containing mineral oil + TERGITOL NP-9 + PEG-2 oleamide at various concentrations (0.1, 0.5, 1 and 2 g)	77
Figure 3.17. Inverted light fluorescence microscopy images of emulsion droplets including mineral oil + TERGITOL NP-9 + PEG-2 oleamide at various concentrations (0.1, 0.5, 1 and 2 g).....	78
Figure 4.1. Variations in current versus time recorded in range of +1mV at the OCP for the brine solution and various WBEs under (a) static module, and linear motion (dynamic) module at different speeds of (b) 2 mm/s, (c) 5 mm/s and (d) 10 mm/s.....	86

Figure 4.2. Potentiodynamic polarization curves of steel samples immersed in (a) brine solution and (b) WBE 4 under the static condition (no motion) and linear motion condition at different speeds of 2, 3.5, 5, and 10 mm/s.....88

Figure 4.3. Variations in OCP and current versus sliding time for the brine solution and various WBEs at different sliding speeds (a) 2 mm/s, (b) 3.5 mm/s, (c) 5 mm/s and (d) 10 mm/s.....91

Figure 4.4. Polarization curves of steels immersed in (a) brine solution and (b) WBE 4 at four different sliding speeds 2, 3.5, 5, and 10 mm/s.....93

Figure 4.5. (a) Variations in COF versus sliding time and average COF values for brine solution and various WBEs at different sliding speeds (a₁ and a₂) 2 mm/s, (b₁ and b₂) 3.5 mm/s, (c₁ and c₂) 5 mm/s, and (d₁ and d₂) 10 mm/s.....96

Figure 4.6. Optical microscopic images of wear tracks on steel samples after tribo-corrosion test at various sliding speeds (a₁ to a₄) 2 mm/s, (b₁ to b₄) 5 mm/s and (c₁ to c₄) 10 mm/s.....98

Figure 4.7. Cross-sectional wear track profiles and volume losses of steel samples worn in various solutions at sliding speeds of (a₁ and a₂) 2 mm/s, (b₁ and b₂) 3.5 mm/s, (c₁ and c₂) 5 mm/s, and (d₁ and d₂) 10 mm/s.....99

Figure 4.8. Specific wear rate concerning the solution at four sliding speeds 2, 3.5, 5, and 10 mm/s.....100

Figure 4.9. SEM micrographs and EDS analysis of steel surfaces after corrosion test in the brine and WBE 4 under the static condition (a₁ and a₂), and linear motion (dynamic) condition at two speeds: (b₁ and b₂) 2 mm/s, and (c₁ and c₂) 5 mm/s.....101

Figure 4.10. SEM micrographs and EDS analysis of worn surfaces after tribo-corrosion test in brine solution at various sliding speeds (a) 2 mm/s, (b) 3.5 mm/s, (c) 5 mm/s and (d) 10 mm/s. The attached table shows the concentrations (wt%) of different elements on the worn surfaces.....103

Figure 4.11. SEM micrographs and EDS analysis of worn surfaces after tribo-corrosion test in WBE 4 at various sliding speeds (a) 2 mm/s, (b) 3.5 mm/s, (c) 5 mm/s and (d) 10 mm/s. The attached table shows the concentrations (wt%) of different elements on the worn surfaces.....	105
Figure 4.12. A schematic view of the tribo-corrosion mechanism for 1018 carbon steel immersed in the brine solution at different sliding speeds.....	108
Figure 4.13. A schematic illustration of (a) the adsorption process of PEG-2 oleamide on the surface of carbon steel and (b) the tribo-corrosion mechanism for steel immersed in the WBE 4 containing PEG-2 oleamide under different sliding speeds.....	109
Figure 5.1. Molecular structures of two corrosion inhibitors under study: (i) PEG-6 isotridecyl phosphate and (ii) PEG-2 oleamide.....	116
Figure 5.2. FTIR spectra of (a) PEG-2 oleamide and (b) PEG-6 isotridecyl phosphate.....	117
Figure 5.3. Turbidity values versus NTU for the formulated WBEs over a period of 4 h.....	120
Figure 5.4. Zeta potentials of the formulated WBEs consisting of mineral oil + TERGITOL NP- 9 + PEG-6 isotridecyl phosphate.....	122
Figure 5.5. (a) Current density and (b) COF evolution versus the sliding time; (c) volume losses of carbon steel samples immersed in the brine solution and various WBEs.....	125
Figure 5.6. Polarization curves (a) and electrochemical data (b) for steel samples immersed in the brine solution and various WBEs during tribo-corrosion tests at sliding speeds 2 mm/s.....	126
Figure 5.7. Variations in current density versus sliding time for samples immersed in (a) brine solution, (b) WBE(A2) and (c) WBE(A3) at different sliding speeds: 2 mm/s, 3.5 mm/s, 5 mm/s and 10 mm/s.....	130

Figure 5.8. Polarization curves of steel samples immersed in (a) the brine solution, (b) WBE(A2) and (c) WBE(A3) at four different sliding speeds, including 2, 3.5, 5 and 10 mm/s.....	131
Figure 5.9. Variations in COF as a function of sliding time and average COF values for (a ₁ and a ₂) brine, (b ₁ and b ₂) WBE (A2) and (c ₁ and c ₂) WBE (A3) at different sliding speeds.....	134
Figure 5.10. Volume losses for steels immersed in the brine solution, WBE(A2), and WBE (A3) at different sliding speeds.....	135
Figure 5.11. Total volume losses (V _{total}), volume losses by wear (V _{wear} or V _w), volume losses by corrosion (V _{corr} or V _c), and volume losses by wear-corrosion synergy (V _{syn}) of samples immersed in (a) brine, (b) WBE (A2), (c) WBE (A3), at different speeds.....	136
Figure 5.12. Langmuir adsorption isotherm for carbon steel in (a) WBE (A2) and (b) WBE (A3) at different sliding speeds.....	139
Figure 5.13. SEM images and EDS data of worn surface experienced test in the brine solution at different sliding speeds (a) 2 mm/s, (b) 5 mm/s and (c) 10 mm/s.....	141
Figure 5.14. SEM images and EDS data of worn surfaces tested in WBE (A2) at different sliding speeds (a) 2 mm/s, (b) 5 mm/s and (c) 10 mm/s.....	143
Figure 5.15. XPS survey spectra of worn surface immersed in WBE (A2) at two different sliding speeds (a) 2 mm/s and (b) 5 mm/s.....	145
Figure 5.16. High-resolution XPS spectra of worn surface tested in WBE (A2) at 5 mm/ for P 2p, C 1s, O 1s and Fe 2p.....	146
Figure 5.17. Schematic tribo-corrosion mechanism of 1018 carbon steel immersed in WBE (A2) containing PEG-6 isotridecyl phosphate.....	149

Figure 6.1. Evolution of the current density versus the sliding time for carbon steel samples before, during and after potentiostatic tribo-corrosion tests in the (a) brine, (b) WBE (B1), (c) WBE (B2) and (d) WBE (B3) at different loads.....	158
Figure 6.2. Nyquist diagrams for carbon steel plates immersed in the brine solution (a), WBE (B1) (b), (c) WBE (B2) (c) and WBE (B3) (d), at loading and unloading conditions. The measured data point is depicted as certain marker styles, while solid curves show the fitted curves.....	160
Figure 6.3. Variations in COF versus sliding time and average COF values for (a) brine solution, (b) WBE (B1), (c) WBE (B2) and (d) WBE (B3) at different contact forces 2, 4, 8 and 10 N....	163
Figure 6.4. Total volume losses (μm^3) and specific wear rate ($\mu\text{m}^3/\text{Nm}$) of samples worn in the brine solution (a), WBE (B1) (b), WBE (B2) (c), and WBE (B3) (d) at different contact forces...164	164
Figure 6.5. SEM images and EDS data of worn surfaces tested in brine solution at different contact forces (a) 2 N, (b) 4 N, (c) 8 N, and (d) 10 N.....	168
Figure 6.6. SEM images and EDS data of worn surfaces tested in WBE (B3) at different contact forces (a) 2 N, (b) 4 N, (c) 8 N, and (d) 10 N.....	170
Figure 6.7. XPS survey spectra of worn surface immersed in WBE (B3) at two different contact forces (a) 2 N and (b) 10 N.....	171
Figure 6.8. High-resolution XPS spectra of worn surface tested in WBE (B3) at 2 N for P 2p, C 1s, O 1s and Fe 2p.....	172
Figure 6.9. Schematic diagram of the tribo-corrosion mechanism of carbon steel immersed in (a) brine solution and (b) WBE (B3) under different contact forces.....	175
Figure 6.10. The (a) OCP and (b1 to b4) potentiodynamic polarization curves for 1018 carbon steel in different solutions under 2 mm/s and 10 N.....	176

Figure 6.11. Current density evolution versus the sliding time before, during and after sliding for carbon steel samples immersed in the (a) brine solution, (b) WBE (B1), (c) WBE (B2) and (d) WBE (B3) under different applied potentials.....177

Figure 6.12. Nyquist diagrams for carbon steel coupons immersed in the brine solution (a), WBE (B1) (b), (c) WBE (B2) (c) and WBE (B3) (d), at different applied potentials. The measured data point is depicted as certain marker styles, while solid curves show the fitted curves.....179

Figure 6.13. Variations in COF versus sliding time and average COF values for (a) brine solution, (b) WBE (B1), (c) WBE (B2) and (d) WBE (B3) at different applied potentials.....182

Figure 6.14. Volume losses (μm^3) and specific wear rate ($\mu\text{m}^3/\text{Nm}$) of steel samples worn in the brine solution (a), WBE (B1) (b), WBE (B2) (c), and WBE (B3) (d) at different applied potentials.....184

Figure 6.15. SEM images and EDS data of worn surface experienced test in the brine solution at different applied potentials (a) -0.1 V, (b) 0 (OCP) and (c) +0.1 V.....186

Figure 6.16. SEM images and EDS data of worn surface experienced test in the WBE (B3) at different applied potentials (a) -0.1 V, (b) 0 (OCP) and (c) +0.1 V.....189

Figure 6.17. XPS survey spectra of worn surface immersed in WBE (B3) at two different applied potentials (a) -0.1 V and (b) +0.1 V.....190

Figure 6.18. Schematic diagram of the tribo-corrosion mechanism of 1018 carbon steel immersed in WBE (B3) at (a) cathodic potential, (b)OCP, and (c) anodic potential.....194

Chapter 1 Introduction

1.1 introduction

Drilling fluids, as one of the essential requirements for drilling deep wells in the oil and gas industry, are employed to deliver different tasks such as transporting the drilled cuttings from the borehole to the surface, cooling and lubricating the drilling equipment such as the drill bit, and drill string, cleaning the well, reducing friction between the drill string and both sides of well, minimizing drawback impact to the environment and protecting the metal equipment from wear, corrosion, and oxidation, etc. [1-7]. Drilling fluids significantly influence the effectiveness and overall cost of drilling operations, so employing drilling fluids with unsuitable properties can lead to severe problems throughout the drilling process. Generally, Base fluids can be divided into three categories: water and oil [2,3,6,7]. Emulsion-based drilling fluids have recently attracted substantial attention in contemporary drilling operations as an essential class of drilling fluid systems. Emulsion-based drilling fluids are sorted into three different types based on the nature of the dispersed part, including oil-in-water (O/W) emulsion, water-in-oil (W/O) emulsion, and multiple emulsions [5-8]. Among these, oil-in-water emulsions are considered as most suitable drilling fluids because of their low cost, convenient preparation, and environmental friendliness. However, oil-in-water emulsion drilling fluids present corrosion problems primarily because they are subject to contamination from dissolved gas, salts, and organic acids [3,6].

One of the most crucial problems in the drilling industry is the corrosion of drilling metallic equipment, which causes not only economic losses but also problems related to effectiveness, safety and protection of resources. The harsh conditions of the well and reservoirs medium due to the presence of acidic gases like CO₂, H₂S, dissolved oxygen gas, corrosive salt ions such as Cl⁻,

K^+ and Na^+ , and other factors such as extreme pressure and temperature in drilling conditions accelerate cathodic and anodic reactions of metallic equipment as a result of its interaction with its surroundings, which makes the surface of components such as drill bit, drill string, drill collar suffer from corrosion effects [6,9-14]. Indeed, the corrosion process on the surface of this equipment affects not only the chemical behaviors of metal or metal alloys but also changes their physical behaviors and mechanical performances, leading to loss of materials, leaking, product loss and, at times, ultimate failure [6,13,14]. Consequently, before a critical point of failure is reached, the equipment needs to be replaced.

Wear is another leading cause of material loss during drilling and extraction due to many physical and mechanical contacts between different components with sides of the well and casing (metal-rock or metal-metal contact), especially for drilling processes of deeper wells [15-17]. Different kinds of wear can occur in the drilling industry where abrasive, erosive, fatigue and corrosive wear are known as the main wear mechanisms of drilling tools used for the well drilling process, causing malfunction of these tools with the potential of catastrophic failures [15-18]. Therefore, wearing of drilling equipment during the drilling of a wellbore is regarded as one of the most critical problems in the drilling industry, creating various damages such as fatigue, buckling, washout, twist-off, and tooth loss, leading to lowered production efficiency, waste valuable materials and higher costs [15-17].

However, the combination of wear and corrosion, known as tribo-corrosion, can be more detrimental to the drilling equipment. Tribo-corrosion is an irreversible material transformation resulting from the simultaneous exposure of drilling equipment to mechanical loading (abrasion, friction) and chemical/electrochemical effects with the surrounding environment, accelerated by challenging operating circumstances such as high temperature, high pressure, and corrosive fluids

[19-23]. During drilling operations, the tribological contacts can intensify the corrosion rate of materials by breakdown or removing the protective film and exposing the electrochemical new surface available to aggressive drilling fluids. Corrosion, on the other hand, can influence the wear process by facilitating the initiation of pits and propagation of cracks on the steel surface. As a result, the volume loss of metallic equipment caused by tribo-corrosion is much higher than the sum of wear and corrosion separately [19-23]. Therefore, the combined impact of mechanical and reactive (chemical-electrochemical) damages accelerates the deterioration of drilling equipment, reducing their performance and lifespan, and raising maintenance costs, negatively impacting the overall productivity and profitability of drilling operations [19,21,24]. To tackle this problem, it is crucial to comprehend the tribo-corrosion performance of drilling equipment under different conditions for optimizing drilling operations and improving equipment efficiency, resulting in both scientific and economic benefits.

The tribo-corrosion performance of metallic equipment during drilling operations can be affected by multiple interdependent variables, such as environmental factors [25-26], material properties [27-28], surface finish [27,29], solution chemistry [30], sliding speed [23], sliding forces [31], and electrochemical potential [32]. This study investigates the effect of three controllable parameters (sliding speed, sliding force and electrochemical potential) and solution chemistry on the tribo-corrosion behavior of metallic equipment immersed in drilling fluids. Controlling the sliding speed during drilling operations significantly impacts the tribo-corrosion resistance of materials by affecting the lubrication regime, which can be changed from a boundary regime to mixed or full-film hydrodynamic lubrication. At low sliding speeds, the lubrication between rubbing surfaces is referred to as boundary lubrication, where the surface asperities are in close contact. The increased sliding speed reduces the contact area between surfaces due to forming a

thick layer. Furthermore, the change in sliding speed would be expected to alter the momentum transfer in the normal direction, thus, providing an upward force on the upper surface. Consequently, a reduction in the contact area between mutual surfaces can occur, which enhances the tribo-corrosion performance. However, if the speed increases beyond a specific critical value, the regime shifts to full-film hydrodynamic lubrication, where the tribo-corrosion resistance of drilling equipment begins to decrease again [33-34]. Sliding force, another crucial controllable parameter during drilling operations, affects materials' anti-tribo-corrosion properties due to mechanical damage and surface deformation. Indeed, the contact pressure during the sliding process creates a friction force which can result in the elimination of surface material and the formation of microscopic defects such as cracks, ploughs, and grooves. These effects can increase the surface area to be exposed to a corrosive environment, accelerating the corrosion process, and ultimately leading to the deterioration and failure of the metallic drilling equipment with severe consequences. Moreover, the sliding force can generate heat which accelerates the corrosion process by increasing the electrochemical reactions on the surface of the drilling equipment [34-37]. The electrochemical potential applied to the drilling equipment determines the direction and magnitude of electron transfer at the metal-electrolyte interface, leading to changes in the electrochemical potential. Depending on the electrochemical potential of the electrode (the electric potential difference between the metal electrode and electrolyte solution), metallic drilling equipment may be protected cathodically or dissolved anodically, impacting the tribo-corrosion rate of metallic equipment during drilling operations [38-40]. Thus, controlling and regulating these controllable factors is essential to provide the long durability and integrity of drilling equipment.

The addition of green corrosion inhibitors in drilling fluid offers a cost-effective and prospective approach to modifying the solution chemistry, resulting in the generation of a protective layer on the drilling equipment's surface [30,41-43]. This film effectively decreases metallic equipment's corrosion processes and wear rate, highlighting the potential benefits of using corrosion inhibitors in the drilling industry. The green corrosion inhibitors bearing heteroatoms with high electron density such as oxygen, nitrogen, sulfur, and phosphorous or those including aromatic rings, double or triple bonds and π -electrons in their chemical structures are considered as adsorption centers which can interact with the metal during drilling operations [3,41-42,47,50]. The adsorption of corrosion inhibitor molecules on the steel-electrolyte interface occurs through physical interaction (electrostatic interaction between corrosion inhibitor and metallic surface) or chemical interaction (donating unshared electrons of adsorption centers in the structure of inhibitor molecules into the free orbital d of metal atoms), forming a protective film on the surface of metallic equipment. This film induced by corrosion inhibitors mitigates the penetration of corrosive ions towards anodic and cathodic sites, thereby reducing the corrosion, wear, and friction between the surfaces in contact [41-42, 44-47]. Thus, combining green corrosion inhibitors and techniques like controlling the sliding speed, sliding force, and electrochemical potential can provide superior protection of drilling equipment against tribo-corrosion.

Despite the significance of the tribo-corrosion behavior of metallic equipment under different conditions in the drilling industry, our understanding of this phenomenon remains limited. Mao et al. [48] examined the corrosive-wear behavior of Cr13 steel casing immersed in various concentrations of oil-in-water drilling fluid. The observed results indicated a reduction trend in the wear rate and mean friction coefficient of steel immersed in drilling fluid as the oil-water ratio enhanced from 0 to 3 percent and then increased when the ratio further enhanced from

3-5. They also reported an increase in the corrosion rate of the Cr13 casing as the oil-water ratio increased from 3 to 5 percent. Change in the degradation mechanism of casings immersed in the drilling fluids was observed from abrasive wear in low concentrations (0-2%) to corrosive wear in high weight percentages of adding diesel oil into drilling fluids (3-5%). In another study, Yao et al. [49] evaluated the effect of benzotriazole and imidazoline on the tribo-corrosion performance of composite reinforced by Tungsten-carbide (WC-FeCuNiSn alloy matrix) for drilling bits used in the saline drilling fluid. The research indicated that benzotriazole could improve the anti-tribo-corrosion properties of WC-based material by reducing the corrosion current density and total weight loss due to the adsorption of inhibitor molecules on the composite surface, generating a protective layer which decreased corrosion and affected the contact condition between the sample surface and counterpart, leading to enhanced resistance of the composite to tribo-corrosion. In another study by Panda et al. [30], the tribo-corrosion inhibition performance of AISI 4715 steel pipe exposed to drilling fluid was examined. The results demonstrated that using two organic corrosion inhibitors effectively improved the wear-corrosion resistance of the steel pipe by creating a protective film on its surface. This film served as a barrier against tribo-corrosion, significantly reducing the degradation of the steel pipe's surface. Ouknin et al. [50] studied the inhibition effect of *Thymus wilddenowii* Boiss & Reut essential oil (TW) on tribo-corrosion of AISI 304 L stainless steel in acidic environments. They observed that the addition of TW oil in 0.5 M H₂SO₄ affected the performance of AISI 304 L with a remarkable reduction in friction, wear, and corrosion during the sliding process, which could be ascribed to chemical adsorption of thymol as a significant compound of TW on the surface of the steel. Brandon et al. [51] studied the corrosion-wear behavior of En24 steel in aqueous drilling mud under various electrochemical potentials and revealed that the tribo-corrosion resistance of En24 steel increased on the

application of a cathodic potential. They also found that applied potential affected the mode of wear from two-body abrasion at the cathodic potential to corrosion-assisted three-body abrasion at the anodic potential. The wear behavior of P110 steel casing samples immersed in oil-based and water-based drilling fluids containing corrosive ions under different sliding loads and speeds was investigated by Osman [52]. They explained that the material loss of casing samples tested in the water-based fluid was more than twice those immersed in the oil-based drilling fluid, and also demonstrated increases and decreases in the wear resistance of P110 steel casing as the normal load and sliding speed increased, respectively. Mao et al. [53] observed that the corrosive wear performance of the drilling pipe varied significantly depending on the rotational speed of the drilling pipe in simulated drilling conditions. They found that the wear rate of drilling pipe against steel case in simulated drilling mud reached the lowest rate and then increased as the sliding velocity increased. Such a behavior was attributed to multiple types of wear, including abrasive, erosive, and corrosive wear.

In the realm of corrosion inhibition research, a substantial part of studies has focused on evaluating the effect of green corrosion inhibitors on the corrosion resistance of carbon steel in aggressive media. However, there exists a notable gap in our understanding of how green corrosion inhibitors affect the tribo-corrosion performance of metallic structures immersed in drilling fluids. This knowledge gap is particularly significant in the context of the drilling industry, where both wear and corrosion processes can severely impact the integrity and longevity of drilling metallic equipment. While previous studies have shed light on the individual aspects of wear and corrosion, the synergistic interaction between these phenomena, known as tribo-corrosion, remains relatively unexplored in the presence of green corrosion inhibitors. This gap in our knowledge underscores the critical need for comprehensive research in this area to mitigate the destructive effects on

drilling equipment. This study seeks to address this gap by focusing on improving the wear, corrosion, and tribo-corrosion resistance of carbon steel immersed in emulsion-based drilling fluids containing green corrosion inhibitors, as well as some controllable parameters such as sliding speed, contact force, and electrochemical potential. By doing so, we aim to contribute to the development of effective green lubricants for industrial drilling systems in aggressive environments to minimize the simultaneous effects of wear and corrosion on metallic equipment. Our research endeavours to elucidate the intricate mechanisms by which green corrosion inhibitors influence the interplay between wear and corrosion, ultimately enhancing the durability and performance of metallic equipment in drilling applications.

Therefore, attempts to improve tribo-corrosion resistance of metallic equipment during drilling operations under various conditions are limited and wear-corrosion synergy occurs inevitably. Thus, it is paramount to study the mechanisms responsible for tribo-corrosion performance to develop effective strategies to suppress wear and corrosion of metallic equipment during drilling operations. This study focuses on exploring green corrosion inhibitors for drilling fluids and investigating effects of various parameters such as sliding speed, sliding force, electrochemical potential, and modifying solution chemistry on tribo-corrosion of carbon steel using different experimental techniques, including electrochemical tests, tribological measurements and surface characterization methods to obtain comprehensive information on the underlying mechanisms that are affecting tribo-corrosion performance. Results of this study are expected to help improve the efficiency and increase the lifespan and reliability of metallic equipment during the drilling process.

1.2 Thesis outline

Based on the above introduction, it is essential to understand the pure wear, pure corrosion, and tribo-corrosion behavior of metallic equipment under different conditions. The literature review shows knowledge gaps in understanding tribo-corrosion mechanisms under other conditions. This thesis comprises seven chapters, briefly describing its structure in the following paragraphs.

Chapter 2, entitled “Green corrosion inhibitors for drilling operation: New derivatives of fatty acid-based inhibitors in drilling fluids against pure corrosion of 1018 carbon steel in CO₂-saturated KCl environments,” provides a comprehensive evaluation of the effect of three different eco-friendly corrosion inhibitors containing heteroatoms oxygen and nitrogen against pure corrosion (without wear) of carbon steel in the simulated drilling fluids by electrochemical techniques. This chapter demonstrates that the presence of corrosion inhibitors changes the solution chemistry of the drilling fluids, thereby influencing the corrosion resistance of carbon steel. The study shows that all corrosion inhibitors have high inhibition capabilities, resulting from the formation of an effective protective film that blocks corrosive ions from attacking the steel surface.

Chapter 3, entitled “Improve the tribo-corrosion performance of oil-in-water emulsion-based drilling fluids by new derivatives of fatty acid-based green corrosion inhibitors,” presents remarkable increase in the tribo-corrosion (synergy between wear and corrosion) resistance of 1018 carbon steel immersed in drilling fluids containing green corrosion inhibitors with oxygen and nitrogen elements (change in solution chemistry) under specific conditions of a sliding force of 10N, speed of 2mm/s and electrochemical potential of 1mV. In addition, the chapter also shows how the concentrations of corrosion inhibitors affect the tribo-corrosion performance of carbon steel and demonstrates that the tribo-corrosion properties of drilling fluids are remarkably

improved by the corrosion inhibitors, evidenced by the significant reduction in corrosion, COF, and wear.

Chapter 4, entitled “Effect of sliding speed on corrosion and tribo-corrosion of carbon steel in emulsion-based drilling fluids with green corrosion inhibitors,” focuses on the effects of the sliding speed on corrosion potential, corrosion rate, COF, and wear rate of the steel under loading (tribo-corrosion) and without loading (pure corrosion) conditions. It is shown that the corrosive wear rate is raised with increasing sliding speed. During both corrosion and tribo-corrosion, increasing the sliding speed reduces the corrosion rate, which re-rose as the sliding speed continuously increases. The green inhibitors decrease corrosion and tribo-corrosion at different sliding speeds.

Chapter 5, entitled “Phosphate-derived green corrosion inhibitors: enhancing anti-tribo-corrosion properties of carbon steel in emulsion-based drilling fluids,” investigates anti-corrosion properties, tribological performance, wear-corrosion synergy, and adsorption isotherm of carbon steel at different sliding speeds with a fixed contact load and fixed electrochemical potential of 1 mV. It is depicted that an increase in sliding speed leads to improved corrosion resistance and frictional resistance of steel during tribo-corrosion experiments, which are attributed to a higher adsorption rate of corrosion inhibitors (containing nitrogen and phosphorous elements) at higher speeds and the effect is more pronounced for corrosion inhibitor containing phosphorous element. Moreover, the presence of corrosion inhibitors suppressed the wear-corrosion synergy compared to brine solution. However, the wear-corrosion synergy of carbon steel increases with increased sliding speeds.

Chapter 6, entitled “Influences of contact forces and electrochemical potential on tribo-corrosion protection of 1018 carbon steel in the drilling fluids by in-situ electrochemical

techniques,” reports the electrochemical and tribological behavior of steel samples immersed in drilling fluids loading with corrosion inhibitors containing three different heteroatoms (oxygen, nitrogen and phosphorous) at different cathodic-anodic potentials (-0.3, -0.1, 0, 0.1, 0.3 V vs OCP) and contact forces (2, 4, 8, 10) at a sliding speed of 2 mm/s. It is shown that the anti-tribo-corrosion resistance of steel samples, especially in the solution without corrosion inhibitors, reduced with increasing sliding forces and potentials from cathodic towards anodic condition due to intensified mechanical wear and a more substantial synergistic effect between wear and corrosion.

Chapter 7 summarizes the findings and proposes ideas for future work. The references used in this thesis are listed in alphabetical order.

Chapter 2 Green corrosion inhibitors for drilling operation: New derivatives of fatty acid-based inhibitors in drilling fluids against corrosion of 1018 carbon steel in CO₂-saturated KCl environments¹

2.1 Introduction

The drilling fluid is one of important components in the oil/gas well drilling operation, which is circulated in the wellbore. The selection and designing of a proper drilling fluid influence the drilling process, including moving cuttings from the bottom of well to the surface, declining environment impact, reducing surface temperature of machinery from friction and protecting it from oxidation and corrosion, etc. [5,7,55-57]. There are different types of drilling fluid, which may be categorized into two basic types: oil-based and water-based drilling fluids [7]. In recent years, more attention has been paid to emulsion-based drilling fluids [5], which have three different types, including oil-in-water (O/W) emulsion-based drilling fluid, water-in-oil (W/O) emulsion-based drilling fluid and multiple emulsions. The oil-in-water emulsion-based fluid or water-based emulsion fluid contains oil as a dispersed phase in water. This type of drilling fluid is the most favorable fluid among all types due to its low cost, availability, and eco-friendliness. However, the corrosivity of water-based emulsion drilling fluids is a serious problem during drilling operation [58-61].

Corrosion is a major cause of deterioration and failure of steel drilling equipment, a growing threat in the drilling industry, resulting in economic, environmental pollution, safety and

¹ A version of this chapter has been published. M.j. Palimi, Y. Tang, V. Alvarez, E. Kuru, D.Y. Li Green corrosion inhibitors for drilling operation: New derivatives of fatty acid-based inhibitors in drilling fluids for 1018 carbon steel in CO₂-saturated KCl environments, *Materials Chemistry and Physics*, 288 (2022) 126406.

technological irreparable consequences [10]. During drilling processes, corrosion caused by CO₂ has been recognized as one of the most destructive corrosion forms in the drilling industry. There are various sources for CO₂ coming into drilling fluids such as excessive carbonates like sodium carbonates in the drilling fluids, invasion of CO₂-containing natural gas formations into drilling fluids and decomposition of drilling fluid additives at high temperatures and high pressures. The performance and properties of drilling fluids can be influenced by dissolved CO₂ gas due to the formation of carbonic acid (H₂CO₃) resulting from the reaction of CO₂ with water. As a result, the interaction between steel and the surrounding medium containing CO₂ causes the formation of iron carbonate (FeCO₃) as the corrosion product, which further accelerates corrosion of the equipment made of steel. Localized and general corrosion occur as two of the most common corrosion processes in the drilling processes [62-65], which need to be prevented or mitigated. The degradation of steel in such corrosive environments can be considerably accelerated if the mechanical attack is involved such as wear due to the corrosion-wear synergy [66,67]. Among various methods for preventing the degradation of steel surface, such as modification of the steel, application of protective coatings, and use of scavengers, etc., corrosion inhibitors are known as one of the most effective and practical approaches for protecting metallic surfaces from degradation in corrosive environments [68-74].

Corrosion inhibitors are chemical substances, which protect materials against corrosion in aggressive environments. The inhibitor adheres to the surface of a metal or alloy to form a protective film, which declines the corrosion rate of the metallic surface in the corrosive environment. The interaction between the metallic surface and the corrosion inhibitor may remarkably affect the performance of corrosion inhibitors through influencing both the dynamics and kinetics of electrochemical reactions during the corrosion process [44, 75]. However, although

many traditional corrosion inhibitors are available for selection, e.g., chromate and phosphate, they are restricted due to their toxicity and content of heavy metals, which negatively influence the surrounding environment. Therefore, it is highly desired to replace the toxic and expensive inhibitors with green ones for various industrial applications [76-78].

In recent years, considerable efforts have been made to develop green corrosion inhibitors such as those extracted from plants, which are eco-friendly and inexpensive, compared to many conventional corrosion inhibitors. Hence, the green inhibitors are considered to be ideal for replacing existing expensive and toxic corrosion inhibitors [79-81]. The plant extracts are classified into organic and aqueous kinds, respectively containing non-polar and polar phytochemicals, both of which can be employed for metal protection in different corrosive environments. The phytochemicals in the green inhibitors include, e.g., amino acids, phlobatannins, glycosides, phenolic compounds, heteroatoms, alkaloids, etc., which determine the performance of the green inhibitors. The polar group in the phytochemicals includes amino, carboxylic acid, amide, hydroxyl, and ester, etc., while the non-polar group includes, e.g., aliphatic chains, aromatic rings, heterocyclic rings, and others. These compounds play a significant role in affecting the adsorption of the phytochemicals on metallic surfaces to protect them from corrosion without causing harm to the environment [80,82]. The adsorption of the phytochemicals may result from physical interaction, chemical interaction, or a combination of both. In general, physisorption occurs through electrostatic interactions between heteroatoms of phytochemicals and metal surfaces due to attraction between their opposite charges. The electrons sharing between lone pair electrons of (N, S, O and P), aromatic rings, double or triple bonds and π -electrons of phytochemicals with free orbital d of metal cause chemical sorption. After adsorption, the phytochemicals produce a protective layer on the metal surface, thereby blocking the surface from

interactions with surroundings, thus affecting the cathodic and anodic reactions of the corrosion process with reduced corrosion rate [46, 80, 83-84].

Studies related to effects of green corrosion inhibitors on corrosion of steels used in oilfield applications can be found in the literature. For instance, Onyyeachu et al. [85] studied the inhibition effect of 2-(2-pyridyl) benzimidazole on API X60 steel in NACE brine solution. They observed that benzimidazole derivative could protect the steel from CO₂ attacks by adsorption N-H group of benzimidazol ring on the metal surface, thus restricting the access for corrosive agents to reach the surface of X60 steel. They reported that corrosion inhibition efficiency increased from 46% to 67.3% with increasing the inhibitor concentration. Xionghu et al [86] reported the addition of benzotriazole in the synthetic-based drilling fluid, which resulted in significant reduction in the corrosion rate of steel. Ghareba et al. [87] investigated the interaction of 12-aminododecanoic as amino fatty acid with steel surface in CO₂-saturated HCl solution, and showed that the 12-aminododecanoic addition in the electrolyte significantly improved the performance of the corrosion inhibition capability. The inhibition efficiency in the presence of 12-aminododecanoic reached 89 % in a low concentration of 3 mM after 2 h immersion, which might benefit from a self-assembled monolayer formed on the metal surface with a tight hydrophobic barrier due to long chain hydrocarbons in the structure. A number of studies were devoted to the use of corrosion inhibitors to decline corrosion of steel in oil and gas fields. Results of relevant studies on representative corrosion inhibitors were summaries in Table 2.1.

Table 2.1. Representative inhibitors and their inhibition efficiencies (η) used for oilfield applications.

Corrosion Inhibitor	Steel	Medium	η (%)	Inhibitor concentration
Gum Arabic [88]	Carbon steel	CO ₂ -saturated KCl environment	67.04	0.5 g/L
5-(benzylthio)-1,3,4-thiadiazol-2-amine [89]	Mild steel	CO ₂ -saturated oilfield produced water	99.4	0.2 mM
5,5-disulfaneyldibis (1,3,4-thiadiazol-2-amine) [89]	Mild steel	CO ₂ -saturated oilfield produced water	99.2	0.025 mM
Lauric acid [90]	Carbon steel	CO ₂ -saturated oilfield produced water	98.6	80 mg/L
Thiourea [90]	Carbon steel	CO ₂ -saturated oilfield produced water	94.6	40 mg/ L
1, 3,5,7 -tetrazaadamantane (TAA) [91]	Mild steel	CO ₂ -saturated oilfield produced water	91.8	74.4 ppm
Imidazoline derivative [92]	Carbon steel	CO ₂ -saturated oilfield produced water	91.2	100 mg/L
5-((benzylthio)methyl)-3-phenyl-2-thioxoimidazolidin-4-one [93]	Carbon steel	CO ₂ -saturated formation water	99.4	0.2 mM
Lemongrass extract [94]	Carbon steel	CO ₂ -saturated oilfield produced water	54.42	700 ppm
(5-(mercaptomethyl)-3-phenyl-2-thioxoimidazolidin-4-one [93]	Carbon steel	CO ₂ -saturated formation water	99.1	0.2 mM

Among green inhibitors, PEG-2 oleamide, GM and GL are three inexpensive and highly eco-friendly fatty acid-based corrosion inhibitors. These three green corrosion inhibitors can also be used as emulsifying, dispersing and lubricating agents in the preparation of drilling fluids. These unique features of PEG-2 oleamide, GM and GL help to produce highly stable drilling fluids which enable to increase the lubricity, reduce frictional resistance, remove heat from moving parts, and

enhance resistance to oxidation, wear and corrosion of steel surfaces during drilling processes. Currently, no information is available regarding corrosion inhibition effects of these green inhibitors on steel exposed to emulsion-based drilling fluids containing the CO₂-saturated KCl used in oilfield applications. Thus, this chapter is focused on the performance of the three green inhibitors in protecting 1018 carbon steel from corrosion when immersed in KCl media containing CO₂ for potential use as additives in emulsion-based drilling fluids as well as the elucidation of the underlying mechanisms.

In this chapter, the corrosion-inhibiting effectiveness of the fatty acid-based corrosion inhibitors was thoroughly evaluated using various electrochemical and chemical techniques, including OCP, EIS, potentiodynamic polarization and weight loss tests. FT-IR and CHNS-O analysis were employed to determine functional groups and compositions of the inhibitors. The surface chemistry and the composition of the layer adsorbed on the surface of steel were analyzed with XPS and SEM-EDS to gain an insight into the mechanisms for corrosion inhibition.

2.2 Experimental

2.2.1 Material

Potassium chloride was purchased from Fisher Scientific Company in order to prepare the base fluid, which was a 5% KCl aqueous solution. Potassium chloride is one of the most commonly used effective stabilizing agents in drilling fluids for shale and clay inhibition via the role of potassium ions in binding platelets of clay, thus limiting their dispersion and swelling during oil well drilling [95]. In the drilling operation, CO₂ is injected into the oil field to help recover more oil from the field by reducing oil viscosity, thus improving the efficiency of the displacement process i.e. displacing the oil from the rock pores, pushing it towards a producing well [96]. However, the dissolved CO₂ and potassium chloride make the drilling fluids corrosive, which can

cause damage to the drilling equipment made of steel. Thus, CO₂-saturated KCl solutions with and without the corrosion inhibitors were used for evaluating the performance of the inhibitors in protecting steel surface exposed to the CO₂-saturated KCl solution environment.

Different substances including (mineral oil, surfactant and three corrosion inhibitors) were added to the base fluid to make water-based emulsions. The mineral oil and TERGITOL NP-9 as surfactant, which was used to obtain a stable emulsion without coalescence of droplets during emulsion process, were provided by GFL Environmental Inc and Univar Canada Ltd., respectively. The three corrosion inhibitors, PEG-2 oleamide, GM and GL were purchased from Triple Point Chemical Ltd, Oleon Co and Croda Canada Ltd, respectively. Molecular structures of PEG-2 oleamide, GM and GL are illustrated in Fig. 2.1 Carbon steel (1018 steel) coupons were provided by Gamry company, which were used to evaluate their corrosion in the formulated WBEs (water-based emulsions), respectively. Table 2.2 gives composition of the carbon steel. For corrosion tests, steel samples were polished with SiC-based emery papers of 400 and 600 grades, followed by cleaning using acetone and isopropyl alcohol. Afterwards, they were washed with distilled water and then dried by a pressed air flow.

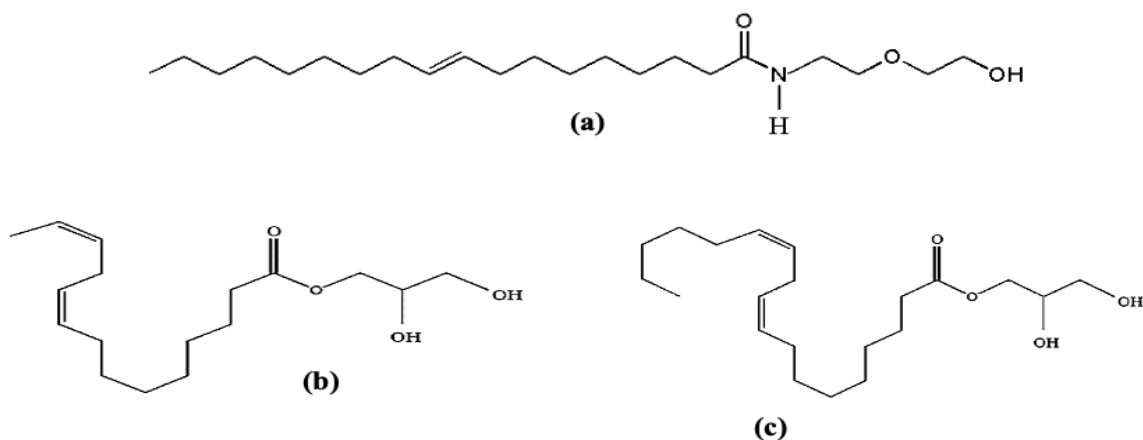


Fig. 2.1. Molecular structure of (a) PEG-2 oleamide, (b) Glycerol myristate (GM), and (c) Glycerol linoleate (GL).

Table 2.2. Composition of carbon steel 1018 specimens (wt.%)

Fe	C	Mn	P	S	Si	Cr	Ni	Cu	Al	Ti
98.90	0.20	0.75	0.011	0.004	0.026	0.02	0.02	0.03	0.035	0.001

2.2.2 Emulsion-based drilling fluids

Various emulsion-based drilling fluids were prepared, which consist of mineral oil, TERGITOL NP-9 (surfactant), corrosion inhibitors (PEG-2 oleamide, GM and GL), brine solution (5 gr KCl in 100 ml DI water) with different weight percentages, respectively. Details about the prepared drilling fluids are given in section 2.3.3 (Tables 2.5 and 2.6). In order to make a specific emulsion-based drilling fluid, the above-listed components with a certain combination were mixed using a mechanical stirrer at a speed of 700 RPM for a period of 30 min.

2.2.3. Characterization

2.2.3.1 FTIR Characterization

FTIR analysis was carried out to investigate the functional groups of three corrosion inhibitors of PEG-2 oleamide, GM and GL) present in the prepared emulsion-based drilling fluids. The spectra were taken in the spectral range of 4000 cm^{-1} to 600 cm^{-1} by a Nicolet 8700 at room temperature.

2.2.3.2 CHNS-O analysis

A Flash 2000 Organic Elemental Analyzer (Thermo Scientific, Cambridge, UK) was employed for CHNS-O elemental analysis in order to determine the total carbon, hydrogen, nitrogen, sulfur and oxygen in the three corrosion inhibitors for more information on their compositions and organic compounds.

2.2.3.3 Turbidity measurement

The stability of prepared water-based emulsions (WBEs) as drilling fluid was evaluated by HACH 2100 AN turbidimetry as an effective technique for studying the stability of an emulsion. In this test, the scattered light determines the emulsion fluctuations which can lead to change of turbidity value. The slope of changes in turbidity values significantly affects the emulsion stability so that the small slope values illustrate a stable emulsion in turbidity versus time plot [59].

2.2.3.4 Zeta potential study

The Zeta potential of emulsion droplets dispersed in the brine solution was measured using Zetasizer Nano-ZS (Malvern Instruments, UK). Zeta potential of prepared WBEs was determined from electrophoretic mobility to investigate the stability of various WBEs. The measurements were repeated three times for each WBE.

2.2.3.5 Electrochemical measurements

A formulated WBE as drilling fluid was placed in a 4-neck electrochemical cell equipped with CO₂ injection, and 3 electrodes including reference, counter and working electrodes. Prior to each test, the prepared WBE was saturated with CO₂ for 45 min. Thereafter, the rotating cylinder electrode containing cylindrical-shaped carbon steel coupons as working electrode was placed in the electrochemical cell, rotating at a speed of 1500 RPM for 2 h. CO₂ was introduced into the prepared WBE during the electrochemical measurement. This process was repeated three times for each WBE presented in Table 6 to ensure the repeatability of the electrochemical tests including EIS and potentiodynamic polarization which were performed after 2 hr. The corrosion resistance of cylindrical-shaped carbon steel specimens immersed in WBEs loaded with various corrosion inhibitors was evaluated with OCP, EIS and Polarization tests using a GAMRY instrument with a frequency range of 100 kHz ~ 200 mHz and perturbation of ± 10 mV at open circuit potential. The

polarization tests were carried out in the range of ± 250 mV from OCP at a sweep rate of 1 mV/s. The experiments were performed in a three-electrode cell consisting of a graphite (counter electrode), Ag/AgCl (reference electrode) and rotating cylinder electrode (working electrode). Triplicates were provided for each sample for the EIS measurements.

2.2.3.6 Surface analysis

SEM-EDS model Zeiss Evo M10 SEM-EDS (Zeiss, Oberkochen, German) was used to examine the surface morphology and the composition of the carbon steel coupons after CO₂ corrosion. It is important to note that while EDS provides valuable insights into the elemental composition of materials, it has certain limitations, particularly in accurately measuring carbon content. To overcome these limitations and obtain a more precise assessment of carbon content and its chemical environment, complementary techniques such as x-ray photoelectron spectroscopy (XPS) was employed. XPS provides detailed information about the chemical state and bonding environment of carbon and other elements on the surface of carbon steel, offering a more comprehensive analysis that complements the data obtained through EDS. Thus, composition of the protective film formed on sample surface and its chemical bond formation at the film/steel interface was investigated by XPS equipped with a concentric hemispherical analyzer.

2.3 Results and discussion

2.3.1 FTIR measurement

Considering the structures of corrosion inhibitors, various points where they may interact with the surface of steel need to be determined. Thus, identification and comparison of the functional groups of bonds within corrosion inhibitors molecules existed in WBEs were made through analysis with the FTIR spectroscopy. Fig. 2.2 depicts the FTIR spectra of the three fatty acid-based

corrosion inhibitors, PEG 2-oleamide, GM and GL. The main peaks and corresponding functional groups of the corrosion inhibitors are listed in Table 2.3.

As shown in Fig 2.2 and Table 2.3, adsorption bands at around 720 cm^{-1} corresponds to the vibration of C-H group due to the presence of long hydrocarbon chains in the structures of the three corrosion inhibitors. The FTIR spectra also show that all the corrosion inhibitors have two adsorption peaks at 1350 and 1460 cm^{-1} consisting of CH_2 and CH_3 bending modes, respectively. The FTIR peaks at 2850 and 2920 cm^{-1} indicate C-H asymmetric and symmetric stretching modes of PEG 2-oleamide, GM and GL. The peaks observed at 1190 , 1540 and 3300 cm^{-1} are referred to C-N stretching vibration, N-H bending and stretching vibrations, respectively, indicating the presence of nitrogen atom in the structure of PEG-2 oleamide (Fig.2.2(a)) which can be adsorbed on the 1018 carbon steel through donor-acceptor interactions. The C=C and C=O stretching bands are clearly visible at 1640 and 1700 cm^{-1} in the FTIR spectra which is correlated to the presence of unsaturated fatty acid in the corrosion inhibitor structure of PEG-2 oleamide [97]. Figs. 2.2(b), 2.2(c) and Table 2.3 show two absorption bands at 1040 and 1240 cm^{-1} wavenumbers attributed to C-O-C stretching modes, describing the compound in these corrosion inhibitors. In addition, the peaks in the region between 1090 and 1160 cm^{-1} indicate by the presence of C-O stretch bands for GM and GL. The bands at 1560 cm^{-1} and 1740 cm^{-1} can be ascribed to C=C stretching bond and C=O stretching peak due to the presence of unsaturated fatty acid in the structure of GM and GL. The absorption band at around 3410 cm^{-1} confirms the presence of O-H stretching vibration for GM and GL [98]. These findings reveal that PEG-2 oleamide has nitrogen and oxygen which are considered as active sites for interacting with the carbon steel. Whereas GM and GL have oxygen in their structures that are capable to react with the steel surface [99].

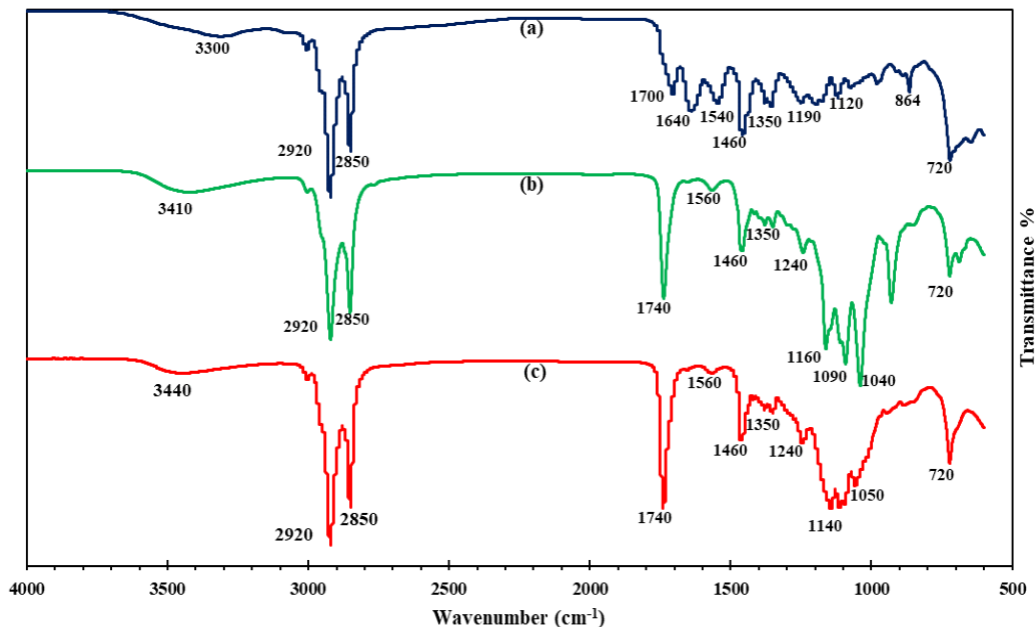


Fig. 2.2. FTIR spectrum of (a) PEG-2 oleamide, (b) GM and (c) GL used in WBEs preparation.

Table 2.3. Prominent absorption peaks obtained from FTIR spectra of the three fatty acid-based corrosion inhibitors and corresponding functional groups [97-99]

Corrosion inhibitor	Wavenumber (cm ⁻¹)	Functionality
PEG-2 oleamide	1190	C-N stretching vibration
	1350,1460	CH ₂ and CH ₃ bending
	1540	N-H bending vibration
	1640	C=C stretching vibration
	1700	C=O stretching vibration
	2850	C-H symmetric stretching mode
	2920	C-H asymmetric stretching mode
	3300	N-H stretching vibration
GM	1040, 1240	C-O-C stretching
	1090, 1160	C-O stretching
	1350,1460	CH ₂ and CH ₃ bending
	1560	C=C stretching
	1740	C=O stretching vibration
	2850	C-H symmetric stretching mode
	2920	C-H asymmetric stretching mode
3410	O-H stretching vibration	

GL	1050, 1240	C-O-C stretching
	1050, 1140	C-O stretching
	1350,1460	CH ₂ and CH ₃ bending
	1560	C=C stretching
	1740	C=O stretching vibration
	2850	C-H symmetric stretching mode
	2920	C-H asymmetric stretching mode
	3440	O-H stretching vibration

2.3.2 CHNS-O analysis

Results of the CHNS-O analysis for the three corrosion inhibitors of PEG-2 oleamide, GM and GL are presented in Table 2.4.

Table 2.4. Values of CHNS-O elemental analysis for the three corrosion inhibitors and theoretical values based on their structures

Sample	% C		% H		% N		% O	
	Measured values	stoichiometric values						
PEG-2 oleamide	71.65	71.54	10.99	11.65	3.29	3.79	14.07	13.01
GL	71.29	71.38	11.15	10.48	-	-	17.56	18.13
GM	68.13	68.68	10.66	9.76	-	-	21.21	21.54

As shown, the values determined by CHNS-O analysis are very close to the theoretical values. According to Table 2.4, a small amount of nitrogen (3.29%) was detected in the structure of PEG-2 oleamide while two other corrosion inhibitors do not contain nitrogen. In addition, no sulfur was detected in the inhibitors. The high percentages of carbon indicate long carbon chains in the structure of fatty acid-based inhibitors known as long-chain fatty acids. These types of corrosion

inhibitor (more than six carbons) due to their hydrophobic nature prevent water to be adsorbed by the metal surface, leading to the inhibition effect [100].

2.3.3 Stability results

The stability of the formulated water-based emulsions (WBEs) as the drilling fluids is crucial and needs to be evaluated. In order to determine the optimum concentrations of mineral oil, TERGITOL NP-9 as surfactant, and the corrosion inhibitor PEG-2 oleamide, various WBEs were prepared with 65% mineral oil and different weight percentages of the surfactant (0 to 35%) and the corrosion inhibitor (0 to 35%) by dilution with the brine solution. Table 2.5 lists the prepared drilling fluids denoted as WBE (a) to (g), which were prepared by mixing 0.1g (Mineral oil + TERGITOL NP-9 + PEG-2 oleamide) in 99.9 g brine. The stability of the prepared WBEs was evaluated by turbidity measurements and zeta potential analysis.

Table 2.5 Formulated water-based emulsions (WBEs) as drilling fluid

Solution	Ingredient
WBE (a)	0.1g (65% Mineral oil + 35% TERGITOL NP-9) in 99.9 g brine solution
WBE (b)	0.1g (65% Mineral oil + 30% TERGITOL NP-9 + 5% PEG-2 oleamide) in 99.9 g brine solution
WBE (c)	0.1g (65% Mineral oil + 20% TERGITOL NP-9 + 15% PEG-2 oleamide) in 99.9 g brine solution
WBE (d)	0.1g (65% Mineral oil + 10% TERGITOL NP-9 + 25% PEG-2 oleamide) in 99.9 g brine solution
WBE (e)	0.1g (65% Mineral oil + 5% TERGITOL NP-9 + 30% PEG-2 oleamide) in 99.9 g brine solution
WBE (f)	0.1g (65% Mineral oil + 3 % TERGITOL NP-9 + 32% PEG-2 oleamide) in 99.9 g brine solution
WBE (g)	0.1g (65% Mineral oil + 0 % TERGITOL NP-9 + 35% PEG-2 oleamide) in 99.9 g brine solution

2.3.3.1 Turbidity results

The stability of various WBEs was determined by measured turbidity values of the WBEs for a period of 4 h, which are illustrated in Fig. 2.3.

As shown, the turbidity of all the formulated WBEs declines with time until saturation. One may see that WBE (c) and WBE (f) show the highest stabilities due to lower slopes of their turbidity curves within 4 h. While WBE (d) and WBE (e) show the lowest stabilities, compared to other emulsions, evidenced by significant reductions of 166 and 136 NTU in turbidity value over a period of 4 h, respectively. Other WBEs also depict relatively lower stabilities.

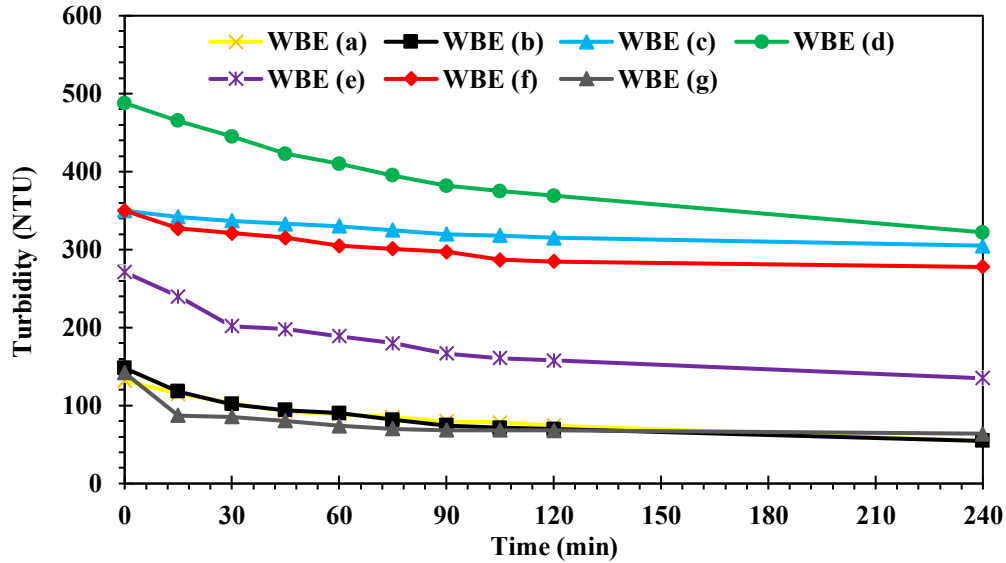


Fig. 2.3 Turbidity values of the prepared WBEs measured at different time intervals.

2.3.3.2 Zeta potential measurement

Zeta potential is another important parameter for evaluating the stability of the oil-in-water emulsions i.e., WBE (a) to (g). Zeta potential is related to the strength of repulsive force between droplets formed in aqueous phase and their surface charges affect the WBEs stability. Zeta potential values of the prepared WBEs are shown in Fig. 2.4.

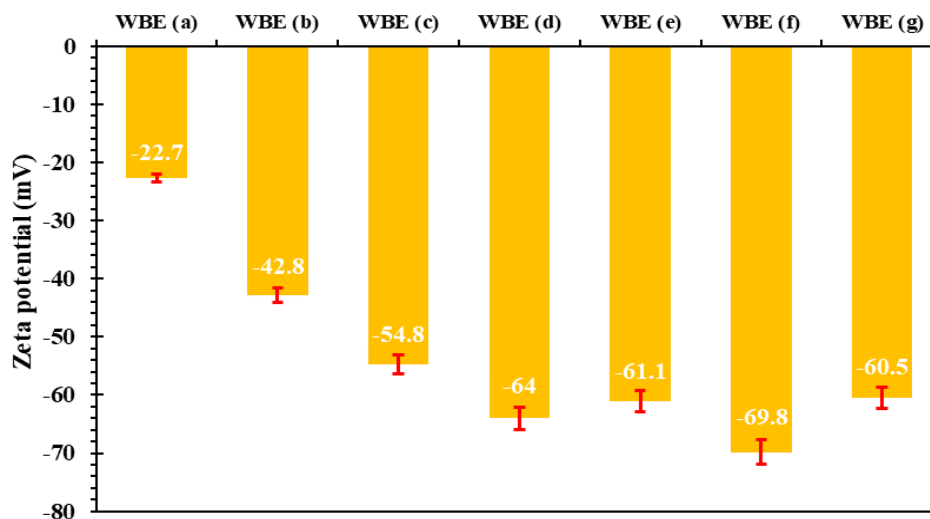


Fig. 2.4 Zeta potentials of the formulated WBEs listed in Table 5.

According to Fig. 2.4, all prepared WBEs depicted negative zeta potentials which can be attributed to the presence of non-polar hydrocarbons in the structure of ingredients consisting mineral oil, TERGITOL NP-9 and PEG-2 oleamide in the WBEs [101]. Three prepared WBEs with the highest weight percentages of surfactants [35 % in WBE (a), 30 % in WBE (b) and 20 % in WBE (c)] show the lowest absolute zeta potential values of approximately -22.7 mV to -54.8 mV. In fact, high concentrations of surfactant lead to the formation of micelles in the continuous phase, resulting in a solubilization effect on the surface of surfactants at the interface between dispersed phase and continuous phase. This effect causes an incomplete surface coverage on the emulsion droplets in the brine solution with reduced strength of the interface film. Thus, the layer adsorbed on the surface of emulsion droplets is not capable to effectively reduce the interfacial tension between droplets and aqueous phase. As a result, weak emulsion stability can occur due to the agglomeration and coalescence of emulsion droplets [102]. However, the addition of TERGITOL NP-9 with lower concentrations ($\leq 10\%$) exhibits larger absolute zeta potential values [-60.5 mV for WBE (g) to -69.85 mV for WBE (f)]. These large absolute zeta potential values may be correlated to high steric and electrostatic repulsion between emulsion droplets which

prevents the aggregation of droplets dispersed in the aqueous phase. Therefore, the addition of surfactant molecules with appropriate concentration can be effectively adsorbed at the oil-water interface, resulting in a reduction in interfacial tension and thus an increase in the emulsion stability. Fig. 2.4 also shows that the highest absolute zeta potential value was obtained for WBE (f) with 65% mineral oil + 3% surfactant + 32 % corrosion inhibitor. This indicates that repulsive forces between the emulsion droplets formed in the brine solution dominate their attraction forces, leading to the formation of highly stable WBEs.

Based on the results of turbidity and zeta potential measurements (Figs. 2.3 and 2.4), WBE (f) combining 65% mineral oil, 3% surfactant and 32% corrosion inhibitor (PEG-2 oleamide) is the most stable water-based emulsions (WBEs). Thus, this stable combination was selected to prepare WBEs with various corrosion inhibitors, PEG-2 oleamide, GM and GL, in order to evaluate and compare their corrosion inhibition performances for 1018 carbon steel. Table 6 lists the formulated water-based emulsions (WBEs) as the drilling fluids.

Table 2.6 Formulated water-based emulsions (WBEs) as drilling fluid

Solution	Ingredient
WBE 0	Brine solution as a reference solution: 5 gr KCl in 100 ml DI water [103, 104]
WBE 1	0.1g (Mineral oil) in 99.9 g brine solution
WBE 2	0.1g (65% Mineral oil + 35% TERGITOL NP-9) in 99.9 g brine solution
WBE 3	0.1g (65% Mineral oil + 3% TERGITOL NP-9 + 32% GL) in 99.9 g brine solution
WBE 4	0.1g (65% Mineral oil + 3% TERGITOL NP-9 + 32% PEG-2 oleamide) in 99.9 g brine solution
WBE 5	0.1 g (65% Mineral oil + 3% TERGITOL NP-9 + 32% GM) in 99.9 g brine solution

2.3.4 Corrosion performance studies

2.3.4.1. OCP measurements

Fig. 2.5 depicts values of OCP of steel samples immersed in various solutions over different immersion durations. As shown in Figure 5, more positive OCP values can be determined when

carbon steel coupons were immersed in WBEs containing corrosion inhibitors, compared to WBEs without corrosion inhibitors. Results of the tests demonstrate the positive effect of the three fatty acid-based corrosion inhibitors on OCP of the carbon steel samples. The most positive OCP value was obtained when the steel samples were exposed to WBE 4 containing PEG-2 oleamide for all immersion times, which is approximately at -0.55 V. The result depicts that PEG-2 oleamide is the most effective corrosion inhibitor in restricting corrosive agents in contact with the metal surface through forming a more protective layer. Among all solutions, WBE 1 and brine solution lead to lower OCP values.

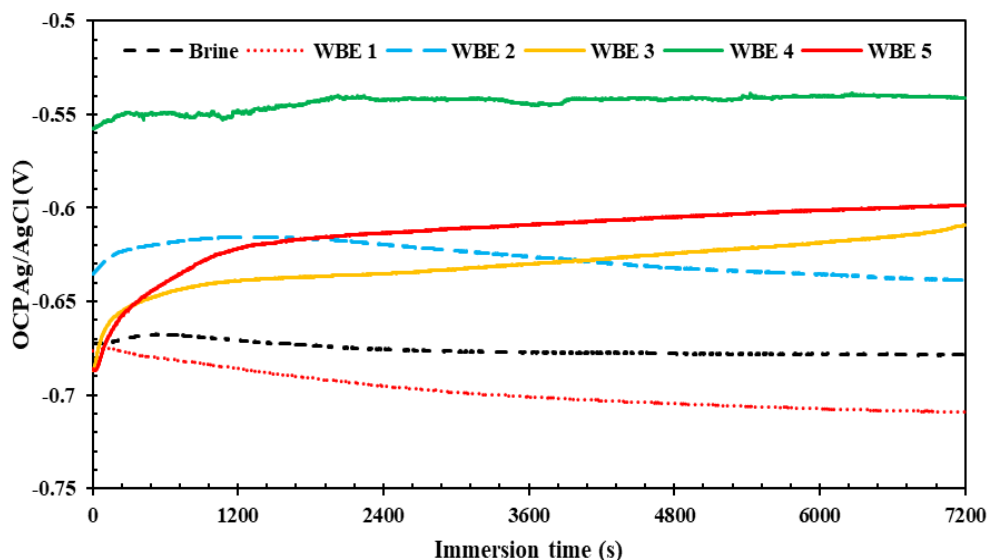


Fig. 2.5. Variations in OCP versus immersion time for the 1018 carbon steel samples immersed in the brine solution and various WBEs under the influence of CO₂ corrosion.

2.3.4.2. EIS measurements

Electrochemical performance of the carbon steel samples immersed in various WBEs under the influence of CO₂ after 2h was investigated through EIS analysis. Fig 2.6 illustrates the Bode and Nyquist plots of the steel samples exposed to the brine solution (5 wt.% KCl solutions) and WBEs after immersion for 2 h.

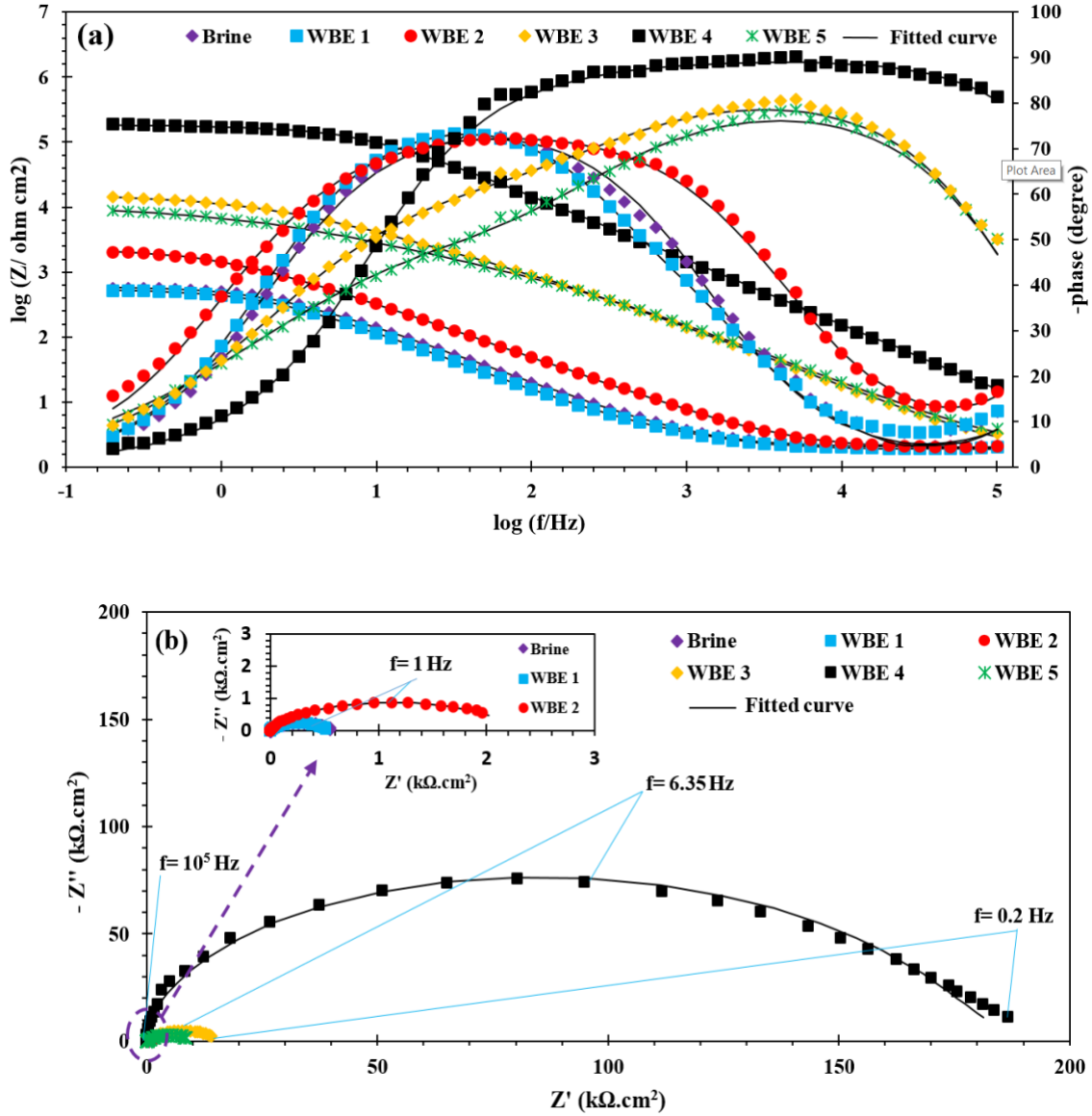


Fig. 2.6. The EIS results as Bode (a) and Nyquist (b) diagrams for carbon steel coupons immersed in the brine solution and WBEs for 2 h involving CO₂ corrosion. The measured data point is depicted as certain marker styles, while the fitted curves are shown by solid curves.

Fig. 2.6 shows that all the Nyquist plots are in the form of semicircle and there is only one relaxation time in the impedance diagram for the sample immersed in the brine solution after 2 h, suggesting that there was only one charge transfer process during the anodic dissolution of the steel. However, two relaxation times were emerged for samples after being immersed in the WBEs

for 2 h. This explains that a corrosion-protective layer formed on the surface of the carbon steel samples immersed in the WBEs. In addition, the diameter of the Nyquist plot is increased by the addition of corrosion inhibitors, PEG-2 oleamide, GM and GL. WBE 4 including PEG-2 oleamide displays the largest diameter of semicircle, indicating a remarkable enhancement in corrosion inhibition performance. Electrochemical parameters were determined from the result shown in Fig 2.6 through modeling Nyquist and Bode plots utilizing equivalent electrical circuits as illustrated in Fig. 7 [105,106].

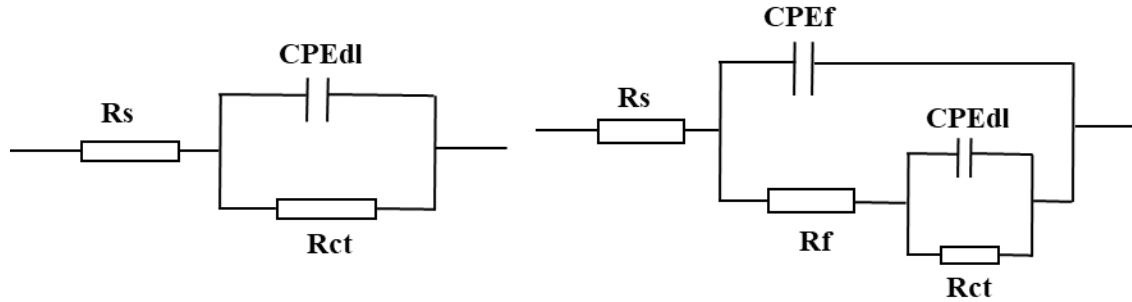


Fig. 2.7. Equivalent circuits used to model impedance data for brine solution (right) and various WBEs (left)

In the model, R_s , R_{ct} , R_f , CPE_f and CPE_{dl} are solution resistance, charge transfer resistance, film resistance, constant phase element of film capacitance and constant phase element of double layer capacitance, respectively. Double layer capacitance (C_{dl}) and film capacitance (C_c) values were obtained using eq. (1) [105-107].

$$C_x = (Q_x * R_x^{1-n})^{\frac{1}{n}} \quad (1)$$

where C_x is the capacitance of the double layer or film capacitance, Q_x the admittance of CPE double layer or film, R_x the charge transfer resistance or film resistance, and n is the empirical exponent. The inhibition efficiency ($\eta\%$) of carbon steel samples exposed to various water-based emulsion fluids can be obtained using eq. (2) [108].

$$\eta\% = 100 \times \left(1 - \frac{R_p. \text{brine}}{R_p. \text{WBE}}\right) \quad (2)$$

The electrochemical parameters extracted from Fig 2.7 and eq. (2) are listed in Table 2.7.

Table 2.7. Electrochemical parameters extracted from impedance data for the carbon steel samples exposed to the brine solution and different water-based emulsion fluids involving CO₂ corrosion.

Sample	R _{ct} (kΩ.cm ²)	CPEdl		C _{dl} (μF.cm ⁻²)	R _f (kΩ.cm ²)	CPEf		C _f (μF.cm ⁻²)	R _p = (R _{ct} + R _f) (kΩ.cm ²)	η %
		Y ₀	n			Y ₀	n			
		(Ω ⁻¹ .cm ⁻²)				(Ω ⁻¹ .cm ⁻²)				
Brine	0.58	183 × 10 ⁻⁶	0.88	135.1	-	-	-	-	0.58	-
WBE 1	0.53	35.3 × 10 ⁻⁶	0.95	28.8	0.011	170 × 10 ⁻⁶	0.88	72.4	0.541	~ 0
WBE 2	2.23	92.60 × 10 ⁻⁶	0.84	68.8	1.96	183.8 × 10 ⁻⁹	1	0.183	4.19	86.16
WBE 3	14.5	11.03 × 10 ⁻⁶	0.63	3.77	1.23	2.245 × 10 ⁻⁶	0.92	1.36	15.73	96.31
WBE 4	189	247.4 × 10 ⁻⁹	0.48	0.009	0.42	100.9 × 10 ⁻⁹	1	0.100	189.42	99.70
WBE 5	9.40	25.16 × 10 ⁻⁶	0.58	8.86	0.92	2.427 × 10 ⁻⁶	0.90	1.24	10.32	94.38

According to Table 2.7, the minimum R_{ct} value was detected for steel sample exposed to the brine solution and WBE 1, meaning that the steel has the lowest corrosion resistance in these solutions. It was also noticed that the presence of mineral oil alone in WBE 1 had no effect on the inhibition efficiency. Theoretically, the mineral oil can provide a protective layer on the surface to mitigate corrosion. However, such a function strongly depends on the dispersion of the mineral oil in the aqueous phase. In the present case, WBE 1 containing mineral oil did not act as an effective barrier to inhibit corrosion of steel. The reason is that the mineral oil alone may not play an effective role in improving the corrosion resistance, since the mineral oil cannot well disperse in water because of non-polar hydrocarbons in its structure, making the mineral oil less effectively in preventing the attack of corrosive agents to the metal surface. Consequently, low impedance, low charge transfer resistance, high corrosion rate and more negative OCP were observed for steel

immersed in WBE 1 containing mineral oil. Even the brine solution shows better anti-corrosion behavior than WBE1. The better performance of the brine solution should be ascribed to the formation of oxide layer, which could be somewhat more protective, compared to the mineral oil layer (WBE 1) formed on the metal surface. However, if a suitable surfactant is added to WBE1, it can enhance the oil-water interaction and thus help the mineral oil to reach a proper dispersion in water with improved effectiveness in resisting corrosion of steel immersed in the solution. For instance, WBE2 containing a combination of mineral oil and surfactant shows an improved resistance to corrosion.

As demonstrated, the addition of three fatty acid corrosion inhibitors, including GL, PEG-2 oleamide and GM in WBE 3, WBE 4 and WBE 5, resulted in remarkable increases in R_{ct} , respectively. As shown, WBE 4 containing PEG-2 oleamide led to the maximum R_{ct} value with inhibition efficiency of 99.70%, compared to other WBEs (96.31% for WBE 3 and 94.38% for WBE5) after 2h immersion. Moreover, the lowest C_{dl} value was obtained for steel specimen immersed in WBE 4. The double layer capacitance results from the formation of a double layer between the charged metal surface and solution. The existence of PEG-2 oleamide compound on the surface of the carbon steel can affect electrical layer by replacement of water molecules with PEG-2 oleamide. This indicates that PEG-2 oleamide is the most effective corrosion inhibitor among the three inhibitors, which was adsorbed on the surface of carbon steel, forming a protective layer against corrosion.

Fig.2.8 illustrates the phase angle values (negative) at high frequency (100 kHz) and polarization resistance, calculated from the EIS data, which are useful parameters for evaluating the corrosion resistance. In a circuit where a resistor and capacitor are mixed together in a parallel manner, the phase difference between voltage and current is an important indicator for the

capacitive behavior of samples. The more negative the phase angle, the stronger the capacitive behavior. The high capacitive behavior of a sample reflects its high resistance to the charge transfer through the capacitor, corresponding to a phase angle of near -90 degree. However, the current can pass through the resistor with ease when a sample shows low capacitive behavior, corresponding to a phase angle of near 0 degree.

Fig. 2.8(a) illustrates that the phase angle measured at 100 kHz was the least negative for steel samples immersed in the brine solution (-12.17 degrees) and that of WBE1 was at a similar level. Samples immersed in the WBEs containing corrosion inhibitors after 2 h showed more negative phase angles. The most negative phase angle value (-80.5 degree) was observed for sample immersed in WBE 4 containing PEG-2 oleamide [see Fig.2.8(a)]. The presence of PEG-2 oleamide in the WBE 4 should form a more protective layer on the steel surface, so AC current at 100 kHz tends to pass through the double layer capacitor due to its high charge transfer resistance rather than to pass through its resistor, rendering the phase angle remains near -90 degree [109,110].

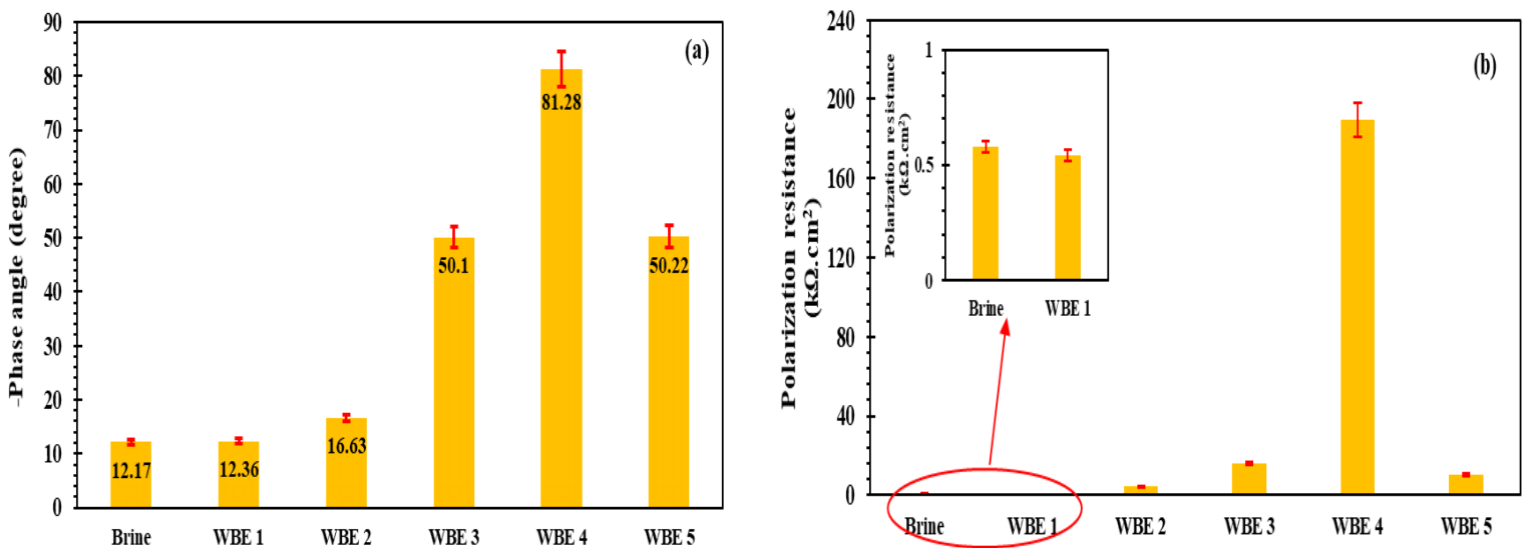


Fig. 2.8. The values of (a) phase angle at high frequency and (b) polarization resistance of steel samples immersed in the brine solution and various WBEs under CO₂ corrosion after 2 h.

Polarization resistance (sum of R_{ct} and R_f) is a well-known electrochemical parameter which reflects the corrosion inhibition effectiveness of a system. Fig. 2.8(b) depicts the polarization resistances of steel samples in various solutions. As shown, the polarization resistance of the carbon steel increases in the WBEs containing the corrosion inhibitors (see Table 2.7), benefiting from the improvement in the inhibitive layer on the steel surface. The maximum polarization resistance was achieved by WBE 4 containing PEG-2 oleamide, which should be strongly adherent to the carbon steel surface. Based on the data obtained from the EIS measurement, it can be concluded that PEG-2 oleamide provides excellent corrosion inhibition in the water-based emulsion systems used as the drilling fluid.

2.3.4.3. Polarization tests

Fig. 2.9 illustrates the potentiodynamic polarization plots of the carbon steel samples in the brine solution and various water-based emulsion fluids, respectively. As shown, the presence of the three different corrosion inhibitors remarkably affect both anodic and cathodic branches of the polarization curves, showing strong corrosion inhibition. The reductions in the anodic and cathodic current densities reflect the retardation of the cathodic reaction and decline in the anodic dissolution of carbon steels by the added inhibitors. The inhibiting effect of the inhibitors is related to their adsorption on the steel surface.

The corrosion potential (E_{corr}), corrosion current density (i_{corr}), corrosion rate, anodic Tafel slope (β_a) and cathodic Tafel slope (β_c) were determined from the polarization curves and are presented in Table 2.8. The inhibition efficiencies ($\eta_{Tafel}\%$) of the steel samples immersed in various WBEs were calculated using the following equation [111].

$$\eta_{Tafel} = \frac{i_{corr} - i_{corr}^{(i)}}{i_{corr}} \times 100 \quad (3)$$

where i_{corr} and $i_{corr}(i)$ are corrosion current densities for carbon steel samples in solutions without and with the corrosion inhibitor, respectively.

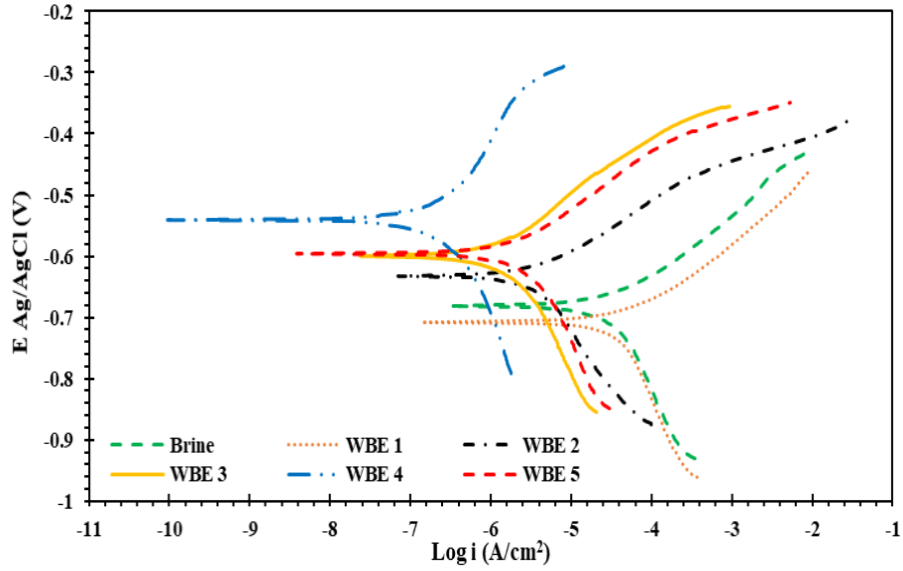


Fig. 2.9. Polarization curves of carbon steel samples in the brine solution and different WBEs for 2 h involving CO_2 corrosion.

Table 2.8. Values of corrosion current density, corrosion potential, cathodic and anodic Tafel slopes, corrosion rates of carbon steel samples immersed to the brine solution and different water-oil emulsions involving CO_2 corrosion.

sample	E_{corr} vs SCE (V)	i_{corr} ($\mu A/cm^2$)	Corrosion rate (mpy)	β_a (V/decade)	β_c (V/decade)	$\eta_{Tafel}\%$
Brine	-0.68 ± 0.03	13.1 ± 1.2	1.98 ± 0.5	0.046 ± 0.025	0.066 ± 0.028	-
WBE 1	-0.71 ± 0.04	14.2 ± 1.5	2.28 ± 0.8	0.041 ± 0.020	0.074 ± 0.03	~ 0
WBE 2	-0.63 ± 0.03	2.0 ± 0.80	0.300 ± 0.1	0.053 ± 0.023	0.079 ± 0.027	84.73 ± 1.0
WBE 3	-0.60 ± 0.02	0.59 ± 0.08	0.09 ± 0.003	0.062 ± 0.023	0.062 ± 0.024	95.49 ± 0.9
WBE 4	-0.54 ± 0.02	0.09 ± 0.02	0.01 ± 0.001	0.070 ± 0.020	0.070 ± 0.022	99.31 ± 0.4
WBE 5	-0.59 ± 0.03	0.91 ± 0.10	0.13 ± 0.005	0.056 ± 0.026	0.066 ± 0.021	93.05 ± 0.8

According to Table 2.8, the three corrosion inhibitors make the corrosion potential moved to more positive values, which affect the anodic reaction more than the cathodic reaction. The addition of the corrosion inhibitors decreases the corrosion current densities and corrosion rates remarkably, which are correlated to the formation of protective thin layer on the metal surface which restricts the access of corrosive agents to reach the metal surface. The minimum corrosion current density or corrosion rate was obtained when the carbon steel was immersed in WBE 4 containing PEG-2 oleamide, which showed the best corrosion inhibitive performance. Based on the inhibition efficiency values, adding PEG-2 oleamide to WBEs led to an excellent inhibitive performance (99.31%), compared to two other corrosion inhibitors. This is attributed to the formation of a more effective protective layer with stronger adsorption on the iron surface.

2.3.5. Surface characterization

2.3.5.1 SEM analysis

Surface morphologies of the steel samples immersed in the brine solution and different WBEs involving CO₂ corrosion (by introducing CO₂ into the WBEs during the immersion tests) were examined with SEM as presented in Fig. 2.10.

Fig.2.10 (a) displays the formation of deposits due to the penetration of corrosive ions onto the surface of carbon steel after immersion in the brine solution. These deposits are also seen on the surface of samples exposed to WBE1 and WBE 2, indicating that the mineral oil with surfactant cannot prevent corrosion of the carbon steel. However, no deposits are observed on surface of the sample immersed in WBE 4 which contains PEG-2 oleamide. Two other corrosion inhibitors of GL and GM in WBE 3 and WBE 5 prevent corrosion of the steel to some degree but minor deposits are still present on steel samples immersed in WBE 3 and WBE 5, respectively. The surface

appearances of the samples after immersion in different solutions are consistent with results of other tests and analyses described earlier.

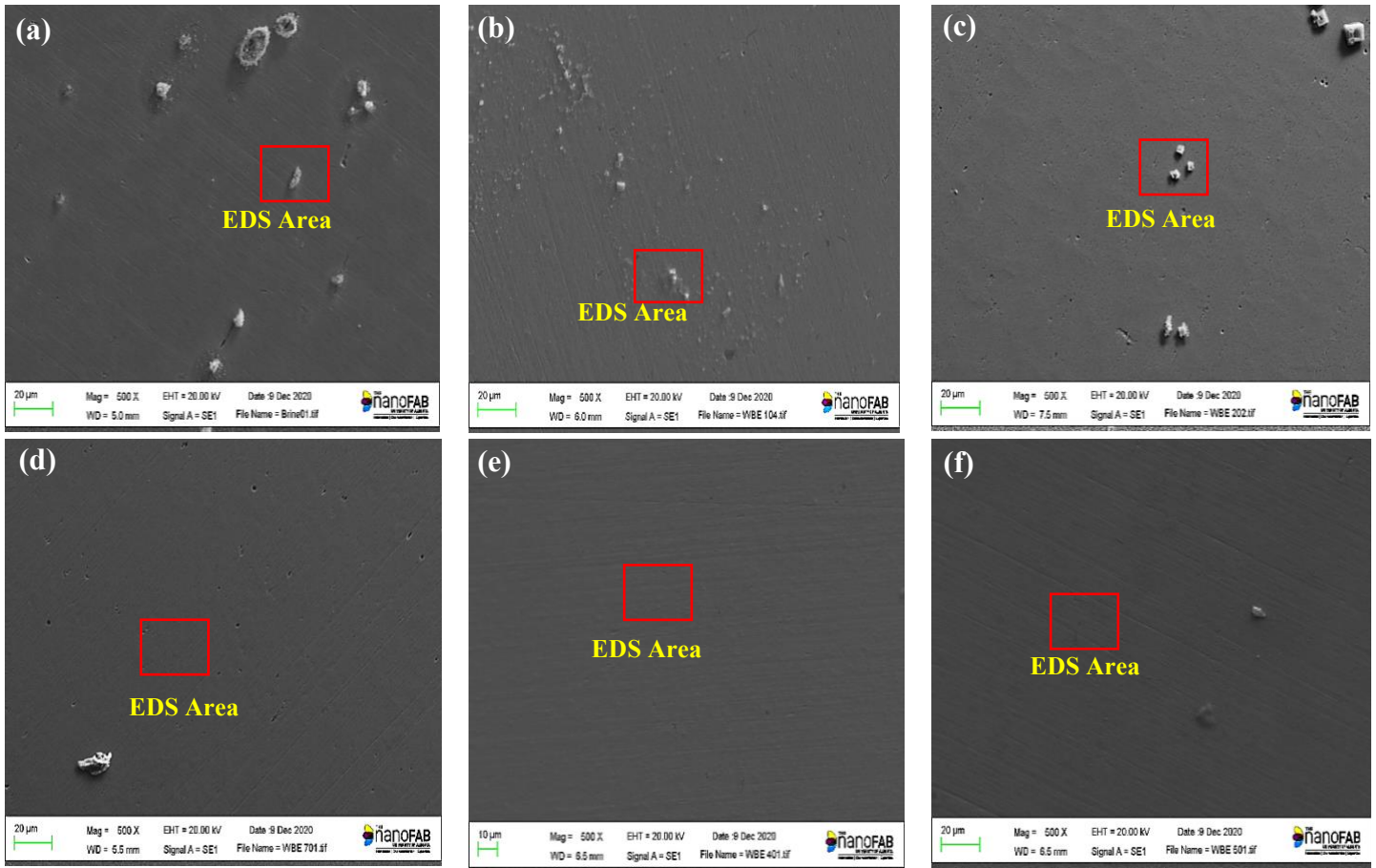


Fig. 2.10. SEM micrographs of 1018 carbon steel sample surfaces exposed to (a) brine solution, (b) WBE 1, (c) WBE 2, (d) WBE 3, (e) WBE 4 and (f) WBE 5, involving CO₂ corrosion.

Surface compositions of the above samples were analyzed with EDS. Table 2.9 lists elements detected on surfaces of the samples. The highest concentration of oxygen was detected on surface of the steel sample immersed in the brine solution. Besides, the presence of aggressive agents including chloride and potassium indicates that the cations and anions reached and penetrated the surface of the carbon steel. The oxygen concentration was reduced on the surfaces of samples exposed to WBE 1 and WBE 2, indicating that mineral oil and surfactant can decline the oxidation on the steel surface, but corrosive chemicals such as chlorine and potassium were still detected on

the samples. However, no corrosion agents were detected on surface of the sample immersed in WBE 4 containing PEG-2 oleamide, and the concentration of oxygen on the sample surface is lower. In addition, nitrogen was detected on this sample surface, suggesting that the nitrogen-containing PEG-2 oleamide formed a protective film on the sample to mitigate corrosion. The presence of minor deposits and higher concentrations of oxygen on samples immersed in WBE 3 and WBE 5 suggest that these two corrosion inhibitors, GL and GM, are less effective than PEG-2 oleamide.

Table 2.9. EDS data (percent concentrations of elements, wt.%) obtained from surfaces of steel samples exposed to different solutions involving CO₂ corrosion.

Solution	Fe	O	C	N	K	Cl
Brine solution	94.2	2.1	3.6	-	0.1	0.1
WBE 1	87.6	1.1	11.1	-	-	0.1
WBE 2	91.2	1	7.7	-	0.1	-
WBE 3	83.4	1	15.6	-	-	-
WBE 4	85.9	0.8	13.2	0.1	-	-
WBE 5	84.6	1	14.3	-	-	0.1

It may need to be mentioned that the electrochemical tests show that the WBE 1 solution cannot inhibit the corrosion of the metal substrate (see Figs. 2.6 and 2.9 as well as Tables 2.7 and 8), however, it seems from the SEM images (Fig. 2.10) that the steel sample exposed in WBE1 solution suffer less corrosion, compared to that exposed to the brine solution. As a matter of fact, the mineral oil used in this study is distillates (petroleum) - hydrotreated light naphthenic made of long chain hydrocarbons, which cannot be well dispersed well in the brine solution. Although the SEM-EDS analysis shows a higher concentration of carbon detected on the surface of steel immersed in WBE 1 due to the presence of mineral oil, this thin layer couldn't protect the steel

surface effectively against attacks of corrosive ions and a high amount of deposits distributed on the entire steel surface. Take a closer look at the SEM images, more areas of steel surface after immersion in WBE 1 are covered by deposits, compared to the situation of sample tested in the brine solution. Although the local area covered by deposits on the steel surface tested in WBE 1 appear smaller (with less oxygen) than that on sample tested in the brine solution, the deposits cover a larger total area (accumulated) and are more distributed on the steel surface tested in WBE1.

2.3.5.2. XPS analysis

The surface layers of steel samples respectively exposed to WBE 2, WBE 4 and WBE 5 were studied through XPS analysis, compared with sample surface exposed to the brine solution (reference). XPS spectra of the steel surfaces exposed to the brine solution and various WBEs involving CO₂ corrosion are presented in Fig. 2.11. Relevant values extracted from XPS are given in Table 2.11.

□

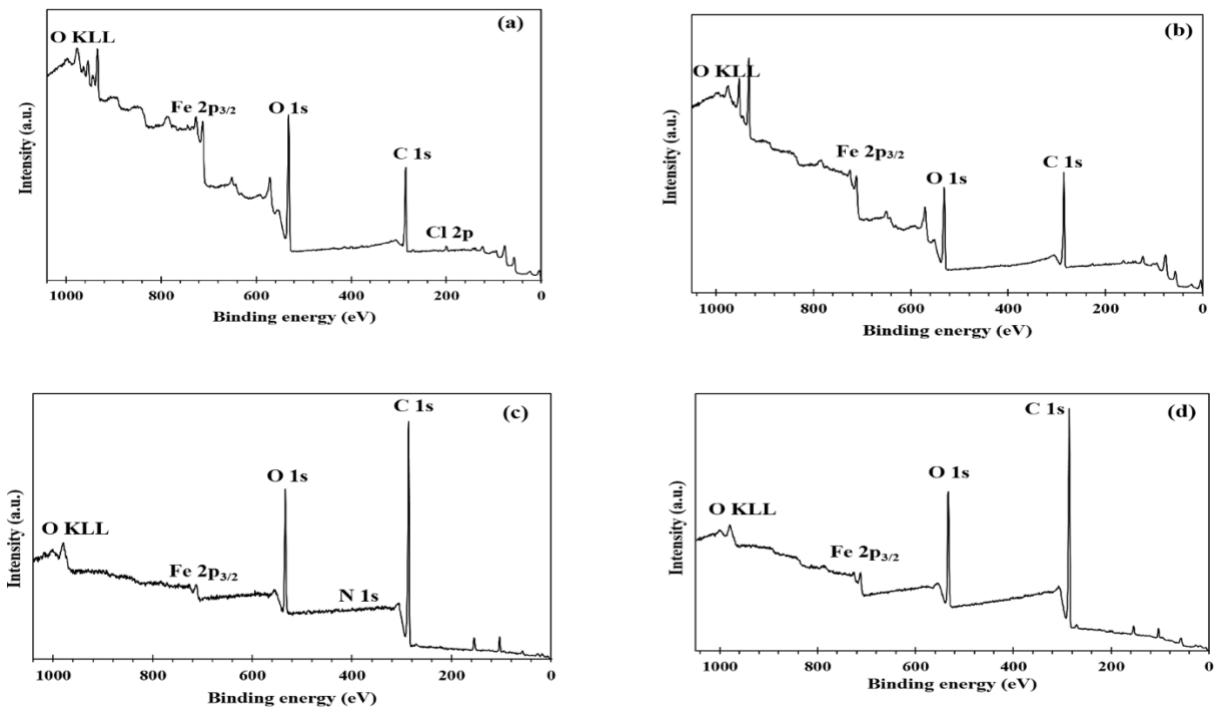


Fig. 2.11. XPS survey spectra of carbon steel surfaces respectively exposed to (a) the brine solution, (b) WBE 2, (c) WBE 4, and (d) WBE 5, involving CO₂ corrosion.

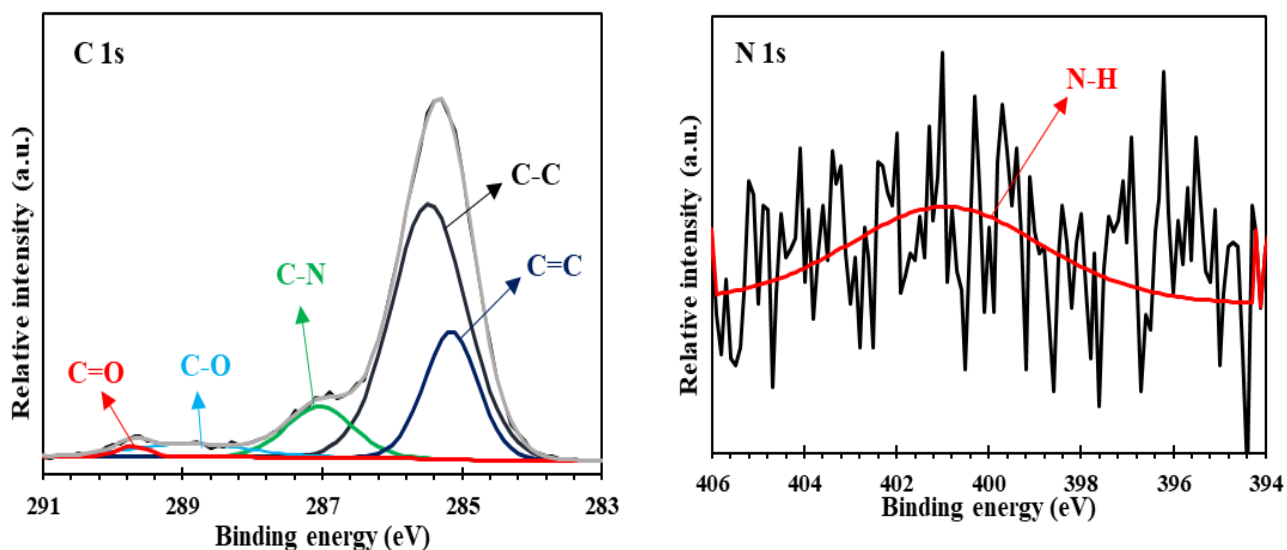
Table 2.10. Binding energies and concentrations of various elements on the steel surfaces exposed to the brine solution and WBE 2, 4 and 5 involving CO₂ corrosion, respectively.

Name	elements	Binding energy (eV)	Element (%)
Brine	Cl 2p	~ 200	1.09
	C 1s	~ 285	62.27
	O 1s	~ 531	28.97
	Fe 2p _{3/2}	~ 712	7.67
WBE 2	Cl 2p	~ 200	0
	C 1s	~ 285	67.69
	O 1s	~ 531	25.57
	Fe 2p _{3/2}	~ 712	6.74
WBE 4	Cl 2p	~ 200	0
	C 1s	~ 285	81.34
	N 1s	~ 400	0.38
	O 1s	~ 531	17.79
	Fe 2p _{3/2}	~ 712	0.49
WBE 5	Cl 2p	~ 200	0
	C 1s	~ 285	80.6
	O 1s	~ 531	17.85
	Fe 2p _{3/2}	~ 712	1.55

According to the XPS spectra shown in Fig. 2.11 and data in Table 2.10, Cl, C, N, O and Fe are the main elements detected on surface of the carbon steel samples exposed to different solutions. The Cl signal at the binding energy of 200 eV with a concentration of 1.09 % on surface of the sample immersed in brine solution indicates that the steel surface was subjected to corrosion in which Cl ions made considerable contribution. A sharp peak with a high amount of 28.97 % came from oxygen element at binding energy of 200 eV, resulting from oxidation reaction on surface of this steel sample. However, no corrosion agents with Cl ions were detected on samples exposed to other three WBEs, suggesting that corrosion inhibitors and surfactant provided

sufficient hindrance to corrosion. In addition, the intensity of oxygen element detected on the steel samples exposed to the WBEs declined, especially when the corrosion inhibitors were added. The lowest percentage of oxygen element (17.79%) was detected on the steel sample exposed to WBE 4 which contained PEG-2 oleamide. The presence of N element on the steel surface exposed to WBE 4 is an indication of adsorption of the inhibitive layer or film on surface of the steel sample, which protected the steel from corrosion. A very sharp peak of carbon (81.34%) is present at binding energy of 285 eV due to the presence of long carbon chain in the structure of PEG-2 oleamide. The hydrocarbon chains of this corrosion inhibitor are able to keep water molecules and corrosive ions away from the steel surface [112, 113].

In order to better understand the composition and characteristic bonds of the protective film formed on the steel surface exposed to WBE 4 containing PEG-2 oleamide, high-resolution XPS spectra were obtained through deconvolution of multiple peaks in the C 1s, N 1s, O 1s and Fe 2p_{3/2} regions, which are shown in Fig. 2.12. Corresponding data are presented in Table 2.11.



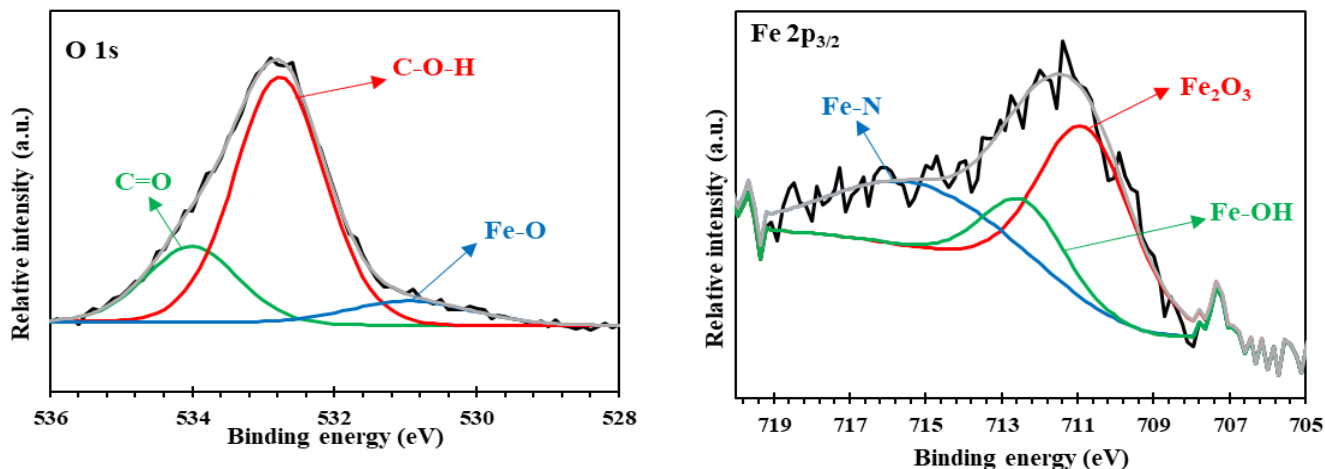


Fig. 2.12. High resolution XPS spectra of detected elements on the steel surface immersed in WBE 4 and their deconvolution after CO₂ corrosion.

Fig. 2.12 and Table 2.11 show that C 1s signal can be fitted into five Gaussian–Lorentzian peaks at different binding energies of 285.10, 285.48, 287, 289.04 and 289.71 eV, corresponding to C=C, C-C, C-N, C-O and C=O bonds, respectively. The C-C bond has the maximum carbon concentration, originating from long carbon chain in the corrosion inhibitor structure of PEG-2 oleamide. The O 1s spectra of the carbon steel surface are deconvoluted into three components. Fe-O bonds may correspond to iron oxide such as Fe₂O₃ and Fe₃O₄ derived from deconvoluted spectra related to O 1s signal at binding energy of 530.96 eV. C-O-H and C=O bonds are two other components acquired from deconvolution of O 1s at binding energies of 532.78 and 534.03 eV, respectively. The deconvolution of Fe 2p_{3/2} XPS spectra leads to three peaks at different binding energies. The two peaks at the lower binding energies around 711.11 and 713.17 eV can be ascribed to iron oxides such as Fe₂O₃ and Fe-OH, respectively. The higher binding energy is attributed to the Fe-N group. The XPS spectrum of N 1s shows only one peak with no need for deconvolution at binding energy of 400.84 eV that corresponds to N-H bond. The above results

prove that the protective layer adsorbed chemically on the steel sample contains molecules of PEG-2 oleamide in the added corrosion inhibitor [113-117].

Table 2.11. Data obtained from deconvoluted XPS spectra of steel surface immersed in WBE 4 after CO₂ corrosion.

Name of convoluted spectrum	Characteristic bonds	Binding energy (eV)	% Composition in each element
C 1s	C=C	285.1	21.24
	C-C	285.4	60.51
	C-N	287	11.97
	C-O	288.8	5.31
	C=O	289.71	0.97
N 1s	N-H	400.9	100
O 1s	Fe-O	530.96	7.49
	C-O-H	532.7	72.83
	C=O	534.03	19.68
Fe 2p _{3/2}	Fe ₂ O ₃	710.78	50.06
	Fe-OH	712.40	18.12
	Fe-N	715.36	31.82

2.3.6. Corrosion inhibition mechanism of fatty acid-based green inhibitors

The mechanism for the corrosion protection of 1018 carbon steel exposed to CO₂-saturated 5% KCl environment could be described by the formation of a protective layer on the steel surface. Based on experimental findings, PEG-2 oleamide acted as a more effective corrosion inhibitor than GL and GM to protect 1018 carbon steel from corrosion when immersed in KCl media containing CO₂. PEG-2 oleamide due to the presence of nitrogen in its structure has lower electronegativity than oxygen, making nitrogen a better electron donor than oxygen. In addition, the long hydrophobic hydrocarbon chains in PEG-2 oleamide structure can provide further

protection, since the hydrophobic tail helps keep corrosive agents like chloride ion and water molecules away from the metal surface, thus enhancing the inhibition effect.

More analysis was conducted for further insight into the inhibition mechanism of the corrosion inhibitors and identification of the active sites responsible for the interaction between corrosion inhibitors and carbon steel. Since corrosion inhibitor molecules exist in two different forms: neutral and protonated, adsorption of fatty acid-based inhibitor molecules on the surface of carbon steel can occur through physical and chemical adsorption processes. In acidic solutions due to presence of CO_2 gas in the brine solution, the surface of carbon steel initially has positive charges that attract Cl^- ions to attach to the steel surface. Physical adsorption can then take place through electrostatic interaction between the protonated form of inhibitor molecule and the steel surface with adsorbed Cl^- ions (FeCl^-). In the meanwhile, the corrosion inhibitors containing nitrogen and/or oxygen are able to form chemisorptive bonds with the steel surface, preventing the occurrence of electrochemical dissolution reactions. The corrosion inhibitors in neutral form may be adsorbed on the steel surface through donor-acceptor interactions between lone electron pairs of these two heteroatoms (nitrogen and oxygen) and free orbital d of iron [118]. Fig. 2.13 shows the corrosion inhibition mechanism of PEG-2 oleamide on the surface carbon steel.

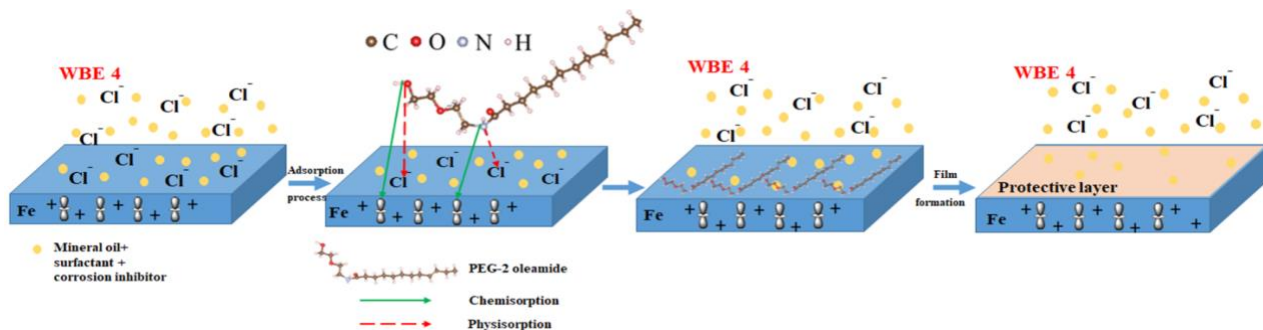


Fig. 2.13. Mechanism of PEG-2 oleamide adsorption on 1018 carbon steel in CO_2 -saturated 5% KCl environment

2.4 Conclusions

A comprehensive study was conducted to investigate inhibition effects of three green fatty acid-based corrosion inhibitors, Polyethylene glycol-2 oleamide (PEG-2 oleamide), Glycerol myristate (GM) and Glycerol linoleate (GL), on corrosion of 1018 carbon steel in 5% KCl solution containing CO₂, using experimental techniques. The study is oriented to the applications of the green inhibitors as additives in drilling fluids for the oil industry. The following conclusions are drawn:

1. Electrochemical tests (OCP, EIS and polarization) and weight loss measurements show that all the three corrosion inhibitors in the emulsion-based fluid effectively suppress corrosion of carbon steel in the aggressive environment involving CO₂ corrosion. The inhibitors generate physical and chemical adsorption interactions with the steel surface, forming a protective film to protect the steel from attacks by corrosive agents. Among the three inhibitors, PEG-2 oleamide performs the best. The 2h-immersion tests showed that GM and GL decreased the corrosion rate in the brine solution by 60% ~70% while PEG-2 oleamide decreased the corrosion rate by 90%.
2. PEG-2 oleamide is adsorbed on the steel surface by donor-acceptor interactions between lone electron pairs and free orbital d of iron, forming a more protective layer to block the access for the corrosive agents to reach the steel substrate. The protective layer is adherent to the steel surface mainly by Fe-N bonding, detected by XPS analysis. The presence of nitrogen element in the chain plays a remarkable role in enhancing intermolecular electrostatic interactions, leading to stronger binding between PEG-2 oleamide and the carbon steel. The longer hydrophobic hydrocarbon chains in PEG-2 oleamide further enhances its corrosion inhibition effect.

Chapter 3 Improve the tribo-corrosion behavior of oil-in-water emulsion-based drilling fluids by new derivatives of fatty acid-based green corrosion inhibitors²

3.1 Introduction

During oil well drilling in the oil industry, various components of drilling equipment, e.g., pipes, valves and casings, encounter tribological attacks. Adhesive wear, erosion-corrosion, abrasive wear, and fatigue wear are known as main wear modes occurring in the oil drilling operation, making the drill equipment severely worn which could trigger catastrophic failures [16,119]. During drilling operations, mechanical, physical, and chemical interactions may take place simultaneously at the contact between the components such as drill bits, drill pipe, drill collar with sides of the well and casing (metal-rock or metal-metal contact), resulting in friction and wear problems which are more prevalent in deeper wells [54,56]. Moreover, because of the presence of acidic gases, dissolved oxygen gases, and salt ions, etc., the oilfield environment is very corrosive, making the wear more severe due to the wear-corrosion synergy [120]. Corrosion is the chemical degradation of a material caused by irreversible interfacial interaction or reaction with its surrounding aggressive environment [120-121]. The synergistic attack by wear and corrosion, also known as tribo-corrosion, may result in much large material loss, compared to those caused by wear and corrosion separately. Tribo-corrosion is one of serious issues for drilling tools [122-125]. To understand tribo-corrosion under specific conditions, one needs to investigate the separate

² A version of this chapter has been published. M.j. Palimi, Y. Tang, M. Wu, V. Alvarez, M. Ghavidel, E. Kuru, Q.Y. Li, Wei Li, D.Y. Li, Improve the tribo-corrosion behavior of oil-in-water emulsion-based drilling fluids by new derivatives of fatty acid-based green inhibitors, *Tribology International* 174 (2022) 107723.

processes and their mutual influences, which are responsible for the resultant damage to materials [120-129].

Application of drilling fluids during the well drilling process is mandatory for reducing friction, and mitigating corrosion and corrosive wear or tribo-corrosion by forming a protective film to minimize direct contact between rubbing surfaces, helping improve the tribo-corrosion resistance of metal surfaces, thus increasing the effectiveness and service life of the drilling equipment [130-132]. The selection of appropriate drilling fluids is crucial to the drilling operation [133]. Drilling fluids are divided into two categories: water-based drilling fluids and oil-based drilling fluids [134]. The water-based drilling fluids have attracted great interest and are preferred over oil-based ones due to economic and environmental factors [129-131]. However, the corrosivity of water-based emulsion drilling fluids is a concern and their lower lubrication performance also limits their applications. Therefore, there is a demand of improving the emulsion-based drilling fluids to mitigate the above-mentioned problems towards effective application of the drilling fluids in drilling operations [7, 135-137].

A good emulsion-based drilling fluid should have following characteristics: high lubricity, anti-corrosion capability, proper tribological performance, high stability, and nontoxicity [138]. In order to obtain these desired properties, various additives are often added to drilling fluids such as surfactants, anti-friction agents, and corrosion inhibitors [139]. Traditional emulsion-based drilling fluids contain active elements which are environmentally unfriendliness and their use have been prohibited by environmental regulations. In order to avoid environmental problems, application of green inhibitors and additives with high lubricity is an effective approach [140-141]. The green corrosion inhibitors are those extracted from plants, which generate a molecular protective layer at the interface between metal and surrounding solution through physisorption or chemisorption.

The formed protective layer may act as a physical barrier between the metallic surface and aggressive media, thus restricting the access of corrosive ions to reach the metallic surface and also more or less reducing the contact between two rubbing surfaces. As a result, the tribo-corrosion attack can be weakened. As a result, the presence of green inhibitors in a drilling fluid could markedly improve the fluid's performance [30, 46,142-144].

In chapter 2, a comprehensive study was conducted to investigate the inhibition effects of three green corrosion inhibitors in emulsion-based drilling fluids on the pure corrosion (without wear) of 1018 carbon steel. The chapter 3 aims to obtain comprehensive information on how three new derivatives of green corrosion inhibitors extracted from vegetable oils affect tribo-corrosion performance of 1018 carbon steel, where corrosion is combined with wear. The three different fatty acid-based corrosion inhibitors, Glycerol linoleate (GL), Polyethylene glycol-2 oleamide (PEG-2 oleamide) and Glycerol myristate (GM), were added to emulsion-based drilling fluids for evaluating their effects on friction, wear and corrosion simultaneously under linear sliding conditions using a reciprocating tribometer connected to an electrochemical system. Various combinations of mineral oil, surfactant and corrosion inhibitors were prepared and used as additives mixed with diluted 5% KCl solution to make stable Water-based emulsions (WBEs). Tribo-corrosion performance of 1018 carbon steel samples was investigated using the tribometer incorporated with a three-electrode electrochemical cell containing the WBE. The effectiveness of the three corrosion inhibitors in suppressing corrosive wear was thoroughly evaluated by measuring COF, volume loss, wear track profile, current and potential evolution with time. Worn surfaces were analyzed with a scanning electron microscope (SEM) equipped with the energy dispersive X-ray spectroscopy (EDX) to gain an insight into the mechanism for corrosion inhibition. Moreover, effects of different concentrations (0.1, 0.5 and 1 g) of prepared combination

(mineral oil + TERGITOL NP-9 + PEG-2 oleamide) as additive added to the brine solution on tribo-corrosion of the carbon steel were also analyzed.

It should be mentioned that tribo-corrosion behavior of drilling equipment is influenced by multiple factors, e.g., contact force, sliding speed, electrochemical potential, temperature, fluid composition, and concentration of additives in the drilling fluid. These factors may synergistically affect tribo-corrosion of drilling facilities. Thus, this chapter is focused on the effect of the types of green corrosion inhibitors and their concentration on tribo-corrosion resistance of carbon steel and understanding of underlying mechanisms, e.g., properties and mechanisms for the adsorbed films induced by the inhibitors. The testing condition in this work is limited, e.g., performing corrosive wear tests under a relatively high contact load (10 N) at a fixed sliding speed. Evaluating the protectiveness of the inhibitors under different contact conditions that simulate oil drilling situations would be carried out in follow-up chapters, involving various contact forces, sliding speeds, and durations, in order to use inhibitor-containing drilling fluids effectively for drilling operations under different conditions.

3.2 Experimental

3.2.1 Materials

Consistent with chapter 2, our based fluid consisted of a 5% KCl aqueous solution. A few water based emulsions (WBE) were made by adding substances (mineral oil, surfactant and corrosion inhibitor) to the base fluid. Fig. 2.1 in chapter 2 shows molecular structures of the three fatty acid-based corrosion inhibitors. 1018 carbon steel coupons, as detailed in Table 2.2 and supplied by ALGOMA steel Inc., were used for investigating their tribo-corrosion behaviors in prepared water-based emulsions (WBEs). The mechanical properties of 1018 carbon steel are

listed in Table 3.1. Steel samples were polished with 400, 800 and 1200 grit SiC-based emery papers successively and cleaned with acetone and isopropyl alcohol prior to tribological and tribo-corrosion tests. Sample surfaces were rinsed with distilled water, dried by air pressure, and then placed in a desiccator. The prepared steel samples had their average surface roughness equal to 0.016 μm , determined using an optical profilometer (Zegage 3D, Middlefield, US).

Table 3.1. Mechanical Properties of 1018 carbon steel based on AISI/SAE.

Properties	Tensile strength	Yield strength	Elongation in 50 mm	Hardness (HB)
1018 carbon steel	483 MPa	413 MPa	18 %	143

3.2.2 Preparation of emulsion-based drilling fluids (WBEs)

Various water-based emulsions (WBEs) as drilling fluids were prepared using a mechanical stirrer for this chapter, including mineral oil, TERGITOL NP-9 as surfactant, three corrosion inhibitors of PEG-2 oleamide, GM and GL and brine solution as blank solution (5wt % KCl). Three different concentrations (0.1 g, 0.5 g, and 1 g) of the prepared combinations, including mineral oil, surfactant, and corrosion inhibitor, were used to investigate tribo-corrosion performances of the drilling fluids.

3.2.3 Characterization

3.2.3.1 Particle size distribution

A particle size analyzer (Zetasizer Nano-ZS, Malvern instruments, UK) via dynamic light scattering (DLS) technique was used to measure the size distribution and z-average diameter of dispersed oil in the brine solution. Formulated WBEs of 0.5 ml were added to the sample cell, respectively, to determine the droplet size distribution and average particle size at 25 °C. The

average particle size and the size distribution of particles dispersed in the brine solution were obtained through cumulants method and software match with the instrument, respectively.

3.2.3.2 Inverted light fluorescence microscope

The dispersion of emulsion droplets was studied by placing a drop of a prepared WBE on a glass slide. Emulsions were then observed with an inverted light fluorescence microscope (Model Axiovert 200M, Zeiss, Germany). Samples of oil-in-water emulsions were stained with FITC green and evaluated with a 10x magnification lens.

3.2.3.3 Turbidity evaluation

HACH 2100 AN turbidimetry was applied to evaluate the stability of WBEs containing PEG-2 oleamide at different concentrations.

3.2.3.4 Tribo-corrosion evaluation

A pin-on-disc tribometer (Rtec MFT-5000, San Jose, US) incorporated with an electrochemical system (GAMRY instrument) was used to investigate tribo-corrosion of 1018 carbon steel samples immersed in WBEs with and without corrosion inhibitors. Before the test, a steel sample mounted with epoxy-polyamine glue with its upper surface uncovered (1 cm^2). The sample was used as the working electrode, and a tribo-corrosion cell included an Ag/AgCl (reference electrode) and a platinum (counter electrode). During the test, the steel surface was worn by a cyclically moving silicon nitride ball with a diameter of 4 mm. Besides, a linear reciprocating sliding module was used to measure the coefficient of friction at room temperature under a normal load of 10 N and an oscillating frequency of 0.5 Hz with a sliding displacement of 3 mm, corresponding to a sliding velocity of 2 mm/s. A total sliding time was 1200 s, over which COF, OCP, potentiostatic and

potentiodynamic polarization measurements were carried out simultaneously. Potentiostatic test was performed in a range of 1mV from the OCP in 400 mL of prepared WBEs. Variations in current (I , μA), open circuit potential (OCP) and COF were recorded with respect to time before, during and after the sliding test. The potentiodynamic polarization curves were recorded in the range of ± 250 mV with respect to the OCP of each sample at a scan rate of 0.4 mV/s. The experimental set-up for corrosive-wear tests is depicted in Fig. 3.1. All tests were repeated three times under the identical conditions.

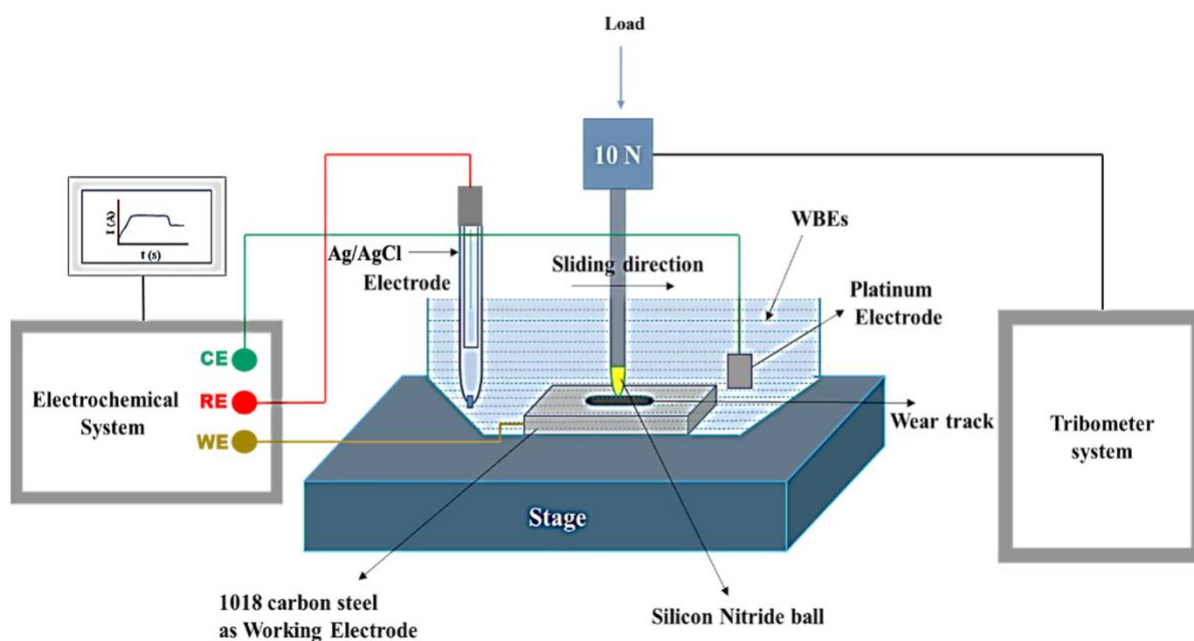


Fig. 3.1. A schematic view of the experimental set-up used for tribo-corrosion tests.

3.2.3.5 Surface characterization

Worn surfaces of samples experienced wear tests respectively in the brine solution and various WBEs were rinsed with distilled water, dried with pressed air flow, and then observed using a Zeiss Evo M10 SEM-EDX (Zeiss, Oberkochen, Germany) to study the morphology and

composition of the surfaces worn in different WBEs. Optical profilometer (Zegage 3D, Middlefield, US) was used to examine the wear track and determine volume loss of the steel samples.

3.3 Results and discussion

3.3.1 Stability analysis of the prepared WBEs

As explained in chapter 2, the stability of emulsion systems is considered as a critical parameter in the preparation of drilling fluids, which plays an important role in determining the fluid's performance. To determine the optimum concentration of ingredients (mineral oil, TERGITOL NP-9, and PEG-2 oleamide), different WBEs were prepared by adding 0.1 g of a mixture consisting of 65% mineral oil and different weight percentages of surfactant (0 to 35%) and corrosion inhibitor (0 to 35%) to the brine solution containing 5% KCl, respectively. Such made WBEs are listed in Table 2.5. The turbidity and zeta potential measurements have been presented in chapter 2 (sections 2.3.3.1 and 2.3.3.2). In this chapter, particle size distribution, and average particle size of the prepared WBEs were analyzed with DLS technique to ensure to have appropriate compositions with high stability.

3.3.1.1 Droplet size measurement

The droplet size distribution and average particle size for various WBEs, including additional combinations of mineral oil + TERGITOL NP-9 + PEG-2 oleamide with various concentrations in the brine solution listed in Table 2.5, were determined with the DLS technique and are displayed in Fig. 3.2.

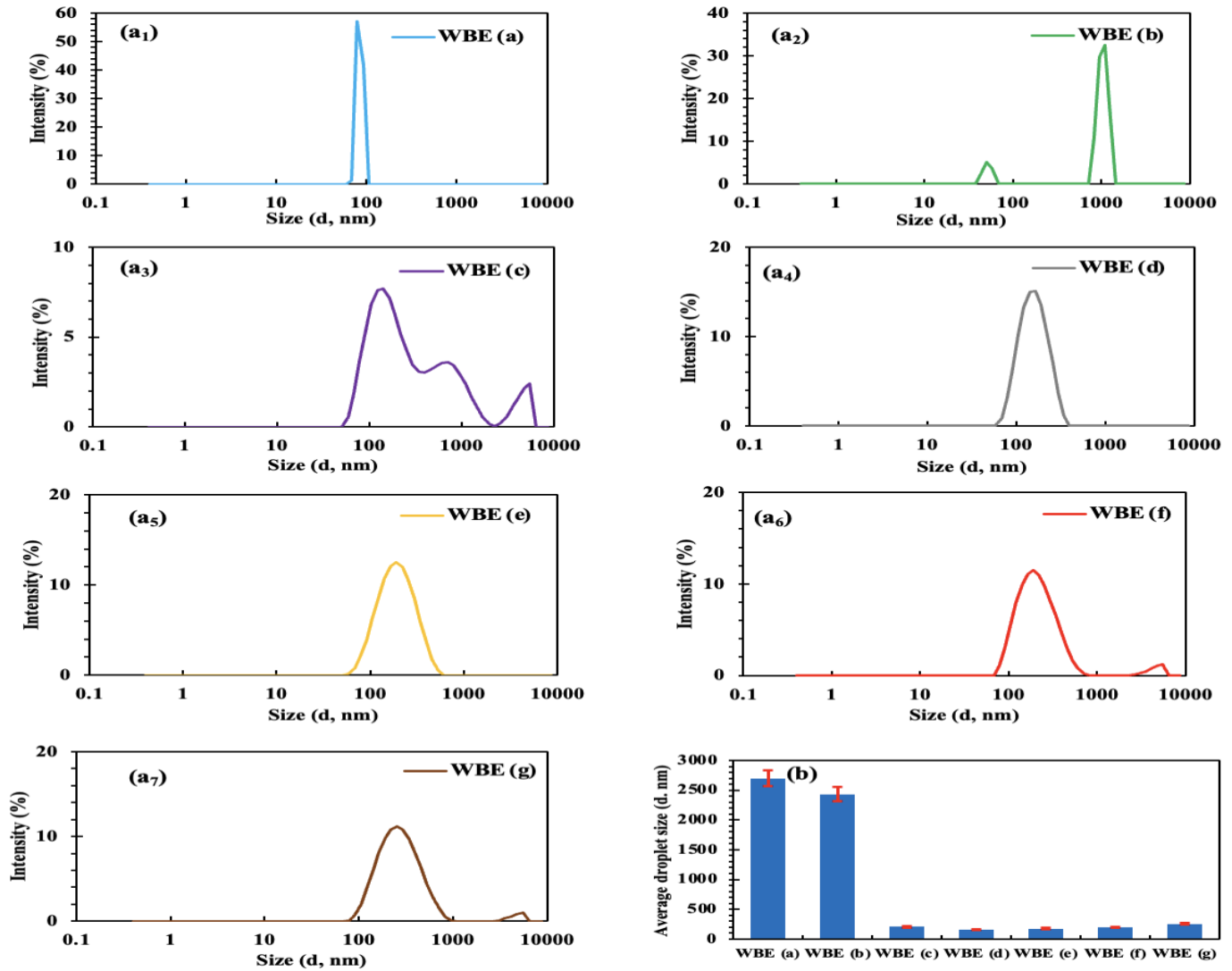


Fig. 3.2. Particle size distribution (a₁ to a₇) and average particle size (b) of the prepared WBEs including mineral oil + TERGITOL NP-9 as a surfactant + PEG-2 oleamide.

It is evident from Fig.3.2 (a₄ to a₇) that particle size distributions of emulsion droplets in the brine solution with low weight percentages of surfactant (0 % to 10%) are not different from those with high concentrations of the surfactants (above 20%). Any little peak shifts among Fig. 3.2 a₄ to a₇ may be related to different degrees of interfacial tension reduction that different combinations provide. However, different behaviors with high intensity can be observed for WBEs loaded with high concentrations of surfactant (Fig. 3.2 a₁ and a₂). This high intensity signal is largely dominated

by bigger aggregated emulsion particles. In fact, TERGITOL NP-9 in high concentrations was not able to be effectively adsorbed on the surface of emulsion droplets and it also showed the lowest ability to decrease interfacial tension. Thus, WBE (a) and WBE (b) had the largest average particle size. It can also be observed from Fig 3.2(b) that the presence of low concentrations of surfactants (0 % to 20%) in the WBEs generates emulsions with much smaller droplets, compared to those having high weight percentages of surfactant (35% in WBE (a) and 30% in WBE (b)). It is known that surfactant molecules at lower concentrations (below 20%) may be effectively adsorbed at the interface between dispersed phase and continuous phase. This adsorbed layer acts as a steric or electrostatic barrier against the aggregation of emulsion droplets, resulting in a very fine droplet size (~ 200 nm) with increased emulsion stability [34]. Once the surfactant concentration reaches the saturation amount, named critical micelle concentration (above 20%), the adsorption amount of surfactants on the interface of oil-water reduces due to the formation of micelles which have a solubilization effect on the surfactant molecules. Thus, interfacial tension increases, leading to a significant increase in the size of emulsion droplets (2431 nm for WBE (a) and 2697 for WBE (b)) [102,147].

Therefore, based on turbidity data, zeta potential and particle size distribution, WBE (f) was selected as a suitable compositional pattern, which was highly stable with average size lower than 200 nm, to make WBEs with corrosion inhibitors listed in Table 3.2, for tribo-corrosion evaluation.

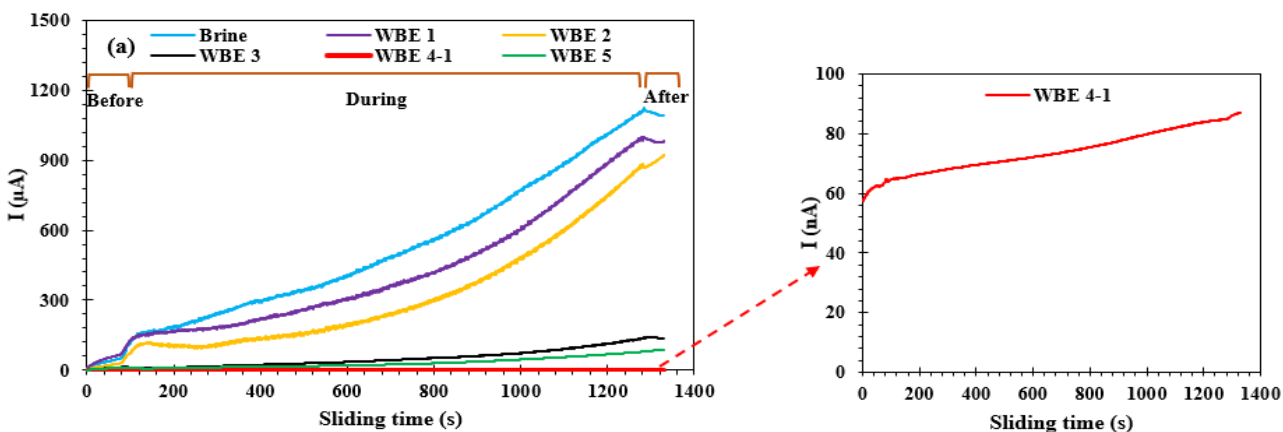
Table 3.2. Water-based emulsions (WBEs) for the present study

Solution	Ingredient
WBE 0	Brine solution as a reference solution: 5 gr KCl in 100 ml DI water [103-104]

WBE 1	0.1g (Mineral oil) in 99.9 g brine solution
WBE 2	0.1g (65% Mineral oil + 35% TERGITOL NP-9) in 99.9 g brine solution
WBE 3	0.1 g (65% Mineral oil + 3% TERGITOL NP-9 + 32% GL) in 99.9 g brine solution
WBE 4-1	0.1g (65% Mineral oil + 3% TERGITOL NP-9 + 32% PEG-2 oleamide) in 99.9 g brine solution
WBE 4-5	0.5g (65% Mineral oil + 3% TERGITOL NP-9 + 32% PEG-2 oleamide) in 99.5 g brine solution
WBE 4-10	1g (65% Mineral oil + 3% TERGITOL NP-9 + 32% PEG-2 oleamide) in 99.0 g brine solution
WBE 4-20	2g (65% Mineral oil + 3% TERGITOL NP-9 + 32% PEG-2 oleamide) in 99.0 g brine solution
WBE 5	0.1g (65% Mineral oil + 3% TERGITOL NP-9 + 32% GM) in 99.9 g brine solution

3.3.2 Tribo-corrosion study

When wear takes place in a corrosive environment, the deterioration of material can be reflected by changes in current and open circuit potential during sliding process. We investigated tribo-corrosion of the steel immersed in various WBEs under linear sliding condition with *in situ* monitoring changes in current, OCP and friction as a function of sliding time (see Figs. 3.3 and 3.4). COF values of samples in different WBEs were calculated for average values during the last 1000 seconds of the tests, during which the frictional curves became stable.



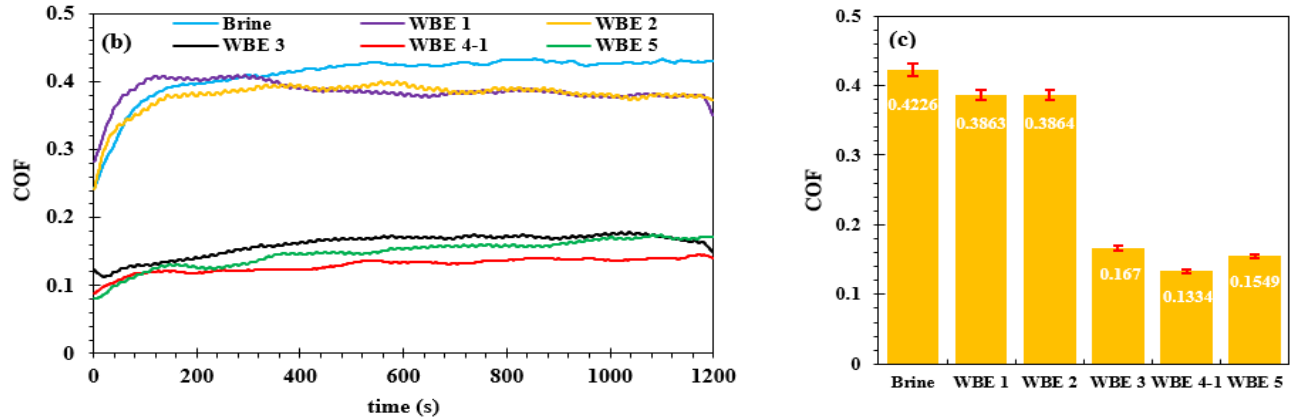


Fig. 3.3 (a) Variations in current and (b) COF versus the sliding time; (c) average COF values for the brine solution and WBEs including mineral oil, TERGITOL NP-9 and three corrosion inhibitors of PEG 2-oleamide, GM and GL.

As shown in Fig. 3.3(a), slow increases in the current of steel samples immersed in various solutions were observed before the sliding process was started. The onset of sliding caused an abrupt rise in the current, which was more pronounced for samples immersed in the brine solution and WBEs without corrosion inhibitors (WBE 1 and 2). During sliding process, current increased continuously with time, indicating that corrosion of steel was enhanced when wear was involved. The brine solution caused the highest current over time, since no any protective film could form on the steel sample immersed in this solution. However, the addition of three corrosion inhibitors in WBE3, WBE 4-1 and WBE 5 remarkably reduced the current and made them saturated quickly. During sliding, current enhanced and reached a value of $136 \mu\text{A}/\text{cm}^2$ for WBE 3, compared to $78.5 \mu\text{A}/\text{cm}^2$ for WBE 5, which was a result of formation of a stronger film to protect the steel from corrosion involving wear. As Fig. 3.3(a) shown, steel samples immersed in WBE 4-1 exhibited a sharp reduction in current (nanoscale); the obtained current showed an approximately value around 85 nano amperes at the end of sliding process, implying that there was slight corrosion and the material loss could be mainly caused by mechanical wear. This means that the formed film was

durable and could be reformed quickly after being damaged during corrosive wear. Figs. 3.3 (b) and (c) show COF values of steel samples immersed to various solutions which were measured simultaneously with current measurement shown Fig. 3.3(a). As illustrated, all the curves have fluctuations throughout the test duration. Higher COF values were obtained during tests in solutions without corrosion inhibitors, especially, for the brine solution which depicted a COF value of about 0.42. WBEs with corrosion inhibitors showed remarkably lowered COF, which were in the range of 0.13~ 0.16. The results indicate that three fatty acid corrosion inhibitors can build-up a protective layer in the contact region between the carbon steel and the silicon nitride ball, effectively reducing friction, which consequently helped reduce wear.

Fig. 3.4 presents changes in open circuit potential (OCP) with sliding time for steel samples immersed in various solutions. Reductions in OCP towards more negative values were observed after immersion of the steel samples in the solutions (before sliding). The decrease in OCP was more pronounced for the brine solution and WBEs without corrosion inhibitors (WBE 1 and 2), and kept decreasing during sliding process and reached more negative values (-0.730 for the brine solution and WBE1, and -0.712 for WBE 2) after a period of 20 min. However, for WBEs with corrosion inhibitors (WBE 3, 4-1, 5), corresponding OCP values decreased less and were rather stable after initial decreases. This further confirms the higher durability of the formed protective layer and its reformation capability benefiting from the corrosion inhibitors. WBE 4-1 containing PEG-2 oleamide performed the best with an approximate value of -0.6 V at the end of sliding. The result illustrates the more effective role of PEG-2 oleamide in blocking corrosive ions to reach metal surface through forming stronger protective layer.

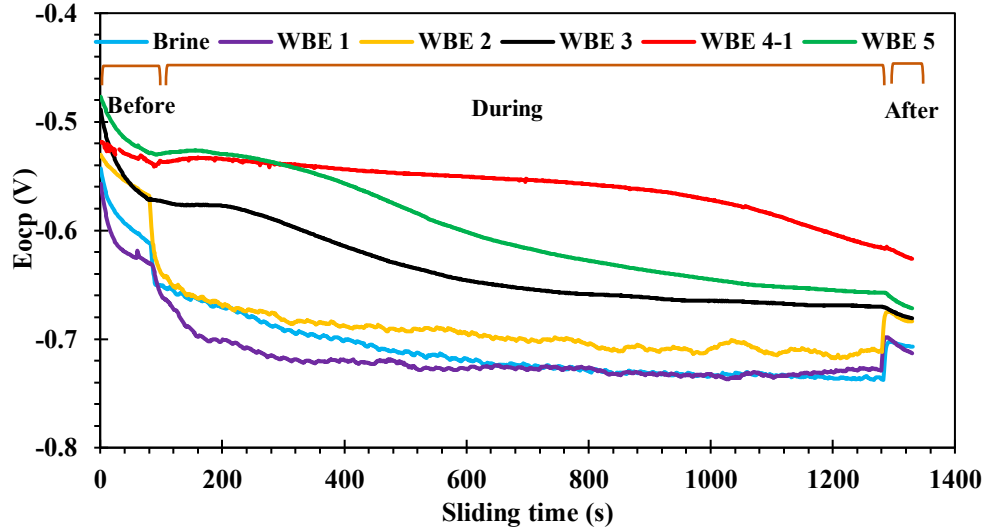


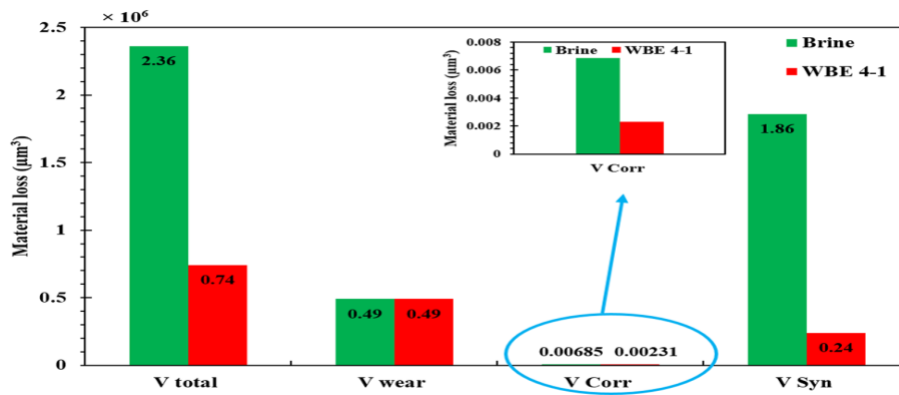
Fig.3.4. Evolution of potential versus time for 1018 carbon steels immersed in brine solution and various WBEs.

For more information, wear-corrosion synergy, and the role the inhibitor played in suppressing the wear-corrosion synergy were analyzed. During the tribo-corrosion test, the total material loss (V_{total}) is the sum of those caused by wear (V_{Wear}), corrosion (V_{Corr}) and wear-corrosion synergy (V_{Syn}),

$$V_{total} = V_{Wear} + V_{Corr} + V_{Syn} \quad (1)$$

where V_{total} was determined from wear test in the corrosive solution such as the brine solution, V_{Wear} was determined by performing the wear test in a solution similar to WBE 4-1 (with corrosion inhibitor) but the corrosive brine component was replaced by DI water, so that corrosion could be eliminated. V_{Corr} was determined based on the corrosion rate measured in the corrosive solution under study. The volume loss caused by the wear-corrosion synergy was thus be calculated as $V_{Syn} = V_{total} - (V_{Wear} + V_{Corr})$. Fig. 8 illustrates results of the tribo-corrosion tests in the brine solution and WBE 4-1, values of four items in eq. (1) were determined and are given in the table attached

to Fig.3.5. As shown, the volume loss of the carbon steel caused by wear in the brine solution is three times as large as that in WBE 4-1. In the brine solution the volume loss caused by wear-corrosion synergy is about 79% of the total volume loss (i.e., the V_{Syn}/V_{total} ratio). With the corrosion inhibitor (PEG-2 oleamide), the tribo-corrosion of the steel in the WBE 4-1 was effectively decreased and the corresponding wear-corrosion synergy was considerably suppressed with the V_{Syn}/V_{total} ratio reduced to 32%.



Solution	V total (µm³)	V wear (µm³)	V Corr (µm³)	V Syn (µm³)
Brine	2.36×10^6	0.49×10^6	6.85×10^3	1.86×10^6
WBE 4-1	0.74×10^6	0.49×10^6	2.31×10^3	0.24×10^6

Fig. 3.5. Volume losses caused by corrosion and tribo-corrosion tests performed in the brine solution and WBE 4-1, respectively. Determined values are given in the attached table.

3.3.2.1 Surface characterization of worn surfaces with an optical profilometer

Microscopic images of the worn surfaces of 1018 carbon steels immersed in various solutions after tribo-corrosion tests are depicted in Fig. 3.6.

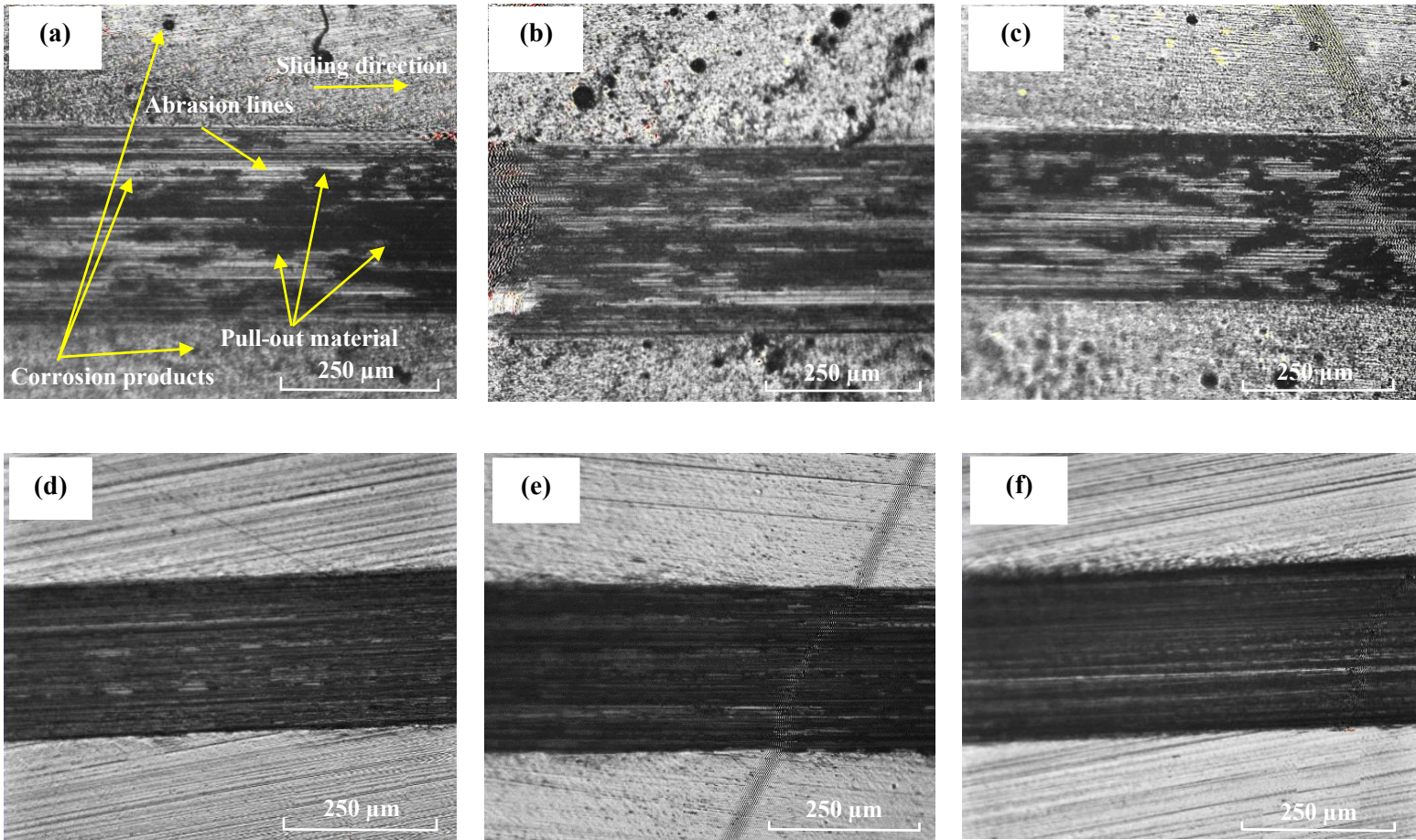


Fig. 3.6. Optical images of wear tracks on steel samples after tribo-corrosion test in (a) the brine solution, (b) WBE 1, (c) WBE 2, (d) WBE 3, (e) WBE 4-1, and (f) WBE 5. Load: 10 N

As shown in Fig. 3.6, severe damage was observed on the samples immersed in the brine solution and WBEs without corrosion inhibitors in both worn and unworn areas. The worn surface in the brine solution was rough with evident debris of corrosion products inside and around the wear track. The oxide layer formed on the steel sample immersed in the brine solution is easily destroyed by mechanical force; thereby, a considerable amount of steel was lost during the sliding test. Regarding WBE1 and WBE2, a thin layer composed of mineral oil could be generated on the sample surface. The formed layer could only provide weak protection against corrosion since corrosion products were still seen in the unworn and worn areas. When a moving silicon nitride

ball came into contact with the carbon steel sample, it enhanced corrosion by removing the corrosion products with more metal surface exposed to the corrosive solution and making the sample more anodic due to the introduced plastic deformation. On the other hand, corrosion enhanced wear by turning steel into poor oxide scale and increasing stress concentrations due to the resultant irregularities (such as pits). The addition of three corrosion inhibitors remarkably improved the anti-tribo-corrosion capabilities of carbon steel samples immersed in WBE 3, WBE 4-1 and WBE 5. As shown in Fig. 3.6, the presence of corrosion inhibitors caused little sign of corrosion products on the worn and unworn surfaces of the carbon steel samples. Worn surfaces of carbon steel samples immersed in WBE 3, 4-1 and 5 depict a smooth appearance with much fewer defects, indicating the effective presence of corrosion inhibitors in suppressing corrosion and thus corrosion-wear synergy. This may be correlated to the build-up of a chemisorbed or physisorbed protective film with high strength on the surface of carbon steel that creates a barrier effect between rubbing surfaces.

The volume loss that reflects the corrosion-wear action on the surface of steels was measured using an optical profilometer. Fig. 3.7 illustrates cross-sectional wear track profiles of samples tested in various solutions.

According to Fig. 3.8, volume loss of the sample immersed in brine solution is much greater (depth: 4.70 μm ; width: 338.6 μm) than those of samples immersed in WBEs containing corrosion inhibitors. The volume losses, depths and widths of wear tracks on samples tested in WBE 1 and 2 are also large, which can be attributed to easy removal of layer comprised of mineral oil on the wear track. The lowest volume loss (depth: 1.94 μm ; width: 170.4 μm) was determined on the sample tested in WBE 4-1 containing PEG-2 oleamide, which forming a protective layer to minimize the damage to the steel surface caused by wear and corrosion.

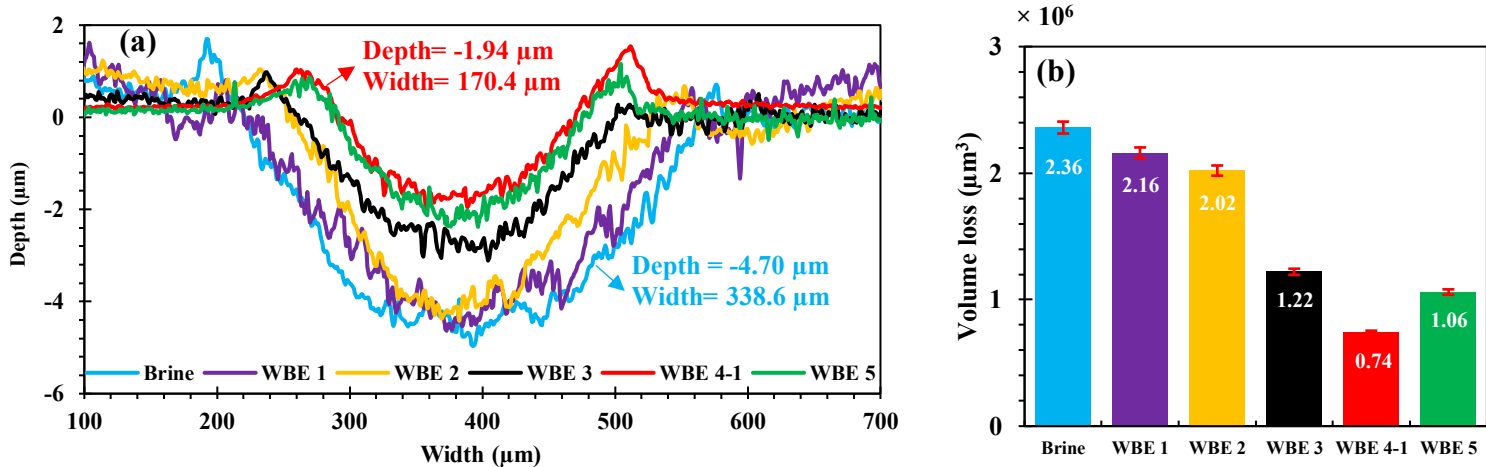
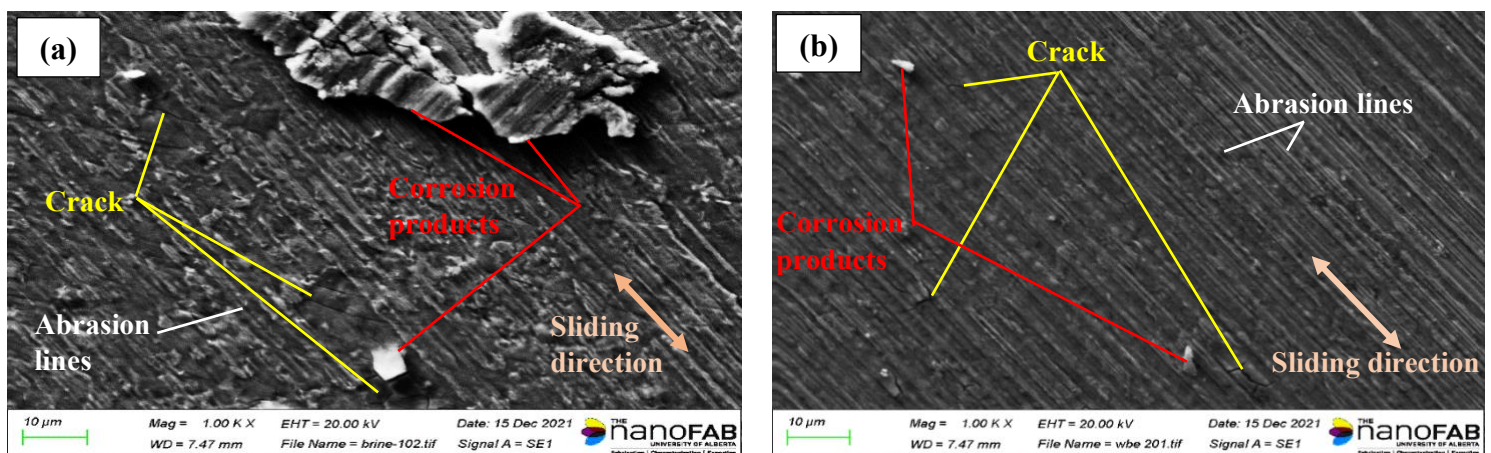
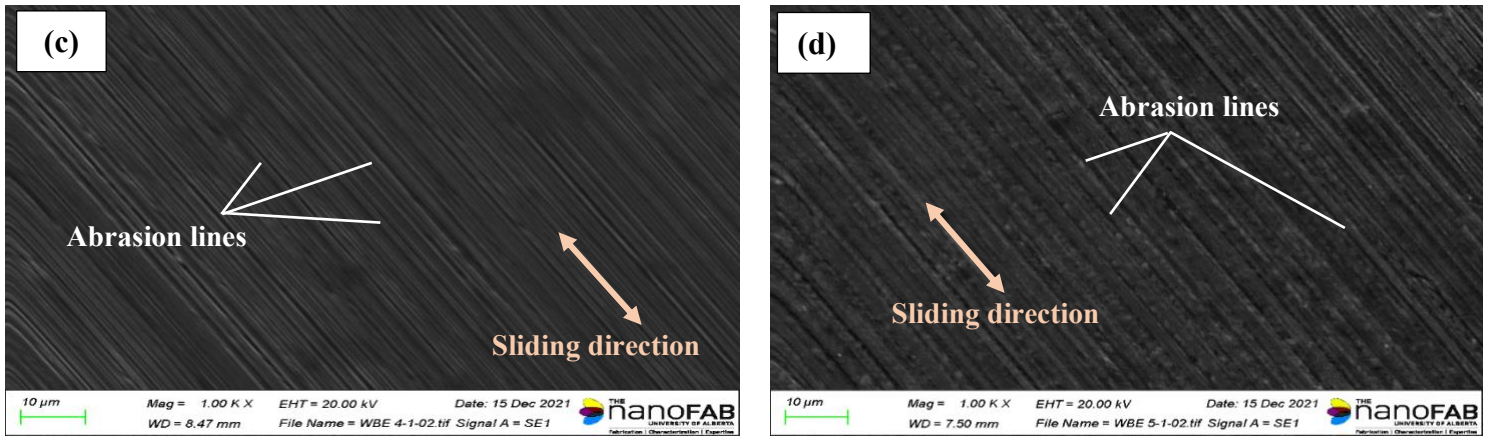


Fig. 3.7. Cross-sectional wear track profiles (a) and volume losses (b) measured by optical profilometer for 1018 carbon steels immersed tested in the brine solution and various WBEs.

3.3.2.2 Surface characterization of worn surfaces by SEM-EDX

More detailed worn surface analysis was carried out using SEM-EDX to examine the morphology and composition of wear tracks on samples tested in the brine solution and different WBEs. Figure 3.8 depicts SEM micrographs and EDS analysis of worn surfaces experienced tribo-corrosion tests in the brine solution and WBEs 2, 4-1 and 5.





Solution	Fe	O	C	Mn	N	K	Cl
Brine solution	71.12	14.80	12.70	0.53	-	0.1	0.84
WBE 2	72.02	12.73	14.11	0.61	-	-	0.52
WBE 4-1	78.83	6.27	14.35	0.55	-	-	-
WBE 5	74.85	10.03	14.64	0.49	-	-	-

Fig. 3.8. SEM micrographs and EDS analysis of worn surfaces after tribo-corrosion tests in (a) brine solution, (b) WBE 2, (c) WBE 4-1, and (d) WBE 5.

Fig. 3.8 shows an evident difference on the wear track appearance between samples tested in the brine solution and those tested in WBEs containing corrosion inhibitors (WBE 4-1 and WBE 5). Fig. 3.8 (a) reveals the presence of microcracks in the wear track of sample immersed in brine solution. The signs of corrosion products in worn surfaces are more evident which can be a consequence of corrosion occurring in the wear track. The EDS analysis confirmed that there was a significant amount of oxygen (14.80 wt%), potassium (0.1 wt%) and chloride (0.84 wt%) detected in the wear track, which came from the oxidized material and the presence of corrosive ions remaining in the tribological contact. A rough appearance with signs of corrosion products and microcracks were also observed on worn surface of the sample tested in WBE 2 but less severe,

compared to those on the sample tested in the brine solution. This shows that combination of mineral oil and surfactant reduced the damage but did not provide an effective barrier to the corrosive wear attack. However, the corrosion inhibitors, especially PEG 2-oleamide in WBE 4-1, the worn surface became smoother without signs of corrosion products and cracks. The EDS analysis of abraded regions revealed a minor amount of oxygen and no presence of corrosive ions including potassium and chloride in the wear track of the samples tested in WBE 4-1 and WBE 5. The detected increase in carbon amount should be caused by retaining of adsorbed the corrosion inhibitor on the worn surface, which helped inhibit corrosion and weaken the corrosion-wear synergy due to the generation of a protective layer that reduced the access for corrosive chemicals to reach the metal surface as well as the direct contact between the wearing surfaces.

Based on the results, the best anti-tribo-corrosion performance was obtained for steel samples immersed in WBE 4-1 containing mineral oil, surfactant and PEG 2-oleamide (see Table 3.2). For more information, effect of the combination (mineral oil + surfactant + corrosion inhibitors of PEG 2-oleamide) with increasing contents (0.1, 0.5 and 1 g) in brine solution (see Table 3.2) on tribo-corrosion of the steel sample was also studied. The current-time and COF-time curves measured for steel samples immersed in WBE 4-1, WBE 4-5 and WBE 4-10 are displayed in Fig. 3.9.

Fig. 3.9 shows the current-time and friction-time curves of steel samples immersed in WBEs 4-1, 4-5 and 4-10, respectively. Different solutions showed more or less different behaviors during initial stage of the tribo-corrosion test. WBE 4-1 and WBE 4-5 showed lower current and lower COF values than those of WBE 4-10. During the sliding process, currents of samples immersed in WBE 4-1 and WBE 4-10 increased, especially WBE4-10, and reached approximate values of 84.9 and 160 nA at the end of sliding test, respectively. The currents of the samples immersed in WBE 4-5, after initial declination, reached a relatively steady state with a value of 54 nA. In addition,

WBE 4-5 showed superior lubricity performance with its COF around 0.06, compared to WBE 4-1 and WBE 4-10 which reached average COF values of 0.14 and 0.16, respectively. This indicates that increasing the concentration up to 0.5 g reduced the current and COF values due to the formation of a more uniform and stronger protective film, which helped reduce friction, wear, corrosion, and corrosion wear. However, further increasing the concentration did not further reduce the current and COF, which could be attributed to lower stability and weaker dispersion of emulsion droplets into the brine solution. This has been further demonstrated and discussed in section 3.3.5.

Worn surfaces of 1018 carbon steel samples tested in WBEs 4-1, 4-5 and 4-10 were also examined using optical profilometer and SEM-EDS. Optical microscopic images of the worn surfaces of the samples are shown in Fig. 3.10.

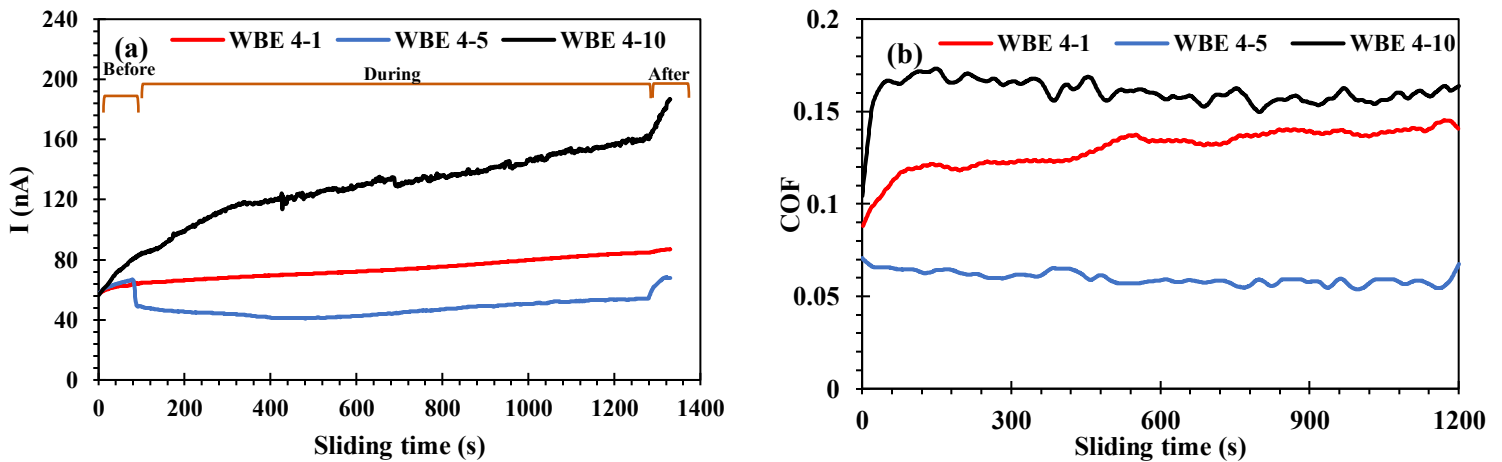


Fig. 3.9 Current-time curves for steel samples in WBE 4 containing the combination (mineral oil + surfactant + inhibitor of PEG 2-oleamide) at various concentrations (0.1, 0.5 and 1 g).

Fig. 3.10 shows abrasion lines inside the wear track. Corrosion of the steel samples in both unworn and worn areas was remarkably suppressed when immersed in the WBEs containing PEG -2 oleamide. This helped mitigate the corrosion-wear synergy and thus the damage to the steel

during the tribo-corrosion test. According to Fig.3.10(d), when the concentration of formulated combinations increased to 0.5 g in 99.5 g brine solution, the volume loss reached the lowest value ($0.4543 \times 10^6 \mu\text{m}^3$), consistent with the minimum corrosion current as shown in Figure 3.9(a). Further increasing in the concentration up to 1 g in 99 g brine solution (WBE 4-10) did not enhance the benefits but increased the volume loss. At this concentration, the corrosion appeared to be increased, evidenced by the current measurement as Fig. 3.9(a) illustrates, which should be responsible for the increase in volume loss.

SEM-EDS was employed to examine the wear track morphologies of the steel samples after testing in WBEs 4-1, 4-5 and 4-10, respectively, which are shown in Fig. 3.11.

According to Fig. 3.11, no obvious corrosion products can be found on the wear track of steels after a tribo-corrosion test, confirmed by EDS analysis (no chloride and potassium ions). Fig. 3.11(a) also depicts that the surfaces become smoother with increasing concentration of the combination (mineral oil + TERGITOL NP-9 + PEG-2 oleamide) up to 0.5 g in the brine solution. In addition, the existence of nitrogen element (0.1 wt.%) shows a higher deposition of PEG-2 oleamide, which contains nitrogen, on the worn surface with increasing the carbon content from 14.35 wt.% to 15.55 wt.% and the oxygen content from 6.27 to 7.98 wt.%, respectively. Thus, a highly coverage protective film was generated on the wear track, leading to marked reductions in friction, wear, corrosion and corrosive wear. However, with further increasing the amount of the combination in the brine solution (WBE 4-10), deeper abrasion lines are observed on the worn surface. This indicates that excessive concentration of the combination affects the tribo-corrosion behavior of the steel negatively due to weaker dispersion of emulsion droplets and lack of effective film formation on the worn surface.

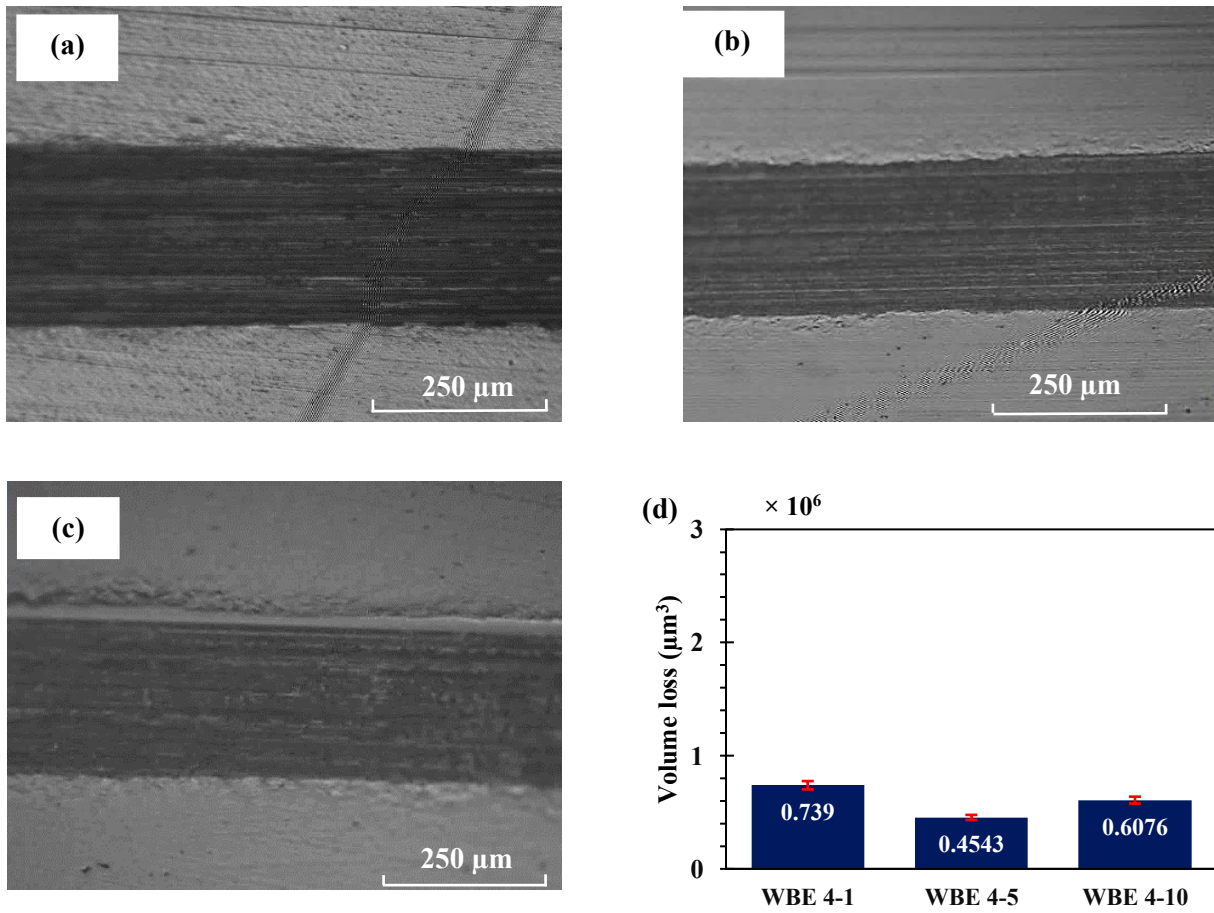
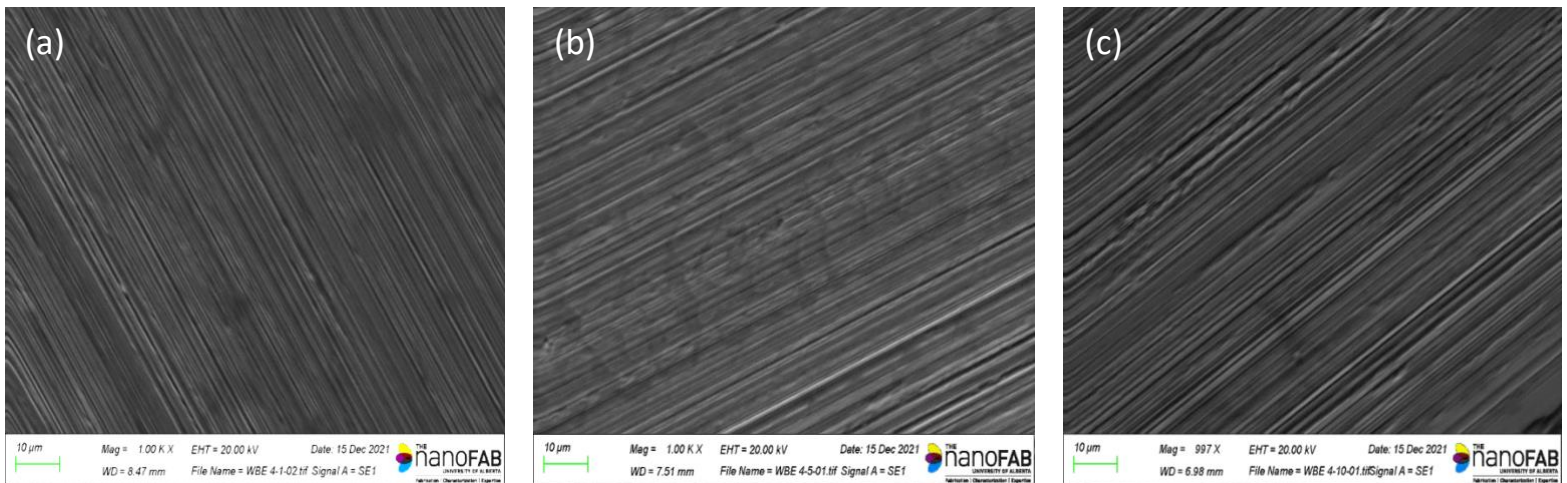


Fig. 3.10 Optical microscopic images of wear tracks on steel samples after tribo-corrosion tests in (a) WBE 4-1, (b) WBE 4-5, (c) WBE 4-10, and (d) corresponding volume losses.

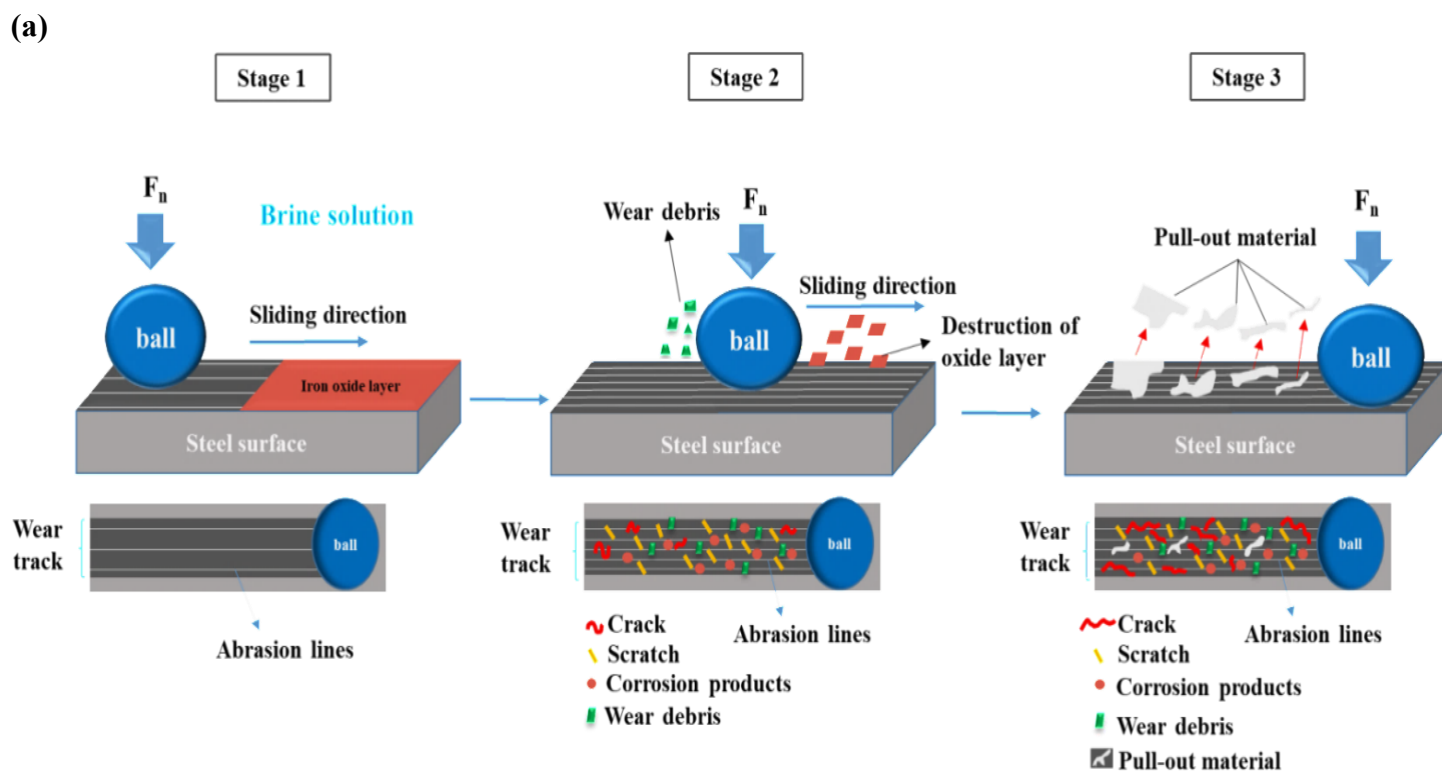


Solution	Fe	O	C	Mn	N	K	Cl
WBE 4-1	78.83	6.27	14.35	0.55	-	-	-
WBE 4-5	75.72	7.98	15.55	0.65	0.1	-	-
WBE 4-10	73.35	6.06	19.97	0.62	-	-	-

Fig. 3.11. SEM-EDS worn surfaces of steel samples after tribo-corrosion testing in (a) WBE 4-1, (b) WBE 4-5, (c) WBE 4-10.

3.3.3 Tribo-corrosion mechanisms of samples immersed in various solutions

Fig.3.12 schematically illustrates the mechanism for tribo-corrosion of carbon steel immersed in the brine solution and WBEs containing corrosion inhibitor (PEG-2 oleamide), respectively.



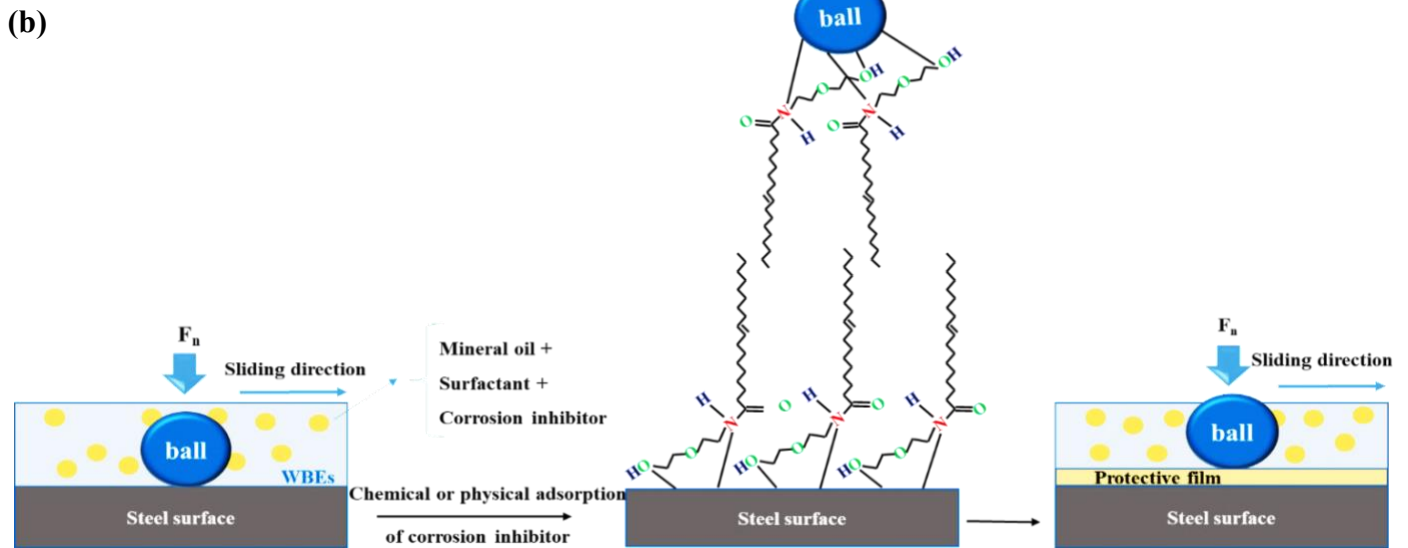


Fig. 3.12. Schematic illustration of the mechanism for tribo-corrosion of steel samples immersed in (a) the brine solution and (b) WBEs containing PEG-2 oleamide.

When the carbon steel is immersed in the brine solution, a porous oxide layer begins to form on the metal surface. The formed film is neither protective against the penetration of corrosive ions nor able to withstand the wearing force during corrosive wear. Through plowing, the silicon nitride ball caused abrasion lines (stage 1 in Fig. 3.12(a)). The porous oxide layer can be removed easily, leading to the exposure of fresh surface area of the steel to wear and corrosion. Besides, micro-scratches and micro-cracks can be generated during wear in the corrosive medium (stage 2 in Fig 3.12(a)). The micro-cracks propagate beneath the worn surface, causing delamination. Moreover, corrosion can increase the surface irregularity, providing sites for micro-crack initiation and propagation due to enhanced stress concentrations, leading to more delamination and larger material loss (stage 3 in Fig 3.13(a)). Wear debris can be generated on the metal surface, which reacts with the electrolyte to form oxide particles and cause more or less three-body abrasion.

The mechanism for tribo-corrosion of the carbon steel immersed in the WBEs containing PEG-2 oleamide is summarized in Fig. 3.12(b). During the sliding process, corrosion inhibitor molecules

can be adsorbed on the steel surface through physical or chemical interactions or both. The physical adsorption may occur via electrostatic interaction between protonated form of corrosion inhibitor molecule and the metal surface with negative charge. Furthermore, PEG-2 oleamide can be adsorbed chemically on the steel surface by the interaction between lone electron pairs of two heteroatoms (nitrogen and oxygen) and free orbital d of iron, leading to the formation of a protective film. This protective film does not only reduce the contact between the carbon steel and the counter-body but also limits the access for corrosive agents to reach the metal surface and mitigates the hydrogen evolution reaction, thereby reduce friction, wear and corrosion.

3.3.4 Stability of WBEs consisting of PEG 2-oleamide at various concentrations

In order to understand why excessive concentrations of the combination (65% mineral oil + 3% TERGITOL NP-9 + 32% PEG-2 oleamide) in the brine solution caused negative effect on the resistance to tribo-corrosion, stabilities of WBEs 4-1, 4-5, 4-10 and 4-20 were studied by visual observation, turbidity measurements, particle size distribution, zeta potential and inverted light fluorescence microscope.

3.3.4.1 Visual observation

The visual observation of all WBEs containing the combination (65% mineral oil + 3% TERGITOL NP-9 + 32% PEG-2 oleamide) at different weight concentrations (0.1, 0.5, 1 and 2 g) versus time is illustrated in Fig. 3.13.

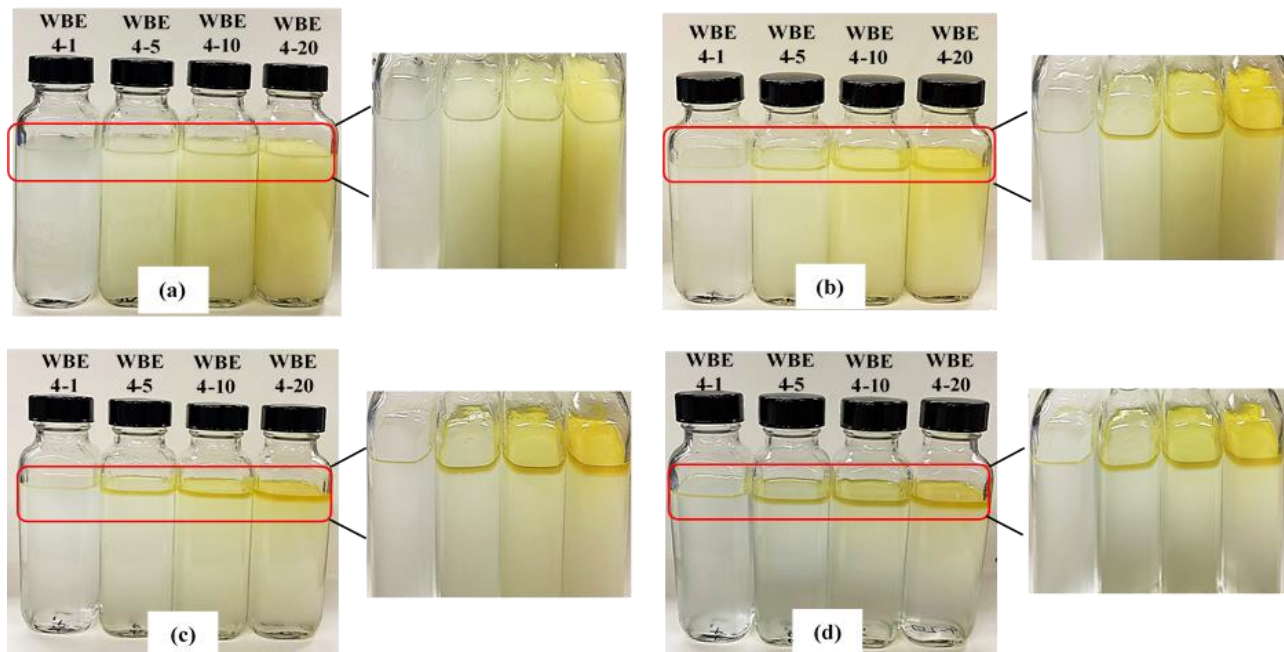


Fig. 3.13. Visual observation regarding the stability of formulated WBEs containing the combination (mineral oil + surfactant + PEG 2-oleamide) at various concentrations (0.1, 0.5, 1 and 2 g in the brine solution, forming WBEs of 100 g, respectively): (a) after mixing; (b) 5 minutes after mixing, (c) 2 h after mixing and (d) 6 h after mixing.

Fig. 3.13 shows that all the WBEs were stable after mixing, although the phase separation occurred over time. A partial phase separation for WBEs having higher concentrations (WBE 4-10 and WBE 4-20) was observed after 5 minutes. The thickness of the separation layer with emulsion droplets (the yellowish layer) in the brine solution increased with time, especially after 2 and 6 h. This indicates that the emulsion droplets dispersed in the aqueous phase tend to accumulate at higher concentrations, leading to phase separation over time and thus negatively affecting the stability of the WBEs. However, no significant separation was observed after 6 h for WBEs with lower concentrations (WBE 4-1 and WBE 4-5).

3.3.4.2 Turbidity measurement

For quantitative information, turbidity measurements were performed to further evaluate the effect of the amount of the combination in the brine solution (from 0.1 g to 2 g) on the stability of the prepared WBEs. Fig. 3.14 presents the determined turbidity values of the WBEs for a period of 2 h.

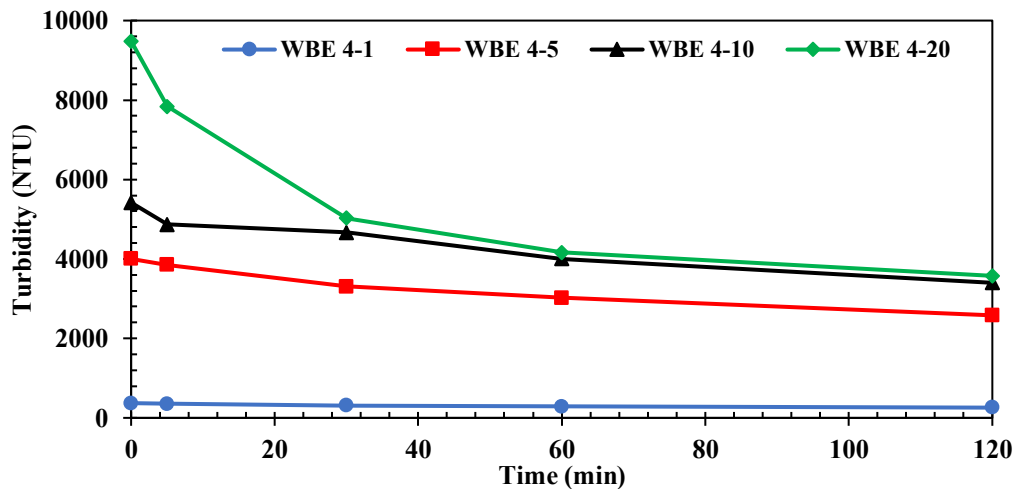


Fig. 3.14 Turbidity values of WBE 4 containing different amounts (0.1, 0.5, 1 and 2 g) of the combination (65% mineral oil + 3% TERGITOL NP-9 + 32% PEG-2 oleamide) in the brine solution versus time.

As shown, the turbidity of the WBEs with the combination (65% mineral oil + 3% TERGITOL NP-9 + 32% PEG-2 oleamide) at different concentrations (0.1, 0.5, 1 and 2 g) decreases with respect to time. WBE 4-1 and WBE 4-5 show the highest stability due to lower changes in the slopes of the turbidity curve during 2 h. However, the lowest stability was observed for WBEs with higher concentrations (WBE 4-10 and WBE 4-20), indicating significant reduction of 2018 and 5909 NTU in turbidity value for a period of 2 h. Aggregation of emulsion-based droplets dispersed in the brine solution occurred with excessive increase in the amount (1 g in 99

g brine solution and 2 g in 98 g brine solution listed in Table 3.2) of the combination. As a result, the stability of droplets formed in aqueous phase is reduced, evidenced by larger reductions in slope of the turbidity curves of WBE 4-10 and WBE 4-20.

3.3.4.3 Particle size distribution

The particle size distribution of the emulsion droplets reflects the agglomeration of droplets. Fig. 3.15 shows the average droplet sizes and distributions in WBEs having the combination of mineral oil + TERGITOL NP-9 + PEG-2 oleamide at various concentrations (0.1, 0.5, 1 and 2 g) in the brine solution.

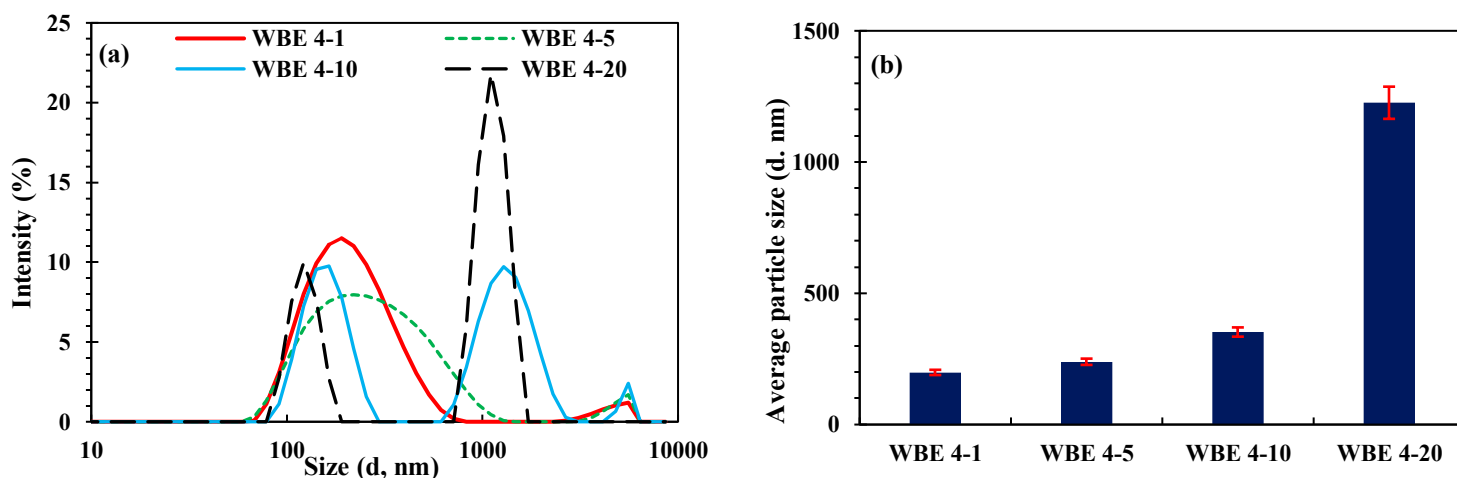


Fig 3.15 Particle size distribution (a) and average particle size (b) of prepared WBEs containing mineral oil + TERGITOL NP-9 + PEG-2 oleamide at various concentrations (0.1, 0.5, 1, & 2 g).

As shown in Figs. 3.15 (a) and (b), the variation in concentration of the combination (mineral oil + TERGITOL NP-9 + PEG-2 oleamide) in the aqueous solution affected the particle size distribution profile with remarkable change in average size of emulsion droplets from 198.6 nm in WBE 4-1 to 1226 nm in WBE 4-20. Fig. 3.15 also shows that WBEs with higher concentrations (1 g for WBE 4-10 and 2 g for WBE 4-20) of the combination were not as stable

as those with lower concentrations (WBE 4-1 and WBE 4-5). The emulsion droplets tended to aggregate, and the size of emulsion droplets increased considerably to 352.5 in WBE 4-10 and 1226 in WBE 4-20. In addition, the bimodal particle size distribution with two sharp peaks was shown by WBE 4-10 and WBE 4-20 due to the aggregation of emulsion droplets with the largest average particle size, corresponding to poor stability of the WBEs containing larger amounts of the combination. WBE 4-10 and WBE 4-20 presented a population of emulsion droplets with an average diameter around 142 and 122 nm, and a major population with 1280 and 1110 nm of mean diameter, respectively. Micrographs of WBE 4-10 and WBE 4-20 (Figs. 3.15 (a) and (b)) confirm the presence of larger droplets forming many aggregated droplets, attributed to the formation of two sharp peaks around 1100 nm. Such two peaks were not observed for WBEs with low concentrations of the combination (WBE 4-1 and WBE 4-5). Clearly, excessive increase in concentration (above 0.5 g) of the combination can cause changes in the particle size distribution and increase the average particle size, leading to reduction in stability of the WBEs.

3.3.4.4 Zeta potential measurements

The results of measurements of zeta potential of emulsion droplets containing mineral oil, TERGITOL NP-9, and PEG-2 oleamide at various concentrations are depicted in Fig. 3.16. The results of zeta potential are consistent with the results of visual observation and turbidity measurements.

According to Fig. 3.16, the emulsion droplets formed in the aqueous phase have a negative surface charge due to the presence of non-polar hydrocarbons in the structure of the ingredients. The zeta potential of emulsion droplets changed significantly with increasing the concentration of the combination (65% mineral oil + 3% TERGITOL NP-9 + 32% PEG-2 oleamide) in brine

solution. When the concentration was increased to 0.5 g in 99.5 g brine solution, the zeta potential of droplets reached the maximum (-71.8mV). The high absolute value generated large repulsive force between droplets, preventing agglomeration of the emulsion droplets when dispersed in the brine solution, thus ensuring the stability of emulsion droplets [148]. However, with further increasing the concentration to 2 g in 98 g brine solution, the zeta potential of emulsion droplets decreased to a minimum value (-50.4). It is clear that the excessive increase in the concentration of the combination (1 and 2 g) can lead to aggregation of emulsion droplets in the brine solution, reducing the stability of the emulsion droplets with the lowest zeta potential for the WBEs having the high concentrations.

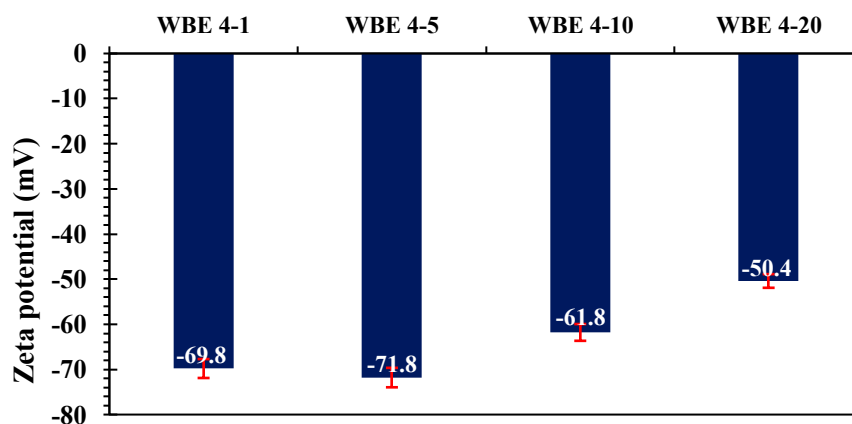


Fig. 3.16 The zeta potential of formulated WBE containing mineral oil + TERGITOL NP-9 + PEG-2 oleamide at various concentrations (0.1, 0.5, 1 and 2 g).

3.3.4.5 Observation with inverted light fluorescence microscope

Micrographs of emulsion droplets containing mineral oil + TERGITOL NP-9 + PEG-2 oleamide inside the brine solution at various concentrations (0.1, 0.5, 1 and 2 g) are illustrated in Fig. 3.17, which were taken with an inverted light fluorescence microscope.

As Fig 3.17 shows, the microstructures of WBEs with low concentrations (0.1 g for WBE 4-1 and 0.5 gr for WBE 4-5) display small droplets with uniform dispersion in the brine solution. However, increasing the concentration of combination (mineral oil + TERGITOL NP-9 + PEG-2 oleamide, 1 and 2 g) in the brine solution led to the formation of emulsion droplets with various sizes, which agrees with the results of particle size distribution (Fig. 3.15). Additionally, WBE 4-10 and WBE 4-20 display many aggregated droplets which are promoted by reduction in the zeta potential of emulsion droplets (Fig. 3.16) and electrostatic screening effects [149]. Therefore, a sharp increasing in concentration causes an intense agglomeration of emulsion droplets into aqueous phase, resulting in reduced the stability of formulated WBEs.

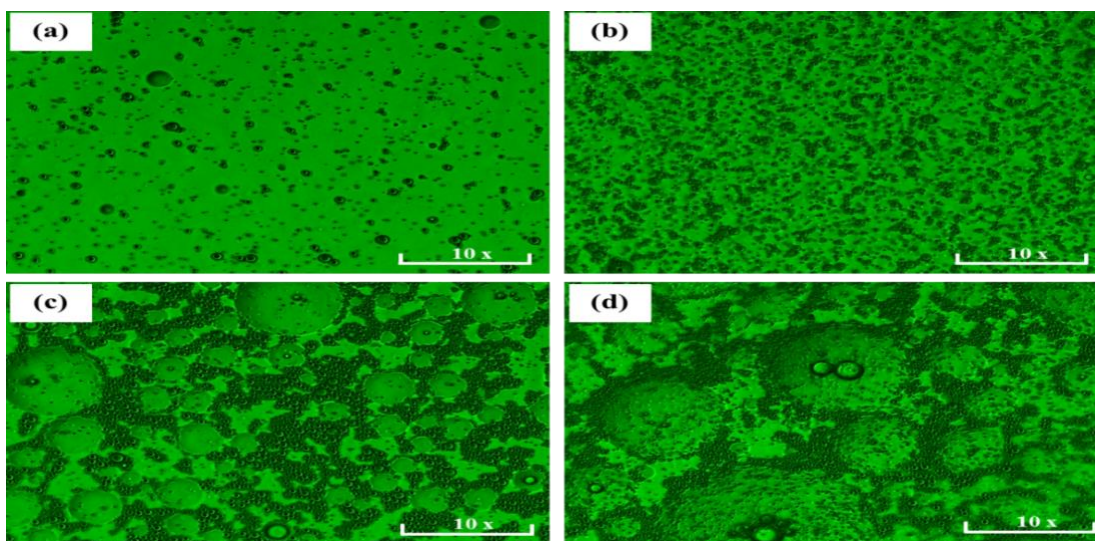


Fig. 3.17 *Inverted light fluorescence microscopy images of emulsion droplets including mineral oil + TERGITOL NP-9 + PEG-2 oleamide at various concentrations (0.1, 0.5, 1 and 2 g).*

3.4 Conclusions

Effects of three new derivatives of fatty acid-based corrosion inhibitor on tribo-corrosion of carbon steel in various WBEs and the brine solution were investigated. The effect of the concentration of the combination (mineral oil+ surfactant + corrosion inhibitor) in the brine

solution on the protectiveness of the best emulsion system, WBE 4-1, was also studied. Results of this chapter are summarized as follows:

1. Based on measurements of zeta potential and particle size distribution, the combination (65% mineral oil+ 3% surfactant+ 32% corrosion inhibitors) was added to the brine solution with different concentrations to make WBEs, which are stable.
2. The WBEs containing the corrosion inhibitors significantly improved the performance of carbon steel samples during tribo-corrosion; WBE 4-1 containing PEG-2 oleamide performed the best.
3. Effects of three different concentrations (0.1, 0.5 and 1 g) of the combination (65% mineral oil+ 3% surfactant+ 32% corrosion inhibitors) in the brine solution on tribo-corrosion of the carbon steel were investigated. It is demonstrated that increasing the concentration of the combination up to 0.5 g in 99.5 g brine solution resulted in the highest effectiveness.

Chapter 4 Effect of sliding speed on corrosion and tribo-corrosion of carbon steel in emulsion-based drilling fluids with green corrosion inhibitors³

4.1 Introduction

Tribo-corrosion is the wear of materials in corrosive environments involving synergistic attacks of wear and corrosion [19, 30, 124, 150-154]. A good example of tribo-corrosion is the corrosive wear of drilling facilities used in oil and gas drilling operations, where steel components e.g., drill bits, drill pipe, and drill collar, are in dynamic contact with rock or metals in corrosive environments, leading to their premature failure caused by the mechanical attack and corrosion-induced material degradation [30, 54, 56, 120, 155]. Therefore, it is important to evaluate the tribo-corrosion performance of materials under different conditions to clarify underlying mechanisms.

The tribo-corrosion of metallic equipment in the drilling environment is influenced by temperature, pressure, drilling fluid, applied load, sliding speed, and additives in the drilling fluid [155-156]. The above-mentioned factors may considerably change the nature and degree of material damage. Among these factors, the sliding speed is a controllable parameter, which could be adjusted to influence the kinetics of tribo-corrosion attack on materials. The sliding speed can change the lubrication regime from boundary lubrication to mixed or full-film hydrodynamic lubrication. As the sliding speed increases, the boundary lubrication regime decreases drastically, leaving a thicker lubricant layer between the moving surfaces where both surface asperities are separated. Besides, the change in the sliding speed is expected to vary the momentum transfer in

³ A version of this chapter has been published. M.j. Palimi, V. Alvarez, E. Kuru, W. G. Chen, D.Y. Li, Effects of sliding speed on corrosion and tribo-corrosion of carbon steel in emulsion-based drilling fluids with green corrosion inhibitors, *Journal of Bio- and Tribo-Corrosion* 9, 2 (2023). <https://doi.org/10.1007/s40735-022-00722-9>.

a normal direction, thus providing an upward force on the upper surface. As a result, a reduction in the real area of contact between two sliding surfaces can take place, which may reduce the tribo-corrosion attack. Thus, controlling the sliding speed may lead to improved drilling effectiveness and minimized tribo-corrosion of the drilling facilities [34,157].

Modification of the drilling fluid with additives such as organic corrosion inhibitors is another feasible approach to improve the drilling effectiveness and service life of drilling facilities via mitigating encountered corrosion and wear [158-161]. The corrosion inhibitors can be adsorbed on a metallic surface and generate a thin layer that protects the metal surface from corrosive dissolution and wear [161-164]. Recent advances in metallic substrates' corrosion protection are largely focused on low cost and eco-friendly effective corrosion inhibitors or "green corrosion inhibitors," which are basically organic substances [161, 165-166]. Among organic corrosion inhibitors, plant extracts have found increasing applications as green corrosion inhibitors due to their abundance and presence of non-polar and polar phytochemicals in their structures. The adsorption of the phytochemicals on the steel surface may result from physisorption and chemisorption, leading to the form of a protective film on the metal surface which is mainly responsible for enhancing tribo-corrosion behavior of metallic materials [162-164, 167-172].

Although some studies can be found in the literature, which report the effect of sliding speed on the tribological behavior of metals [34, 54, 173-178], there is very little information about the kinetic response of steels to tribo-corrosion in the drilling fluids containing green corrosion inhibitors, or about how the sliding speed influences the effectiveness of the green inhibitors in protecting the steels. Such information is of importance for the effective application of the green inhibitors in suppressing tribo-corrosion of metallic equipment used in the oil industry since tribo-corrosion is a dynamic process, and the inhibitor-induced lubricating film involves growth,

damage, and re-growth processes. Obtaining the information and elucidating the underlying mechanism are the main objectives of this study.

This chapter is focused on investigating the kinetic response of 1018 carbon steel to pure corrosion (without wear) and tribo-corrosion (wear-corrosion synergy) in emulsion-based drilling fluids containing three green corrosion inhibitors at low sliding speeds (as crucial factor which significantly influences the tribo-corrosion of drilling equipment) under the boundary lubrication condition. The low speeds with resultant relatively stable sample-counterpart contact facilitated *in situ* measuring corrosion potential, current, and corrosion rate during corrosion and tribo-corrosion processes, which would help obtain the information on the kinetic response with desired preciseness. As for the effects of high speeds on the kinetic response in other lubrication regimes, they would be arranged in follow-up studies. The emulsion-based drilling fluids under study contained three fatty acid-based corrosion inhibitors, respectively: Glycerol linoleate (GL), Polyethylene glycol-2 oleamide (PEG-2 oleamide), and Glycerol myristate (GM). Samples of 1018 carbon steel were tested in the drilling fluids using a pin-on-disc tribometer integrated with an electrochemical system to investigate their dynamic corrosion and tribo-corrosion at various sliding speeds. Potentiostatic and potentiodynamic polarization techniques were employed to monitor OCP, current density, corrosion potential, and corrosion current under the influence of the sliding speed with and without sample-pin contact. For tribo-corrosion evaluation, COF, volume loss, and specific wear rate samples at different sliding speeds were measured. A scanning electron microscope (SEM) equipped with the energy dispersive X-ray spectroscopy (EDX) was used to investigate the worn surface morphology, and composition of the layer adsorbed on the worn surface to understand the synergistic wear-corrosion attack at different sliding speeds.

4.2 Experimental procedure

4.2.1 Material and water-based emulsions (WBEs) preparation

Coupons of 1018 carbon steel with dimensions $2 \times 2 \times 0.5 \text{ cm}^3$ were prepared in a standard manner using mechanical grinding and polishing before tribo-corrosion tests. Before immersion in a tribo-corrosion cell, the sample was mounted in epoxy-polyamine glue, leaving a surface area of $1 \times 1 \text{ cm}^2$ uncovered for testing. To prepare water-based emulsions (WBEs), mineral oil, surfactant (TERGITOL NP-9) and three green corrosion inhibitors including PEG-2 oleamide, GM, and GL were added to the base fluid, a 5% KCl aqueous solution.

As explained in chapters 2 and 3 (turbidity, zeta potential and DLS measurements), a combination of 65 % mineral oil, 3 % surfactant, and 32 % corrosion inhibitor has opted as the highly stable composition for making the drilling fluids. Table 2.6 lists the formulated water-based emulsions (WBEs) as the drilling fluids for this chapter.

4.2.2 Tribo-corrosion and corrosion tests

The tribo-corrosion and corrosion experiments were performed using a pin-on-disc reciprocating tribometer. A three-electrode electrochemical cell was connected to the tribometer, having an Ag/AgCl as the reference electrode, a platinum plate as the counter electrode, and the carbon steel sample (1 cm^2) as the working electrode. The electrochemical cell was placed above the stage of the tribometer to perform the tests in linear reciprocating motion with and without contact between the sample and the counterpart. A Si_3N_4 ball of 4 mm in diameter was used as the counterpart. A normal force of 10 N and a reciprocating displacement of 3 mm was applied to the carbon steel sample. The experimental set-up for the tribo-corrosion tests is schematically shown in Fig. 3.1.

To investigate the effects of linear reciprocating motion with and without sample-counterpart contact on corrosion and tribo-corrosion, the tribo-corrosion and corrosion tests were carried out under the following conditions:

1- Tribo-corrosion study:

Linear motion of the Si_3N_4 ball pin at various sliding speeds (2, 3.5, 5, and 10 mm/s) under a load of 10 N.

2- Corrosion study:

Static module: no linear motion and no contact between the pin and the sample.

Linear motion (dynamic) module: linear motion of sample at different speeds (2, 3.5, 5, and 10 mm/s) without contact between the pin and the sample.

The tests were performed at room temperatures for a period of 1200s with *in situ* monitoring changes in COF, OCP, potentiostatic, and potentiodynamic polarization (PDP). Potentiostatic tests were performed at an applied anodic potential of +1mV from the OCP in 400 mL of the prepared WBEs. The current (I, μ A), open circuit potential (OCP), and COF were measured concerning time before, during, and after the sliding test. The PDP curves were recorded in the range of ± 250 mV concerning the OCP of each sample at a scan rate of 0.4 mV/s. All experiments were triplicated to ensure the reproducibility of the measurements.

4.2.3 Surface characterization

Surface examination, including morphology and composition, is vital for analyzing the effectiveness of the green corrosion inhibitors and their interactions with the steel sample surface. Surfaces of samples that experienced tribo-corrosion tests in different solutions were cleaned with distilled water and subsequently dried with air pressure. Optical microscopy was employed to observe different samples' surface morphology and wear track. In addition, a 3D optical

profilometer (Zegage 3D, Middlefield, US) was used to study the total volume loss of worn surfaces immersed in various WBEs. The total volume loss caused by the tribo-corrosion test was determined from the cross-section profile of the wear track in which values of depth and width were measured in various locations along the wear track. The following formula was used to obtain the specific wear rate (W) in $\mu\text{m}^3/\text{Nm}$ [180].

$$W = \frac{V}{Fd} \quad (1)$$

where V , d , and F are the total volume loss (μm^3), the total sliding distance (m), and normal load (N), respectively.

The surface morphology and chemical composition of carbon steel samples after corrosion and tribo-corrosion tests in different WBEs were examined by Scanning electron microscope (SEM) equipped with the energy dispersive X-ray spectroscopy (EDX), Zeiss Evo M10, Oberkochen, Germany.

4.3 Results and discussion

4.3.1 Corrosion of steel under static and dynamic conditions

When steel samples are immersed in a corrosive environment under static and dynamic conditions, the material degradation may be evaluated by measuring current over time and the potentiodynamic behavior of the samples. The curves of current over immersion time monitored in static and linear motion (dynamic) modules (2, 5, and 10 mm/s) without sample-pin contact in the brine solution and various WBEs are depicted in Fig. 4.1.

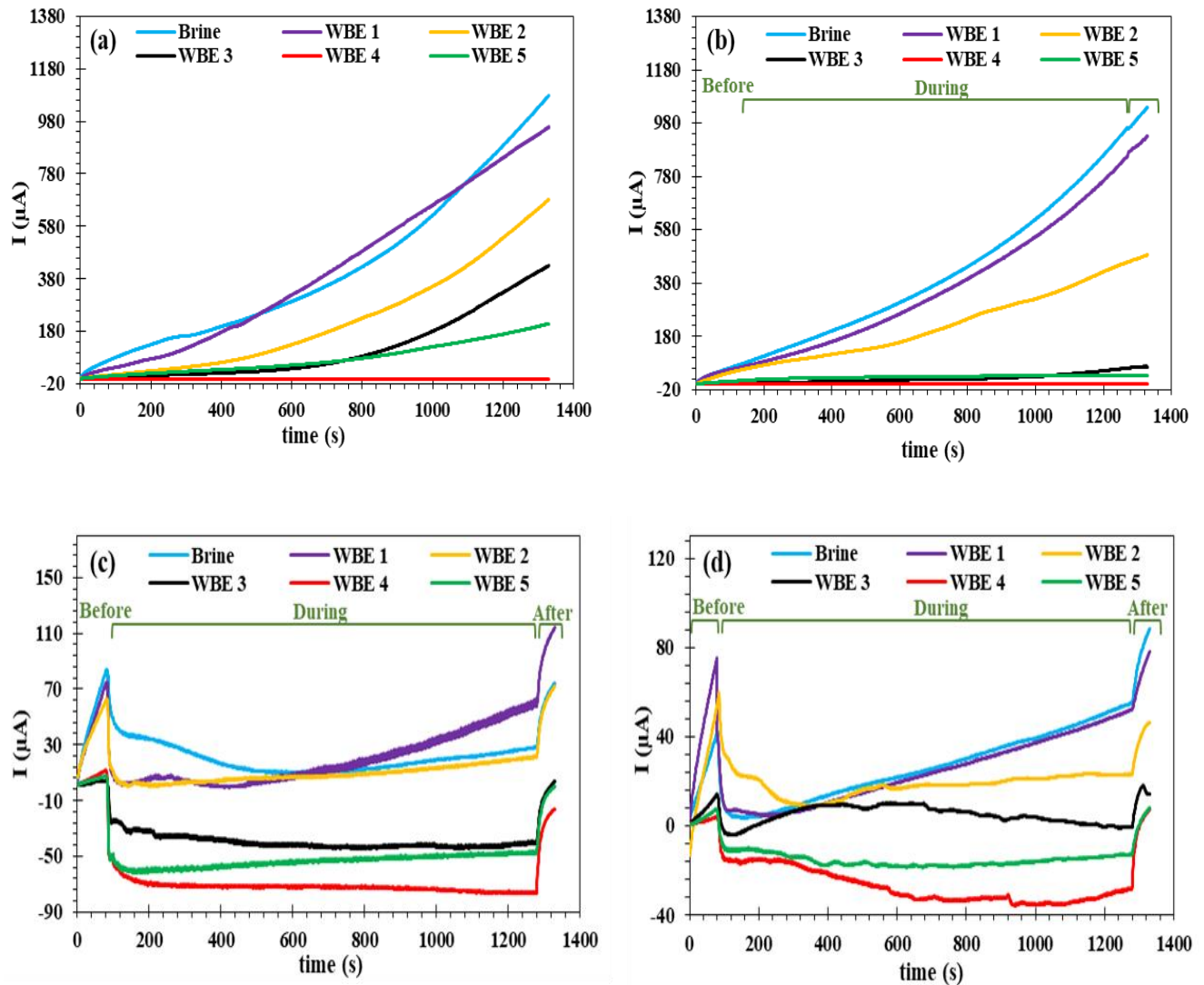


Fig. 4.1. Variations in current versus time recorded in range of $+1\text{mV}$ at the OCP for the brine solution and various WBEs under (a) static module, and linear motion (dynamic) module at different speeds of (b) 2 mm/s , (c) 5 mm/s and (d) 10 mm/s .

Fig. 4.1 (a) illustrates variations in current for steel samples immersed in different solutions in the static module where there was no motion during the test. Figs 4.1 (b) - (d) show variations in current at different speeds (linear motion module) in three regions: before, during, and after running linear motion. At the low speed (2 mm/s), variations in current show similar trends compared to those of measurements in the static module (Fig.4.1(a)). The current continuously

increased before, during, and after the test in the linear motion, indicating little influence of the low speed on the current evolution versus time. However, the situation changed when testing at higher speeds. As shown in Figs.4.1 (c) and (d), at higher speeds (5 and 10 mm/s), the current quickly increased before the pin started to move, especially in the brine and WBEs solutions without the corrosion inhibitors. Once the pin started to move, a sharp decrease in current occurred. It was noticed that for samples immersed in WBEs containing corrosion inhibitors (WBE 3, 4, and 5), the currents became negative. The sliding speed of 5 mm/s led to the lowest current over time, corresponding to the lowest dynamic corrosion of the steel at this speed. After the linear motion was stopped, the values of current re-increased. The above phenomena indicate that the movement of the steel sample at the higher speeds dynamically affected corrosion of the steel in the drilling fluids by influencing the diffusion rate of oxygen and the formation of more effective protective films (for steel tested in WBE 3, 4 and 5) on the metal surface which can occur at higher speeds. The presence of the corrosion inhibitors in WBE3, WBE 4, and WBE 5 remarkably reduced the currents under all tested speeds and made them saturated quickly. WBE 4 containing PEG-2 oleamide showed the most superior corrosion performance, especially at 5 mm/s, with an approximate value of $-76 \mu\text{A}$ at the end of linear motion, which was a result of the formation of a more protective layer to protect the steel from corrosion cathodically.

Polarization curves of steel samples immersed in brine solution and WBE 4 were determined under the static condition (no motion) and dynamic (linear motion) conditions at four different speeds. Obtained curves from the corrosion tests are presented in Fig. 4.2. According to Fig. 4.2(a), the curves of steel samples immersed in the brine solution shifted to more positive potentials (more anodic potentials) when the test condition was changed from the static state to linear motion. However, polarization curves of samples tested in WBE 4 moved to more negative

potentials by varying the speed from 0 to 10 mm/s, as shown in Fig. 4.2(b). In addition, both anodic and cathodic branches of the polarization curves of samples immersed in WBE 4 were affected by the speed, shifting towards lower current densities, especially at higher speeds. It was noticed that the curves were influenced considerably by the addition of corrosion inhibitor in WBE 4, compared to the situation of brine solution. The electrochemical parameters, including corrosion potential (E_{corr}), corrosion current density (i_{corr}), corrosion rate, anodic Tafel slope (β_a), and cathodic Tafel slope (β_c), were determined from polarization curves and are given in Table 4.2.

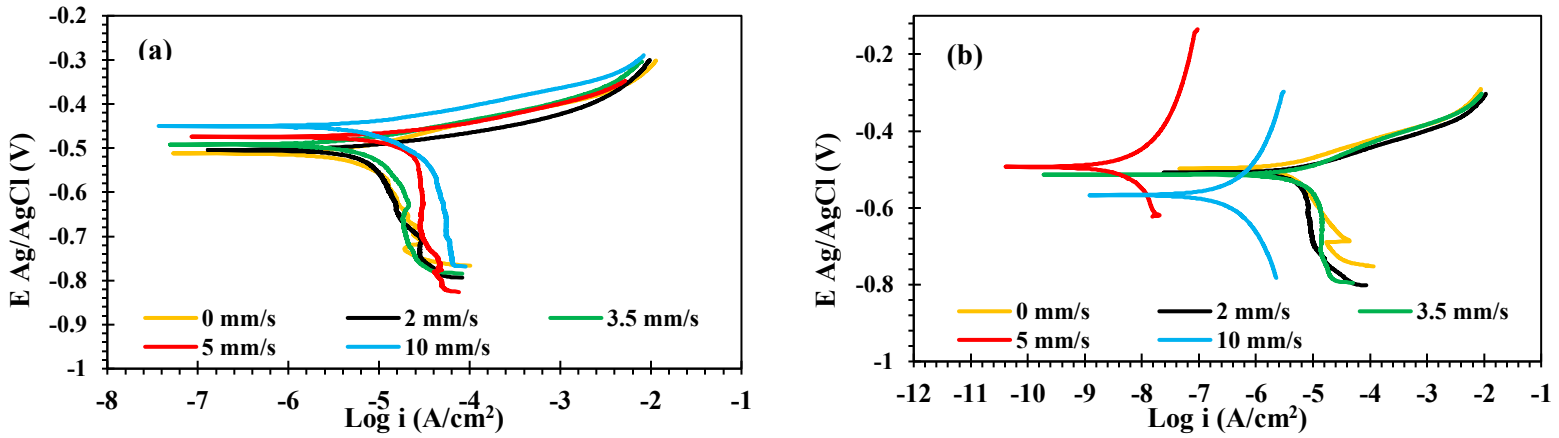


Fig. 4.2. Potentiodynamic polarization curves of steel samples immersed in (a) brine solution and (b) WBE 4 under the static condition (no motion) and linear motion condition at different speeds of 2, 3.5, 5, and 10 mm/s.

From Table 4.1 it is clear that E_{corr} for samples immersed in the brine solution increased from -0.512 V in the static condition to more positive values of E_{corr} and reached -0.450 V at 10 mm/s. However, an opposite trend was observed when tested in WBE 4, which showed that E_{corr} shifted from -0.497 V to -0.567 V as the speed was increased. The i_{corr} and corrosion rate of steels immersed in the brine solution and WBE 4 under static conditions (0 mm/s) were higher than those determined in the linear motion condition. The i_{corr} and corrosion rate of steels immersed in tested solutions declined with increasing the speed up to 5 mm/s. However, continuously increasing the

speed did not further reduce i_{corr} and corrosion rate. This indicates the noticeable influence of speed on the improvement of corrosion resistance of steels immersed in both brine solution and WBE 4 which are consistent with results shown in Fig. 4.1.

Compared to those tested in the brine solution, samples immersed in WBE 4 containing corrosion inhibitor exhibited the lowest i_{corr} and corrosion rate at all speeds; especially at 5 mm/s i_{corr} and corrosion rate reached the minima of about $0.0011 \mu\text{A}/\text{cm}^2$ and 0.0005 mpy, respectively. This remarkable improvement in corrosion resistance would be ascribed to the generation of a molecular protective layer at the electrode/electrolyte interface to protect the steel from corrosion [33]. Such protection appeared to be enhanced at higher speeds. More discussions on the effects of speed on corrosion rate in both the brine solution and WBEs are given in section 4.4 (Discussion).

Table 4.1. Values of corrosion current density, corrosion potential, cathodic and anodic Tafel slopes, the corrosion rate of steel sample immersed in the brine solution, and WBE 4 under the static condition and linear motion condition at different speeds 2, 3.5, 5, and 10 mm/s

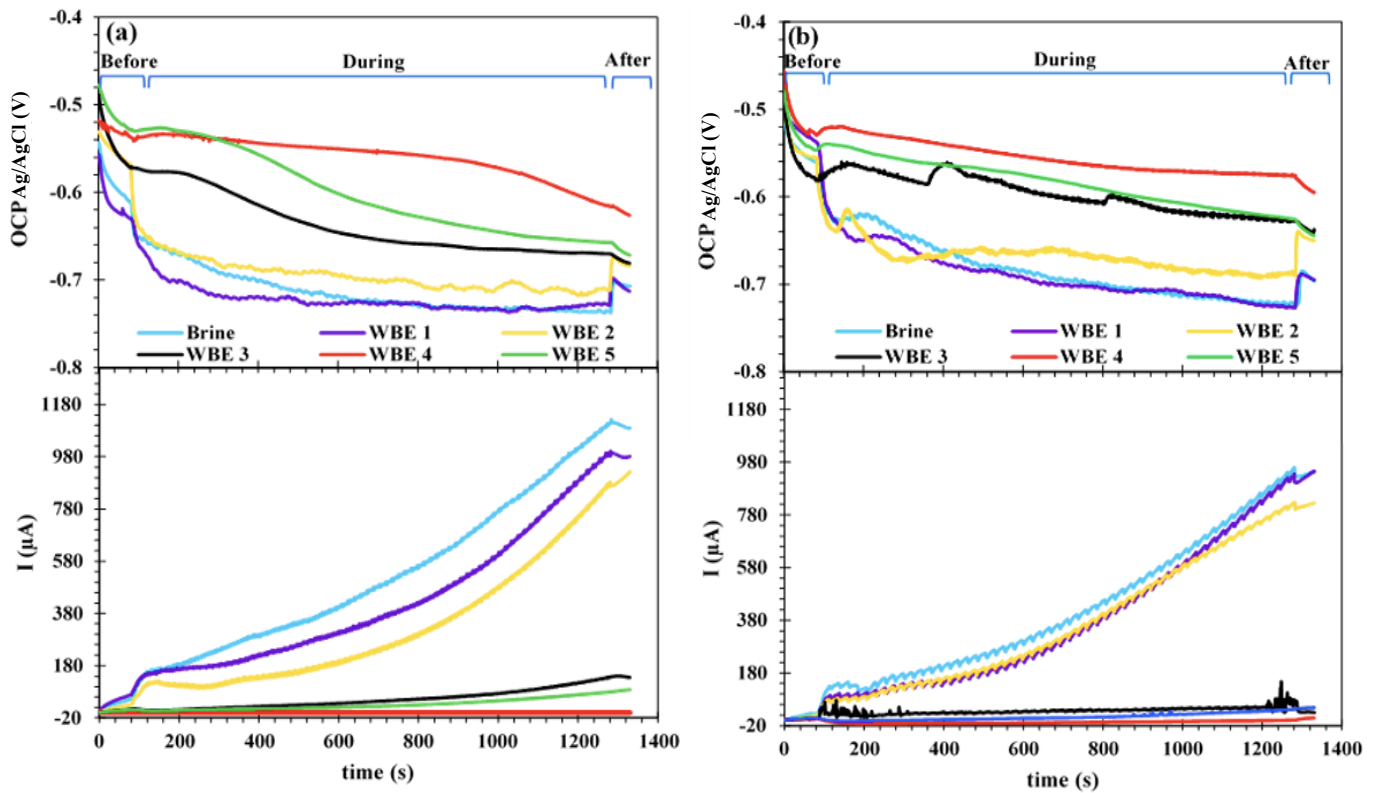
Solutions	E_{corr} (V)	i_{corr} ($\mu\text{A}/\text{cm}^2$)	Corrosion rate (mpy)	β_a (V/decade)	β_c (V/decade)
Brine- 0 mm/s	-0.512	6.46	2.96	0.062	0.192
Brine- 2 mm/s	-0.504	6.05	2.77	0.031	0.245
Brine- 3.5 mm/s	-0.492	5.74	2.63	0.047	0.124
Brine- 5 mm/s	-0.474	2.89	1.32	0.015	0.021
Brine- 10 mm/s	-0.450	4.55	2.09	0.028	0.057
WBE 4- 0 mm/s	-0.497	2.88	1.32	0.046	0.078
WBE 4- 2 mm/s	-0.508	2.06	0.94	0.028	0.046
WBE 4- 3.5 mm/s	-0.551	1.93	0.88	0.225	0.243
WBE 4- 5 mm/s	-0.493	0.0011	0.0005	0.032	0.032
WBE 4- 10 mm/s	-0.567	0.11	0.05	0.064	0.064

4.3.2 Tribo-corrosion

We investigated tribo-corrosion of the steel samples immersed in various WBEs at various sliding speeds with *in situ* monitoring changes in current, OCP, and COF versus the sliding time. In addition, potentiodynamic polarization tests were performed to evaluate corrosion rate of steels at the different sliding speeds.

4.3.2.1 Effect of sliding speed on corrosion during tribo-corrosion tests

Fig. 4.3 displays the continuous evolution of OCP and current before, during, and after the sliding processes at four sliding speeds in the brine solution and different WBEs.



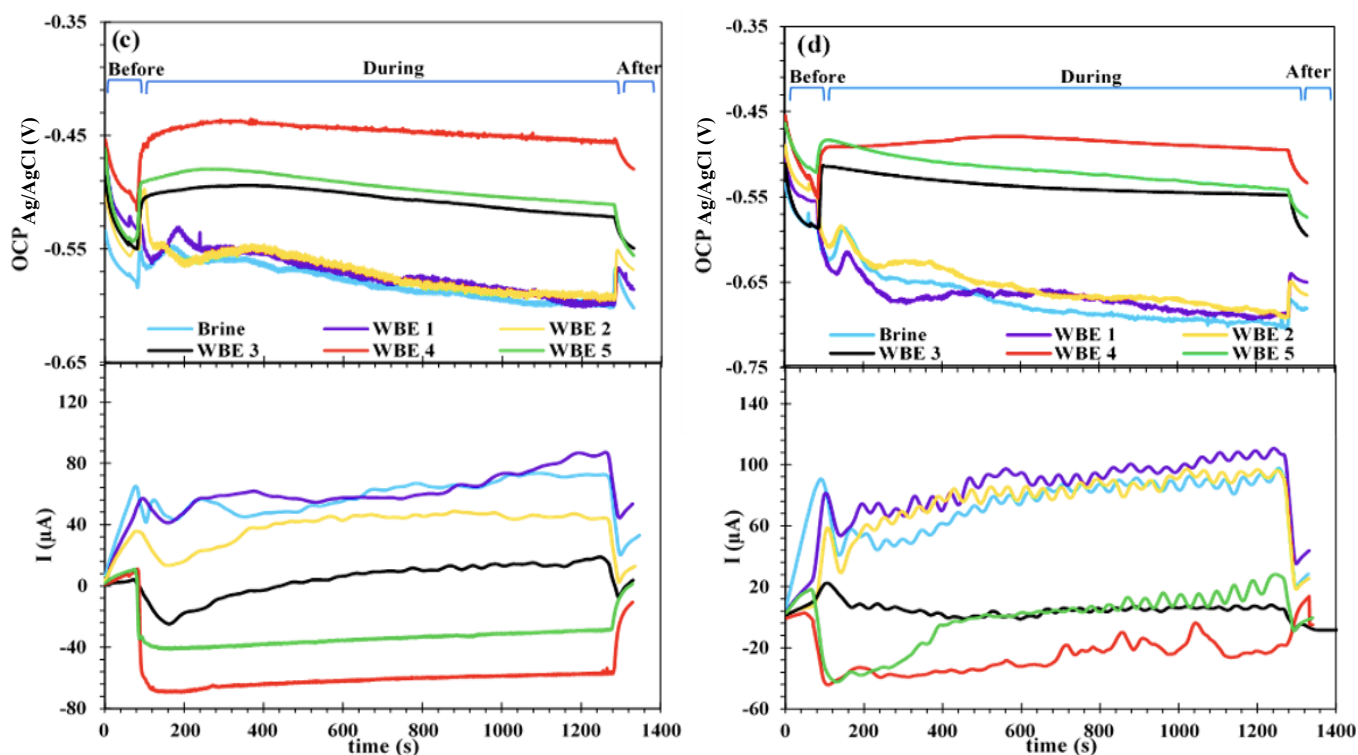


Fig. 4.3. Variations in OCP and current versus sliding time for the brine solution and various WBEs at different sliding speeds (a) 2 mm/s, (b) 3.5 mm/s, (c) 5 mm/s and (d) 10 mm/s.

As shown in Fig. 4.3, the current and OCP curves show fluctuations during the sliding process, especially at higher sliding speeds, which should be related to the protective layer generation, breakdown, and re-forming during tribo-corrosion tests. As illustrated, in general, there was an initial increase in current and a sharp drop in OCP before the sliding process was started. Once the sliding process started, an increase in the current value and a reduction in OCP at lower sliding speeds (2 and 3.5 mm/s in Fig. 4.3a and 4.3b) were observed due to the damage or removal of the oxide film (in the brine solution) or lubricating film (in the WBEs) by the counterpart i.e. the silicon nitride ball pin, leading to the exposure of bare material to the electrolyte and counterpart. During sliding action at lower speeds, the current was increased gradually while OCP decreased towards more negative values, which are more obvious for samples immersed in the brine solution

and WBEs 1 and 2. The results reflect the occurrence of wear-accelerated corrosion. In contrast, at higher sliding speeds, 5 and 10 mm/s, a rapid drop in current and a large up-shift in OCP occurred at the beginning of the sliding process, followed by stabilization during the subsequent sliding process shown in Figs. 4.3 c and 4.3 d. The observed phenomena indicate a positive effect of sliding speed on the improvement in the tribo-corrosion performance of the steel. The speed of 5 mm/s led to the best performance with the lowest current and most positive OCP during the sliding process. The improvements were however less for the tests at 10 mm/s. After the sliding process was stopped, the current showed a slight increase, and values of OCP shifted towards more negative potential with time, which could be ascribed to the reaction of a fresh metal area on the worn surface with electrolyte, leading to further corrosion of the worn surfaces.

Results also demonstrated superior tribo-corrosion performance of steel samples immersed in the solutions with the corrosion inhibitors, where the current showed the lowest values and OCP exhibited the most positive values at all sliding speeds. Among three corrosion inhibitors, PEG-2 oleamide demonstrated the greatest effectiveness in suppressing corrosion and thus corrosion-wear synergy. As shown, the current reduced from around +80 nA at 2 mm/s to -57 μ A at 5 mm/s as well as OCP shifted from around -0.61 V at 2 mm/s to about -0.45 V at 5 mm/s.

4.3.2.2 Effect of sliding speed on polarization curves

Polarization curves during tribo-corrosion at different sliding speeds were obtained for steel samples immersed in the brine solution and WBE 4. Fig 4.4 shows the polarization curves for steel samples at four sliding speeds and under an applied load of 10 N. Figs. 4.4(a) and (b) display that sliding action made the curves for samples tested in both brine and WBE 4 move to more anodic potentials, where the greater shift devotes to higher sliding speeds. For samples immersed in WBE 4 with the corrosion inhibitor, increasing the sliding speed remarkably affected

both cathodic and anodic branches with significant shifts towards lower current densities, which are more profound at 5 and 10 mm/s. In addition to the sliding speed, the presence of a corrosion inhibitor changed the shape of polarization curves. The electrochemical data determined from the polarization tests are provided in Table. 4.2.

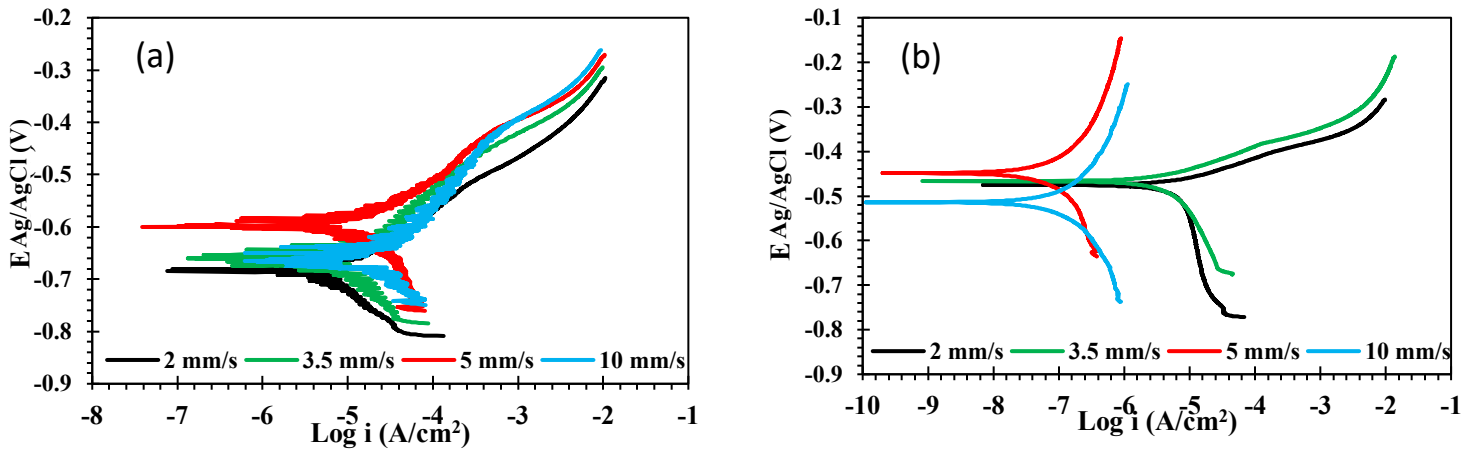


Fig. 4.4. Polarization curves of steels immersed in (a) brine solution and (b) WBE 4 at four different sliding speeds 2, 3.5, 5, and 10 mm/s.

Table 4.2. Values of corrosion current density, corrosion potential, cathodic and anodic Tafel slopes, the corrosion rate of steel samples immersed in the brine solution, and WBE 4 at various sliding speeds.

Solutions	E_{corr} (V)	i_{corr} ($\mu\text{A}/\text{cm}^2$)	Corrosion rate (mpy)	β_a (V/decade)	β_c (V/decade)
Brine- 2 mm/s	-0.684	6.76	3.10	0.093	0.147
Brine- 3.5 mm/s	-0.660	6.26	2.87	0.061	0.108
Brine- 5 mm/s	-0.597	3.21	1.47	0.039	0.047
Brine- 10 mm/s	-0.660	4.88	2.24	0.049	0.047
WBE4- 2 mm/s	-0.475	2.61	1.19	0.026	0.045
WBE4- 3.5 mm/s	-0.467	2.35	1.07	0.038	0.067
WBE4- 5 mm/s	-0.449	0.04	0.02	0.097	0.097

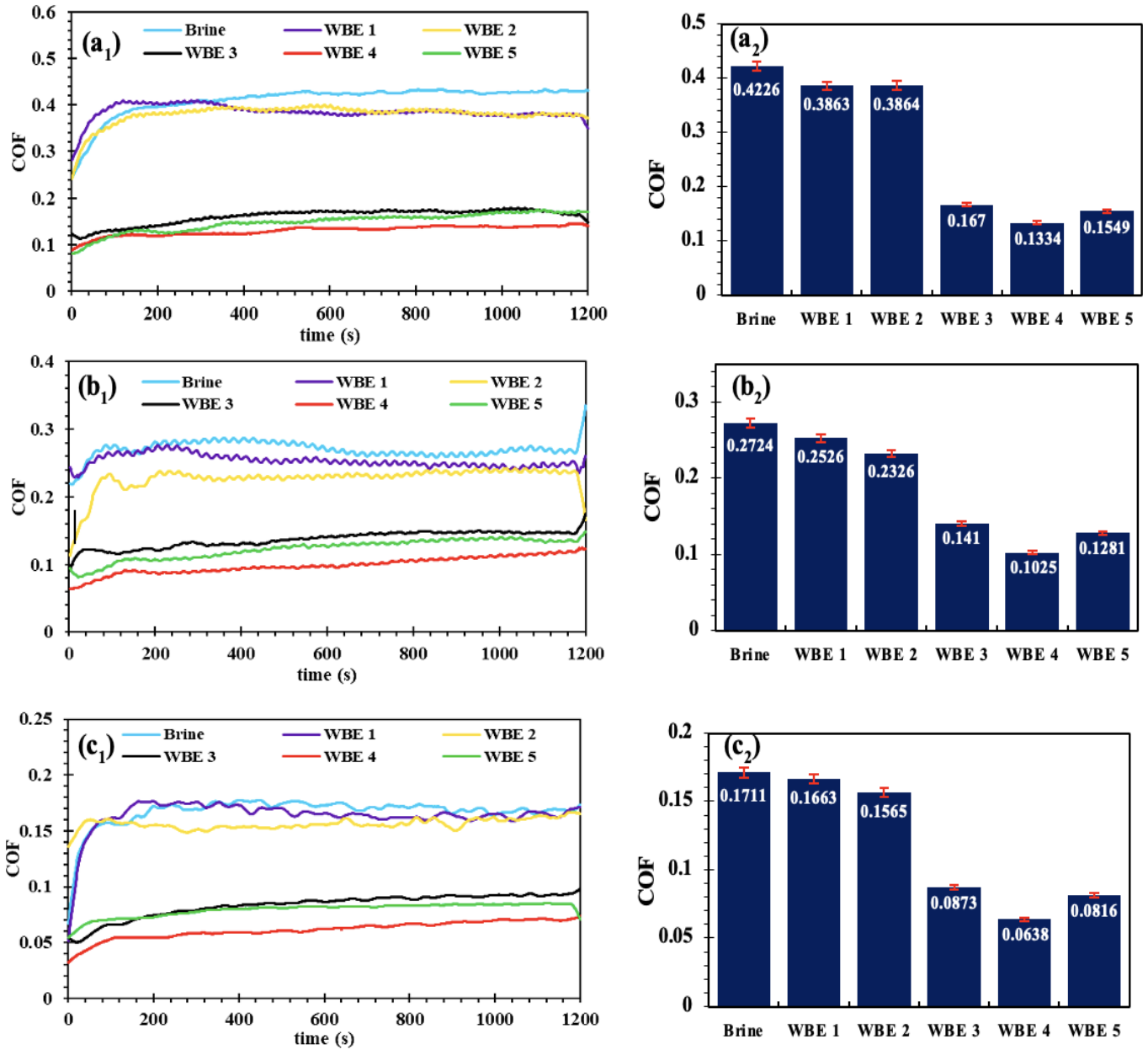
WBE4- 10 mm/s	-0.514	0.19	0.08	0.245	0.234
---------------	--------	------	------	-------	-------

Table 4.2 shows noticeable reductions in i_{corr} and corrosion rate of steels immersed in both the brine solution and WBE4 with increasing the sliding speed up to a certain value (5 mm/s). The elevated tribo-corrosion resistance of samples by increasing sliding speed may be ascribed to the effective re-formation of lubricating film on the metal surface to inhibit direct contact between the sample and the pin in the corrosive environment. The lowest corrosion rates were determined for steel samples immersed in the brine solution ($i_{\text{corr}} = 3.21 \mu\text{A}/\text{cm}^2$, corrosion rate= 1.47 mpy) and WBE 4 ($i_{\text{corr}} = 0.04 \mu\text{A}/\text{cm}^2$, corrosion rate= 0.02 mpy) at sliding speed of 5 mm/s. However, the excessive increase in sliding speed from 5 mm/s to 10 mm/s caused re-increases in i_{corr} and corrosion rate, which agrees with the results of OCP and current versus time measurements shown in Fig. 4.3. The underlying mechanisms are discussed in Section 4.4 (Discussion). The electrochemical parameters obtained for steel immersed in WBE 4 show that the corrosion inhibitor shifted E_{corr} towards more positive values (range between -0.475 V to -0.514 V) with lowered i_{corr} , indicating notable reductions in the corrosion rate at different sliding speeds. The fatty acid-based corrosion inhibitor can build up a protective film on the steel [41], protecting the steel from corrosion involving wear at any sliding speed.

Comparing corrosion and tribo-corrosion of steel samples under tested conditions, wear increased i_{corr} and corrosion rate (see Tables 4.1 and 4.2). As mentioned earlier, the increases in i_{corr} and corrosion rate during tribo-corrosion are due to the mechanical removal of the film formed on the metal surface, leading to the exposure of the bare metal surface to the corrosive medium. In addition, wear introduced plastic deformation which made the metal surface more anodic and thus more prone to corrosion.

4.3.2.3 Effect of sliding speed on friction

Fig. 4.5 shows the COF ~ time curves and mean values of COFs of steel samples immersed in different solutions at four sliding speeds under a contact load of 10 N. The mean COF values were determined for average values during the last 1000 seconds of the tests during which the frictional curves became stable.



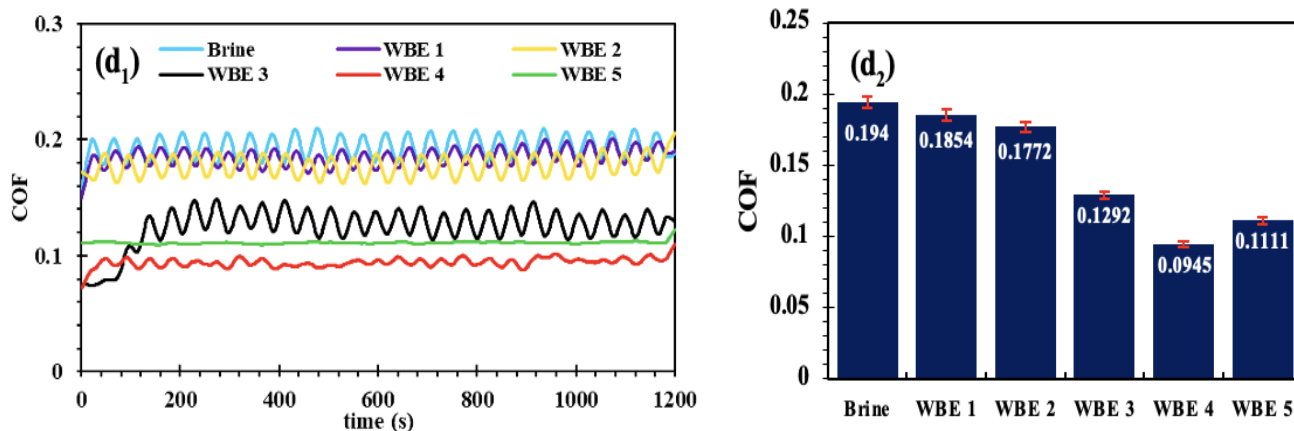


Fig. 4.5. Variations in COF versus sliding time and average COF values for brine solution and various WBEs at different sliding speeds (*a*₁ and *a*₂) 2 mm/s, (*b*₁ and *b*₂) 3.5 mm/s, (*c*₁ and *c*₂) 5 mm/s, and (*d*₁ and *d*₂) 10 mm/s.

As shown in Fig. 4.5 (*a*₁ to *d*₁), all the COF ~ time curves show fluctuations during the tribo-corrosion tests due to the wear of the sample surface. The COF curves are influenced by the sliding speed. The highest COF values were determined at the sliding speed of 2 mm/s. The COFs decreased as the sliding speed was increased to 3.5 mm/s and further dropped to minima at the sliding speed of 5 mm/s for the brine solution and various WBEs. However, further increasing the sliding speed (10 mm/s) did not further reduce but slightly raised the COF values.

The COF curves were strongly influenced by the corrosion inhibitors. For all the sliding speeds, maximum COF values were obtained in solutions without the corrosion inhibitors, especially the brine solution, which led to the average COF equal to 0.42 at 2 mm/s and 0.17 at 5 mm/s. In contrast, when tested in WBE 4 (PEG-2 oleamide), the COF decreased to 0.13 at 2 mm/s and 0.06 at 5 mm/s. The decrease in COF by the corrosion inhibitor should benefit from the formation of a protective layer on a sample surface.

4.3.3 Wear and worn surface analysis

At the end of tribo-corrosion tests, worn surfaces of the samples tested in the brine solution and WBEs containing corrosion inhibitors were analyzed using an optical profilometer. Fig. 4.6 depicts microscopic images of the steel samples tested in various solutions at different sliding speeds. As shown, the wear track width of samples tested in different solutions increased with increasing the sliding speed, accompanied by more wear volume losses. This happened because a higher sliding speed would generate a larger force when the asperities strike or plow the target surface, leading to an increased wear rate.

The presence of PEG-2 oleamide, GM, and GL in WBEs distinctively affected morphological appearances of the worn and unworn surface areas, as shown in Fig. 4.6. In both the worn and unworn areas, the sample immersed in brine solution showed severe damage with rough surfaces and corrosion products inside and outside the wear tracks at different sliding speeds from 2 to 10 mm/s. The lower wear resistance of the steel tested in the brine solution is attributed to the easy removal of the oxide layer by mechanical force and prone to corrosion. Compared to the brine solution, WBE 3, 4, and 5 containing corrosion inhibitors considerably reduced wear track width and surface irregularities with little sign of corrosion products on smooth surfaces, indicating the high effectiveness of the corrosion inhibitors in suppressing corrosion and the corrosion-wear synergy.

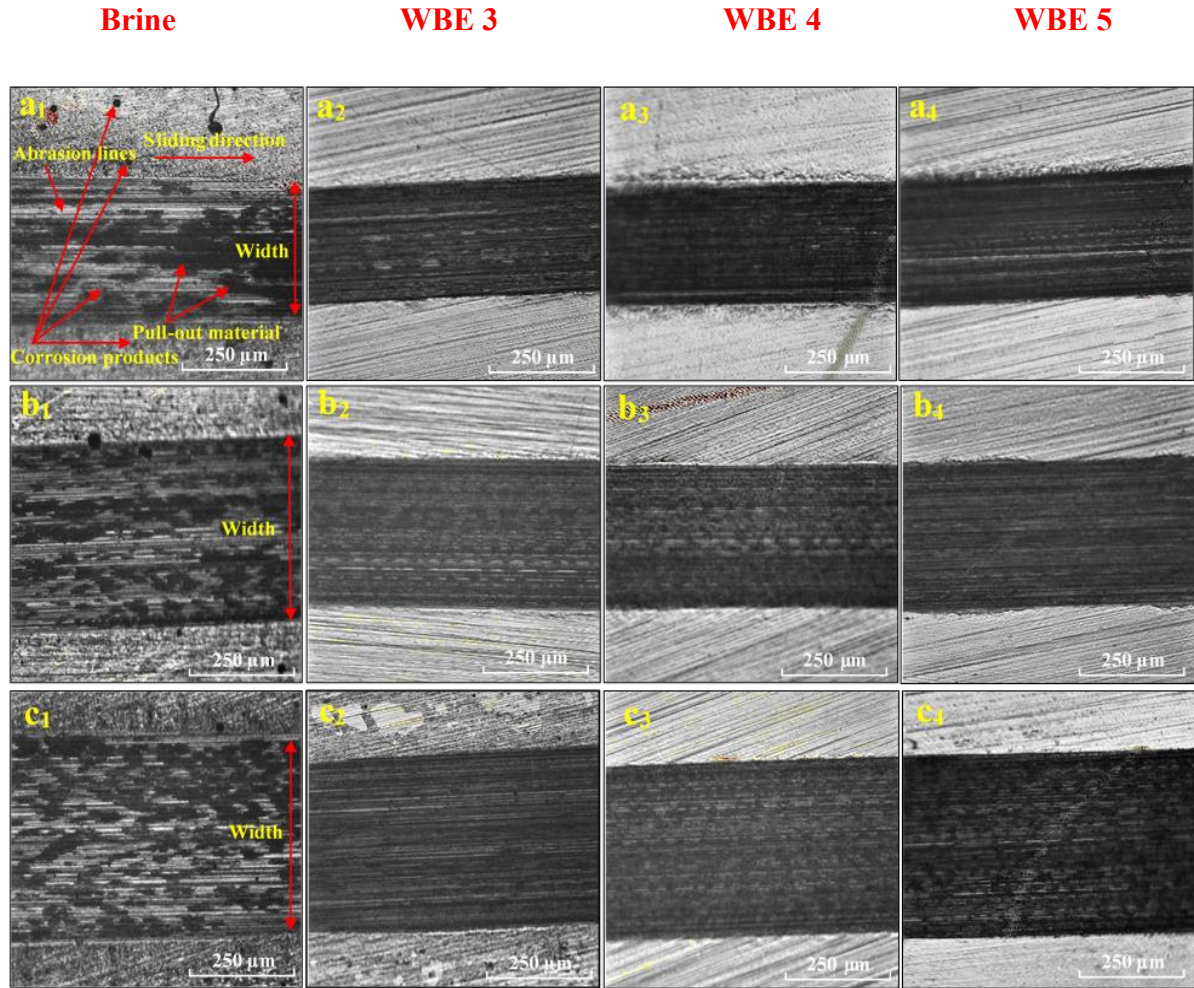


Fig. 4.6 Optical microscopic images of wear tracks on steel samples after tribo-corrosion test at various sliding speeds (a1 to a4) 2 mm/s, (b1 to b4) 5 mm/s and (c1 to c4) 10 mm/s.

Cross-sectional profiles of wear tracks were examined using the optical profilometer to determine volume losses by measuring the depths and widths of wear tracks on samples tested in different solutions at different sliding speeds, which are plotted in Fig. 4.7. As shown, the depth and width of wear track and corresponding volume loss increased as the sliding speed was increased from 2 mm/s to 10 mm/s. At any sliding speed, the sample tested in the brine solution always had the largest volume losses, and the WBEs containing corrosion inhibitors effectively reduced the volume loss. The volume losses of samples immersed in WBE 1 and 2 without corrosion inhibitors are also large. WBE 4 containing PEG-2 oleamide performed the best.

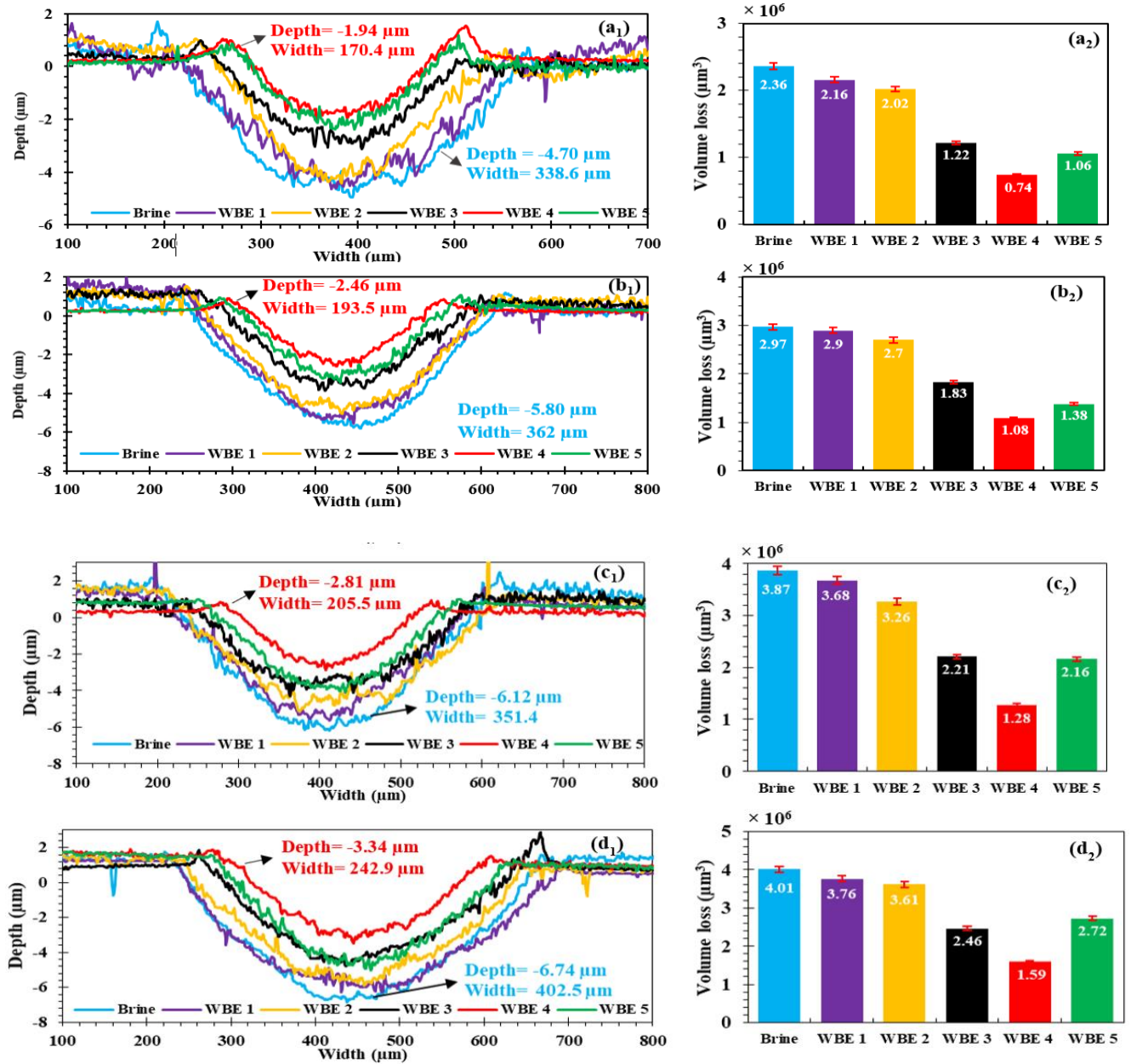


Fig. 4.7. Cross-sectional wear track profiles and volume losses of steel samples worn in various solutions at sliding speeds of (a₁ and a₂) 2 mm/s, (b₁ and b₂) 3.5 mm/s, (c₁ and c₂) 5 mm/s, and (d₁ and d₂) 10 mm/s.

Based on the volume losses and the wear testing condition, the specific wear rates [W, expressed by eq. (1)] of samples tested in different solutions at various sliding speeds were calculated and are illustrated in Fig. 4.8. As shown, the specific wear rate increased with increasing

the sliding speed from 2 mm/s to 10 mm/s, which is valid for all the solutions. The brine solution resulted in the highest specific wear rates for all the sliding speeds. The specific wear rate was markedly reduced when tested in WBEs containing corrosion inhibitors (WBE 3, 4, and 5) at any sliding speed. As illustrated, WBE 4 showed the best performance.

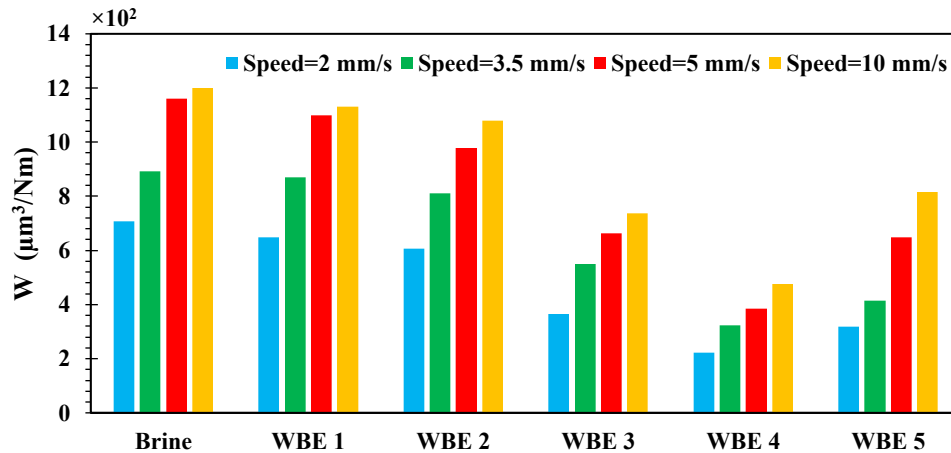


Fig. 4.8. Specific wear rate concerning the solution at four sliding speeds 2, 3.5, 5, and 10 mm/s.

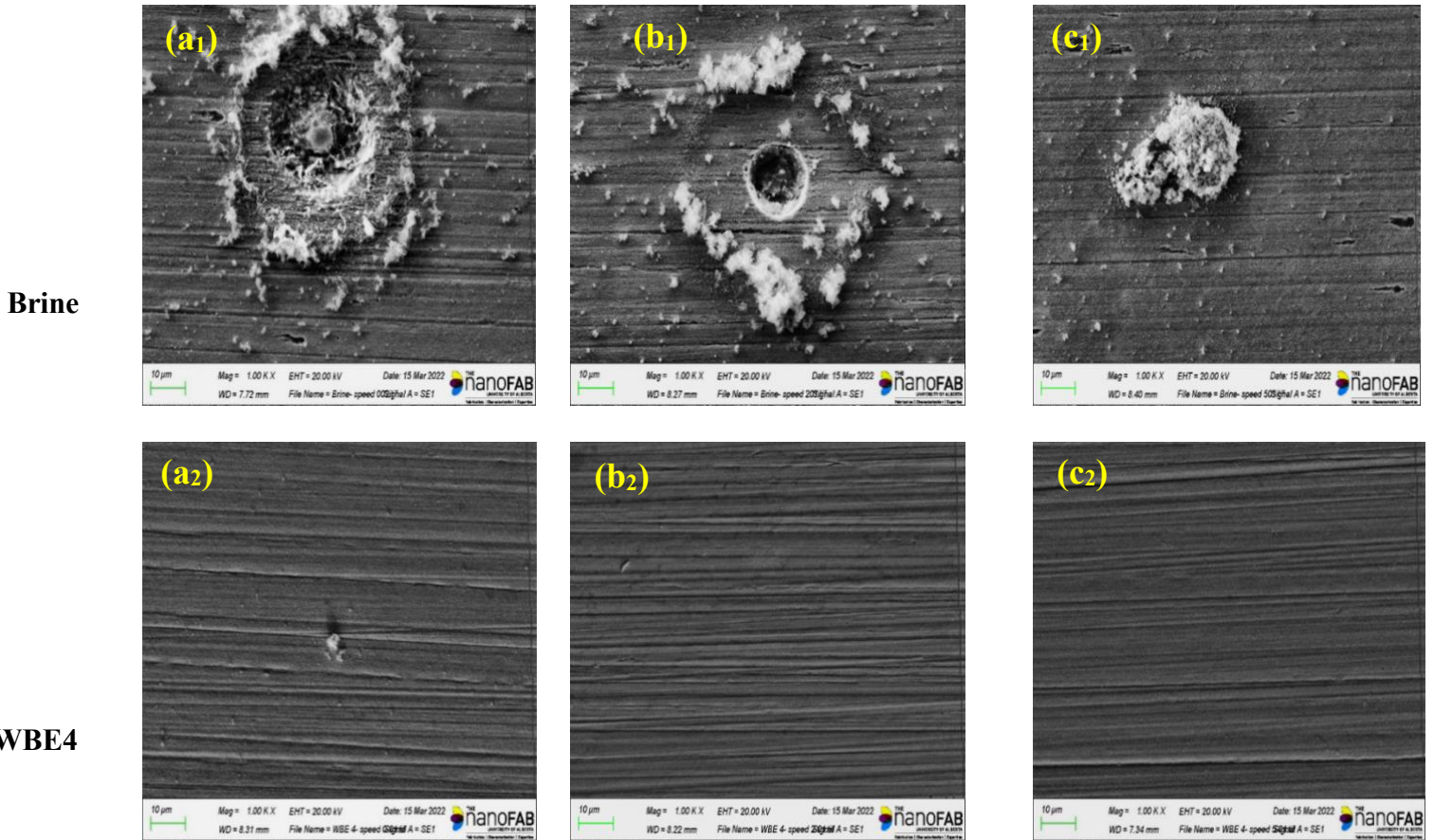
4.3.4 Further surface characterization by SEM-EDX

The surfaces of samples after the corrosion and tribo-corrosion tests were further characterized by SEM-EDX to better understand the beneficial effect of the corrosion inhibitors on corrosion and tribo-corrosion of the samples concerning the linear motion speed.

4.3.4.1 Corrosion

Fig. 4.9 presents SEM-EDX results obtained for steel samples tested in the brine solution and WBE 4 under static and linear motion (dynamic) conditions. Fig. 4.9(a₁) shows that the most surface area of the sample immersed in the brine solution under the static condition was covered by corrosion products, showing a rough appearance with large pits and nano-scale pits distributed on the surface. The EDS analysis detected oxygen (9.10 wt.%), potassium (0.02 wt.%), and chloride (0.11 wt.%) on the corroded surface of the steel under static conditions, coming from the

oxidized steel and the electrolyte, which is a consequence of the reaction between the steel and the solution.



Solution	Fe	O	C	Mn	N	K	Cl
Brine- 0 mm/s	79.70	9.10	10.39	0.68	-	0.02	0.11
Brine- 2 mm/s	85.30	7.36	6.46	0.77	-	0.05	0.06
Brine- 5 mm/s	88.54	3.50	7.09	0.81	-	0.03	0.03
WBE 4- 0 mm/s	90.41	1.12	7.56	0.87	-	0.03	0.01
WBE 4- 2 mm/s	90.55	0.82	7.71	0.91	-	0.01	-
WBE 4- 5 mm/s	88.77	0.60	9.88	0.62	0.12	-	0.01

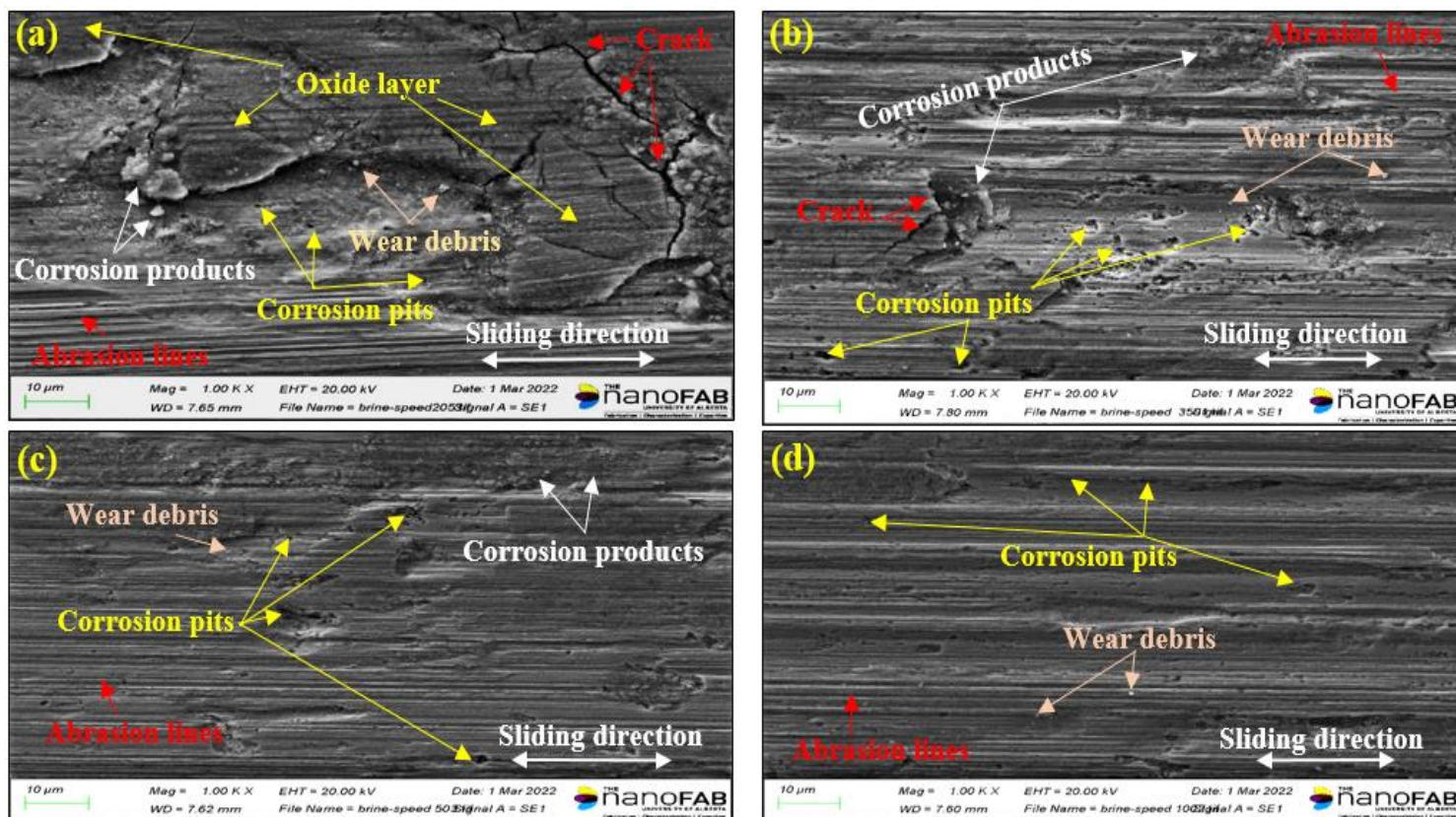
Fig. 4.9. SEM micrographs and EDS analysis of steel surfaces after corrosion test in the brine and WBE 4 under the static condition (*a*₁ and *a*₂), and linear motion (dynamic) condition at two speeds: (*b*₁ and *b*₂) 2 mm/s, and (*c*₁ and *c*₂) 5 mm/s.

Corrosion products and corrosion pits were also presented on the steel surface tested under linear motion conditions but were less severe compared to the situation of testing under the static condition. The EDS analysis showed that the oxygen concentration on the steel surface was reduced to 7.36 wt%, along with potassium (0.05 wt%) and chloride (0.06 wt%), when tested at the motion speed of 2 mm/s. A further change in the surface morphology and composition of the sample tested at a higher speed of 5 mm/s [Fig. 4.9(c₁)], and detected oxygen had a lower amount (3.50 wt%), along with chloride (0.03 wt%) and potassium (0.03 wt%).

When tested in WBE 4, fewer defects were observed on the sample surface. The sample surface was smooth with almost no sign of corrosion pits under different conditions, as shown in Figs. 4.9 a₂ ~ c₂. Under the static condition (Fig. 4.9 (a₂)), small debris of corrosion products was observed on the surface with oxygen concentration (1.12 wt%), minor potassium (0.03 wt%), and chloride (0.01 wt%). The EDS results also revealed the carbon content of 7.56 wt% adsorbed on the steel surface. Under the dynamic conditions with motion speeds of, e.g., 5 mm/s, the detected concentrations of oxygen were much lower (0.60 wt% O, 0.01 wt% Cl) but more carbon (9.88 wt%) and nitrogen (0.12 wt%), which came from the corrosion inhibitor film, were detected on the steel sample surface. It is clear that the movement helps mitigate corrosion, since the corrosion inhibitor forms a protective layer on the metal surface, thus blocking the access of corrosive ions to reach the metal surface.

4.3.4.2 Tribo-corrosion

The morphology and composition of wear tracks on samples that experienced tribo-corrosion tests in the brine solution and WBE 4 at different sliding speeds were also examined with SEM-EDS. Results are illustrated in Figs. 4.10 and 4.11.



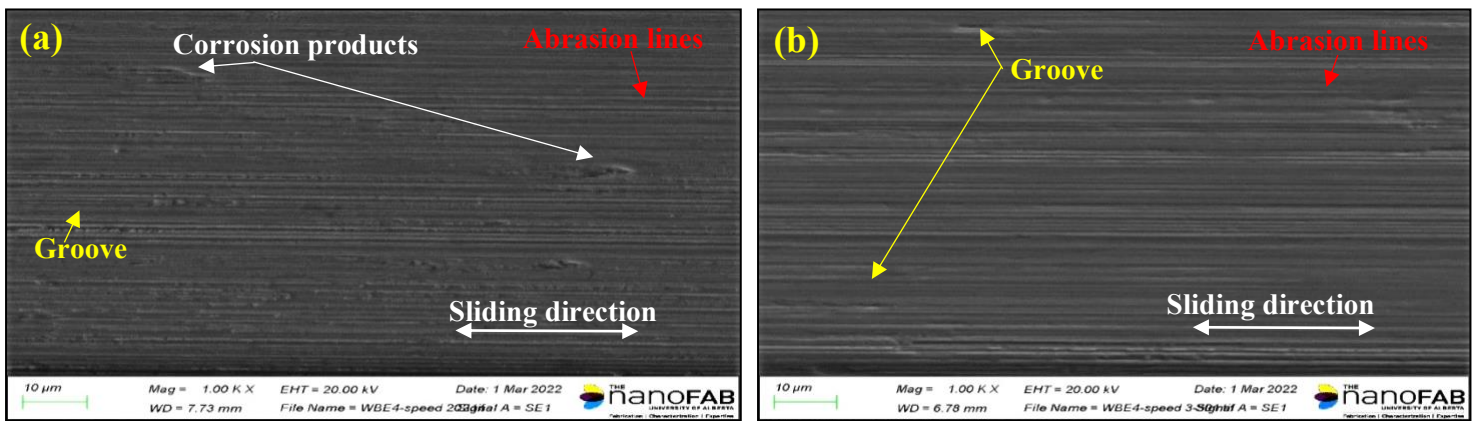
Brine Solution	Fe	O	C	Mn	K	Cl
2 mm/s	75.27	14.16	9.59	0.5	0.01	0.47
3.5 mm/s	82.47	7.09	9.68	0.67	0.01	0.08
5 mm/s	86.94	3.70	8.60	0.72	0	0.04
10 mm/s	87.37	3.36	8.49	0.74	0.02	0.02

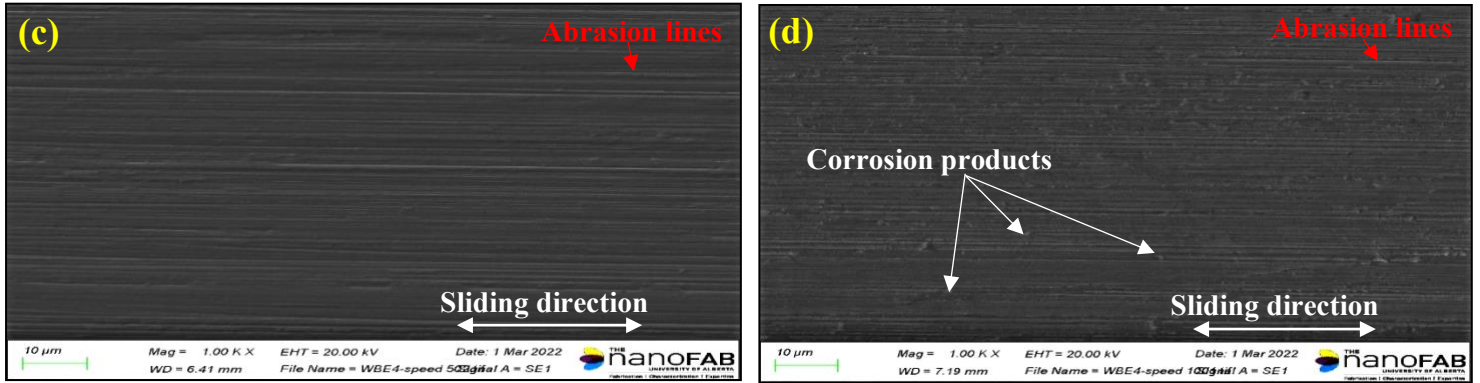
Fig. 4.10. SEM micrographs and EDS analysis of worn surfaces after tribo-corrosion test in brine solution at various sliding speeds (a) 2 mm/s, (b) 3.5 mm/s, (c) 5 mm/s and (d) 10 mm/s. The attached table shows the concentrations (wt%) of different elements on the worn surfaces.

Fig. 4.10(a) shows a loose oxide layer covering most parts of the wear track when the sample experienced a tribo-corrosion test at the lowest sliding speed (2 mm/s), which had many micro-cracks and was partially delaminated during the wearing action. The presence of corrosion products, corrosion pits, and wear debris resulted from the wear-corrosion synergy. The EDS analysis confirmed that there was a high oxygen concentration (14.16 wt%) along with chloride

(0.47 wt%) and potassium (0.01 wt%) on the worn surface. At 3.5 mm/s, the worn surface still looked rough but showed fewer corrosion products, wear debris, delamination areas, and micro-cracks. At higher sliding speeds (5 mm/s and 10 mm/s) as illustrated in Figs. 4.10 (c) and (d), no oxide layer was observed on the worn surfaces, and the worn surfaces were smoother with fewer corrosion products, micro-cracks, and pits. Based on the EDS analysis, oxygen content and corrosion products on the wear tracks were reduced significantly (3.70 wt% O, 0.04 wt% Cl at 5 mm/s; and 3.36 wt% O, 0.02 wt% K, 0.02 wt% Cl at 10 mm/s). Moreover, worn surfaces during the sliding process at higher sliding speeds showed lower dissolution rates of iron, corresponding to higher iron contents on the worn surfaces, e.g., 86.94 wt.% at 5 mm/s and 87.37 wt.% at 10 mm/s).

Fig. 4.11 presents SEM micrographs of worn surfaces that experienced tribo-corrosion tests in WBE 4 at different sliding speeds.





WBE 4	Fe	O	C	Mn	N	K	Cl
2 mm/s	84.52	4.20	10.49	0.77	-	0.01	0.01
3.5 mm/s	81.67	5.47	12.04	0.80	-	0.01	0.01
5 mm/s	70.38	1.95	26.82	0.80	0.04	0.01	-
10 mm/s	83.24	3.09	12.87	0.78	-	0.01	0.01

Fig. 4.11 SEM micrographs and EDS analysis of worn surfaces after tribo-corrosion test in WBE 4 at various sliding speeds (a) 2 mm/s, (b) 3.5 mm/s, (c) 5 mm/s and (d) 10 mm/s. The attached table shows the concentrations (wt%) of different elements on the worn surfaces.

As shown, the worn surface of samples tested in WBE 4 showed much less damage without signs of corrosion pits and micro-cracks, compared to those tested in the brine solution at the different sliding speeds. All the samples showed a similar appearance. Abrasion grooves, more corrosive ions (chloride and potassium ions), and higher oxygen content can be found (EDS analysis) on the wear track of samples tested at lower speeds (Figs. 4.11 (a) and (b)). Fig. 4.11(c) depicts that the abraded region inside the wear track became smoother as the sliding speed was increased to 5 mm/s. In addition, the presence of nitrogen (0.04 wt%), increased carbon amount from 10.49 wt% to 26.82 wt%, and reduced oxygen concentration from 4.20 wt% to 1.95 wt% all are the indication of higher deposition of the protective layer on the wear track when the sliding speed increased from 2 mm/s to 5 mm/s. The larger coverage of the protective layer, resulting from the corrosion inhibitor, on the worn surface, would help reduce friction, corrosion, and corrosive

wear. However, with further increasing the sliding speed to 10 mm/s, the amounts of oxygen and corrosion products re-increased while carbon concentration dropped sharply to 12.87 wt% on the worn surfaces, which could be attributed to a possible factor that the re-growth rate of the inhibitor film on the worn surface was lower than the damage rate during the tribo-corrosion test as the higher sliding speed.

4.4 Discussion

The performance of drilling fluids used for oilfield drilling operations can largely benefit from an additive of corrosion inhibitors, which help reduce friction, corrosion, and tribo-corrosion [181]. This chapter reveals that the performance of the drilling fluid is also influenced by the sliding speed since it affects the damage and re-growth of the oxide layer or the inhibitor-induced film on the metal surface, which has been demonstrated by the results of corrosion and tribo-corrosion tests for the carbon steel samples immersed in the brine solution and various WBEs. In this section, further discussions are given for a better understanding of the effect of the sliding speed on corrosion, friction, and corrosive wear of the steel in the solutions.

4.4.1 Friction

As shown earlier, COFs of steel samples immersed in various solutions decreased with increasing the sliding speed from 2 mm/s to 5 mm/s (Fig. 4.5). At low speeds, the pin was in contact with rougher sample surfaces, especially when tested in the brined solution with more corrosion and more oxide formed (Figs. 4.6 and 4.10), leading to higher COF values. As the sliding speed was increased, the surfaces became smoother or less rough due to reduced corrosion (Tables 4.1 and 4.2, Figs. 4.6 and 4.10) and increased removal of corrosion products, leading to lowered COF. However, further increasing the sliding speed re-increased corrosion (Tables 4.1 and 4.2)

and raised the lateral resistant force or resistance to the pin's movement associated with elevated dynamic wearing force, which could be responsible for the re-increased COF and wear volume loss as illustrated in Figs. 4.5 and 4.7, respectively.

4.4.2 Tribo-corrosion

As shown in Fig.4.3, at lower sliding speeds (2 and 3 mm/s), the more negative the OCP value, the larger the corrosion rate and corrosion current density (Table 4.2). During slow sliding, there is more time for the oxide layer to develop on the worn surface tested in the brine solution. The common corrosion product formed on the carbon steel immersed in the brine solution is iron oxyhydroxide (FeOOH), which can be present with two different structures, lepidocrocite (γ -FeO(OH)) and goethite (α -FeO(OH)) [182]. This loose oxide layer cannot effectively protect the steel from the wearing force in the corrosive medium. Thus, higher currents and corrosion rates were observed due to the easier damage or removal of the oxide layer, making larger fresh metal surfaces to corrosion and wear. When tested in WBEs containing the corrosion inhibitors (WBE 3, 4, and 5) at low sliding speeds, corrosion was considerably reduced by the corrosion inhibitor-induced protective film on the sample surface, which consequently reduced the wear-corrosion synergy and, thus the material loss.

When the tribo-corrosion test was performed in the brine solution, the OCP shifted to a higher positive value, accompanied with reduced current and corrosion rate as the sliding speed was increased. However, as the sliding speed increased, much less oxide layer formed on the worn surfaces at higher sliding speeds confirmed by SEM-EDS analysis (Fig.4.10). As shown, the amount of oxygen reduced from 14.16 wt% at 2 mm/s to 3.70 wt% at 5 mm/s, which may be related to a shorter latent time at the higher sliding speed that was insufficient for corrosive agents to react with the steel to form an oxide layer with large coverage on the worn surface, although the

reduced oxide amount was also influenced by the removal of oxide scale by the wearing force. A higher sliding speed may enhance disturbing the penetration of the corrosive agents to reach the metal surface. The above-mentioned could be the reasons for reduced current and corrosion rate at higher sliding speeds. However, further increasing the sliding speed may increase the rate of damage to the oxide layer or scale compared to its growth rate, thus increasing the corrosion rate, as Table 4.3 indicates.

Fig 4.12 depicts a schematic of the tribo-corrosion mechanism as a combination of abrasion and corrosion for steel immersed in the brine solution at various sliding speeds.

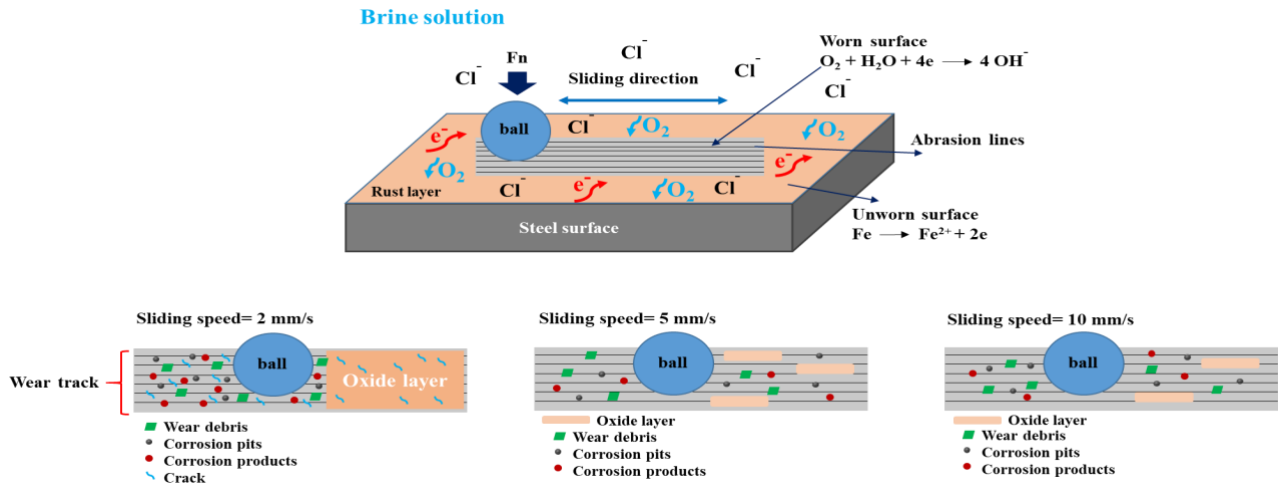


Fig. 4.12. A schematic view of the tribo-corrosion mechanism for 1018 carbon steel immersed in the brine solution at different sliding speeds.

The situation was somewhat similar when the tribo-corrosion tests were performed in WBEs 3, 4, and 5. As Table 4.3 illustrates, in WBE4, when the sliding speed was increased from 2 mm/s to 10 mm/s, the corrosion rate decreased first, reached the minimum at 5 mm/s, and then increased as the speed increased to 10 mm/s (1.19 mpy at 2 mm/s, 1.07 mpy at 3.5 mm/s, 0.02 mpy at 5 mm/s, 0.08 mpy at 10 mm/s). Different from the situation of testing in the brine solution, here

the surface layer was an inhibitor-induced film. A higher sliding speed appeared to dynamically promote the absorption of the corrosion inhibitor and form a protective film with a larger coverage on the sample surface, though it was more or less damaged by wearing force, evidenced by higher carbon and N concentrations (from the inhibitor film) and reduced iron concentration on sample surface as shown in the table attached to Fig.4.11. Such an improved film helped reduce the penetration of the corrosive agents to reach the metal surface, thus decreasing the corrosion rate and the wear-corrosion synergy. However, continuously increasing the sliding speed may enhance the damage rate to the inhibitor-induced film by wearing, compared to its re-growth rate, thus increasing the corrosion rate, as the table in Fig.4.11 indicates. The tribo-corrosion mechanism of carbon steel tested in WBE 4 is corrosive abrasion, as schematically shown in Fig. 4.13.

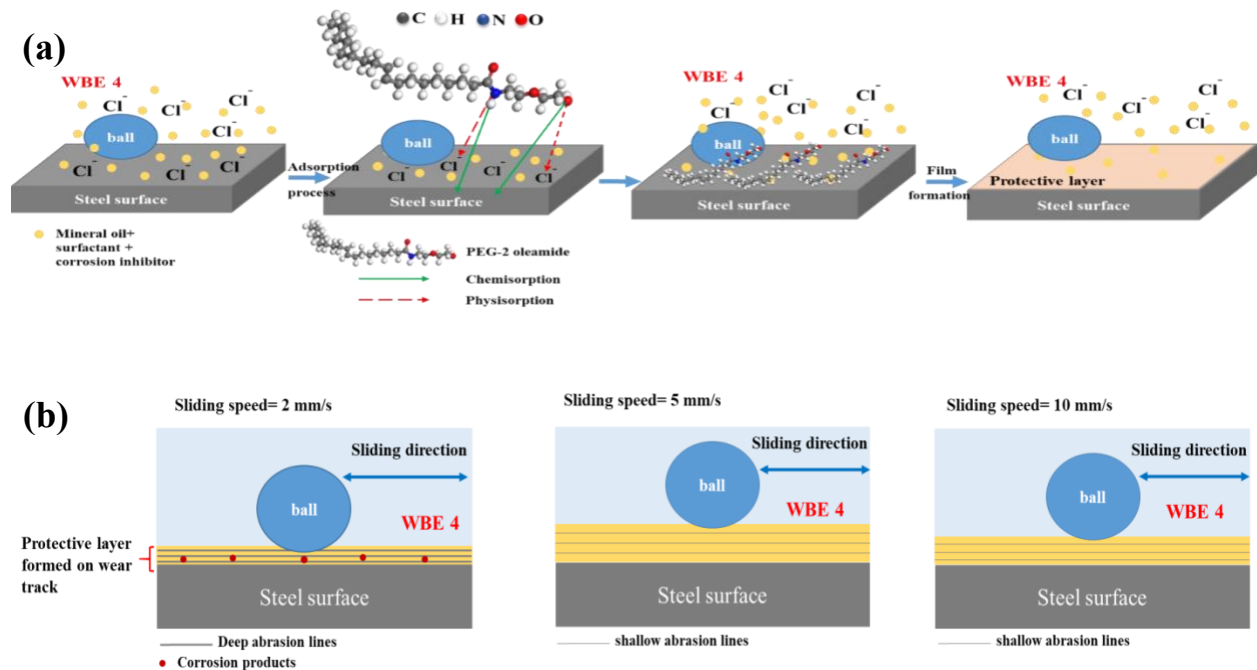


Fig. 4.13. A schematic illustration of (a) the adsorption process of PEG-2 oleamide on the surface of carbon steel and (b) the tribo-corrosion mechanism for steel immersed in the WBE 4 containing PEG-2 oleamide under different sliding speeds.

4.4.3 Effect of speed on corrosion

According to Fig.4.1 and Table 4.1, larger corrosion current densities and corrosion rates were determined as steel samples were tested in various solutions under static conditions. When tested in the brine solution under the static condition, more oxygen and corrosive agents such as potassium and chloride ions were detected on the steel sample surfaces. The linear motion (dynamic module) of samples at lower speeds (2 mm/s and 3.5 mm/s) played a little role in affecting the current and corrosion rates during the process. However, the corrosion rates of samples in the brine solution and WBEs decreased remarkably with increasing speed. As shown, when tested in the brine solution at a higher sliding speed of 5 mm/s, the corrosion current density and corrosion rates markedly decreased. The increase in speed could disturb or mitigate the penetration of oxygen and corrosive ions into the metal surface, thus slowing down the electrochemical reactions and corrosion rate of carbon steels (2.96 mpy at 0 mm/s, 2.77 mpy at 2 mm/s, 2.63 mpy at 3.5 mm/s and 1.32 mpy at 5 mm/s). However, the speed was sufficiently higher, and depletion of dissolved metal ions in the vicinity of the sample surface was enhanced, which could help accelerate the corrosion reaction and increase the corrosion rate to 2.09 mpy at 10 mm/s.

In the tests performed for steels immersed in WBE 3, 4, and 5 at higher sliding speeds (5 and 10 mm/s), current values and corrosion rates decreased considerably, with the lowest values recorded at 5 mm/s. According to the SEM-EDS analysis (Fig.4.10), the speed of 5 mm/s resulted in a thicker and more effective corrosion-protective film (higher concentrations of C and N while the lower concentration of Fe on the sample surface), which blocked the surface from interaction with surroundings, thus reducing the corrosion rate (1.32 mpy at 0 mm/s, 0.94 mpy at 2 mm/s, 0.88 mpy at 3.5 mm/s, 0.0005 mpy at 5 mm/s and 0.05 mpy at 10 mm/s). However, if the sliding speed is sufficiently high, the corrosion rate may increase again due to the enhanced depletion of

dissolved metal ions in the vicinity of the sample surface. This might explain why the corrosion rate determined at 10 mm/s was higher than that determined at 5 mm/s.

In addition to the sliding speed, the addition of corrosion inhibitors in the emulsion-based fluid substantially affected its effectiveness in suppressing corrosion and tribo-corrosion of the carbon steel samples. The corrosion inhibitors can be adsorbed on both worn and unworn surfaces physically and chemically. The electrostatic interaction between negatively charged metal surface (FeCl^-) and protonated form of inhibitor molecule causes physical adsorption. Simultaneously, chemical sorption occurs by sharing of electrons between lone pair electrons of nitrogen and oxygen present in corrosion inhibitors with free orbital d of the steel surface. A protective film is then produced on the metal surface as a barrier to corrosive solutions, thus retarding electrochemical attack on the worn and unworn surfaces. In addition, direct contact between metal and counterpart is reduced due to the formed film on the metal surface, helping reduce friction and tribo-corrosion. Fig 4.13(a) displays a schematic representation of the adsorption mechanism of PEG-2 oleamide, which is the most effective corrosion inhibitor among the three inhibitors.

4.5 Conclusions

The objective of this work was to investigate the kinetic response of 1018 carbon steel to corrosion and tribo-corrosion in emulsion-based drilling fluids with and without green corrosion inhibitors. Corrosion and tribo-corrosion of steel samples immersed in various solutions under static and motion conditions were analyzed. Based on the results of this chapter, the following conclusions can be drawn:

- Corrosion of the carbon steel immersed in solutions with and without the corrosion inhibitor decreased when tested under the motion condition, compared with the results of tests under the

static condition. The corrosion behavior of the steel measured during tribo-corrosion tests showed trends of variations in corrosion rate similar to those observed during the corrosion tests. The corrosion rate reached the minimum at the speed of 5 mm/s compared to other speeds in the range of 0 ~ 10 mm/s.

- Although the corrosion rate showed minima at the speed of 5 mm/s, the material volume loss caused by tribo-corrosion continuously increased as the sliding speed increased from 0 to 10 mm/s, accompanied with decreases in corresponding COF values, when the steel was tested in both the brine solution and various WBEs.
- All three corrosion inhibitors added to the drilling fluid under study substantially improved the performance of steel samples during corrosion (both static and dynamic) and tribo-corrosion tests at various sliding speeds. Among the three corrosion inhibitors, PEG-2 oleamide performed the best.

Therefore, the results proved that corrosion inhibitors and linear motion at various speeds could be used as two key factors in improving corrosion and tribo-corrosion resistance of 1018 carbon steel exposed to WBEs, which makes these factors ready to compete in oilfield applications.

Chapter 5 Phosphate-derived green corrosion inhibitors: enhancing anti-tribo-corrosion properties of carbon steel in emulsion-based drilling fluids⁴

5.1 Introduction

Tribo-corrosion in drilling operations has received considerable attention since corrosion and wear can assist each other, significantly increasing damage to materials [183-190]. Wear makes the surface more anodic and removes surface protective films, thus increasing corrosion. On the other hand, corrosion introduces surface irregularities, increases stress concentrations, and may turn the material into poor oxides, leading to faster material removal [191-194]. The tribological contact may involve sliding, rolling, fretting, etc., which speed up corrosion that, in turn, enhances the wear, as mentioned earlier. This synergy between wear and corrosion (V_{syn} : volume loss caused by the wear-corrosion synergy) is determined by the difference between the total material loss (V_{total}) and material losses caused by wear (V_{w}) and corrosion (V_{c}) [191,192,195-199]:

$$V_{\text{syn}} = V_{\text{total}} - (V_{\text{w}} + V_{\text{c}}) \quad (1)$$

V_{syn} may take a fairly large portion of the total material loss (V_{total}), which could be much larger than those caused by corrosion and wear separately [199-200]. It is important to understand details in tribo-corrosion of materials used in drilling operations under various conditions to improve their performance for drilling operations.

There are different approaches to mitigate tribo-corrosion of drilling facilities, including environmental control, protective coatings, and material modification. These approaches need

⁴ A version of this chapter has been published. M.j. Palimi, Y. Tang, S. E. Mousavi, W. Chen, V. Alvarez, E. Kuru, D.Y. Li, Tribo-corrosion behavior of C-steel in water-based emulsion drilling fluids containing green corrosion inhibitors: experimental and computational studies, *Tribology international*.

maintenance and monitoring. Among them, adding corrosion inhibitors in drilling fluids is a cost-effective and the most practical method for protecting metallic components from tribo-corrosion attacks [43, 201-202]. Corrosion inhibitors contain heteroatoms such as oxygen, nitrogen, sulfur, and phosphorous with multiple bonds as adsorption centers, showing excellent corrosion inhibition effects. The inhibitors' function is related to their lower electronegativity and high polarizability. These atoms and the functional groups can cover the surface area of metallic workpieces through physical and chemical adsorption between the surface and the inhibitors, which can suppress corrosion by blocking charge transfer on the metal surfaces, thereby reducing corrosion and tribo-corrosion of the drilling tools [30, 203-206].

The chapter 5 aims to achieve more significant improvements on the tribo-corrosion resistance of 1018 carbon steel by employing corrosion inhibitors containing heteroatoms phosphorous (PEG-6 isotridecyl phosphate) and nitrogen (PEG-2 oleamide). The latter was used mainly for comparison purposes, as its effectiveness have been explained in chapter 3 and 4 [181]. Particular attention was put on the effect of the phosphate-based corrosion inhibitor on the tribo-corrosion of the steel with different sliding speeds, since the sliding speed affects damage and regrowth of the adsorbed protective film on materials during tribo-corrosion, thus influencing the rate of material loss and wear mechanism. The information on the sliding speed's influence on tribo-corrosion would help get an insight into the performance of the inhibitors in drilling fluids against wear, corrosion, and wear-corrosion synergy. PEG-6 isotridecyl phosphate results from the reaction of ethoxylated alcohols with a phosphating compound, producing a mono-ester compound, while PEG-2 oleamide is obtained through reactions to extract fatty acid from vegetable oils with ammonia. The two inhibitors have high solubility in water, low volatility, biodegradable and environmentally friendly. Different weight percentages of mineral oil as base

oil, TERGITOL NP-9 as surfactant and corrosion inhibitors as effective additives were added to a 5% potassium chloride solution to prepare highly stable water-based emulsion drilling fluids (WBE), which were determined through turbidimetry and zeta potential measurements. The benefits of the corrosion inhibitors on the tribo-corrosion performance of steel specimens immersed in the prepared WBEs with and without corrosion inhibitors at different sliding speeds were evaluated using a pin-on-disk tribometer integrated with an electrochemical workstation. The impact of corrosion inhibitors in enhancing anti-tribo-corrosion properties of the steel was analyzed using 3D optical profilometer, potentiostatic and potentiodynamic techniques to determine current density, corrosion current/rate, coefficient of friction (COF), and thus volume losses caused by wear, corrosion, and wear-corrosion synergy. The morphology and chemical composition of wear tracks were examined via SEM-EDS and XPS analyses, respectively. In addition, the adsorption mechanism for the corrosion inhibitor molecules on iron was studied based on the changes in Gibbs free energy.

5.2 Experimental

5.2.1 Raw Materials and WBEs preparation

This chapter reports a study on the corrosive wear of carbon steel in water-based emulsion drilling fluids (WBEs) containing green corrosion inhibitors, PEG-6 isotridecyl phosphate (provided by Croda) and PEG-2 oleamide (purchased from Triple Point). The preparation of WBEs including mineral oil, surfactant and corrosion inhibitors has been explained completely in previous chapters. The molecular structures of PEG-6 isotridecyl phosphate and PEG-2 oleamide are depicted in Fig. 5.1.

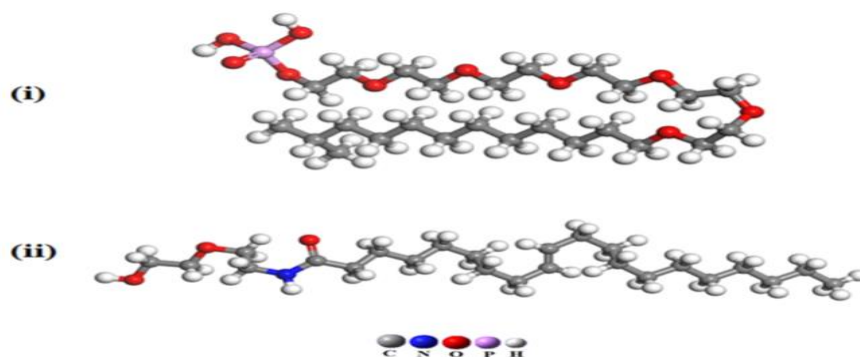


Fig. 5.1 Molecular structures of two corrosion inhibitors under study: (i) PEG-6 isotridecyl phosphate and (ii) PEG-2 oleamide.

5.2.2 Characterization

5.2.2.1 Tribo-corrosion study

As explained in chapter 3 and 4, tribo-corrosion tests were still carried out in a three-electrode electrochemical set-up connected to a pin-on-disc reciprocating tribometer. The normal force applied to the steel sample was 10 N, which moved under a linear reciprocating condition at different sliding speeds (2, 3.5, 5 and 10 mm/s), respectively, over a distance of 3 mm (Fig. 3.1).

In situ electrochemical techniques, e.g., potentiostatic and potentiodynamic measurement, were used to investigate the effect of sliding speed and phosphate-based corrosion inhibitor on the tribo-corrosion behavior of the carbon steel tested in different WBEs. COF as a function of sliding time was recorded during tribo-corrosion tests. The steel samples were immersed in the brine and various WBEs for an hour to reach a steady open circuit potential (OCP) before running the tribo-corrosion tests. Potentiostatic experiments were conducted using a GAMRY instrument at an applied anodic potential of +1mV versus OCP at room temperature. The potentiodynamic polarization (PDP) tests were performed at a scan speed of 0.4 mV/s between potentials of -250 mV to +250 mV around the OCP for each sample under tribo-corrosion conditions to investigate

the electrochemical response of the carbon steel under different testing conditions. Each experiment was repeated at least three times under the identical condition, from which an average value was obtained.

5.2.2.2 Surface analysis

Surface morphology and chemical composition of wear tracks after the tribo-corrosion experiments were investigated with Field-emission scanning electron microscopy (FE-SEM) incorporated with the energy dispersive X-ray spectroscopy (EDX) from Sigma, Germany. A Kratos Axis Ultra model x-ray photoelectron spectroscopy (XPS) was employed to investigate the tribo-corrosion mechanisms of the steel samples tested in different solutions. An optical profilometer, Zegage 3D Middlefield model, was utilized to measure the volume loss caused by tribo-corrosion.

5.3 Experimental Results

5.3.1 FTIR analysis

Fig. 5.2 illustrates the FTIR spectra with main peaks and functional groups related to the corrosion inhibitors.

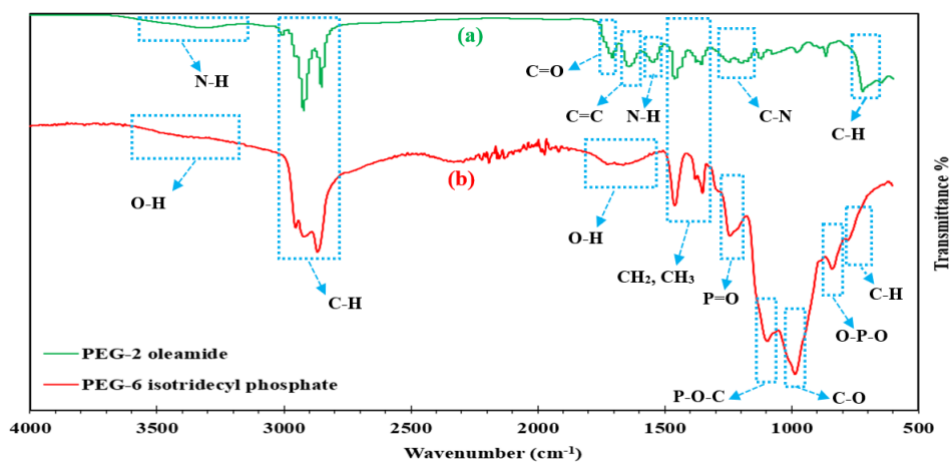


Fig. 5.2 FTIR spectra of (a) PEG-2 oleamide and (b) PEG-6 isotridecyl phosphate

The peaks around 720 cm^{-1} (Fig.5.2(a)) and 779 cm^{-1} (Fig.5.2(b)) are attributed to the vibration of the C-H group because the corrosion inhibitors contain long hydrocarbon chains. The adsorption bands for both corrosion inhibitors appeared at 1350 and 1460 cm^{-1} , referred to as the C-H bending vibration of $-\text{CH}_2-$ and $-\text{CH}_3$, respectively. The FTIR spectra of both corrosion inhibitors exhibit peaks for C-H asymmetric and symmetric stretching vibrations at around 2850 cm^{-1} and 2920 cm^{-1} , respectively. [145]. The adsorption peaks of C-N stretching vibration at 1190 cm^{-1} and N-H bending and stretching vibrations at 1540 and 3300 cm^{-1} verified the existence of the nitrogen atom in the PEG-2 oleamide structure. The stretching bands of C=C and C=O at 1640 and 1700 cm^{-1} (Fig.5.2(a)) are ascribed to the unsaturated fatty acid chain in the structure of PEG-2 oleamide, as discussed in the previous work [97,181]. According to Figs. 5.2(b), peaks adsorbed at 840 , 1096 and 1244 cm^{-1} are attributed to stretching vibrations of O-P-O, P-O-C and P=O bonds, indicating the presence of phosphorous atom in the structure of PEG-6 isotridecyl phosphate. The C-O stretching band is visible at 985 cm^{-1} , describing the compound in the corrosion inhibitors. The FTIR spectra also depict adsorption bands at 1643 and 3420 cm^{-1} , which are related to bending vibration and stretching vibration of the O-H bond, respectively [209-211]. These results illustrate those different heteroatoms, such as oxygen and nitrogen in the structure of PEG-2 oleamide and oxygen and phosphorous in the structure of PEG-6 isotridecyl phosphate, can be adsorbed on the surface of 1018 carbon steel through donor-acceptor interactions. In addition, hydrocarbon chains within corrosion inhibitors can improve tribo-corrosion performance by keeping away water molecules and corrosive ions from the steel surface.

5.3.2 Stability evaluation

As mentioned in previous chapters, Different concentrations of TERGITOL NP-9 (0% to 35%), PEG-6 isotridecyl phosphate (0% to 35%), and mineral oil (65%) were combined with a 5%

potassium chloride solution to obtain the most effective concentrations of these ingredients for achieving WBEs with high stability (Table 5.1). Then, turbidity and zeta potential analyses were carried out to study the stability of the formulated WBEs.

Table 5.1 Prepared water-based emulsions (WBEs)

Solution	Ingredient
WBE (I)	0.1g (65% Mineral oil + 35% TERGITOL NP-9 + 0 % PEG-6 isotridecyl phosphate) in 99.9 g brine solution
WBE (II)	0.1g (65% Mineral oil + 30% TERGITOL NP-9 + 5% PEG-6 isotridecyl phosphate) in 99.9 g brine solution
WBE (III)	0.1g (65% Mineral oil + 20% TERGITOL NP-9 + 15% PEG-6 isotridecyl phosphate) in 99.9 g brine solution
WBE (IV)	0.1g (65% Mineral oil + 10% TERGITOL NP-9 + 25% PEG-6 isotridecyl phosphate) in 99.9 g brine solution
WBE (V)	0.1g (65% Mineral oil + 5% TERGITOL NP-9 + 30% PEG-6 isotridecyl phosphate) in 99.9 g brine solution
WBE (VI)	0.1g (65% Mineral oil + 0 % TERGITOL NP-9 + 35% PEG-6 isotridecyl phosphate) in 99.9 g brine solution

5.3.2.1 Turbidity measurement

Fig.5.3 depicts the measured turbidity values of the WBEs over a period of 4 h. As shown, the turbidity values of the WBEs with a surfactant of high concentrations of [35 % in WBE (I), 30 % in WBE (II) and 20 % in WBE (III)] decreased over time and reached a saturated value after 120 min. However, the low slopes of turbidity ~ time curve were obtained for WBEs with lower concentrations of TERGITOL NP-9 ($\leq 10\%$), especially WBE (V), which shows a slight reduction of 8 NTU in turbidity value for 4 h. The slope of the turbidity ~ time curve reflects the emulsion stability; a smaller slope corresponds to a more stable emulsion. As shown in Fig. 5.3, high turbidity values (500-600 NTU) were obtained for WBEs (IV, V, VI), which contained corrosion inhibitors of high concentrations (25 to 35 %) and surfactant of low concentrations of (0 to 10%). The corrosion inhibitor with high concentrations made the emulsion systems cloudier, leading to stronger light scattering and, thus, higher turbidity. However, WBEs (I, II, III) showed lower turbidity (50-100 NTU) since they contained surfactants of high-concentrations but low-

concentration inhibitors, corresponding to lower turbidity. This observation suggests that TERGITOL NP-9 and PEG-6 isotridecyl phosphate at the optimum values could be effectively adsorbed on the surface of emulsion droplets, providing the highest stability and turbidity via decreasing the interfacial tension between droplets and the aqueous phase and thus increasing the intensity of scattered light.

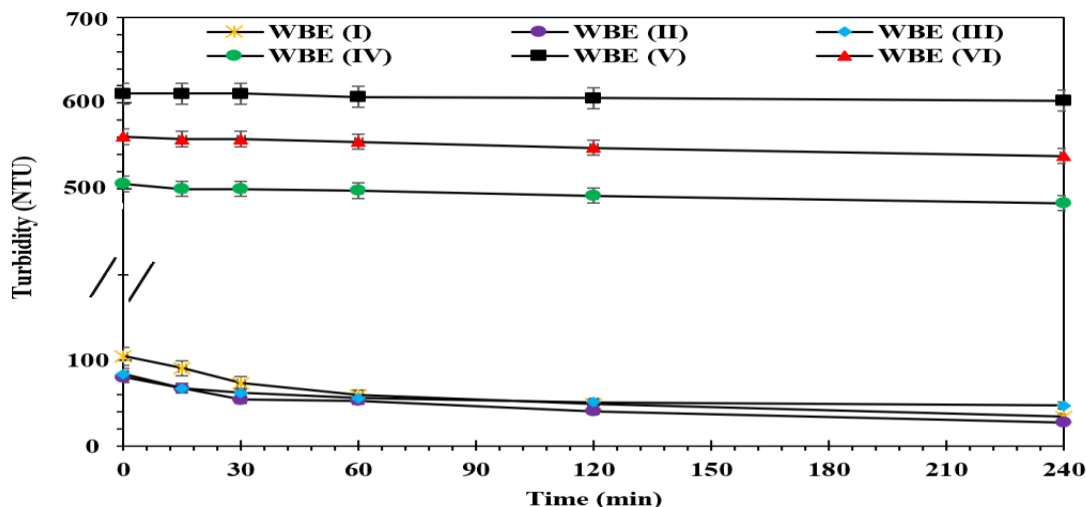


Fig. 5.3 Turbidity values versus NTU for the formulated WBEs over a period of 4 h.

5.3.2.2 Zeta potential

The charge on the surface of oil droplets in WBEs plays a vital role in determining the stability of emulsion-based drilling fluids. This charge can be accurately assessed through the use of zeta potential analysis. Particles with a larger absolute value of zeta potential will separate oil droplets in the emulsion systems more effectively, thus resulting in lesser flocculation and higher stability [212-213]. Influences of weight concentrations of TERGITOL NP-9 and PEG-6 isotridecyl phosphate on the zeta potentials of the formulated WBEs are depicted in Fig. 5.4. As shown, the zeta potentials of all formulated WBEs varied from -22.7 mV to -86.7 mV. Long hydrocarbon chains in the WBEs with the mineral oil, TERGITOL NP-9, and PEG-6 isotridecyl phosphate led to negative zeta potentials for all the prepared WBEs. The emulsion with mineral oil and

surfactant alone (WBE (I)) illustrates the smallest value of surface charge, which can be considered as a flocculated and aggregated emulsion [214]. However, the absolute magnitudes of zeta potential are increased by adding the corrosion inhibitor to the emulsion systems, showing a positive effect of the inhibitor on the electrostatic repulsion between oil droplets. It is also clear from Fig. 5.4 that the WBEs with higher percentages of TERRGITOL NP-9 (above 10%) show lower absolute values of zeta potentials (-45.9 mV in WBE (II), -64 mV in WBE (III) and -69.3 mV in WBE (IV)). Based on the obtained results (turbidity and zeta potential), once the surfactant concentration exceeds 10%, the aggregation of surfactant molecules, so-called micelles, starts to occur, which reduces the adsorption of surfactant at the interface between oil and water. This change in the stability of WBEs can be seen when the surfactant concentration is above 10% (see Figures 5.3 and 5.4).

The emulsions with the minimum weight percentages of TERRGITOL NP-9 (below 5%) and the maximum content of PEG-6 isotridecyl phosphate (above 30%) recorded the largest absolute values of zeta potential (-86.7 mV in WBE (V), -82.5 mV in WBE (VI)). The increased absolute zeta potentials provided strong electrostatic repulsion between oil droplets, inhibiting the oil droplets' flocculation and leading to the high homogeneity of the fluid. As Fig. 5.4 depicts, the highest absolute zeta potential value was recorded for WBE (V) with 65% mineral oil + 5% TERRGITOL NP-9 + 30% PEG-6 isotridecyl phosphate. This observation shows that adding the appropriate concentration of TERRGITOL NP-9 and PEG-6 isotridecyl phosphate can significantly enhance WBEs' stability. Based on Figs. 5.3 and 5.4, WBE (V) was introduced as the most stable WBE to formulate WBEs containing two different corrosion inhibitors (Table 5.2) for tribo-corrosion investigation at different sliding speeds.

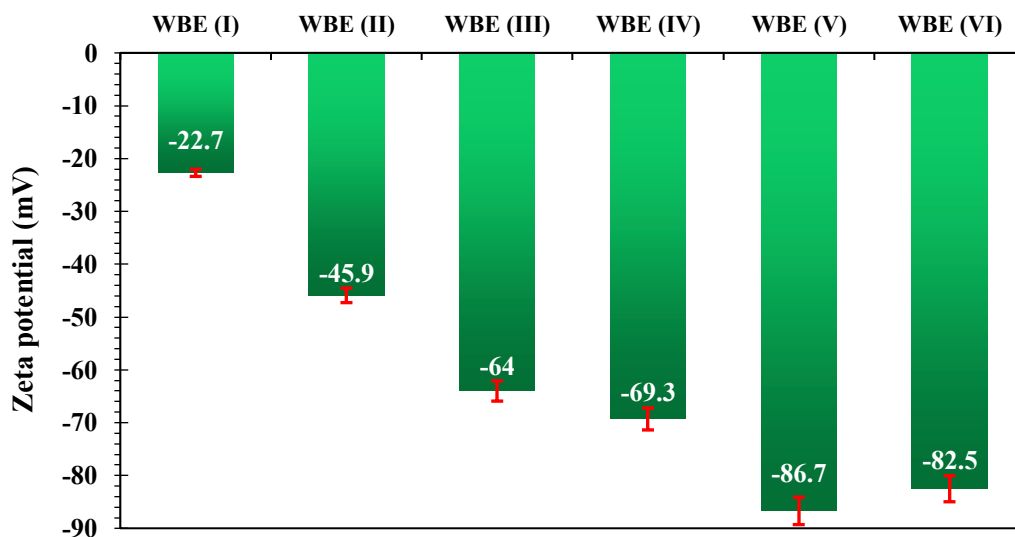


Fig. 5.4 Zeta potentials of the formulated WBEs consisting of mineral oil + TERGITOL NP- 9 + PEG-6 isotridecyl phosphate

Table 5.2 Water-based emulsions (WBEs) for the current research

Solution	Ingredient
WBE (A0)	Brine solution as a reference solution: 5 gr KCl in 95 ml DI water [103-104]
WBE (A1)	0.1g (65% Mineral oil + 35% TERGITOL NP-9) in 99.9 g brine solution
WBE (A2)	0.1g (65% Mineral oil + 5% TERGITOL NP-9 + 30% PEG-6 isotridecyl phosphate) in 99.9 g brine solution
WBE (A3)	0.1g (65% Mineral oil + 5% TERGITOL NP-9 + 30% PEG-2 oleamide) in 99.9 g brine solution

5.3.3 Corrosion and tribo-corrosion behavior

5.3.3.1 Effect of corrosion inhibitors on tribo-corrosion

Fig 5.5 shows variations in current density and COF versus the sliding time in the brine solution and different WBEs, respectively. Corresponding volume losses of the samples are depicted in Fig. 5.5 (c). Variations in the current density of steel samples immersed in various solutions were recorded as a function of time before, during and after the sliding test, as shown in

Fig. 5.5(a). As illustrated, the current density before sliding for all samples tested in the brine and various WBEs is around $0.038 \mu\text{A}/\text{cm}^2$, indicating a low electrochemical activity of the carbon steel. When the sliding process started, anodic (positive) current densities of the samples were detected as $3.99 \mu\text{A}/\text{cm}^2$ and $3.78 \mu\text{A}/\text{cm}^2$, respectively, for tests in the brine solution and WBE (A1). In contrast, cathodic (negative) and anodic (positive) current densities of steel samples were determined to be $-6.08 \mu\text{A}/\text{cm}^2$ and $0.038 \mu\text{A}/\text{cm}^2$ when tested in WBE (A2) and WBE (A3), respectively. As shown, there were initial sharp increases from $3.99 \mu\text{A}/\text{cm}^2$ to $16.3 \mu\text{A}/\text{cm}^2$ (brine) and $3.78 \mu\text{A}/\text{cm}^2$ to $6.8 \mu\text{A}/\text{cm}^2$ (WBE (A1)), which can be attributed to the damage to the oxide film (brine solution) or surface thin lubricating layer (WBE (A1)) by the moving counterpart, Si_3N_4 ball, resulting in bare steel surface exposed to the electrolyte. The 1018 carbon steel is a non-passive alloy; when immersed in the 5% KCl solution, a porous and loose corrosion product layer can form, composed of iron oxyhydroxide compound [215-217]. This porous rust layer cannot resist further corrosion and the wearing force. Thus, as the wear started, the rust layer was removed quickly, leading to exposure of fresh steel surface to the corrosive solution. This is why current density increased sharply at the beginning of the sliding process. Other factors could also be involved, e.g., the plastic strain caused by wear, which made the surface more anodic and thus further raised the corrosion current. When carbon steel was immersed in WBE (A1) consisting of mineral oil and surfactant, a thin oily film formed [179, 218-219] appeared as the yellowish areas on the steel surface at the end of the sliding process. The film can be damaged during corrosive wear, so the current density increased when the wear process started. Afterwards, the increase in current density became slower until reaching $17.8 \mu\text{A}/\text{cm}^2$ (brine) and $10.8 \mu\text{A}/\text{cm}^2$ (WBE (A1)) during the sliding process. The added corrosion inhibitors in WBE (A2) and WBE (A3) considerably lowered the current density value, especially PEG-6 isotridecyl phosphate in WBE

(A2). As shown in Fig. 5.5(a), the current density for the sample immersed in WBE (A2) loading with PEG-6 isotridecyl phosphate was cathodic (negative) and reached an approximate value of $-6.19 \mu\text{A}/\text{cm}^2$ at the end of the sliding test. This observation indicates that the dissolution rate of carbon steel is negligible, and no corrosion occurred on the worn surface of steel immersed in WBE (A2) during the entire test. Once sliding stopped, without the wear-assisted corrosion, the current density dropped due to the re-formation of the oxide or corrosion product layer on the wear track of samples immersed in the brine solution or a thin oily film on that immersed in WBE (A1). Since the oxide and oily films were porous or non-uniform, it could promote the galvanic effect, which might be responsible for the slight increase in current density after the sliding process ended. While in the solution with inhibitor, i.e., WBE (A2), the continuous re-formation or repairing of the protective layer during sliding could lead to the negative current. Fatty acids and phosphate esters are effective corrosion inhibitors for oilfield applications via forming protective films [220-221]. When the sliding was stopped, the negative current approached zero, corresponding to the completion of the film repairing, showing an increase in current density (from negative to zero) in Fig. 5.5(a). The formation of the protective film was confirmed by surface characterization using SEM-EDS and XPS, which showed that the protective lubricating film covered most areas of worn surface immersed in WBEs with corrosion inhibitors.

Fig. 5.5(b) displays variations in COF of steel samples tested in various solutions, obtained by simultaneously potentiostatic measurements during the tribo-corrosion tests. The COF values of all samples immersed in the solutions increased rapidly at the beginning of sliding due to the running-in between the pin and sample. The COF values became relatively stable over time. Samples tested in the brine solution and WBE (A1) exhibited higher COF values (0.42 and 0.40) and much larger volume losses (1.12×10^6 and $1.05 \times 10^6 \mu\text{m}^3$), compared to samples tested in

WBEs containing corrosion inhibitors (WBE (A2) and WBE (A3)), which showed lower COF values (0.19 and 0.28) and small volume losses (0.36×10^6 and $0.82 \times 10^6 \mu\text{m}^3$). The reduction in COF should result from the lubrication effect of the corrosion inhibitors, which developed a molecular protective film on the steel surface [222], helping decline the volume loss, as shown in Fig. 5.5(c).

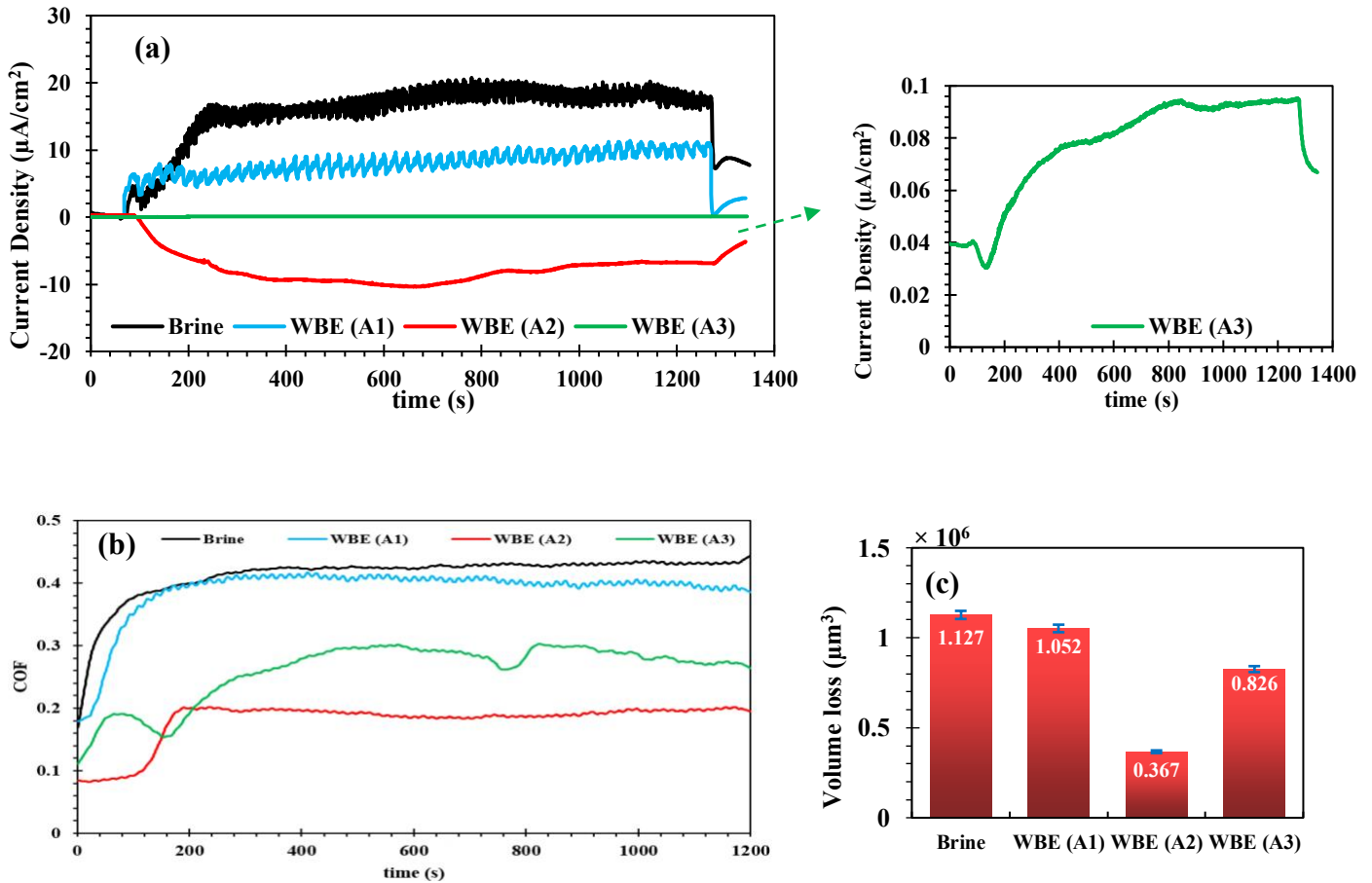


Fig. 5.5 (a) Current density and (b) COF evolution versus the sliding time; (c) volume losses of carbon steel samples immersed in the brine solution and various WBEs.

Fig.5.6 presents potentiodynamic polarization curves of the C-steel samples immersed in the brine solution and various WBEs during tribo-corrosion experiments. This test was carried out during the sliding process, which provides the information on the material's electrochemical

responses and corrosion behavior under the influence of wear with and without corrosion inhibitors at different sliding speeds.

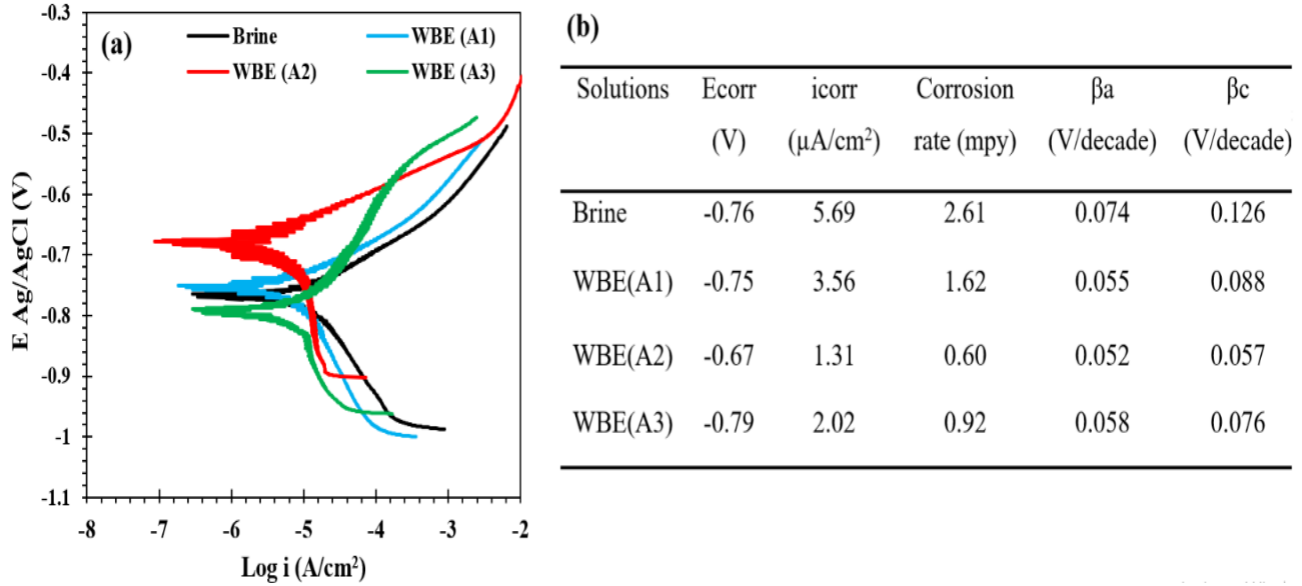


Fig. 5.6 Polarization curves (a) and electrochemical data (b) for steel samples immersed in the brine solution and various WBEs during tribo-corrosion tests at sliding speeds 2 mm/s.

The potentiodynamic polarization tests were performed at a scan speed of 0.4 mV/s between potentials of -250 mV to +250 mV around the OCP for each sample under the tribo-corrosion condition to investigate the electrochemical response of the carbon steel under different testing conditions. Fig. 5.6 (a) shows variations in cathodic (lower) and anodic (upper) branches, influenced by the composition of the drilling fluids (see Table 5.2). For the brine solution, the cathodic region is localized between -0.987 V and -0.767 V on the polarization curve. Within this potential range, the current density exhibits a decreasing trend, indicating the occurrence of reduction reactions at the electrode surface. The anodic branch starts at -0.767 V and extends to -0.486 V. In this potential range, current density shows an increasing trend, suggesting the onset of

oxidation reactions at the electrode surface. The situation is similar for WBE (A1), for which the cathodic and anodic branches are close to those of the brine solution.

For solutions with the corrosion inhibitors, e.g., WBE (A2), the cathodic and anodic branches moved towards more positive potentials. The cathodic branch is localized between -0.90 V and -0.678 V on the polarization curve, and the anodic branch is localized between -0.678 V and -0.419 V. Such shift indicates the positive effect of the corrosion inhibitor in mitigating the cathodic and anodic corrosion processes, thus protecting the surface from corrosion. For WBE (A3), the cathodic and anodic branches move towards more negative potentials where cathodic branch is localized from -0.962 V to -0.797 V and anodic branch is localized between -0.797 V and -0.474 V. For comparison regarding the inhibitors' roles, WBE (A2) with PEG-6 isotridecyl phosphate leads to dominant anodic inhibition with a more positive E_{corr} and a lower i_{corr} . While WBE (A3) PEG-2 oleamide shows a dominant cathodic inhibition with a more negative E_{corr} and a lower i_{corr} .

Relevant electrochemical parameters, including corrosion potential (E_{corr}), corrosion current density (i_{corr}), corrosion rate, and anodic and cathodic Tafel slopes (β_a and β_c), were determined from the polarization curve through Tafel extrapolation techniques [223-225], as presented in Fig. 5.6(b). As Fig 5.6(b) shows, both corrosion inhibitors, PEG-6 isotridecyl phosphate in WBE (A2) and PEG-2 oleamide in WBE (A3), make the corrosion potential moved to more positive and negative values, respectively. For WBE (A2), anodic inhibition was dominant with a more positive E_{corr} [226]. In contrast, a cathodic inhibition was dominant for WBE (A3), showing a more negative E_{corr} than that of the brine solution [227]. It can be seen that carbon steel samples tested in the brine solution showed much higher i_{corr} ($5.69 \mu\text{A}/\text{cm}^2$) and corrosion rate (2.61 mpy) than ones immersed in WBEs with the corrosion inhibitors. WBE (A2) exhibits

the lowest i_{corr} ($1.31 \mu\text{A}/\text{cm}^2$) and corrosion rate (0.60 mpy) under the tribo-corrosion condition. This suggests that PEG-6 isotridecyl phosphate, as a more effective corrosion inhibitor than PEG-2 oleamide, can provide a remarkable capability to help suppress tribo-corrosion of the carbon steel. When in a corrosive environment, the wear and friction processes can enhance the exposure of the metal surface to the brine solution. The increased contact between the corrosive ions and the metal surface accelerates oxidation, leading to higher anodic current densities.

In contrast, the corrosion inhibitors, especially PEG-6 isotridecyl phosphate in WBE (A2), significantly affected the behavior of current densities where cathodic (negative) currents were observed during tribo-corrosion tests. This is attributed to the formation of a protective film induced by the inhibitor, which reduced the electrochemical reaction occurring on the steel surface. The corrosion inhibitor could affect cathodic reduction reactions by decreasing the rate of electron transfer via their adsorption onto the cathodic sites or by changing the reaction mechanism through engaging in chemical reactions with the reactants involved in the electrochemical process, leading to a cathodic current density during tribo-corrosion experiments. Thus, the cathodic current detected for WBE (A2) indicates a reduction reaction occurring at the steel surface, where the inhibitor may act as a cathodic protecting agent, consuming electrons and preventing the oxidation of the metal.

In summary, the addition of corrosion inhibitors (WBE (A2) and WBE (A3)) markedly affects both anodic and cathodic branches on the polarization curves, demonstrating strong inhibition influence on involved corrosion process. This effect was observed through a reduction in the cathodic and anodic current densities, indicating the retardation of the reduction reactions and a decrease in the anodic dissolution of steel samples during the sliding process facilitated by corrosion inhibitors.

5.3.3.2 Effect of sliding speed on corrosion during tribo-corrosion test

Variations in current density before, during and after the sliding test at different sliding speeds in the brine solution and various WBEs were measured and are depicted in Fig. 5.7. Figs. 5.7 (a) and (c) show high current fluctuations for samples tested in the brine solution and WBE (A3), which can be ascribed to the repeated action of formation, destruction, and re-generating of the loose oxide layer (brine solution) or less durable protective lubricating film (WBE (A3)) during sliding against the counterpart. However, the fluctuations observed on all curves recorded for WBE (A2) are smaller, resulting from the formation of a durable protective lubricating layer. From Fig. 5.7, it is also clear that the current densities for samples immersed in all solutions decreased considerably with increasing the sliding speed, especially in the presence of corrosion inhibitors. The highest current density value occurred at the lowest sliding speed (2 mm/s), more profound for steel tested in the brine solution and WBE (A3), which showed anodic currents of $+17.8 \mu\text{A}/\text{cm}^2$ and $+0.093 \mu\text{A}/\text{cm}^2$, respectively, while the cathodic current of $-6.19 \mu\text{A}/\text{cm}^2$ was recorded for WBE (A2). Increasing the sliding speed (3.5 and 5 mm/s) resulted in much smaller current densities for the samples immersed in various solutions. The decrease in current density reflects lowered electrochemical activation of the steel, leading to decreased dissolution rate during the sliding test [228]. This phenomenon shows the role of sliding speed in reducing tribo-corrosion of carbon steel. The adsorption of a protective film on the sample surface (WBEs with corrosion inhibitors) appeared facilitated by a larger sliding speed. During the sliding process, the best performance was observed at 5 mm/s, where the current density values reached the lowest values: $+2.3 \mu\text{A}/\text{cm}^2$ in the brine solution, $-35.3 \mu\text{A}/\text{cm}^2$ in WBE (A2) and $-46.3 \mu\text{A}/\text{cm}^2$ in WBE (A3). However, further increasing the sliding speed (10 mm/s) did not further reduce the current density

but showed an opposite effect, which could be attributed to an increase in the rate of damaging the protective film, compared to the growth or self-repair rate of the protective film.

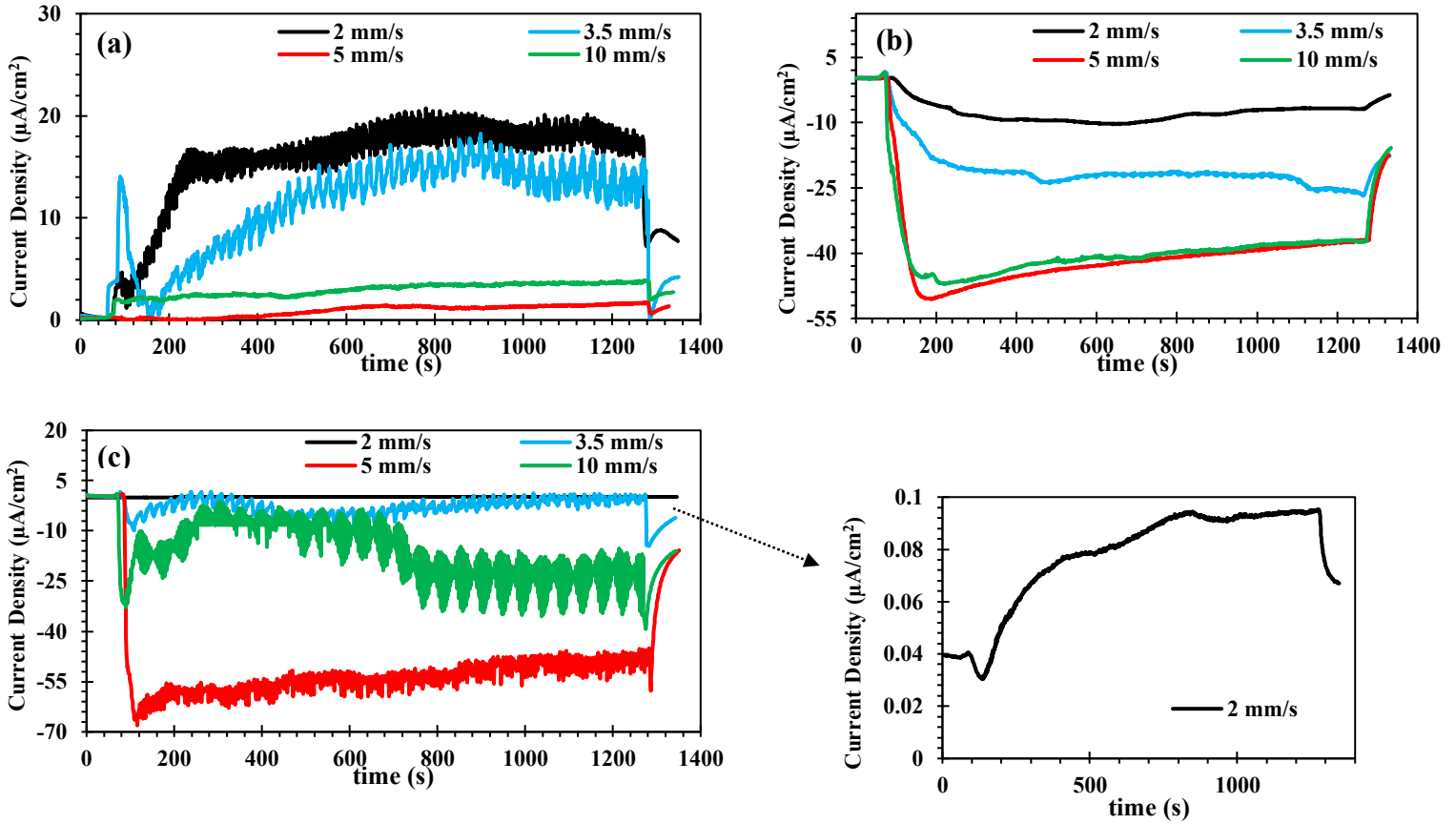
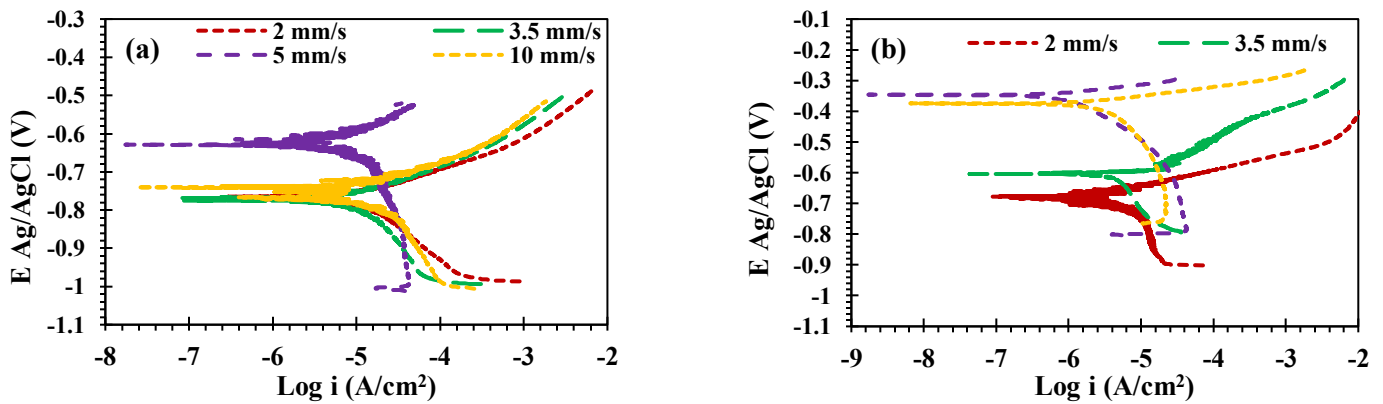


Fig. 5.7 Variations in current density versus sliding time for samples immersed in (a) brine solution, (b) WBE(A2) and (c) WBE(A3) at different sliding speeds: 2 mm/s, 3.5 mm/s, 5 mm/s and 10 mm/s.



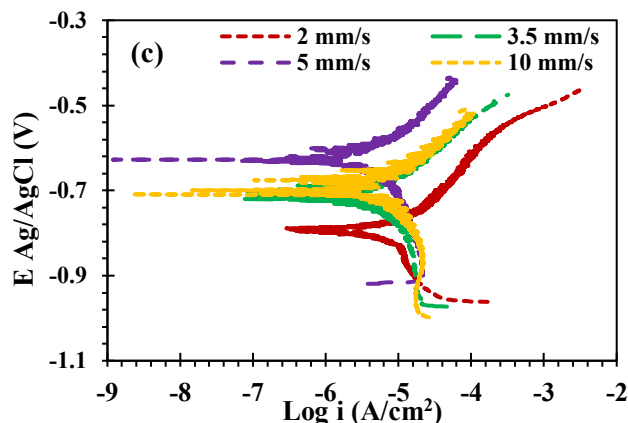


Fig. 5.8 Polarization curves of steel samples immersed in (a) the brine solution, (b) WBE(A2) and (c) WBE(A3) at four different sliding speeds, including 2, 3.5, 5 and 10 mm/s.

For further information, polarization curves and electrochemical kinetic parameters obtained via potentiodynamic tests for carbon steel samples immersed in various solutions under the tribo-corrosion condition at different sliding speeds (2, 3.5, 5 and 10 mm/s) with a contact load of 10 N are shown in Fig. 5.8 and Table 5.3, respectively. Potentiodynamic polarization curves were obtained once sliding action started. As shown, the electrochemical behavior of the steel samples immersed in all solutions changed markedly with increasing the sliding speed. On the one hand, the corrosion potential of all samples anodically shifted, where more significant shifts occurred at higher speeds, but the 5 mm/s led to the largest shift. The more positive corrosion potential at higher sliding speeds would lower the corrosion susceptibility in the solutions. On the other hand, the current densities of steel samples tested in the brine, WBE (A2) and WBE (A3), decreased considerably as the sliding speed increased, which was the most obvious at 5 mm/s.

Table 5.3 Electrochemical parameters calculated via the Tafel extrapolation method for samples immersed in the brine solution, WBE (A2) and WBE (A3) at four different sliding speeds.

Solutions	E_{corr} (V)	i_{corr} ($\mu\text{A}/\text{cm}^2$)	Corrosion rate (mpy)	β_a (V/decade)	β_c (V/decade)
Brine- 2 mm/s	-0.76	5.69	2.61	0.074	0.126
Brine- 3.5 mm/s	-0.77	5	2.29	0.054	0.077
Brine- 5 mm/s	-0.63	2.88	0.97	0.031	0.020
Brine- 10 mm/s	-0.74	3.22	1.26	0.036	0.081
WBE (A2)- 2 mm/s	-0.67	1.31	0.60	0.052	0.057
WBE (A2)- 3.5 mm/s	-0.60	1.08	0.49	0.010	0.018
WBE (A2)- 5 mm/s	-0.35	0.44	0.20	0.011	0.017
WBE (A2)- 10 mm/s	-0.37	0.60	0.28	0.011	0.011
WBE (A3)- 2 mm/s	-0.79	2.02	0.92	0.058	0.076
WBE (A3)- 3.5 mm/s	-0.71	1.83	0.85	0.051	0.058
WBE (A3)- 5 mm/s	-0.63	0.97	0.43	0.024	0.019
WBE (A3)- 10 mm/s	-0.70	1.18	0.68	0.012	0.013

According to Table 5.3, E_{corr} shifted towards more positive values with increasing sliding speed up to 5 mm/s in all three solutions. As shown later, the sliding speed affects the adsorption rate of both corrosion inhibitors on the worn surfaces (see Table 5.4 in section 5.3.3.6). When the speed was low, e.g., 2 mm/s, the protective film caused by the inhibitor formed slowly due to a low adsorption rate, thus lowering the corrosion resistance, and leading to a positive current density. As the sliding speed increased to 5 mm/s, the faster formation of the protective film (due to the increased adsorption rate) reduced the attack by corrosive agents on the worn surface, resulting in a negative current density. However, if the sliding speed continuously increased, the current density would increase due to the faster wear action. The shift in E_{corr} towards more

anodic values is more profound for solutions containing corrosion inhibitors, especially PEG-6 isotridecyl phosphate in WBE(A2). In addition, maximum icorr values and corrosion rates were observed for samples tested at the lowest sliding speed (2 mm/s), showing the poorest tribo-corrosion resistance. Increasing the sliding speed to 5 mm/s reduced corrosion in all three solutions with significant decreases in both icorr and corrosion rate, consistent with the results reported in Fig. 5.8. Again, the sliding speed of 5 mm/s led to the lowest corrosion rate. However, the icorr and corrosion rate rose again with the sliding speed increased from 5 mm/s to 10 mm/s.

5.3.3.3 The effect of sliding speed on Tribological behavior during tribo-corrosion tests

The obtained information on the influence of sliding speed on corrosion would help understand how the sliding speed affected friction and wear of the steel during tribo-corrosion tests. COF and average COF values of steel samples versus time in the brine solution, WBE (A2) and WBE (A3) at different sliding speeds were determined and are depicted in Fig. 5.9. As shown, with increasing sliding speed from 2 to 10 mm/s, COF of steel immersed in all tested solutions decreased. This decrease in COF with increasing sliding speed could be related to surface film damage and re-growth during tribo-corrosion. It should be mentioned that a higher sliding speed shortens the contacting time between the target material and the counterpart, which also helped reduce COF [54, 60, 229]. The COF showed the maximum at the lowest sliding speed (2 mm/s), where steel samples immersed in the brine solution, WBE (A2) and WBE (A3), with their COF values equal to 0.42, 0.19 and 0.28, respectively. When the sliding speed was increased to 3.5 mm/s, a substantial drop in COF was observed, which was further reduced to the lowest values at the highest sliding speed. At 10 mm/s, COF reached a value of 0.12 for the brine solution compared to 0.03 and 0.08 for WBE (A2) and WBE (A3), respectively. Fig. 5.9 (a₂, b₂ and c₂) also shows

the striking effect of corrosion inhibitors, especially PEG-6 isotridecyl phosphate in WBE (A2), on COF reduction at different sliding speeds.

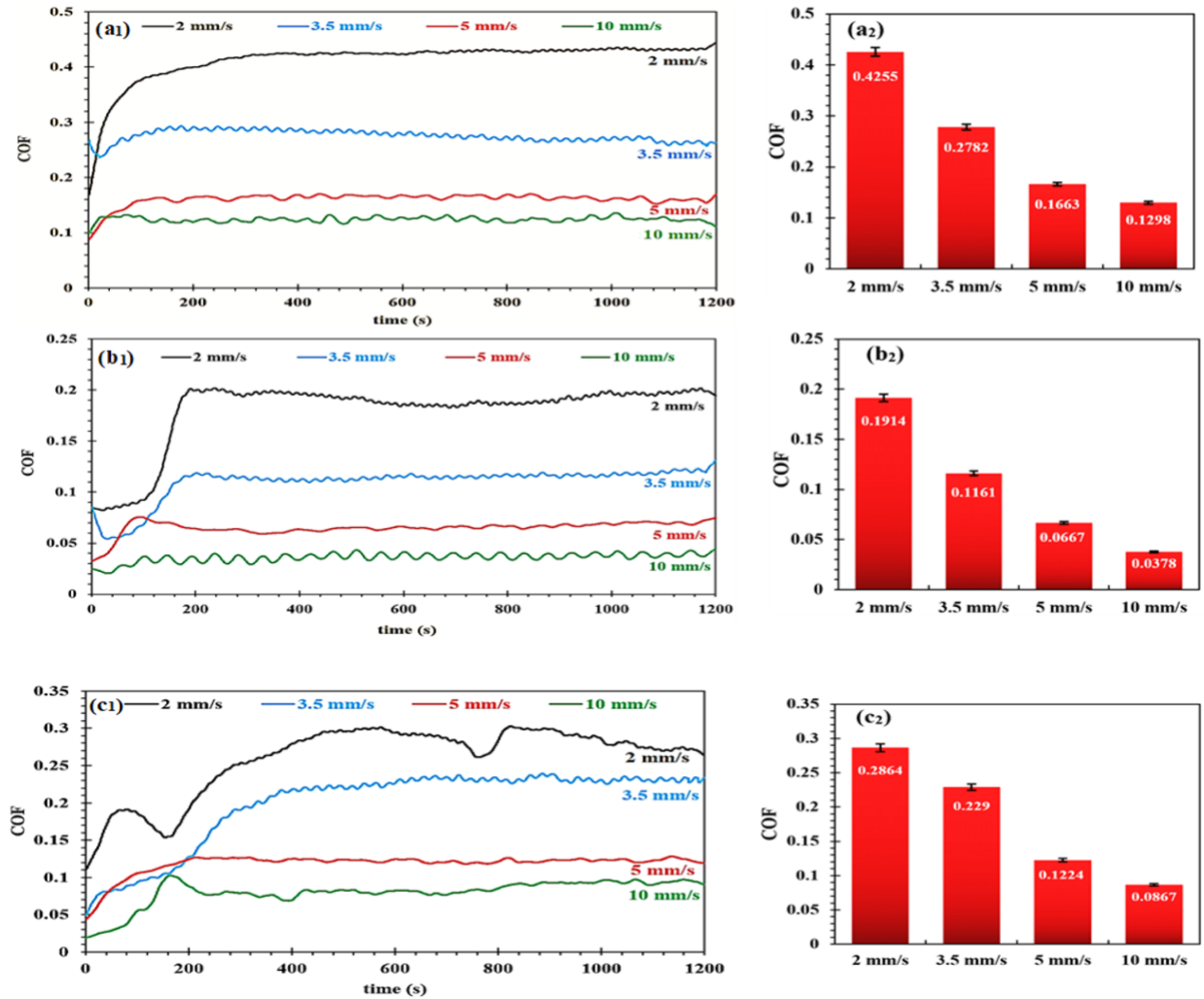


Fig. 5.9 Variations in COF as a function of sliding time and average COF values for (a1 and a2) brine solution, (b1 and b2) WBE(A2) and (c1 and c2) WBE (A3) at different sliding speeds.

After the sliding tribo-corrosion tests, volume losses of samples immersed in the brine, WBE (A2) and WBE (A3) at different sliding speeds were determined using the 3D optical profilometer (Fig. 5.10). As illustrated, volume loss increased with increasing the sliding speed, which was valid for all the solutions. The highest volume loss was observed in the brine solution at all sliding speeds. When tested in WBEs containing corrosion inhibitors (WBEs (A2) and (A3)), the volume

loss values were significantly reduced at all sliding speeds. Among WBEs containing the corrosion inhibitors, WBE (A2) with PEG-6 isotridecyl phosphate demonstrated the best performance.

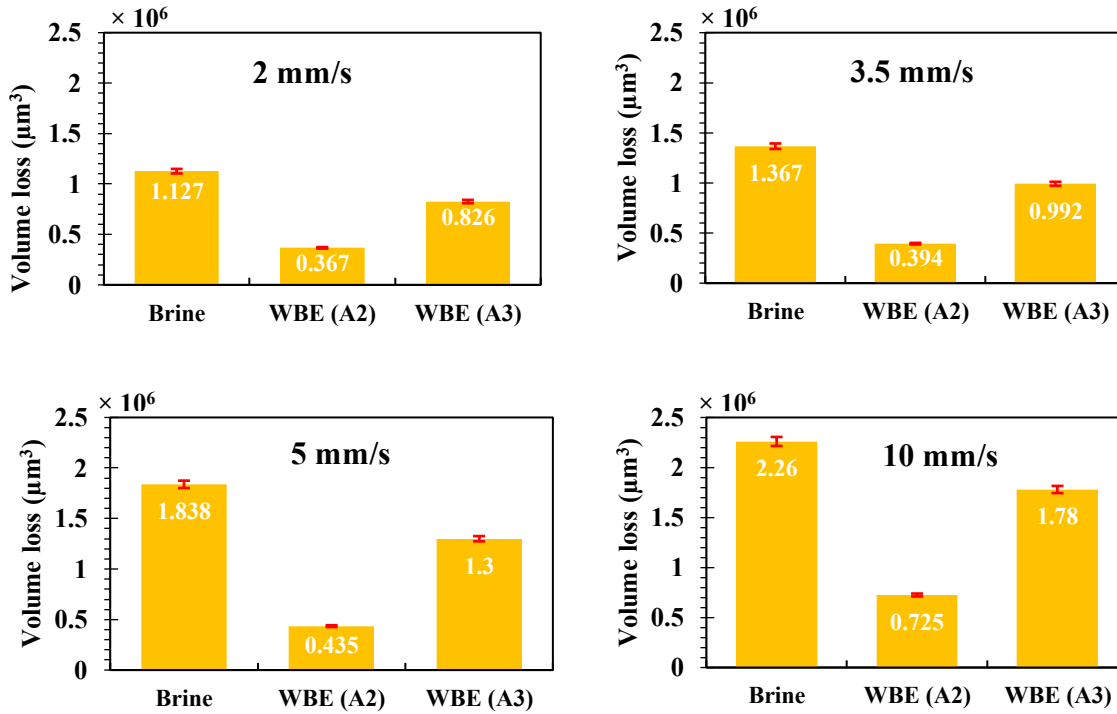


Fig. 5.10 Volume losses for steels immersed in the brine solution, WBE(A2), and WBE (A3) at different sliding speeds.

5.3.3.4 Wear-corrosion synergy

The synergy between corrosion and wear may significantly increase the total damage to materials. The wear-corrosion synergy can be determined by eq. (1), where V_{total} and V_w are respectively the total volume loss and that caused by wear alone without corrosion involved. To obtain V_w , a sliding test was carried out in DI water with the best corrosion inhibitor (PEG-6 isotridecyl phosphate). In this solution, corrosion is eliminated or minimized, while COF would not be affected much when measured in the wet environment. The volume loss was measured using an optical profilometer. For measuring volume loss caused by pure corrosion (V_c), the steel samples were immersed in various solutions, and potentiodynamic polarization (PDP) tests were

carried out for each sample under linear motion (2, 3.5, 5, and 10 mm/s) without sample-pin contact. i_{corr} was obtained through analyzing the PDP curves for each sample at different conditions. V_c was then calculated by employing Faraday's law as follows [230-231]:

$$V_c = \frac{i_{corr} t M}{nF\rho} \quad (2)$$

where i_{corr} , t , M , n , F , ρ present the corrosion current density, experiment time, the atomic mass of carbon steel, number of electrons that participated in the corrosion process, Faraday's constant ($C.mol^{-1}$) and density of iron (g/cm^3), respectively. Fig. 5.11 depicts V_{total} , V_w , V_c and V_{syn} (caused by wear-corrosion synergy) for samples immersed in the brine, WBE (A2) and WBE (A3) at the different sliding speeds.

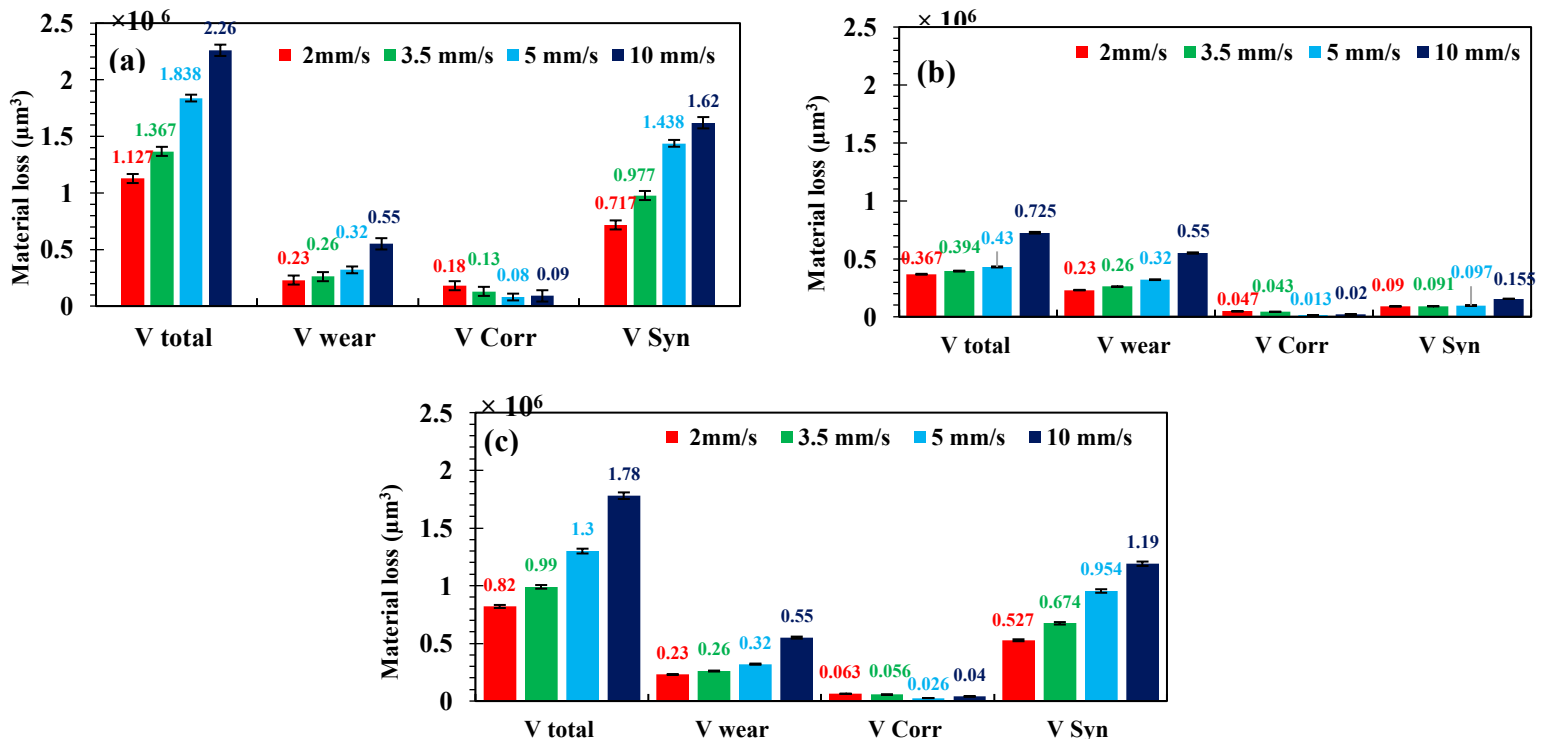


Fig. 5.11 Total volume losses (V_{total}), volume losses by wear (V_{wear} or V_w), volume losses by corrosion (V_{corr} or V_c), and volume losses by wear-corrosion synergy (V_{syn}) of samples immersed in (a) brine, (b) WBE (A2), (c) WBE (A3), at different speeds.

It should be indicated that eq. (2) gives the volume loss caused by pure corrosion without wear involved. I_{corr} was obtained via analyzing the PDP curves for each sample under different conditions, which was used to determine V_c . However, during the tribo-corrosion test, any increment of corrosion caused by wear comes mainly from the wear track because other areas are still under non-contact conditions. Thus, the increment in corrosion current during tribo-corrosion would come from wear-assisted corrosion.

Fig. 5.11 shows V_{total} , V_w , V_c , and V_{syn} in three solutions at different sliding speeds. The corrosion inhibitors, especially PEG-6 isotridecyl phosphate, effectively reduced corrosion (V_c), thus the corrosion-wear synergy (V_{syn}) and consequently the total volume loss (V_{total}). The increases in V_{total} , V_w and V_{syn} with increasing the sliding speed are expected since the tests were performed with a fixed duration, so the sliding distance was longer for higher sliding speed. However, V_c showed a different trend, which decreased with the sliding speed until 5 mm/s and then slightly increased at 10 mm/s. The decrease in V_c should be ascribed to the influence of sliding speed on the adsorption rate of inhibitor molecules on the steel surface as demonstrated in section 5.3.3.5, where Table 5.4 shows that the higher adsorption of inhibitor molecules on the steel surface occurred with increasing sliding speed up to 5 mm/s, confirmed by EDS and XPS analysis that shows an increase in the amount of P and O with the sliding speed. The increase in the adsorption rate corresponded to faster growth or repair of the protective film (containing mineral oil + surfactant + corrosion inhibitor). As a result, corrosion could be reduced.

5.3.3.5 Adsorption isotherm

Tribo-corrosion performance of WBEs with corrosion inhibitors at various sliding speeds is directly related to the adsorption behavior of inhibitor molecules on worn surfaces. To understand the adsorption process on the metal surface, it is essential to calculate thermodynamic

adsorption parameters. Langmuir isotherm model was employed to evaluate the adsorption of corrosion inhibitors on surface of 1018 carbon steel. Fig. 5.12 displays that interfacial adsorption of both corrosion inhibitors followed Langmuir isotherm (with above 0.99 regression coefficient), indicating the generation of the single corrosion inhibitor-induced layer at the interface between solution and carbon steel. Table 5.4 lists the parameters such as adsorption equilibrium constant (K_{ads}) and standard Gibbs free energy of adsorption (ΔG°_{ads}), which can play a significant role in determining the adsorption process (spontaneous or non-spontaneous) and the type of interaction between corrosion inhibitors and the metal surface (chemisorption, physisorption, or both). The change in the standard Gibbs free energy of adsorption (ΔG°_{ads}) can be determined by K_{ads} , which is obtained from the relationship between corrosion inhibitor (C_{inh}) and inhibitor surface coverage (θ) as presented by eqs. (3) and (4) [30]:

$$\theta = \frac{i^{\circ}corr - icorr}{i^{\circ}corr} \quad (3)$$

$$\frac{\theta}{1 - \theta} = K_{ads} \times C_{inh} \quad (4)$$

where i°_{corr} and i_{corr} represent the corrosion current densities of samples immersed in the brine solution and WBEs, respectively. The formula for the calculation of standard Gibbs free energy of adsorption (ΔG°_{ads}) is given by eq. (5) [201, 232]:

$$\Delta G^{\circ}_{ads} = -R T \ln (55.5 \times K_{ads}) \quad (5)$$

where T and R are temperature (K) and universal gas ($Jmol^{-1} K^{-1}$), respectively. Table 5.4 displays the calculated values of K_{ads} and ΔG°_{ads} for carbon steel experienced tribo-corrosion tests in WBE (A2) and WBE (A3) at various sliding speeds, respectively.

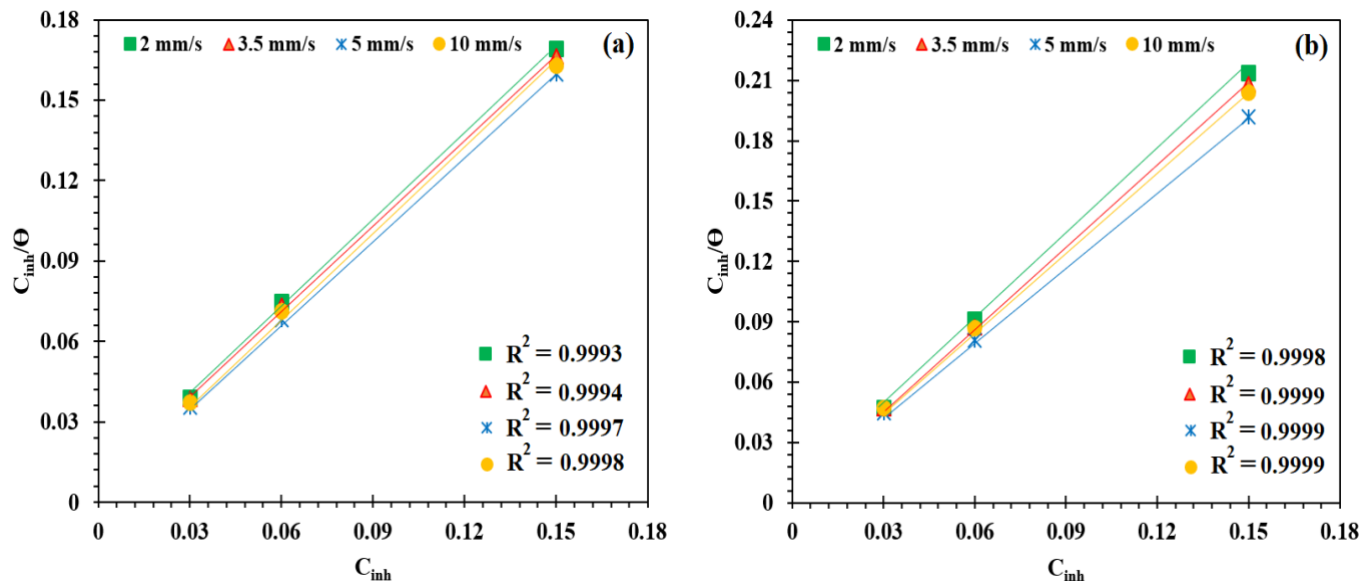


Fig. 5.12 Langmuir adsorption isotherm for carbon steel in (a) WBE (A2) and (b) WBE (A3) at different sliding speeds.

According to Table 5.4, by increasing the sliding speeds to 5 mm/s, a noticeable enhancement in K_{ads} can be seen, especially for PEG-6 isotridecyl phosphate in WBE (A2), suggesting more adsorption of inhibitor molecules on the surfaces during the sliding process. Thus, a more protective lubricating layer could be generated on the steel surface at higher sliding speeds within the speed range under study, providing improved tribo-corrosion resistance at higher sliding speeds (see Figs. 5.7 ~ 5.9). Comparing the two corrosion inhibitors, PEG-6 isotridecyl phosphate shows a much higher K_{ads} value at any sliding speed, implying higher anti-tribo-corrosion capability. The negative ΔG°_{ads} values in Table 5.4 reveal that corrosion inhibitor molecules were adsorbed on the steel surface. According to [233], if the ΔG°_{ads} value is -20 kJ/mol^{-1} or less negative, physisorption takes place between charges of corrosion inhibitor and steel surface; if ΔG°_{ads} values are equal to -40 kJ/mol^{-1} or more negative, the adsorption belongs to chemisorption through electron sharing. According to the ΔG°_{ads} values for WBE (A2) in Table 5.4, which are between -

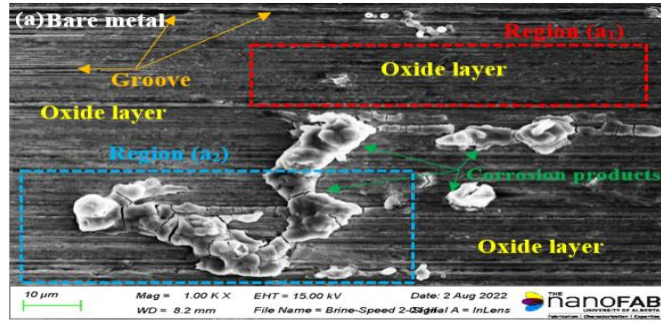
23 and -27 kJ/mol⁻¹ at different sliding speeds, active species on the structure of PEG-6 isotridecyl phosphate may be bound to the metal surface through both physical and chemical adsorption mechanisms. While $\Delta G^{\circ}_{\text{ads}}$ values are noted to occur between -14 and -18, implying that the active inhibiting species of PEG-2 oleamide could be bound to steel surfaces through physical reactions [234-235].

Table 5.4 Langmuir adsorption isotherm parameters for WBE (A2) and WBE (A3) at a different sliding speed

Solution	Speed (mm/s)	K_{ads} (M ⁻¹)	$\Delta G^{\circ}_{\text{ads}}$ (kJ. Mol ⁻¹)
WBE (A2)	2	182.6	-23.1
	3.5	306.1	-24.3
	5	849.6	-26.8
	10	473.8	-25.4
WBE (A3)	2	6.70	-14.7
	3.5	10.1	-15.8
	5	28.1	-18.4
	10	14.1	-16.7

5.3.3.6 Surface characterization of worn samples

After tribo-corrosion tests, SEM-EDS and XPS techniques were employed to analyze the worn surface and composition of layers formed on the wear track. Figs. 5.13 and 5.14 depict details of the wear tracks produced in the brine and WBE (A2) at three different sliding speeds.

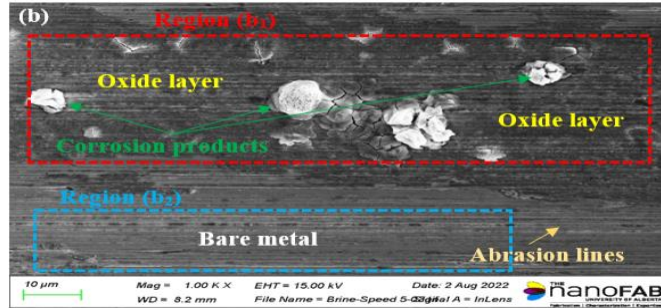


Region (a₁)

Element	Fe	O	C	Mn	Cl	K
Wt. %	76.93	13.66	8.40	0.65	0.33	0.03

Region (a₂)

Element	Fe	O	C	Mn	Cl	K
Wt. %	72.95	18.48	7.30	0.47	0.74	0.05

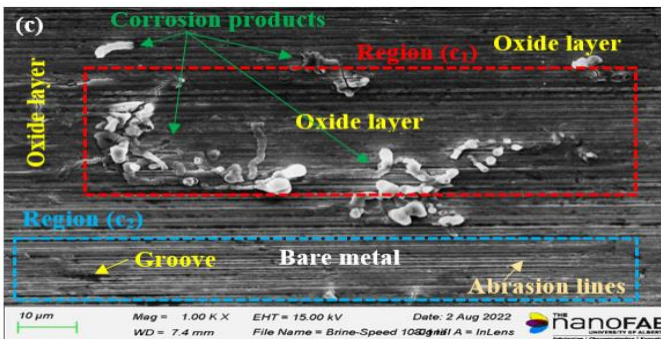


Region (b₁)

Element	Fe	O	C	Mn	Cl	K
Wt. %	81.72	10.72	6.51	0.76	0.28	0.01

Region (b₂)

Element	Fe	O	C	Mn	Cl	K
Wt. %	82.76	5.11	8.20	0.82	0.10	0.01



Region (c₁)

Element	Fe	O	C	Mn	Cl	K
Wt. %	81.40	10.33	7.44	0.49	0.30	0.04

Region (c₂)

Element	Fe	O	C	Mn	Cl	K
Wt. %	85.54	4.89	8.56	0.89	0.11	0.01

Fig. 5.13 SEM images and EDS data of worn surface experienced test in the brine solution at different sliding speeds (a) 2 mm/s, (b) 5 mm/s and (c) 10 mm/s.

As shown in Fig. 5.13, at 2 mm/s, the worn surface is covered by a loose and fragile oxide layer due to the high content of oxygen detected on the wear track (13.66 wt.% to 18.48 wt.%). As Fig. 5.13 (a) illustrates, the wear track comprises deep grooves, microcracks, wear debris and agglomeration of corrosion products caused by corrosive wear. The EDS analysis on regions (a₁) and (a₂) shows that the oxide layer formed on the wear track is rich in oxygen and iron, suggesting that the oxide layer is composed of iron oxyhydroxide (FeOOH) [215]. The EDS analysis also reveals high percentages of corrosive ions such as chlorine (0.33 and 0.74 wt.%) and potassium

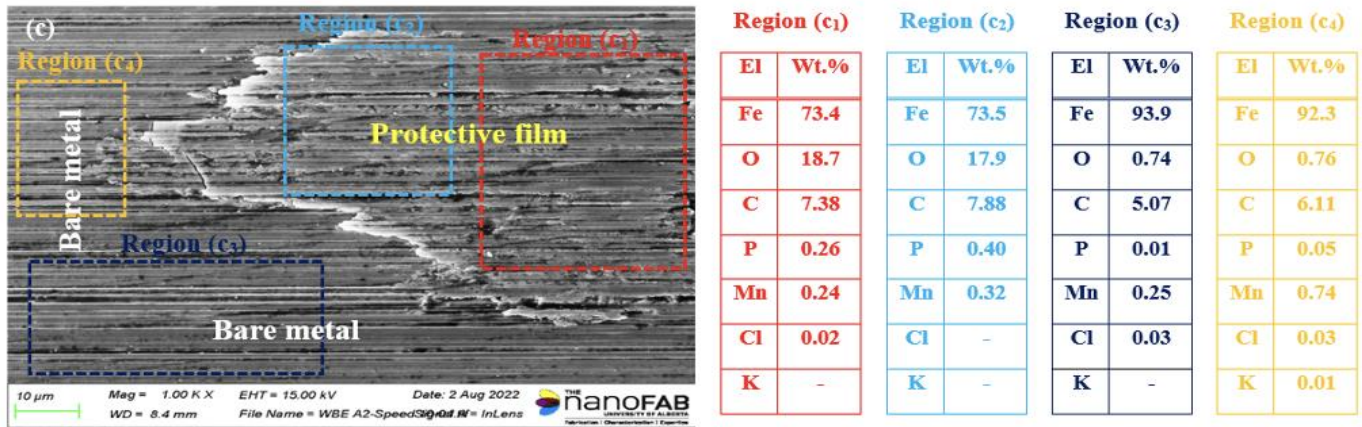


Fig. 5.14 SEM images and EDS data of worn surfaces tested in WBE (A2) at different sliding speeds (a) 2 mm/s, (b) 5 mm/s and (c) 10 mm/s.

SEM-EDS analysis (Fig. 5.14) reveals that a protective lubricating film was generated on the worn surfaces, and its uniformity and composition varied with the sliding speed. Fig. 5.14 (a) indicates the formation of a non-uniform and sporadic protective lubricating layer (e.g., regions (a₁), (a₂) and (a₃)) in different locations of the worn surface tested at the sliding speed of 2 mm/s. The EDS results show that the three selected regions ((a₁), (a₂) and (a₃)) mainly have iron (79.2 to 83.7 wt.%), oxygen (9.20 to 12.9 wt.%), carbon (6.22 to 7.18 wt.%) with low phosphorous content (0.08 to 0.21 wt.%), suggesting the formation of a protective lubricating film on the worn surface during the tribo-corrosion tests. Corrosive ions were also detected on the wear track, which were more detected in the areas without the protective film (region (a₄)). Corrosive agents can penetrate the material in the regions uncovered by the protective layer (0.01 wt.% P, 0.86 wt.% O and 5.15 wt.% C). As the sliding speed increased to 5 mm/s (Fig. 5.14 (b)), a uniform, relatively smooth, and continuous protective lubricating film developed, which covered most areas of the wear track, thus helping reduce corrosion and wear-corrosion synergy. According to EDS results (regions ((b₁), (b₂) and (b₃))), the protective lubricating film resulting from the corrosion inhibitor on the worn surface showed significant increases in oxygen (23.9 to 25 wt.%), carbon (6.92 to 8.94 wt.%)

and phosphorous (0.31 to 0.47 wt.%). The higher concentrations of these elements are a sign of forming a better protective layer at a higher speed (5 mm/s), in accordance with the results obtained from the adsorption isotherm (Fig. 5.12 and Table 5.4 in section 5.3.3.5), where the adsorption rate of corrosion inhibitors on the worn surface increased with sliding speed. This consequently enhanced adsorption, leading to improved protection against wear and corrosion. However, less coverage of protective lubricating film occurred again with further increasing the sliding speed to 10 mm/s (see Fig. 5.14 (c)), which may also be confirmed by reduced amounts of oxygen (17.9 and 18.7 wt.%), carbon (7.38 and 7.88 wt.%) and phosphorous (0.26 to 0.40 wt.%) as determined in regions (c₁) and (c₂) by EDS analysis.

XPS analysis was performed for more information on the composition of the protective lubricating layer or film formed on the worn surfaces with respect to the sliding speed. Fig. 5.15 depicts the XPS survey spectra (0-1100 eV) of worn surfaces tested in WBE (A2) containing PEG-6 isotridecyl phosphate at 2 and 5 mm/s. As shown in Fig. 5.15, the main elemental compositions of the protective layer formed on the wear tracks at 2 and 5 mm/s include Fe, O, C and P. The presence of the P 2p signal at both sliding speeds clarifies that the corrosion inhibitor was successfully adsorbed on the worn surface, improving the tribo-corrosion performance of the steel during the sliding process. Furthermore, no corrosion products with, e.g., Cl and K elements were found on the worn surface at two sliding speeds, indicating that corrosion inhibitor effectively prevented corrosion. A comparison between the situations corresponding to 2 and 5 mm/s indicates that the intensity of O 1s peak was enhanced with increasing the sliding speed; the atomic percentage of O element detected on the worn surface increased from 23.83 % (2 mm/s) to 26.61% (5 mm/s). In addition, the atomic percentage of P 2p detected on the worn surface after the tribo-corrosion test showed an increase from 2.99 % at 2 mm/s to 4.14 % at 5 mm/s. The increase in

atomic percentages of O and P, because of their presence in the structure of PEG-6 isotridecyl phosphate, can be considered as an indication of more adsorption of molecules in the protective layer on the wear track, which occurred with increasing the sliding speed, leading to better protection for the steel against tribo-corrosion.

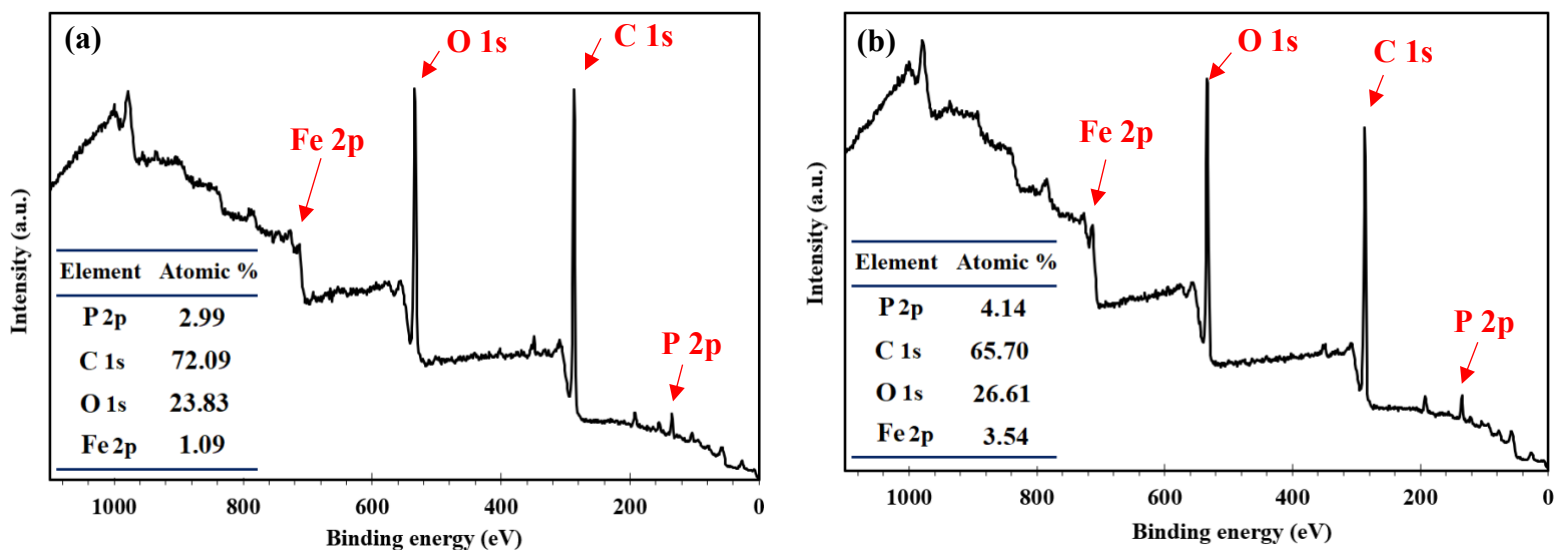
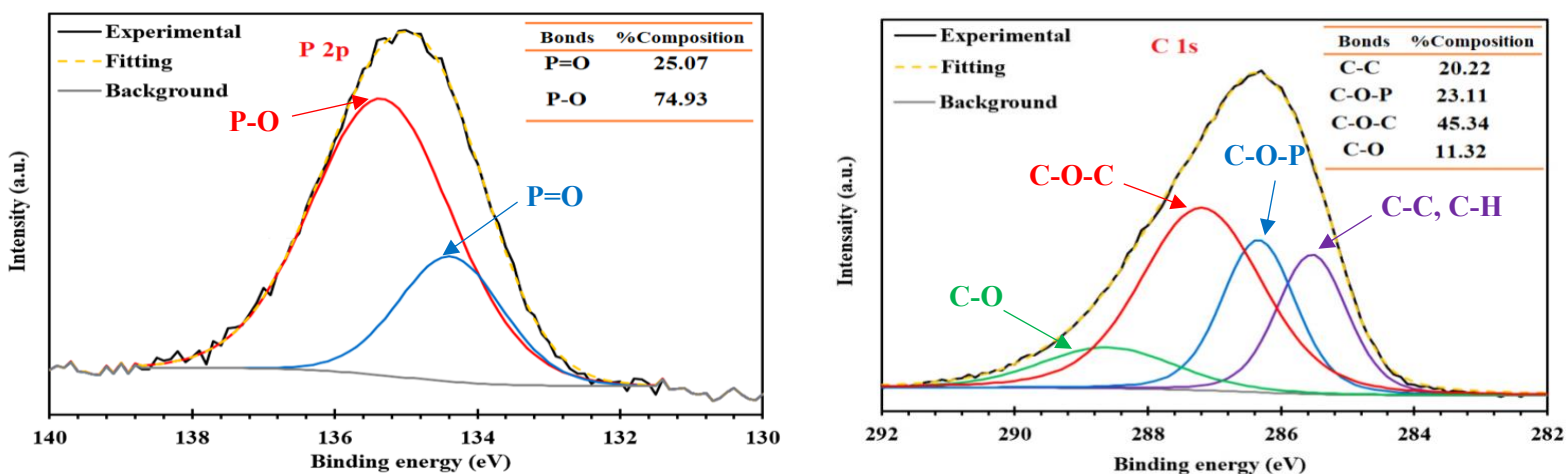


Fig. 5.15 XPS survey spectra of worn surface immersed in WBE (A2) at two different sliding speeds (a) 2 mm/s and (b) 5 mm/s.



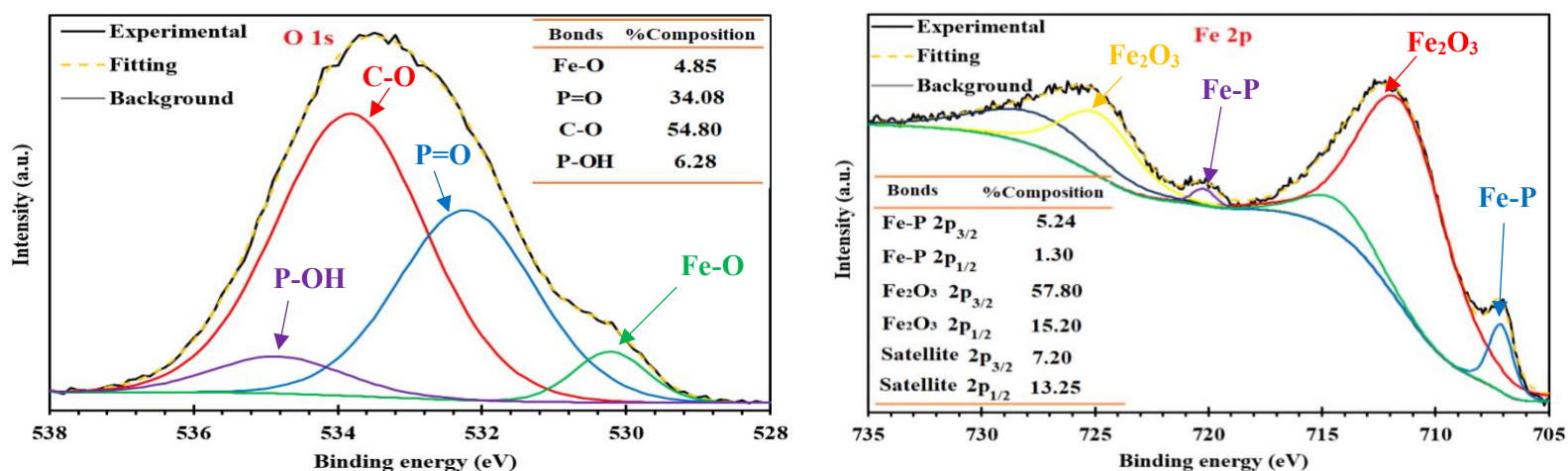


Fig. 5.16 High-resolution XPS spectra of worn surface tested in WBE (A2) at 5 mm/ for P 2p, C 1s, O 1s and Fe 2p.

High-resolution XPS spectra of P 2p, C 1s, O 1s and Fe 2p were also recorded from the worn surface immersed in WBE (A2) at 5 mm/s to determine the characteristic bonds and related composition of each element, results of which are depicted in Fig. 5.16.

Using Gaussian–Lorentzian fitting, high-resolution P 2p signal (Fig. 5.16 (a)) can be deconvoluted into two peaks at 134.34 and 135.38 eV, attributing to P=O and P-O bonds in the corrosion inhibitor of PEG-6 isotridecyl phosphate, respectively [236]. Fig. 5.16 (b) depicts four deconvoluted peaks for C 1s spectra at different binding energies. The peak at a binding energy of 285.54 eV is related to C-C and C-H bonds due to the long hydrocarbon chain in the PEG-6 isotridecyl phosphate molecule. The binding energy of 286.33 eV corresponds to the C-O-P group. The intense peak with the highest carbon concentration was detected at 287.14 eV, which belongs to the ether group (C-O-C), while a broad and small peak recorded at 288.59 eV is associated with C-O bonding, which is a minor contributor to C 1s band [237-238]. The O 1s spectrum of the worn surface is deconvoluted into four components, as illustrated in Fig. 5.16 (c), which are related to Fe-O, P=O, O-C and P-OH at the binding energies of 530.27, 532.22, 533.81 and 534.83 eV, respectively [239-241]. The deconvolution of the Fe 2p region (Fig. 5.16 (d)) shows six peaks at

lower and higher binding energies. Two peaks at binding energies of 707 eV for Fe 2p_{3/2} and 720.21 eV for Fe 2p_{1/2} can be attributed to Fe in the Fe-P bond, representing the grafting of corrosion inhibitor successfully on the worn surface during the tribo-corrosion test. Moreover, the peaks obtained from the deconvolution of Fe 2p at binding energies of 711.39 eV (Fe 2p_{3/2}) and 724.79 eV (Fe 2p_{1/2}) can be ascribed to iron oxidized species caused by surface oxidation, such as Fe₂O₃ and Fe-OH. Besides, the satellite peaks for Fe 2p_{3/2} and Fe 2p_{1/2} at 714.29 eV and 727.53 eV are identifiable [179, 242-244]. Therefore, XPS data confirm the chemisorption of corrosion inhibitor on the worn track during the sliding process in the solution, which is consistent with SEM-EDS results.

In summary, the enhanced physical and chemical adsorption of corrosion inhibitors on the steel surface with increasing the sliding speed should be ascribed to the increased number of adsorbed molecules on the surface. As a result, a protective lubricating film could be generated more quickly than at higher speeds, leading to better protection against tribo-corrosion, which was observed experimentally (adsorption, morphology, and composition of worn surface; see Table 5.4 and Figs. 5.14 and 5.15). However, such a trend is valid only within a limited sliding speed range. As the sliding speed exceeds a certain level, the situation is reversed, i.e., the tribo-corrosion is promoted as the sliding speed is continuously increased.

5.3.4 Tribo-corrosion mechanism of the carbon steel immersed in different solutions

The SEM, EDS, and XPS analyses on the worn surface tested in the brine solution showed that an oxide layer composed of oxidized iron species such as Fe₂O₃ and Fe-OH formed on the wear track of 1018 carbon steel under the tribo-corrosion condition. With the onset of the sliding process at 2 mm/s, initiation and accumulation of corrosion products and wear debris occurred on the oxide

layer. During sliding, the layer generated on the worn surface would be damaged or removed easily because of generally weak and porous iron oxide. This led to fresh metal surfaces being exposed to wear and corrosion. With increasing the sliding speed, the formation of oxide could be accelerated, leading to increased coverage of the oxide film, which should be thinner due to the faster sliding of the counterpart. A thinner film could have stronger adherence to the substrate since the interfacial mismatch stress between the substrate and the film increases with the film's thickness until saturation [245]. This could help maintain a relatively larger coverage, although the faster sliding of the counterpart may enhance the damage to the film. However, further increasing the sliding speed can lead to a negative effect as the damage rate exceeds a critical level.

The tribo-corrosion resistance of steels immersed in the WBEs containing PEG-6 isotridecyl phosphate was considerably enhanced due to the formation of a protective lubricating layer composed of corrosion inhibitor molecules. The PEG-6 isotridecyl phosphate can be adsorbed physically (electrostatic adsorption between protonated molecules of corrosion inhibitors and charged steel surface) and chemically (sharing lone pair electrons of heteroatoms located on corrosion inhibitors (oxygen and phosphorous) with unoccupied orbitals of iron atoms). Fig. 5.17 schematically illustrates the adsorption of the PEG-6 isotridecyl phosphate molecule on the carbon steel surface. The corrosive chloride ions (Cl^-) in the WBE (A2) can be adsorbed electrostatically on the positively charged steel substrate. With an attractive electrostatic adsorption process, the protonated molecules of PEG-6 isotridecyl phosphate are attached to the pre-adsorbed anions on the steel surface; the inhibitor molecule can generate physically adsorbed film on the steel surface. Besides, according to Fig. 5.1, a PEG-6 isotridecyl phosphate molecule has a number of oxygen heteroatoms with one phosphorus heteroatom in its structure. These heteroatoms can share their lone pair electrons with unoccupied orbitals of iron atoms, resulting in the chemical adsorption of

PEG-6 isotridecyl phosphate molecules on the steel surface via their coordinate covalent bonds with iron atoms.

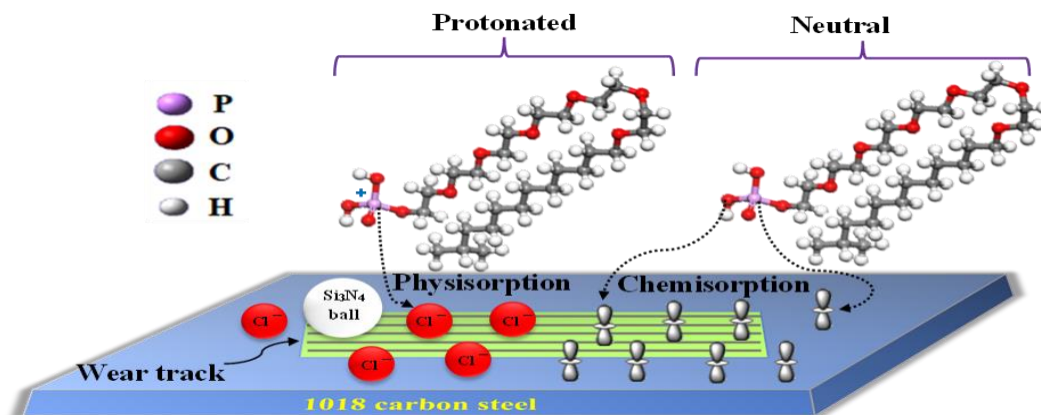


Fig. 5.17 Schematic tribo-corrosion mechanism of 1018 carbon steel immersed in WBE (A2) containing PEG-6 isotridecyl phosphate.

While forming protective films on the steel surface reduces chemical and mechanical interactions, the sliding speed can affect the kinetics of tribo-corrosion attack on the material. Once the sliding starts, the protective lubricating film is mechanically damaged, removed, or partially removed, resulting in increased material loss. The protection capability of the inhibitor film is influenced by the sliding speed. At low sliding speed, the worn surface was protected by a thin protective layer which covered some areas of the wear track, as shown in Fig. 5.14 (a). An increase in sliding speed to 5 mm/s increased the coverage of the protective film, as illustrated in Fig.5.14(b), and EDS, XPS and Langmuir adsorption isotherm confirmed the increased adsorption at 5 mm/s. However, as the speed was increased to 10 mm/s, the surface coverage was reduced, accompanied by a decrease in the tribo-corrosion resistance. The mechanism for the effect of sliding speed on anti-tribo-corrosion of the steel in WBE (A2) and WBE (A3) could be similar to the situation of test in the brine solution as discussed earlier (forming a protective layer, breakdown and re-forming). The only difference is that in the brine solution, the formed film is iron oxide,

while in WEB (A2) and WBE (A3) containing the corrosion inhibitors, the formed film came from the adsorbed inhibitor's molecules (PEG-6 isotridecyl phosphate and PEG-2 oleamide) which build a protective barrier for the steel substrate.

5.4 Conclusions

The effect of PEG-6 isotridecyl phosphate in emulsion-based drilling fluid on the tribo-corrosion of 1018 carbon steel was investigated and compared with that of PEG-2 oleamide. Since the protection of the inhibitor involves damage and regrowth of a protective film, the influence of the sliding speed during corrosive sliding wear tests on the performance of the inhibitor was studied experimentally. The following conclusions are drawn:

- 1- The study on the turbidity and zeta potential revealed that the most stable emulsion-based drilling fluid was obtained by adding a small amount of surfactant (5%), PEG-6 isotridecyl phosphate of a high concentration (30%) and mineral oil (65%) to the brine solution.
- 2- Potentiostatic, potentiodynamic and COF tests demonstrated that the two corrosion inhibitors in the drilling fluids notably reduced current density, corrosion rate, friction and wear of 1018 carbon steel at all sliding speeds. PEG-6 isotridecyl phosphate performed better than PEG-2 oleamide.
- 3- With increasing the sliding speed from 2 mm/s to 5 mm/s, electrochemical parameters such as the corrosion rate decreased. Continuously increasing the sliding speed to 10 mm/s did not further reduce the corrosion rate. However, COF values of carbon steel immersed in various solutions considerably reduced as the sliding speed increased from 2 to 10 mm/s.
- 4- PEG-6 isotridecyl phosphate added in WBE (A2) was more influential in suppressing the wear-corrosion synergy than other solutions due to its effectiveness in reducing corrosion.

- 5- The PEG-6 isotridecyl phosphate molecule is adsorbed physically and chemically on the worn surface, proved by the Gibbs free energy calculation, SEM-EDS and XPS analysis. These tests also demonstrated that more inhibitor molecules adsorbed on the steel surface with an increase in sliding speed up to 5 mm/s. This could be the reason for obtaining the best tribo-corrosion performance of 1018 carbon steel at 5 mm/s.

Chapter 6 Influence of contact forces and electrochemical potential on tribo-corrosion protection of 1018 carbon steel in the drilling fluids by in-situ electrochemical techniques⁵

6.1 Introduction

Tribo-corrosion, which can negatively affect the durability of drilling equipment, is a severe concern for the drilling industry [181,246-250]. Wear can exacerbate the corrosion rate of metallic equipment in drilling fluids by breakdown or eliminating the protective surface layer through mechanical actions. This can lead to the creation of rough surface areas, which can ultimately cause the plastic deformation of drilling equipment. Corrosion, on the other hand, can influence the wear process by facilitating the initiation of pits and propagation of cracks on the steel surface. The combined impact of wear and corrosion accelerates the deterioration of drilling equipment, reducing their performance and lifespan, and raising maintenance costs [19-21, 24, 230, 251]. To tackle this problem, it is crucial to comprehend the tribo-corrosion performance of drilling equipment under different conditions for optimizing drilling operations and improving equipment efficiency, resulting in both scientific and economic benefits.

Metallic equipment's tribo-corrosion performance is affected by multiple interdependent variables, such as environmental factors (temperature [252], humidity [252], pH [253], and corrosive ions [254]), material properties (composition [27], microstructure [255], hardness [29]),

⁵ A version of this chapter will be submitted. M.j. Palimi, Y. Tang, S. E. Mousavi, V. Alvarez, E. Kuru, W. G. Chen, D.Y. Li, Influence of contact forces and electrochemical potential on tribo-corrosion protection of 1018 carbon steel in the drilling fluids by in-situ electrochemical techniques, *Electrochemical Acta*.

surface finish (roughness [29]), sliding velocity [256], applied forces [31] and electrochemical potentials [32]. The type and degree of material damage during drilling operations can be considerably impacted by the aforementioned factors. Among these variables, the sliding force and electrochemical potentials are controllable parameters which can be adjusted to influence the rate at which tribo-corrosion occurs and ultimately mitigate damage to the drilling components [31-32]. Thus, it is imperative to control and regulate these interrelated factors to preserve the durability and integrity of drilling equipment.

Contact forces play an essential role in the tribo-corrosion resistance of metallic equipment, leading to mechanical wear and surface deformation. During the sliding process, the contact pressure between two rubbing surfaces generates a friction force that can lead to the removal of surface material and the formation of microscopic defects such as cracks, ploughs, and grooves. The occurrence of such defects can cause a greater surface area to be exposed to aggressive media, accelerating the corrosion process, and ultimately contributing to the deterioration and failure of the metallic drilling equipment with fatal consequences. Furthermore, heat can be produced by friction sliding, which can aggravate the corrosion process by heightening electrochemical reactions on the surface of drilling equipment. This problem can be further exacerbated by the creation of abrasive particles or contaminants during sliding wear, which enhances the wear rate and exposes a larger surface area of metals to the corrosive agents [19,21,24,30, 34-37,249,257]. The applied electrochemical potential determines the direction and magnitude of electron transfer at the interface between metal and electrolyte, leading to changes in the electrochemical potential of the electrode. These variations in electrochemical potentials can substantially impact the tribo-corrosion rate of metallic equipment during drilling operations. Indeed, depending on the electrochemical potential of the electrode (the electric potential difference between the metal

electrode and electrolyte solution), metallic drilling equipment may be protected cathodically or dissolved anodically [39,258-259]. Thus, optimizing the tribo-corrosion resistance of drilling components and prolonging the material lifespan in harsh environments can be obtained by controlling the sliding force and electrochemical potential.

As a cost-effective and prospective approach, corrosion inhibitors are introduced into drilling fluids to increase the tribo-corrosion performance of drilling equipment [30,246, 260-262]. Previous chapters have detailed the adsorption mechanism of corrosion inhibitors and elucidated how they can generate an inhibitive barrier film at the metal-electrolyte interface through physical and chemical reactions. Thus, combining corrosion inhibitors and techniques like controlling the applied force and electrochemical potential can provide superior protection of drilling equipment against tribo-corrosion.

This chapter investigates the effect of two important parameter such as contact forces and electrochemical potentials on the tribo-corrosion performance of 1018 carbon steel immersed in drilling fluids containing corrosion inhibitors through tribo-corrosion experiments. The wear tracks were then examined using SEM, EDS, XPS, and optical profilometer to evaluate worn surface morphology, chemical composition, volume loss, and specific wear rate.

6.2 Materials and experiments

6.2.1 Materials and emulsion-based drilling fluids preparation

Chapter 6 reports a study on the effect of sliding force and electrochemical potential on Tribo-corrosion performance of 1018 carbon steel immersed in water-based emulsion drilling fluids (WBEs) containing three different corrosion inhibitors Glycerol myristate, PEG-2 oleamide, and PEG-6 isotridecyl phosphate. Figs 2.1 and 5.1 show the molecular structures of three corrosion

inhibitors employed in this chapter. In the earlier chapters, we detailed both the ingredients utilized in formulating WBEs and the process of their preparation. Table 6.1 lists the formulated water-based emulsions (WBEs) as the drilling fluids for this chapter, which prepared based on the turbidity values and zeta potential data explained in chapter 5.

Table 6.1 Water-based emulsions (WBEs) for the current research

Solution	Ingredient
WBE (B0)	Brine solution as a reference solution: 5 gr KCl in 95 ml DI water [103-104]
WBE (B1)	0.1g (65% Mineral oil + 5% TERGITOL NP-9 + 30% Glycerol myristate) in 99.9 g brine solution
WBE (B2)	0.1g (65% Mineral oil + 5% TERGITOL NP-9 + 30% PEG-2 oleamide) in 99.9 g brine solution
WBE (B3)	0.2 g (65% Mineral oil + 5% TERGITOL NP-9 + 30% PEG-6 isotridecyl phosphate) in 99.9 g brine solution

6.2.2 Experiments

The tribo-corrosion performance of carbon steel plates immersed in various WBEs was studied using a linear-reciprocating module of a pin-on-disc tribometer connected to a three-electrode electrochemical workstation. A schematic illustration of the experimental set-up for the tribo-corrosion tests can be seen in Fig. 3.1. All the tribo-corrosion tests were carried out under the following conditions:

- 1- Linear motion of 4 mm Si₃N₄ ball on the carbon steel surface (distance of 3 mm) at various sliding forces (2, 4, 8 and 10N) under anodic applied potential 0.001 V from the open circuit potential (OCP) and sliding speed 2 mm/s.

- 2- Linear motion of 4 mm Si₃N₄ ball on the carbon steel surface (distance of 3 mm) at the selected potentials (-0.3, -0.1, 0, 0.1 and 0.3 V vs OCP) following the measured polarization curves under a load 10 N and sliding speed 2 mm/s.

Before conducting the tribo-corrosion tests, the steel samples were immersed in the brine and various WBEs, for an hour to reach a steady OCP under their respective conditions. After a stable OCP, the current density evolution was recorded before, during and after the sliding wear process to investigate the effect of sliding force and potentials on the tribo-corrosion behavior of the carbon steel tested in different WBEs. Meanwhile, the evolution of COF as a function of sliding time was monitored during the tribo-corrosion experiments. EIS technique was employed after conducting potentiostatic experiments to investigate the effect of mechanical wear on the electrochemical behavior of steel immersed in different WBEs at various levels of applied forces and potentials. EIS was carried out at OCP with an alternating current (AC) amplitude of ± 10 mV over 100 kHz to 10 mHz. The potentiodynamic polarization tests were performed at a scan speed of 0.4 mV/s between potentials of -250 mV to +250 mV around the OCP for each sample under tribo-corrosion conditions.

After the tribo-corrosion tests, the wear tracks of steel plates under various sliding forces and potentials were checked using an optical profilometer (Zegage 3D Middlefield model) to measure the total volume of wear tracks caused by tribo-corrosion. The specific wear rate (W) in $\mu\text{m}^3/\text{Nm}$ was calculated using equation (1) [180,263]:

$$W = \frac{V}{Fd} \quad (1)$$

where V , d and F represent the total volume loss (μm^3), the entire sliding distance (m) and the normal load (N), respectively. All worn surfaces' surface morphological features and chemical

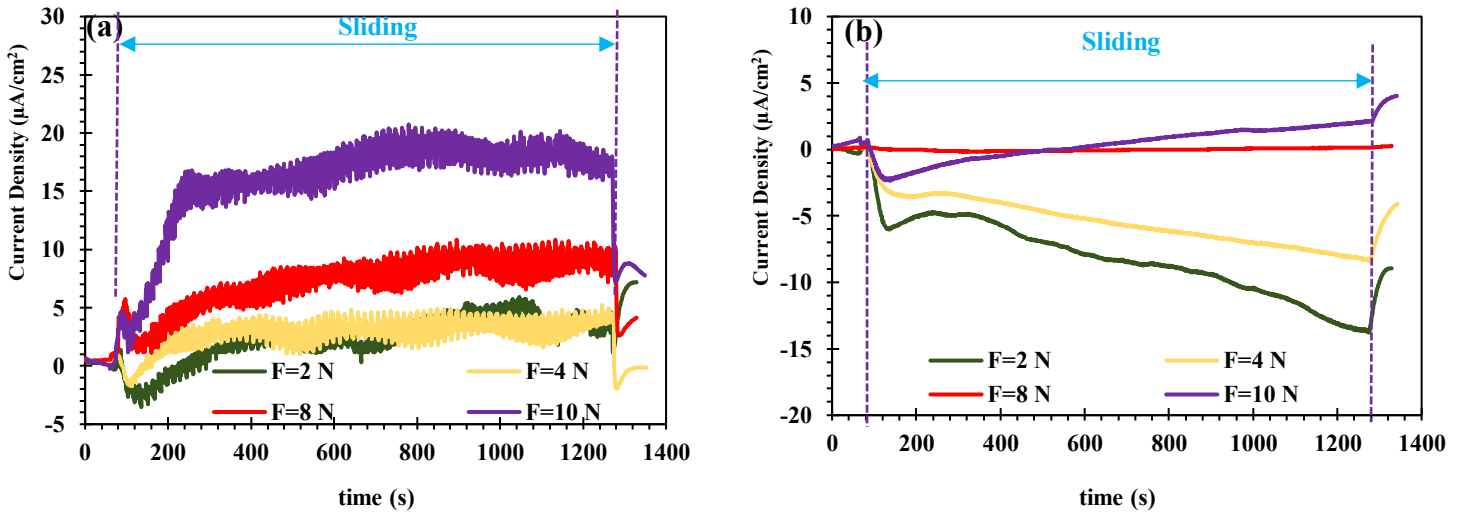
composition were characterized by field-emission scanning electron microscopy (FE-SEM) equipped with energy-dispersive X-ray spectroscopy (EDS) from Sigma, Germany. X-ray photoelectron spectroscopy (XPS, Kratos Axis Ultra model) was used to analyze further the chemical composition, chemical bonds and tribo-corrosion mechanisms of the steel samples tested in different solutions.

6.3 Results and discussion

6.3.1 Tribo-corrosion behavior under different sliding forces

6.3.1.1 Potentiostatic tribo-corrosion tests

Fig. 6.1. displays the current density evolution with time for 1018 carbon steels immersed in the brine and different WBEs with four various applied loads (2, 4, 8 and 10 N).



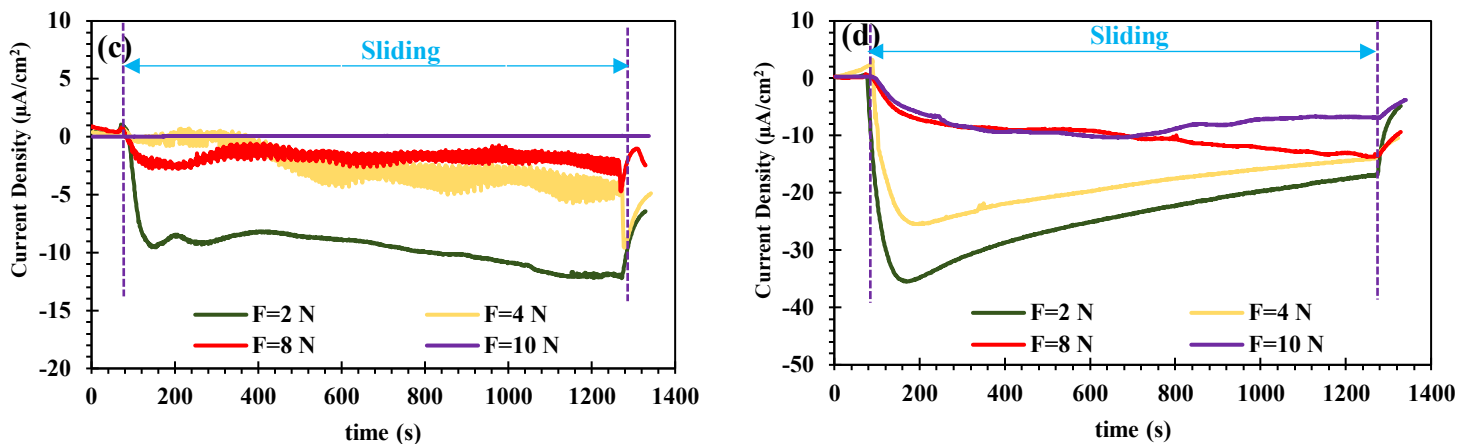


Fig. 6.1. Evolution of the current density versus the sliding time for carbon steel samples before, during and after potentiostatic tribo-corrosion tests in the (a) brine, (b) WBE (B1), (c) WBE (B2) and (d) WBE (B3) at different loads.

As shown in Fig. 6.1, before sliding, the current density values for the samples were negligibly close to zero over time, so that there was no considerable electrochemical reaction occurring on the steel surfaces. When sliding started, changes in current density values were observed under various applied forces for samples immersed in the brine solution and WBEs containing corrosion inhibitors. As shown in Fig. 6.1a, samples immersed in the brine solution under four applied loads experienced a sudden increase in current values as the sliding starts, followed by a decrease. The initial increase in current density values is likely due to the mechanical removal of the pre-formed oxide layer on sample surface or the anodic dissolution of worn surfaces. In contrast, the decrease in current density reflects the generation of a new oxide layer on the sample surface that acts as a barrier to limit further exposure to the corrosive solution. However, as the sliding continued, the oxide layer could become easily damaged or removed, leading to a second increase in current values. Conversely, for samples immersed in the solutions containing corrosion inhibitors, especially PEG-6 isotridecyl phosphate, a sharp decrease in current density values was monitored

with time, which was more pronounced at lower sliding forces. This observation illustrates the influential role of corrosion inhibitors in reducing the electrochemical reaction occurring on the steel surfaces during sliding by forming a protective film on the metal surface. Afterwards, the currents increased steadily with time due to the localized damage to the protective film during the tribo-corrosion experiments. Once the sliding stopped, the current density values for samples immersed in different solutions at four sliding forces approached the initial levels before sliding.

Fig. 6.1a-d also reveal the remarkable impact of sliding force on the tribo-corrosion behavior of steel samples immersed in the tested solutions. The minimum current density values were recorded at the lowest applied sliding force (2N) for different solutions. As the sliding force increased from 2 to 10 N, the current density values gradually increased and reached the maximum values: +16.9 μA in the brine solution, +2.06 μA in WBE (B1), +0.09 μA in WBE (B2) and -6.8 μA in WBE (B3), respectively. This shows that larger contact forces lead to increased corrosion, which can be attributed to increased mechanical wear and the increased contact area between the steel sample and the counterpart, resulting in more material loss.

6.3.1.2 Electrochemical impedance spectroscopy characterization

EIS tests were performed before and after applying different sliding forces on the surface of steel samples immersed in the brine solution and WBEs containing corrosion inhibitors to acquire useful information regarding the effect of force on the electrochemical behavior of the carbon steel. Fig. 6.2 exhibits the Nyquist plots measured after 1200 s sliding under applied forces, compared to non-loaded surfaces.

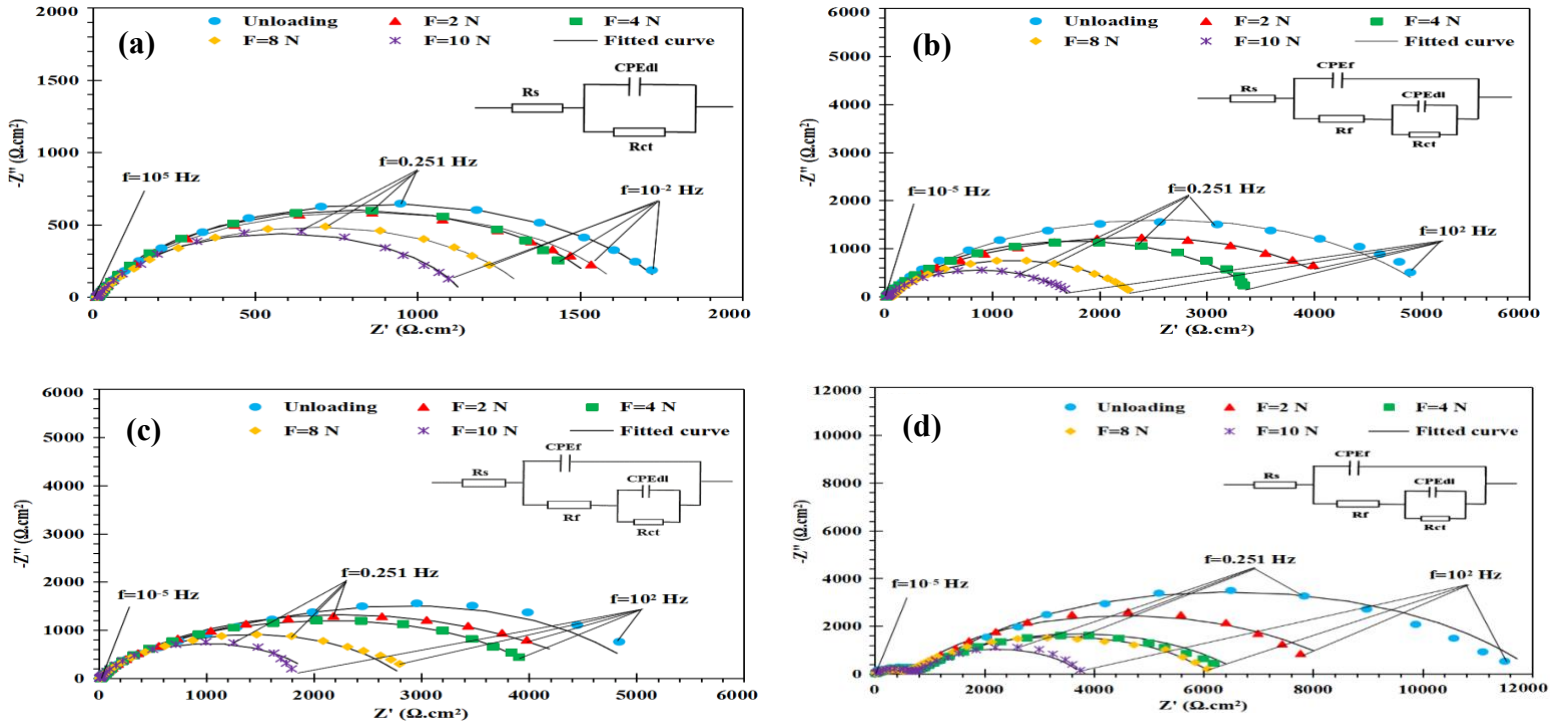


Fig. 6.2. Nyquist diagrams for carbon steel plates immersed in the brine solution (a), WBE (B1) (b), (c) WBE (B2) (c) and WBE (B3) (d), at loading and unloading conditions. The measured data point is depicted as certain marker styles, while solid curves show the fitted curves.

The recorded impedance spectra for steels immersed in various solutions exhibit imperfect semicircles with either one capacitive loop (brine solution) or two capacitive loops (WBEs) whose diameter decreases notably after applying sliding forces during the tribo-corrosion test. This reduction in diameter is increasingly pronounced, with an increase in contact force recorded during tests in all tested solutions. This reduction suggests potential damage to the oxide layer (brine solution), or protective layer (WBEs) formed on the worn surface, increasing the metal surfaces' active sites and thus decreasing their tribo-corrosion resistance. Comparing different solutions, only one time constant (double layer) can be observed in the Nyquist plot of steel immersed in a brine solution. In contrast, a new time constant appeared at a high frequency for samples tested in different WBEs, indicating a protective layer on the steel surface. The distinctive two times

constants are visible in Nyquist plots of the steel samples immersed in WBE (B3) for all contact forces, revealing an effective protective film formed on the worn surface. Different impedance parameters, including R_s (solution resistance), R_{ct} (charge transfer resistance), R_f (film resistance), R_t (total resistance), CPE_{dl} (constant phase element of a double layer), CPE_f (constant phase element of a film) and η (corrosion inhibition efficiency) were obtained by interpreting the EIS data with equivalent electrical circuits shown in Fig. 6.2 and are reported in Table 6.2.

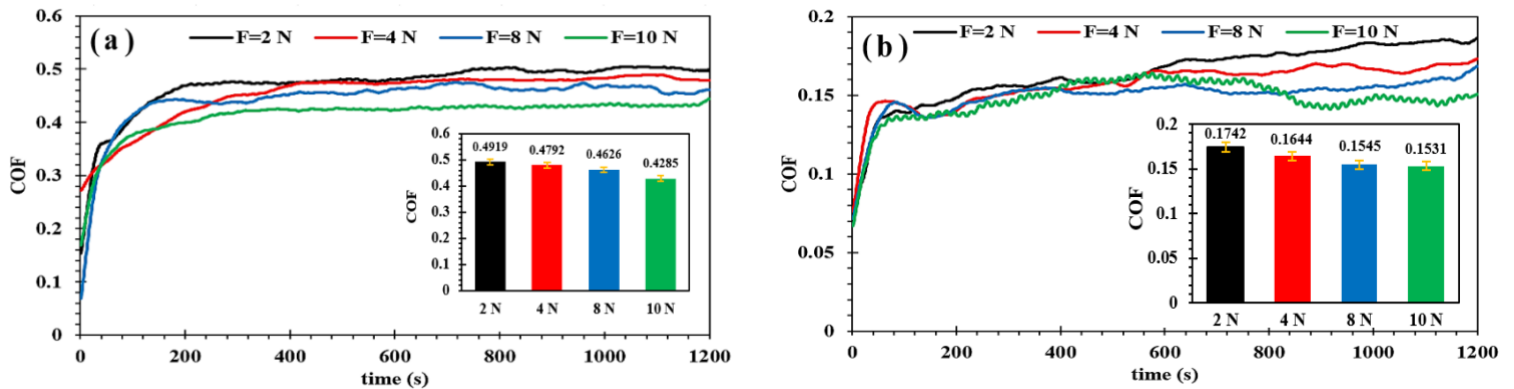
Table 6.2 Electrochemical parameters extracted from impedance data for the carbon steel samples immersed in the brine solution and various WBEs at different sliding forces.

Solution	Force (N)	R_{ct} ($K\Omega.cm^2$)	CPE_{dl}		R_f ($K\Omega.cm^2$)	CPE_f		$R_t=(R_{ct}+R_f)$ ($K\Omega.cm^2$)	η %
			Y_0 ($\Omega^{-1}.cm^{-2}$)	n		Y_0 ($\Omega^{-1}.cm^{-2}$)	n		
Brine	0	1.78	507.2×10^{-6}	0.79	-	-	-	1.78	-
	2	1.59	636.7×10^{-6}	0.81	-	-	-	1.59	-
	4	1.57	705.7×10^{-6}	0.83	-	-	-	1.57	-
	8	1.38	720.7×10^{-6}	0.79	-	-	-	1.38	-
	10	1.13	796.1×10^{-6}	0.83	-	-	-	1.13	-
WBE (B1)	0	5.14	133.5×10^{-6}	0.71	0.030	510.9×10^{-9}	0.98	5.17	66
	2	4.22	133.1×10^{-6}	0.78	0.024	25.2×10^{-6}	0.72	4.24	63
	4	3.49	147.1×10^{-6}	0.76	0.020	38.32×10^{-6}	0.70	3.51	55
	8	2.32	263.5×10^{-6}	0.76	0.017	70.01×10^{-6}	0.68	2.34	41
	10	1.75	400.6×10^{-6}	0.79	0.012	182.8×10^{-6}	0.71	1.76	36
WBE (B2)	0	5.49	100.0×10^{-6}	0.90	0.040	21.5×10^{-6}	0.68	5.43	68
	2	4.87	170.7×10^{-6}	0.74	0.030	71.18×10^{-6}	0.58	4.9	67
	4	4.14	187.1×10^{-6}	0.72	0.027	26.6×10^{-6}	0.76	4.17	62
	8	2.82	233.3×10^{-6}	0.73	0.021	5.1×10^{-6}	0.97	2.84	51
	10	2.01	355.5×10^{-6}	0.79	0.018	76.32×10^{-6}	0.73	2.02	44
WBE (B3)	0	11.17	65.7×10^{-6}	0.70	0.91	1.91×10^{-6}	0.72	12.08	85
	2	7.92	80.5×10^{-6}	0.74	0.86	15.7×10^{-6}	0.49	8.78	82
	4	6.22	118.3×10^{-6}	0.66	0.81	4.18×10^{-6}	0.64	7.03	78
	8	5.74	148.6×10^{-6}	0.64	0.65	1.90×10^{-6}	0.73	6.39	78
	10	3.70	175.1×10^{-6}	0.74	0.67	1.71×10^{-6}	0.76	4.37	74

Table 6.2 summarizes that how the increase in contact force resulted in the reduction of R_{ct} and R_t for all samples immersed in the tested solutions. The minimum resistance values (R_{ct} , R_f , R_t) were obtained at higher contact forces, indicating an increase in the severity of the tribo-corrosion process due to higher contact pressure between the steel surface and ball in various solutions, which can lead to increased electrochemical activity. In addition, the highest and lowest inhibition efficiencies (η) were obtained for samples tested under unloading conditions and a force of 10 N, respectively. According to Table 6.2, the incorporation of three corrosion inhibitors into the solutions, compared to the brine solution, resulted in higher resistance values under all contact forces under study, demonstrating their effectiveness in reducing the severity of the tribo-corrosion process and providing protection to the steel surface against both mechanical wear and chemical corrosion. PEG-6 isotridecyl phosphate showed the best performance among the corrosion inhibitors, with the highest resistance values (R_{ct} , R_f , R_t) and corrosion inhibition efficiency values obtained.

6.3.1.3 Friction and wear study

Variations in COF and average COF values of the samples under different contact forces are shown in Fig. 6.3.



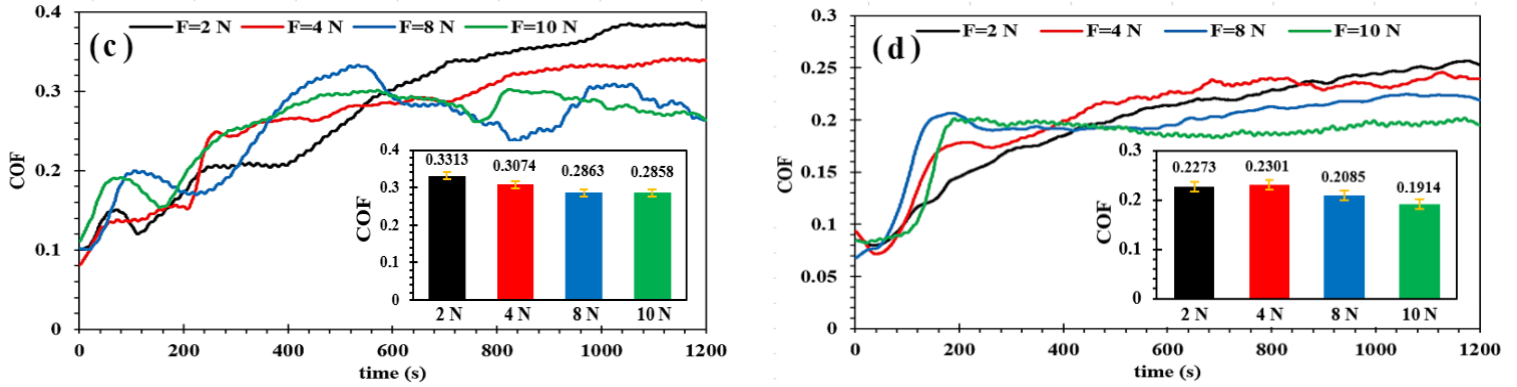


Fig. 6.3. Variations in COF versus sliding time and average COF values for (a) brine solution, (b) WBE (B1), (c) WBE (B2) and (d) WBE (B3) under different contact forces 2, 4, 8 and 10 N.

According to Fig. 6.3, COF displayed a similar decreasing trend with increasing sliding forces in all solutions. Increasing the contact force enhances the contact points between the steel surface and the Si_3N_4 ball. This leads to a larger contact area and more interactions between two surfaces. Thus, when more interactions occur between the two surfaces, the interfacial energy barrier can be reduced, ultimately reducing COF. Fig. 6.3a shows that as the applied force enhanced from 2 to 10 N, the average COF values for the tested samples in the brine solution decreased from 0.49 to 0.42. The addition of corrosion inhibitors largely reduced the average COF values of carbon steel in various WBEs (Fig 6.3b-d). For WBE (B1), the average COF values decreased from 0.17 to 0.15 as the force increased from 2 to 10 N; while for WBE (B2) and WBE (B3), the average COF values decreased from 0.33 to 0.28 and from 0.22 to 0.19, respectively.

After tribo-corrosion tests, we utilized the 3D optical profilometer to measure the total volume losses and specific wear rate of the steel samples tested in the different solutions under applied forces (Fig. 6.4). The results present that the total volume loss and specific wear rate of steels immersed in the WBEs containing corrosion inhibitors, especially WBE (B3), were noticeably lower compared to those tested in the brine solution alone. This finding may be ascribed

to the robust lubrication effect of the corrosion inhibitors, which facilitate the development of a molecular protective film on the surface of the steel. This protective film can reduce the volume loss and wear rate, as depicted in Figure 6.4a-d. Similarly, the best anti-wear performance was observed at the lowest contact force of 2 N, with the minimum values of total volume loss and specific wear rate. The results confirm that the wear resistance of samples immersed in all tested solutions can be weakened by increased contact forces, as indicated by the increased volume loss and wear rate. This observation is likely due to the higher contact pressure between the sliding surfaces at higher applied forces, leading to more significant deformation and damage to the worn surface. Therefore, the electrochemical reactions between the surfaces and the environment can be intensified, causing an increase in the material removal or wear, and corrosion rate, which is consistent with the electrochemical data recorded in Figures 6.1 and 6.2.

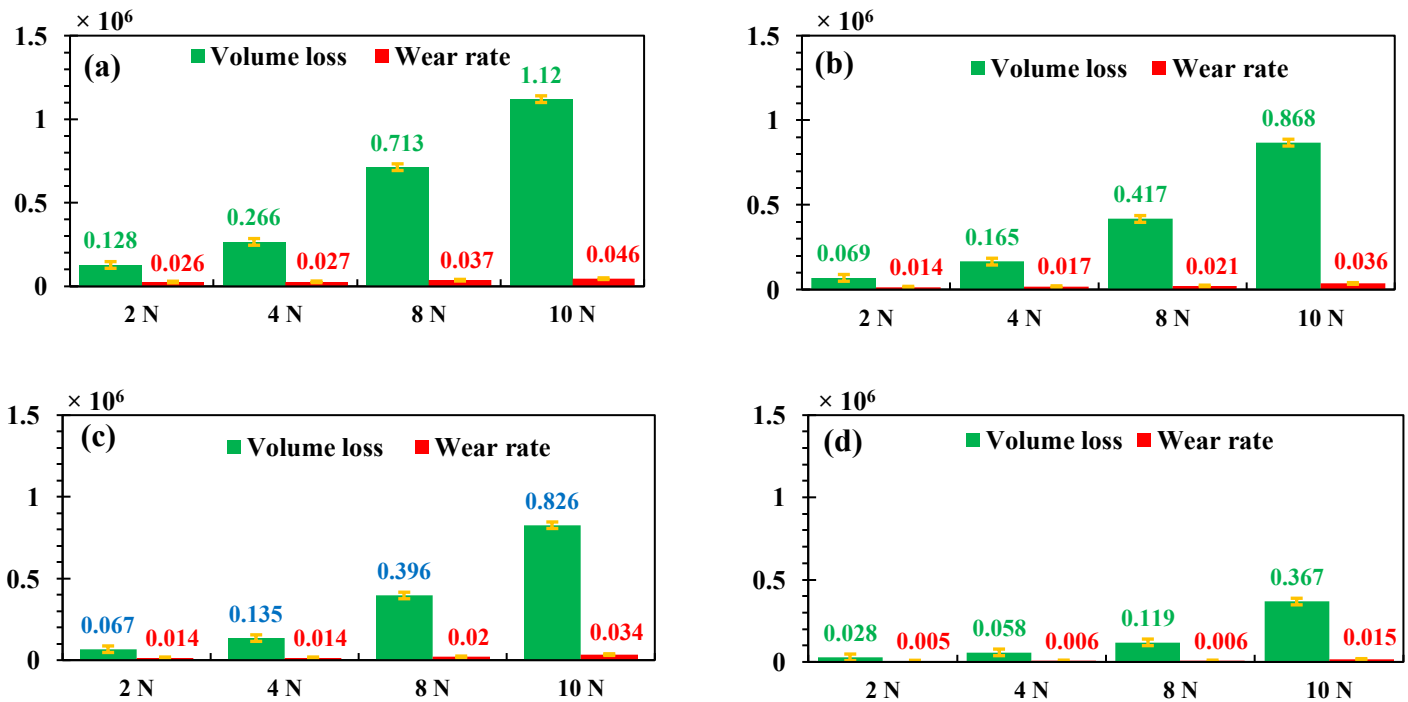


Fig. 6.4 Total volume losses (μm^3) and specific wear rate ($\mu\text{m}^3/\text{Nm}$) of samples worn in the brine solution (a), WBE (B1) (b), WBE (B2) (c), and WBE (B3) (d) under four different contact forces.

6.3.1.4 Wear-corrosion synergy

The combined effect of corrosion and wear can markedly impact material removal. Eq. (2) can be used to examine the synergy between wear and corrosion [264].

$$Vt = Vw + Vc + Vs \quad (2)$$

Where the total volume loss of steel samples (Vt) is determined as the sum of material loss caused by the pure wear (Vw), the material loss caused by the pure corrosion (Vc), and the material loss resulting from synergism (Vs), Vt and Vw were obtained by optical profilometer after test in various solutions (Table 6.1) and a solution like WBE (B3) where DI replaced the corrosive brine component to remove electrochemical reaction occurring within wear track, respectively; meanwhile, Faraday's law according to Eq. (3) was employed to calculate Vc [259, 265].

$$Vc = \frac{i t M}{nF\rho} \quad (3)$$

where i, t, M, n, F, ρ is defined as the current density (A), sliding time (s), the atomic mass of the metal, charge number that participated in the corrosion process, Faraday constant (C.mol⁻¹) and density of iron (g/cm³), respectively. Table 6.3 lists the calculated results for each component.

Table 6.3 Summary of various volume loss components for 1018 carbon steel caused by tribo-corrosion tests under applied forces (2, 4, 8 and 10 N) in different solutions.

Solution	Force (N)	Vt × 10 ⁻⁶ (μm ³)	Vw × 10 ⁻⁶ (μm ³)	Vc × 10 ⁻⁶ (μm ³)	Vs × 10 ⁻⁶ (μm ³)	Vc/Vw	Dominated degradation mechanism
Brine	2	0.128	0.014	0.007	0.107	0.5	Wear-corrosion
	4	0.266	0.040	0.007	0.219	0.18	Wear-corrosion
	8	0.713	0.057	0.007	0.649	0.12	Wear-corrosion
	10	1.12	0.230	0.007	0.883	0.03	Wear
WBE (B1)	2	0.069	0.014	0.003	0.052	0.21	Wear-corrosion
	4	0.165	0.040	0.003	0.122	0.08	Wear

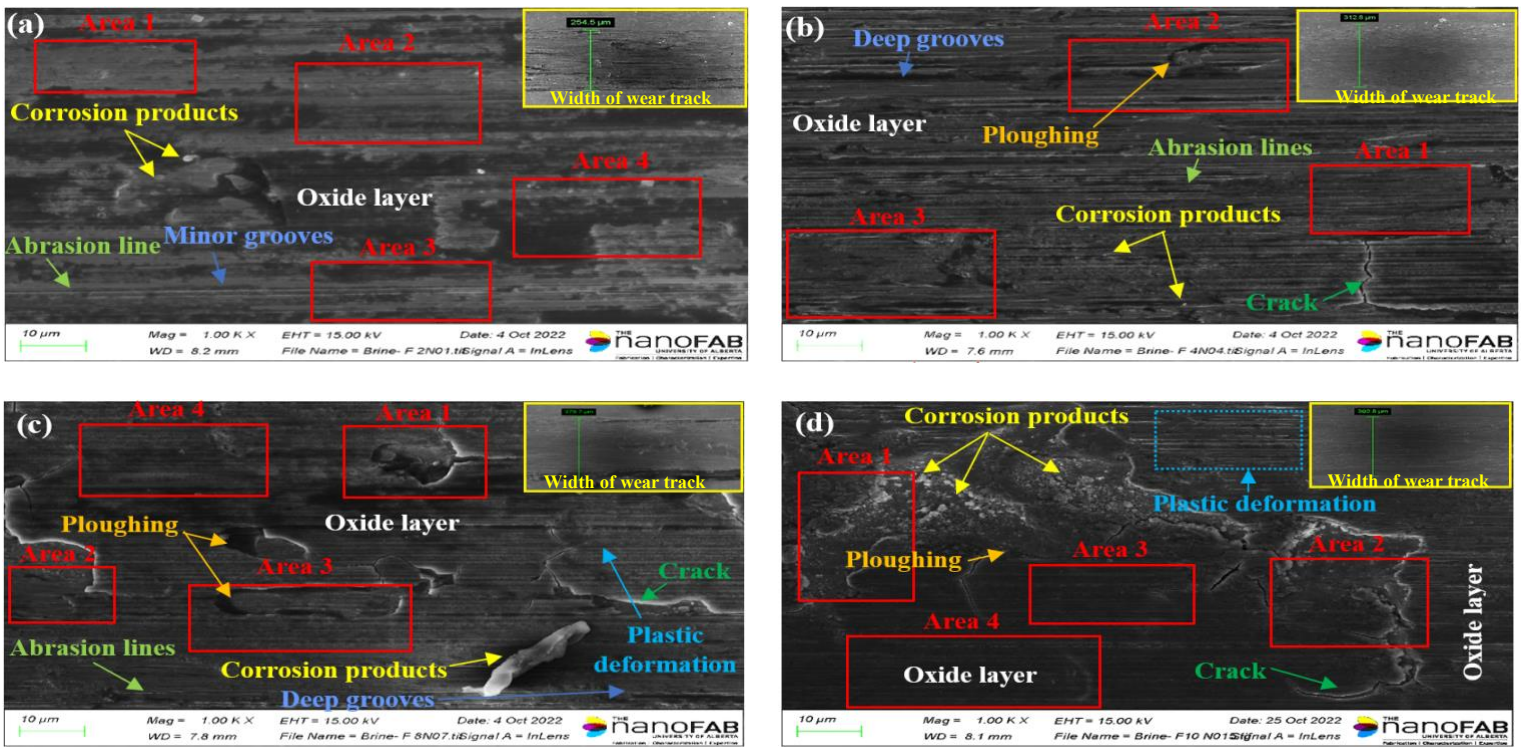
	8	0.417	0.057	0.003	0.357	0.05	Wear
	10	0.868	0.230	0.003	0.635	0.01	Wear
WBE (B2)	2	0.067	0.014	0.002	0.051	0.14	Wear-corrosion
	4	0.135	0.040	0.002	0.093	0.05	Wear
	8	0.396	0.057	0.002	0.337	0.03	Wear
	10	0.826	0.230	0.002	0.594	0.008	Wear
WBE (B3)	2	0.028	0.014	0.001	0.013	0.07	Wear
	4	0.058	0.040	0.001	0.017	0.02	Wear
	8	0.119	0.057	0.001	0.061	0.01	Wear
	10	0.367	0.230	0.001	0.136	0.004	Wear

According to Table 6.3, at an applied force of 2 N, the lowest value of V_s component was obtained for the steel sample immersed in different solutions: 0.107 for brine, 0.052 for WBE (B1), 0.051 for WBE (B2), and 0.013 for WBE (B3). The increased contact force enhanced the synergistic effect for all tested solutions. The corresponding values of the increment in V_s due to the synergy effect between wear and corrosion at 10 N are 0.883, 0.635, 0.594, and 0.136 for brine, WBE (B1), WBE (B2), and WBE (B3), respectively. As for the V_c/V_w ratio [30, 266], it is observed that at the lowest contact force, the dominant mechanism for the material loss is corrosion-accelerated wear for brine solution, WBE (B1) and WBE (B2). This suggests that the corrosion reactions at the steel-environment interface was active, which accelerated the wear process. However, for WBE containing PEG-6 isotridecyl phosphate, the dominant mechanism was mainly wear, since PEG-6 isotridecyl phosphate effectively reduced the corrosion reaction of the steel surface with the corrosive environment, which is consistent with the results of the potentiostatic test (Fig. 6.1). As the contact force increased, the material loss in brine solution, WBE (B1) and WBE (B2) were more caused by wear. This is attributed to the fact that, under higher forces, the mechanical wear increased and became dominant over corrosion. For WBE (B3),

the dominant mechanism under different contact forces remained wear, since the PEG-6 isotridecyl phosphate was effective in suppressing corrosion, while V_w , due to greater contact pressure, was also increasing. As a result, the V_c/V_w ratio decreased with increasing the contact force as shown in Table 6.3.

6.3.1.5 Surface morphology and elemental composition analysis of wear track

The morphology and elemental composition of the wear tracks after tribo-corrosion tests in the brine solution and WBE (B3) under different applied forces were examined by SEM-EDS. Fig. 6.5 and 6.6 present the SEM micrographs and EDS analysis taken from the wear track after tribo-corrosion experiments on samples immersed in brine solution and WBE (B3) under different forces of 2, 4, 8 and 10 N.



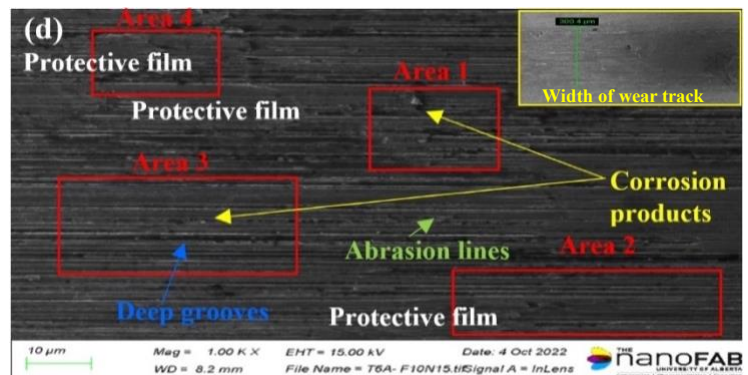
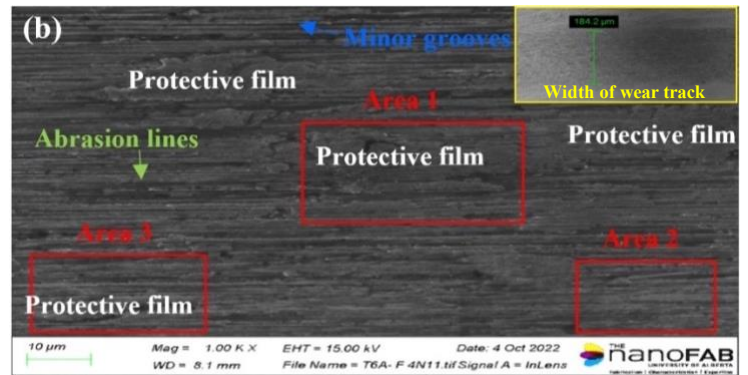
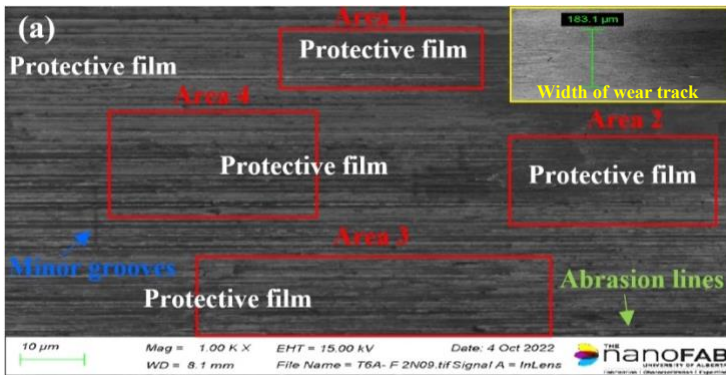
Brine solution		Fe	O	C	Mn	K	Cl
Force = 2 N	Area 1	87.38	3.75	8.34	0.37	0.14	0.04
	Area 2	88.93	1.24	8.92	0.66	0.10	0.14
	Area 3	88.76	1.02	9.35	0.73	0.00	0.14
	Area 4	87.27	2.79	9.56	0.17	0.15	0.06
Force = 4 N	Area 1	86.91	4.71	8.03	0.13	0.13	0.10
	Area 2	85.90	6.41	6.99	0.40	0.27	0.03
	Area 3	86.82	3.42	7.35	0.38	0.08	0.15
Force = 8 N	Area 1	75.59	13.72	9.95	0.14	0.08	0.52
	Area 2	72.43	14.70	11.38	0.34	0.03	1.12
	Area 3	77.31	11.50	10.51	0.19	0.23	0.25
	Area 4	77.10	12.53	9.06	0.18	0.00	1.13
Force = 10 N	Area 1	80.9	11.60	6.84	0.05	0.00	0.62
	Area 2	83.35	9.29	6.69	0.13	0.11	0.42
	Area 3	70.45	17.74	10.04	0.46	0.10	1.21
	Area 4	75.75	16.07	7.35	0.10	0.16	0.57

Fig .6.5 SEM images and EDS data of worn surfaces tested in brine solution at different sliding forces (a) 2 N, (b) 4 N, (c) 8 N, and (d) 10 N.

For the sample tested in the brine solution at 2 N, visible minor grooves can be seen in the wear track, indicating the occurrence of abrasive wear, which was caused by asperities on the Si₃N₄ ball and particles of wear debris inside the wear track. The results also display that fewer corrosion products were present on the worn surface under a force of 2 N, as shown in Fig. 6.5a. However, as the contact force was increased, deeper grooves, microcracks, ploughing, more obvious abrasion, and plastic deformation were observed on the worn surface. The widened area of wear track covered by corrosion products and oxide layer, which was more pronounced when tested under 10 N (Fig. 6.5b-d). The morphology of cracks showed that the oxide layer formed on the worn surface was brittle, making it more susceptible to flaking-off. In addition, the width of wear track increased from 254.5 μm to 392.8 μm as the contact force was increased from 2 to 10 N, showing an increase in the contact area which can considerably affect the tribo-corrosion behavior of steels. The obtained SEM micrographs are consistent with the data presented in sections 3.1.1

to 3.1.4. The EDS analysis of the regions identified in Fig. 6.6a-d reveals that the oxide layer formed on the wear track is mainly composed of iron oxyhydroxide (FeOOH) due to its high concentration of oxygen and iron [267]. The amount of oxygen on the worn surface increased with increasing the contact force (from 1.02-3.75 wt.% at 2 N to 9.29-17.74 wt.% at 10 N), indicating that more worn surface area was oxidized during the tribo-corrosion test. This oxide layer formed within the wear track is highly vulnerable to wear-induced damage in a corrosive medium. Moreover, the content of chloride and potassium as corrosive ions also increased with increasing the contact force, suggesting that more corrosive ions were gathered as the contact force increased. Thus, it can be inferred that the increase in the contact force can promote the tribo-corrosion process with more severe material degradation.

SEM-EDS results for the worn surfaces immersed in WBE (B3) under various sliding forces are presented in Fig. 6.6.



WBE (B3)		Fe	O	C	P	Mn	K	Cl
Force = 2 N	Area 1	75.52	11.67	12.25	0.55	0.00	0.00	0.02
	Area 2	88.76	4.20	6.29	0.32	0.41	0.01	0.00
	Area 3	88.93	2.52	7.39	0.33	0.81	0.02	0.00
	Area 4	91.88	1.73	5.41	0.24	0.75	0.00	0.00
Force = 4 N	Area 1	83.40	7.50	8.04	0.54	0.45	0.00	0.06
	Area 2	89.35	2.20	7.12	0.43	0.86	0.01	0.03
	Area 3	89.48	1.87	7.91	0.13	0.61	0.00	0.00
Force = 8 N	Area 1	85.63	3.66	9.84	0.17	0.57	0.04	0.10
	Area 2	91.62	0.76	7.14	0.13	0.22	0.00	0.12
	Area 3	88.70	0.88	9.18	0.21	0.92	0.00	0.12
	Area 4	83.34	4.68	11.43	0.25	0.17	0.00	0.14
Force = 10 N	Area 1	86.26	3.47	9.46	0.27	0.38	0.12	0.04
	Area 2	86.05	4.36	8.69	0.26	0.42	0.02	0.20
	Area 3	91.92	0.61	6.40	0.14	0.78	0.04	0.10
	Area 4	88.28	2.71	8.77	0.05	0.40	0.00	0.04

Fig .6.6 SEM images and EDS data of worn surfaces tested in WBE (B3) at different sliding forces (a) 2 N, (b) 4 N, (c) 8 N, and (d) 10 N.

Fig. 6.6 demonstrates a remarkable improvement in the anti-tribo-corrosion properties of the steel by adding the PEG-6 isotridecyl phosphate to the WBE. The wear track analysis revealed smooth surfaces with no signs of microcracks, ploughing, or deformation at all sliding forces. Additionally, the EDS data showed fewer corrosive ions inside the wear track, compared with those in the brine solution, indicating that the corrosion inhibitor protected against mechanical and chemical wear. According to the results, under lower applied forces, more considerable coverage of protective film was present on the worn surface of the steel, confirmed by higher concentrations of oxygen and phosphorous, compared to the situation under higher forces. Despite this, PEG-6 isotridecyl phosphate remained effective even under higher applied forces and provided marked protection against tribo-corrosion, as shown in Figs. 6.6c and 6.6d. It is also worth noting that with increasing the contact force, deeper grooves occurred on the wear track, and the width of the wear track increased from 183.1 μm at 2 N to 300.4 μm at 10 N. This may be ascribed to increased contact

pressure between the steel and the counter-face, which can lead to more material removal from the wear track.

To obtain detailed information on the chemical composition and functional group of the film resulting from PEG-6 isotridecyl phosphate, XPS analysis was conducted on the worn surface immersed in WBE (B3) under different forces after the tribo-corrosion test. Figs. 6.8 and 6.9 display the overall XPS spectra and the high-resolution deconvoluted spectra of P 2p, C 1s, O 1s, and Fe 2p_{3/2} signals from wear track obtained in WBE (B3) at 2 N and 10 N. The overall XPS spectrum of the worn surface immersed in the WBE (B3) reveals that the protective layer generated on the wear track includes P 2p, C 1s, O 1s, and Fe 2p. As shown in Fig. 6.7, the intensity of P 2p and O 1s peaks decreased with increasing the contact force, where the atomic percentage of P and O elements detected within the wear track decreased from (3.22% and 24.72%) at 2 N to (2.99% and 23.83%) at 10 N. This suggests that the increased contact force damaged the protective layer generated on the worn surface, thus decreasing the surface protection against wear and corrosion.

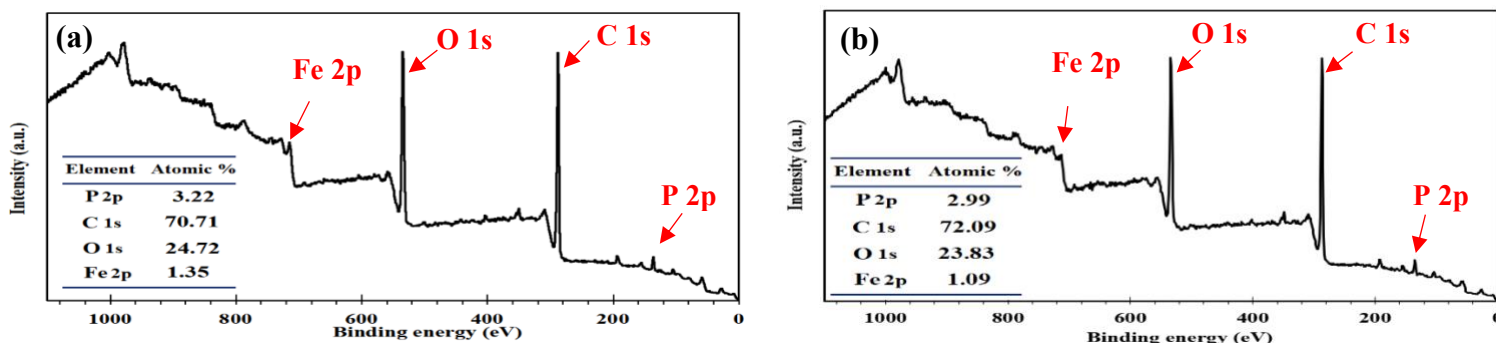


Fig. 6.7 XPS survey spectra of worn surface immersed in WBE (B3) at two different sliding forces (a) 2 N and (b) 10 N.

From Fig. 6.8a, it can be observed that deconvolution of P 2p region resulted in P=O (134.01 eV) and P-O (135.10 eV) bonds, which are indicative of the presence of phosphate compound formed in the wear track [236]. The C 1s spectrum (Fig. 6.8b) was deconvoluted into four peaks at binding

energies of 285.44, 286.19, 287.03, and 288.31 eV, corresponding to C-C, C-O-P, C-O-C, and C-O bonds, respectively. This observation confirms that the organic compounds in the PEG-6 isotridecyl phosphate successfully adsorbed onto the wear track during tribo-corrosion tests [237,268]. As presented in Fig. 6.8c, the peaks detected at binding energies of 530.31, 532.19, 533.70 and 535 eV in the O 1s spectrum also confirm the presence of Fe-O, P=O, C-O, and P-OH bonds on the worn surface [240,269]. Six peaks at different binding energies were identified after deconvolution analysis of the Fe 2p signal. The grafting of the corrosion inhibitor on the steel surface tested in WBE (B3) was verified by detecting the Fe-P bond at 707 eV for Fe 2p_{3/2} and 720.21 eV for Fe 2p_{1/2}. In addition, the appearance of two peaks at binding energies of 711.39 eV (Fe 2p_{3/2}) and 724.79 eV (Fe 2p_{1/2}) can be ascribed to the presence of iron oxidized species, such as Fe₂O₃ and Fe-OH, resulting from surface oxidation during sliding process. Two satellite peaks for Fe 2p_{3/2} and Fe 2p_{1/2} can be observed at 714.29 eV and 727.53 eV, respectively [114,270].

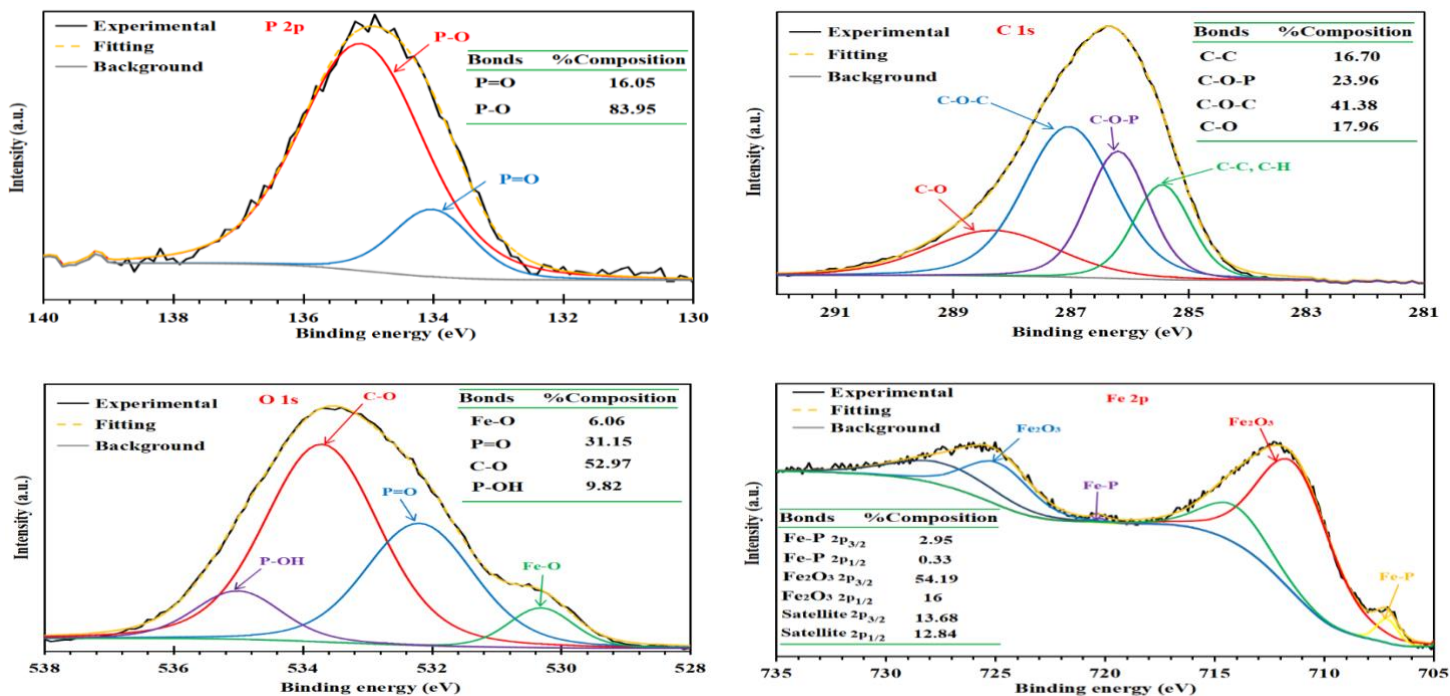


Fig. 6.8 High-resolution XPS spectra of worn surface tested in WBE (B3) at 2 N for P 2p, C 1s, O 1s and Fe 2p.

6.3.1.6 Tribo-corrosion mechanism under different forces

Fig. 6.9 depicts a schematic representation of the tribo-corrosion mechanism of 1018 carbon steel in a brine solution and WBE (B3), studied through SEM-EDS and XPS analysis of wear track. When the steel samples were tested in the brine solution, an oxide film of Fe_2O_3 and Fe-OH formed on the carbon steel surface under the static condition. However, once the sliding process starts, the oxide film on the steel can be damaged or removed, exposing a new metal surface to tribo-corrosion. As shown in Fig. 6.9a, shallow abrasion lines and minor grooves formed inside the wear track at a sliding force of 2 N. As the contact force applied on the steel surface increased to 8 and 10 N, the mechanical stress on the surface intensified, leading to plastic deformation and different forms of surface damage to the steel, such as microcracks, ploughing, deep groove, and abrasive lines (Fig. 6.9a). These surface damages can act as active sites to promote corrosion in the wear track. As depicted in Fig. 6.9a, more chloride ions can penetrate exposed metallic areas on the worn surface under higher contact forces, generating and accumulating corrosion products, consistent with SEM-EDS results (Figs. 6.8c and 6.8d). The increased mechanical stress can increase wear debris formation, which reacts with the electrolyte to form oxide particles that act as abrasive particles, causing more damage to the steel surface. In addition, the width of the wear track increased with increasing contact force, providing more sites for corrosion, resulting in an increase in the wear track's electrochemical activity. Consequently, the combined actions including increased mechanical wear, changes in electrochemical activities, and increased exposure surface area under larger contact forces can cause more delamination, increased material loss and a decrease in the corrosion resistance of the carbon steel in the brine solution (Figs. 6.1, 6.2 and 6.4).

The presence of corrosion inhibitors in the drilling fluid, particularly PEG-6 isotridecyl phosphate, can notably improve the tribo-corrosion performance of steel under different applied forces due to the generation of a protective layer on the steel surface. As shown in Fig. 6.9b, PEG-6 isotridecyl phosphate can be adsorbed on the steel surface through physisorption (electrostatic interaction) or chemisorption (share their lone pair electrons of heteroatoms such as N, O, and P with unoccupied orbitals of iron atoms). This corrosion inhibitor-induced protective film not only restricts the penetration of corrosive ions to the surface of carbon steel but also decreases the direct contact between mutual surfaces, where no signs of plastic deformation, ploughing, and microcracks were observed under different applied forces (Fig. 6.6). Moreover, the number of corrosion products detected within the wear track was considerably lower than those immersed in the brine solution.

However, increasing the contact force can harm the tribo-corrosion resistance of carbon steel immersed in WBE (B3) as it can lead to more severe mechanical wear and damage to the protective film formed on the worn surface.

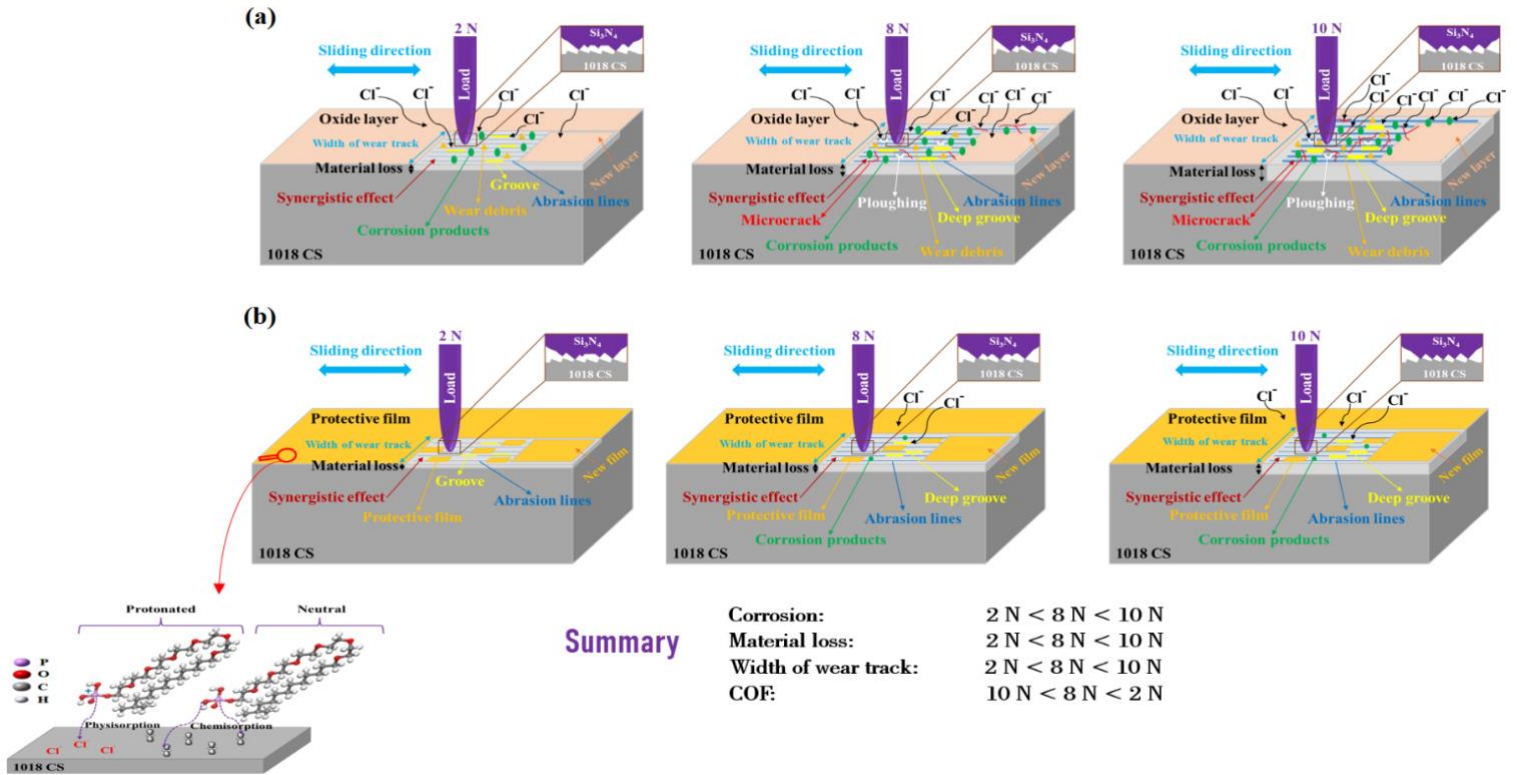


Fig. 6.9 Schematic diagram of the tribo-corrosion mechanism of carbon steel immersed in (a) brine solution and (b) WBE (B3) under different applied forces.

6.3.2 Tribo-corrosion behavior under different applied potentials

6.3.2.1 Potentiodynamic measurements

Fig. 6.10a displays variation in OCP for carbon steels immersed in brine solution and various WBEs under a sliding speed of 2 mm/s and a force of 10 N. Before sliding, the OCP values of all tested solutions depicted the steady state and the values for WBE containing corrosion inhibitors were more positive than that for the brine solution. During sliding, the OCP values for samples immersed in the brine, WBE (B1) and WBE (B2) dropped towards more negative values due to the damage or removal of protective film by the Si_3N_4 ball. However, a shift toward a positive direction was detected for the steel sample tested in WBE (B3), indicating the positive role of

PEG-6 isotridecyl phosphate in improving the tribo-corrosion resistance of carbon steel. After the sliding process, the OCP values shifted positively, which can be correlated to reforming the oxide layer (brine) or inhibitor-induced protective film (WBEs) within the wear track.

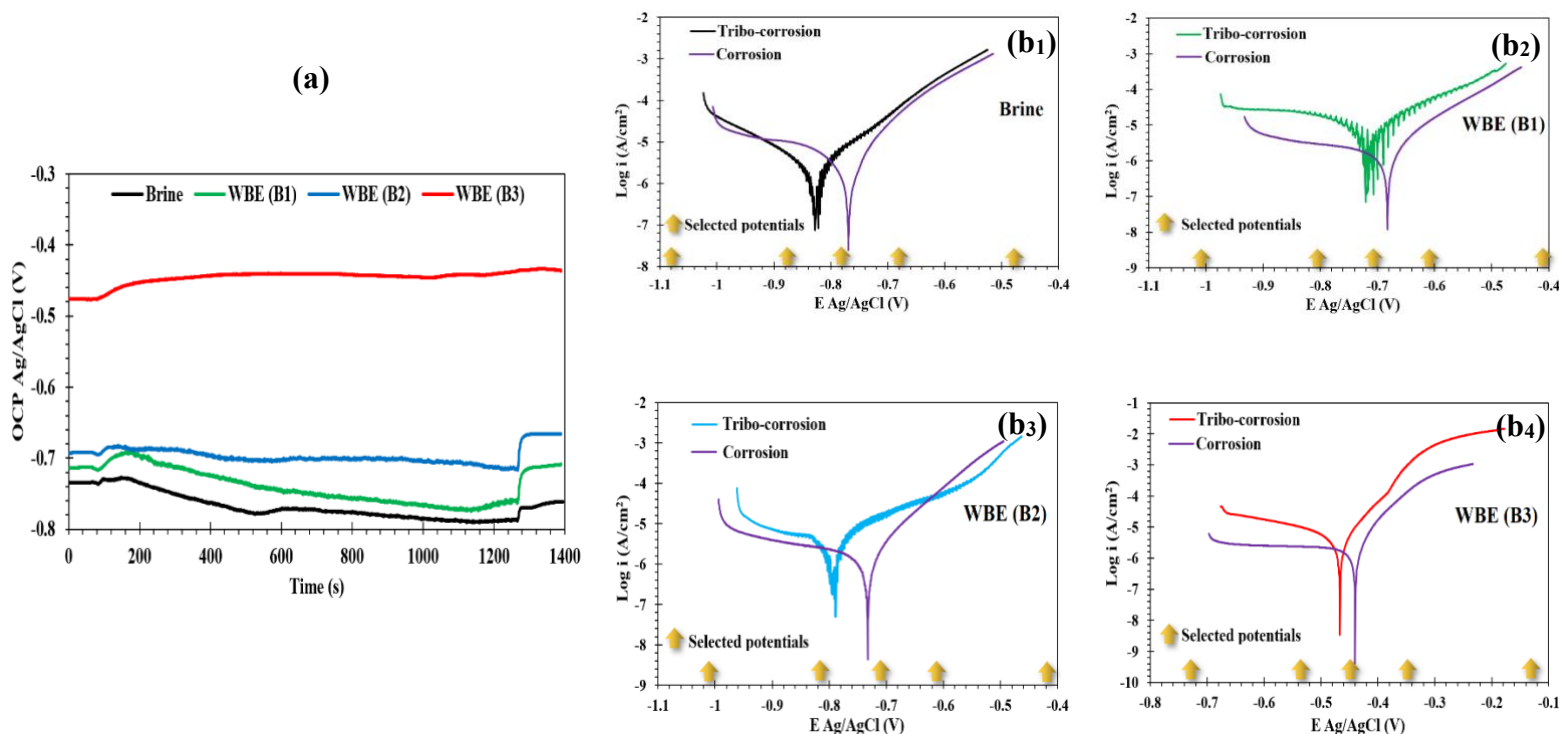


Fig. 6.10 The (a) OCP and (b1 to b4) potentiodynamic polarization curves for 1018 carbon steel in different solutions under 2 mm/s and 10 N.

As Fig. 6.10b₁-b₄ shows, tribological conditions and the addition of corrosion inhibitors affected the overall polarization behavior of steel samples in different solutions. Under corrosion conditions, corrosion inhibitors in different WBEs shifted the polarization curves towards more positive potentials (more anodic potentials) and lower current densities by affecting both anodic and cathodic branches of polarization curves. Therefore, corrosion inhibitors can reduce chloride ions' activity and permeability, enhancing carbon steel's corrosion resistance. Under tribo-corrosion conditions, the corrosion potentials monitored in different solutions moved towards

At the lowest applied potentials (-0.3 and -0.1 V vs OCP), where the steel samples immersed in all tested solutions were cathodic under corrosion and tribo-corrosion conditions, negative current densities were recorded before sliding due to the dominant cathodic reduction reaction of dissolved oxygen. The measured current density values remained negative during and after sliding, confirming that no corrosion occurred, and material loss measured can be ascribed to pure mechanical wear. From Fig. 6.11 a-d, more negative current values were detected for samples immersed in WBEs containing corrosion inhibitors, especially PEG-6 isotridecyl phosphate, than in brine solution. This demonstrates that corrosion inhibitors can affect cathodic reduction reactions in two different ways: by decreasing the rate of electron transfer through their adsorption onto the cathodic sites or by changing the reaction mechanism through engaging in chemical reactions with the reactants involved in the electrochemical process, resulting in a more negative current density. With the applied potential approaching 0 V (OCP), the current density increased positively and became positive during sliding for the steel specimen immersed in the brine solution. While a negative current density was also recorded for samples tested in the solutions loaded with corrosion inhibitors. This indicates that corrosion inhibitors could form an effective protective film on the metal surface at OCP, suppressing the anodic dissolution of the metal. When the potential was shifted towards anodic potentials (0.1 and 0.3 V), the onset of the sliding process led to a gradual increase in current density values, followed by stabilization during the subsequent sliding process, as presented in Fig. 6.11. The maximum current density values were measured at 0.3 V vs OCP, implying that anodic dissolution rate of samples was the highest at this potential. Furthermore, the increased current density values during the sliding process suggest the synergistic effect of wear and corrosion, resulting in more severe tribo-corrosion damage. However, the addition of corrosion inhibitors in the WBE caused a reduction in the anodic dissolution rate, thus

mitigating the tribo-corrosion damage, as confirmed by the lower current densities compared with that of samples tested in the brine solution.

6.3.2.3 EIS study

EIS experiments were conducted to investigate the change in the electrical properties of the electrode-electrolyte interface under controlled tribo-corrosion conditions. Fig. 6.12 illustrates the Nyquist plots of steel samples tested in different solutions at varying potentials.

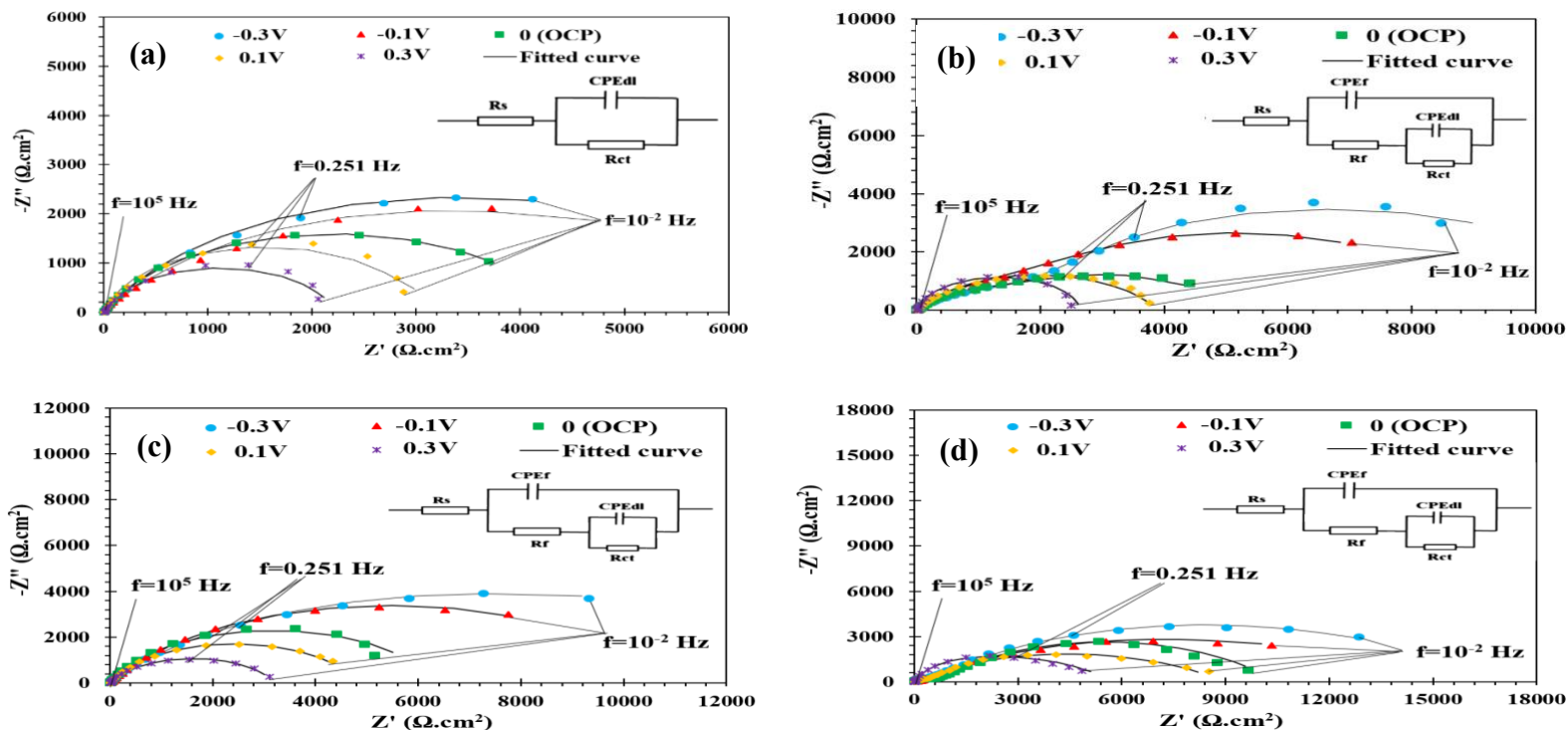


Fig. 6.12 Nyquist diagrams for carbon steel coupons immersed in the brine solution (a), WBE (B1) (b), (c) WBE (B2) (c) and WBE (B3) (d), at different applied potentials. The measured data point is depicted as certain marker styles, while solid curves show the fitted curves.

Fig. 6.12 shows that Nyquist plots are all semicircle arcs whose diameters depend on the applied potentials and the solution chemistry. The notable increase in arc diameters as the applied potential shifted from anodic to cathodic regions and in the presence of corrosion inhibitors indicates an increased impedance value of the steels under tribo-corrosion conditions. From Fig.

6.12, two time constants fitted into two RC equivalent electrical circuits were employed for steels immersed in different WBEs, demonstrating a protective film was generated at the steel-electrolyte interface due to the adsorption of corrosion inhibitor molecules. However, it was found that the steel sample tested in the brine solution had only one time constant, indicating the occurrence of a singular charge transfer process during the anodic dissolution of the carbon steel. Table 6.4 presents the quantitative electrical parameters extracted from EIS data for samples subjected to different applied potentials in the brine and various WBEs.

Table 6.4 Fitted results of EIS spectra for the carbon steel samples exposed to the brine solution and various WBEs at different applied potentials, force=10 N and sliding speed=2 mm/s.

Solution	Potential (V)	R_{ct} ($K\Omega.cm^2$)	CPE_{dl}		R_f ($K\Omega.cm^2$)	CPE_f		$R_t=(R_{ct}+R_f)$ ($K\Omega.cm^2$)	η %
			Y_0 ($\Omega^{-1}.cm^{-2}$)	n		Y_0 ($\Omega^{-1}.cm^{-2}$)	n		
Brine	-0.3	6.91	625×10^{-6}	0.79	-	-	-	6.91	-
	-0.1	6.24	593×10^{-6}	0.70	-	-	-	6.24	-
	0	4.40	837×10^{-6}	0.79	-	-	-	4.40	-
	+0.1	3.10	654×10^{-6}	0.90	-	-	-	3.10	-
	+0.3	2.20	591×10^{-6}	0.87	-	-	-	2.20	-
WBE (B1)	-0.3	9.12	124×10^{-6}	0.86	3.29	82.87×10^{-6}	0.55	12.41	44.3
	-0.1	6.18	192×10^{-6}	0.78	3.40	107.5×10^{-6}	0.66	9.58	34.9
	0	3.20	257×10^{-6}	0.86	1.78	173.5×10^{-6}	0.60	4.98	11.6
	+0.1	3.01	252×10^{-6}	0.98	0.80	191.2×10^{-6}	0.70	3.88	20.1
	+0.3	2.65	325×10^{-6}	0.90	0.002	477.8×10^{-6}	0.82	2.65	16.9
WBE (B2)	-0.3	14.89	80×10^{-6}	0.78	0.041	144.0×10^{-6}	0.55	14.93	53.7
	-0.1	10.85	104×10^{-6}	0.71	0.020	40.40×10^{-6}	0.71	10.87	42.6
	0	6.34	184×10^{-6}	0.80	0.014	51.14×10^{-6}	0.70	6.35	30.7
	+0.1	4.82	232×10^{-6}	0.79	0.008	80.96×10^{-6}	0.76	4.82	35.7
	+0.3	2.86	277×10^{-6}	0.90	0.003	241.4×10^{-6}	0.74	2.86	23.1
WBE (B3)	-0.3	16.17	47×10^{-6}	0.60	0.97	35.76×10^{-6}	0.48	17.14	59.7
	-0.1	14.28	52×10^{-6}	0.67	0.95	104.0×10^{-6}	0.33	15.23	59.1
	0	9.92	65×10^{-6}	0.62	0.74	10.38×10^{-6}	0.69	10.66	58.8
	+0.1	8.36	81×10^{-6}	0.67	0.68	45.40×10^{-6}	0.50	9.04	65.7
	+0.3	4.51	167×10^{-6}	0.88	0.005	80.79×10^{-6}	0.66	4.51	51.2

According to Table 6.4, the highest R_t values were observed for samples polarized at cathodic potentials (-0.3 and -0.1 V vs OCP), suggesting that reduction reactions of various species, such as dissolved oxygen, occurred in the electrolyte. The reduced concentration of dissolved oxygen in the electrolyte causes a decrease in the rate of corrosion reactions occurring on the steel surface. This is because reduction reactions of various species in the electrolyte consume electrons, which diminish their availability for other electrochemical reactions and ultimately slow down the corrosion process. However, as the applied potential increased, resistance values (R_{ct} , R_f , R_t) and corrosion inhibition efficiency (η) of steel specimens immersed in all the solutions decreased. The minimum corrosion resistance of steel samples was obtained at the highest applied anodic potentials (0.1 and 0.3 V vs OCP), implying that anodic reactions, such as metal oxidation, occurred rapidly on the surface of the steel. This leads to the breakdown of the oxide layer in brine solution or protective lubricating film in WBEs, increasing the corrosion rate of 1018 carbon steel. Table 6.4 also reveals that the addition of corrosion inhibitors in WBEs resulted in much higher corrosion inhibition of carbon steel in an aggressive environment.

6.3.2.4 The effect of electrochemical potential on wear and friction behavior

Fig. 6.13 shows the recorded changes in COF values during the tribo-corrosion tests, including the evolution of COF with sliding time and the average COF values at different applied electrochemical potentials.

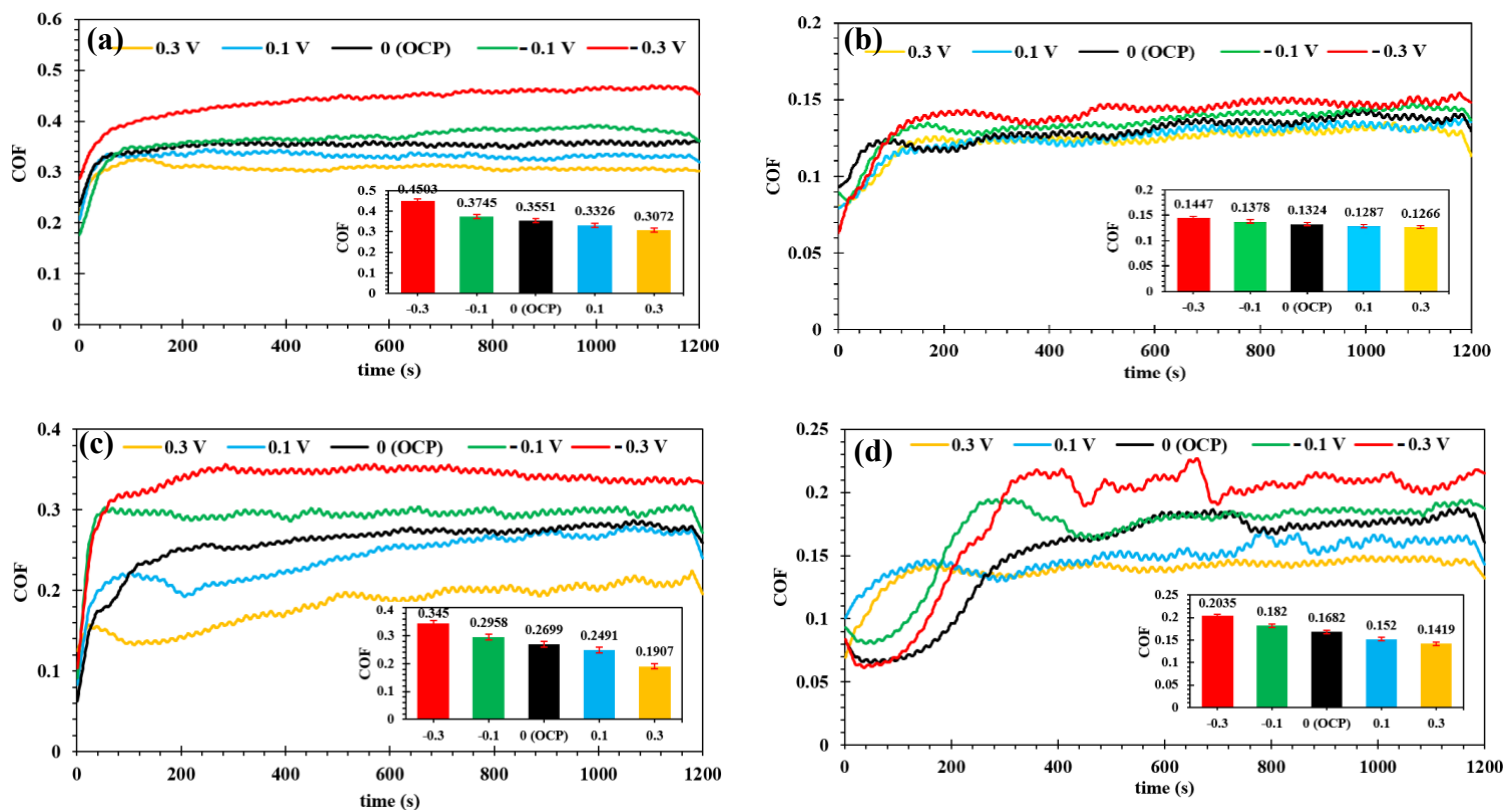
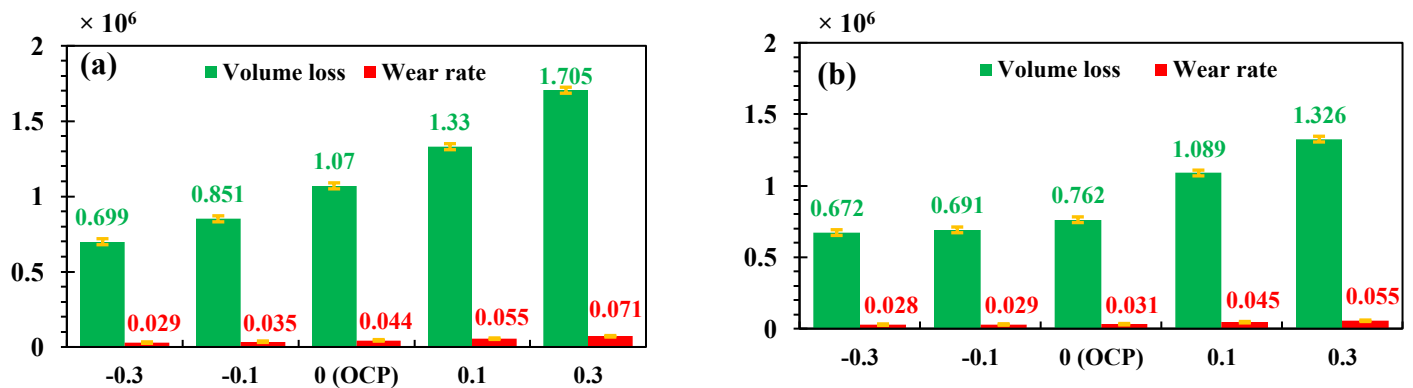


Fig. 6.13 Variations in COF versus sliding time and average COF values for (a) brine solution, (b) WBE (B1), (c) WBE (B2) and (d) WBE (B3) at different applied potentials.

According to Fig. 6.13, once sliding started under tribo-corrosion conditions, the COF values abruptly increased and reached a steady state with local fluctuations. Electrochemical potentials significantly affected the COF of carbon steels immersed in different solutions. The lowest COF values were achieved under the anodic potentials (0.30 in brine, 0.12 in WBE (B1), 0.19 in WBE (B2), and 0.14 in WBE (B3) at 0.3 V vs OCP, respectively). This reduction can be attributed to the release of ions during sliding at anodic conditions, which may lead to tribofilm deposition inside the wear track, thus preventing direct contact between rubbing surfaces. Furthermore, the roughness of the steel surface caused by corrosion and the formation of the pits, ploughs, and corrosion products decreases the real contact area between the steel and Si_3N_4 ball, giving lower friction at anodic potentials. Fig. 6.13 also illustrates that average COF values of steel

samples immersed in the tested solutions increased with the decrease in the applied potentials, where the maximum average COF was provided under cathodic potentials (0.45 in brine, 0.14 in WBE (B1), 0.34 in WBE (B2), and 0.20 in WBE (B3) at -0.3 V vs OCP, respectively). This may be due to the suppression of ions released under cathodic conditions, which prevents the formation of tribofilm on the worn surface.

After potentiostatic tribo-corrosion experiments, wear tracks generated under all the tested conditions were examined to measure total volume loss and specific wear rate, as shown in Fig. 6.14. The results illustrate that both total volume loss and specific wear rate gradually increased with applied potentials and the carbon steels tested in different solutions exhibited the lowest total volume loss and specific wear rate at the cathodic potentials (-0.3 and -0.1 V). This can be correlated to the negligible corrosion dissolution of steel samples at cathodic potentials, resulting in minimal wear rate and volume loss through mechanical wear. However, the corrosive attack during OCP and anodic potentials (0.1 and 0.3 V) caused an increase in material loss; thus, the combined effect of corrosion and wear resulted in a notable increase in volume loss and wear rate.



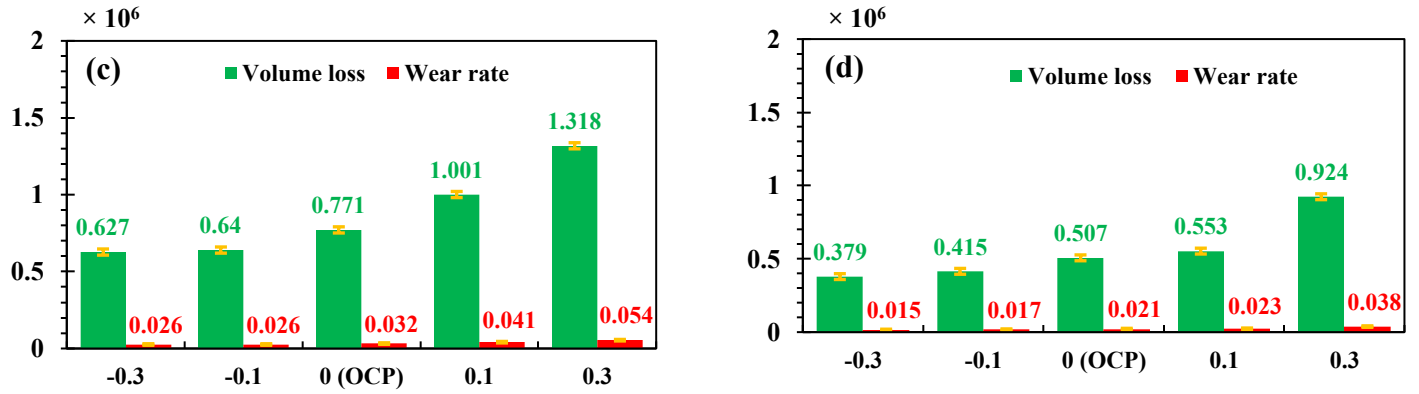


Fig. 6.14 Volume losses (μm^3) and specific wear rate ($\mu\text{m}^3/\text{Nm}$) of steel samples worn in the brine solution (a), WBE (B1) (b), WBE (B2) (c), and WBE (B3) (d) at different applied potentials.

6.3.2.5 Synergistic effect

As mentioned, increased electrochemical potential can contribute to the synergistic effect between wear and corrosion. Table 6.5 presents the quantitative calculation of various volume losses for 1018 carbon steel under different experimental conditions.

Table 6.5 Summary of different volume loss components for 1018 carbon steel at applied potentials of -0.3, 0, 0.1, and 0.3 V vs OCP after tribo-corrosion test in various solutions.

Solution	Potential (V vs OCP)	$V_t \times 10^{-6}$ (μm^3)	$V_w \times 10^{-6}$ (μm^3)	$V_c \times 10^{-6}$ (μm^3)	$V_s \times 10^{-6}$ (μm^3)	V_c/V_w	Dominated degradation mechanism
Brine	-0.3	0.699	0.379	~0	0.32	0	Wear
	0 (OCP)	1.070	0.379	0.065	0.626	0.17	Wear-corrosion
	0.1	1.330	0.379	0.093	0.858	0.25	Wear-corrosion
	0.3	1.705	0.379	0.179	1.147	0.47	Wear-corrosion
WBE (B1)	-0.3	0.672	0.379	~0	0.293	0	Wear
	0 (OCP)	0.762	0.379	0.022	0.361	0.06	Wear
	0.1	1.089	0.379	0.039	0.671	0.10	Wear-corrosion
	0.3	1.326	0.379	0.078	0.869	0.20	Wear-corrosion

	-0.3	0.627	0.379	~0	0.248	0	Wear
WBE (B2)	0 (OCP)	0.772	0.379	0.019	0.374	0.05	Wear
	0.1	1.003	0.379	0.038	0.586	0.10	Wear-corrosion
	0.3	1.318	0.379	0.073	0.866	0.19	Wear-corrosion
	-0.3	0.379	0.379	0	0	0	Wear
WBE (B3)	0 (OCP)	0.507	0.379	0.007	0.121	0.01	Wear
	0.1	0.553	0.379	0.016	0.158	0.04	Wear
	0.3	0.924	0.379	0.038	0.507	0.10	Wear-corrosion

In this study, V_w was obtained with a cathodic potential of -0.3 V and in the presence of PEG-6 isotridecyl phosphate (WBE (B3)) because the anodic corrosion reactions on the steel surface were inhibited and volume loss occurred by basically pure wear. The volume loss caused by pure corrosion at the cathodic potential (-0.3 V) can be neglected due to the minimal corrosion rate at this potential. However, when the applied potential was shifted towards the higher values, an increase in the magnitude of V_c was observed, especially in the brine solution. This is likely due to carbon steel's accelerated anodic dissolution rate at anodic potentials, intensifying the corrosion damage. Table 6.5 displays that the synergistic effect was enhanced by changing the potential from cathodic to anodic regions. This suggests the accelerated corrosion process under anodic potentials led to a more severe synergistic effect, resulting in greater total material loss. Regarding V_c/V_w [30,266], wear and corrosion-assisted wear played a dominant role in the tribo-corrosion performance of steel at different potentials. At -0.3 V, wear mainly dominated the degradation process of steels tested in all solutions. At OCP, the overlooked degradation mechanism for steel immersed in the brine solution changed to corrosion-accelerated wear. At the same time, there was no change in the degradation mechanism for WBEs, indicating the influence of corrosion inhibitors in suppressing corrosion inside the wear track at OCP. At the anodic applied potential of 0.3 V,

wear corrosion was determined as the dominant mechanism during the tribo-corrosion process for all tested solutions. It is worth noting that the terms V_c and V_s contributed to 0.10 % and 0.67 % of V_t for the brine solution, while these contributions were significantly reduced in the presence of corrosion inhibitors, to 0.05 % and 0.65 % for WBE (B2 and B3), 0.04 % and 0.54 % for WBE (B3), respectively.

6.3.2.6 Morphologies and component analysis of the worn surfaces

Figs. 6.15 and 6.16 show the SEM images and chemical composition taken of the wear tracks of steel samples in the brine solution and WBE (B3) at different applied potentials.

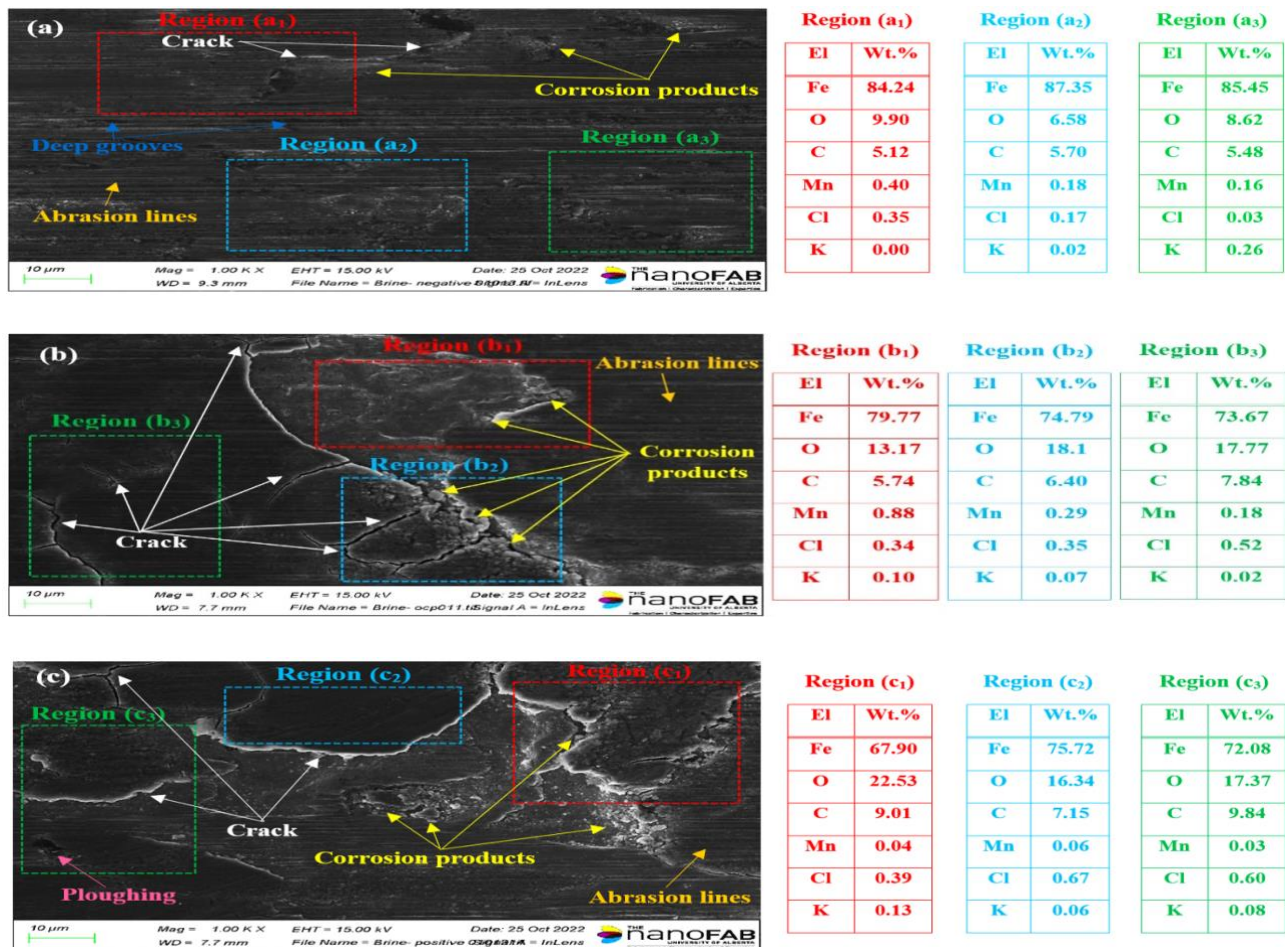


Fig. 6.15 SEM images and EDS data of worn surface experienced test in the brine solution at different applied potentials (a) -0.1 V, (b) 0 (OCP) and (c) +0.1 V.

The surface analysis of the abraded sample under -0.1 V cathodic potential showed that corrosion dissolution at this condition was negligible, and the rubbing effects on the worn surface were more pronounced than corrosion effects. This indicates that the steel degradation of carbon steel under cathodic polarization is mainly due to mechanical wear. In Fig. 6.15a, signs of scratches/grooves parallel to the sliding direction can also be observed in the wear track, indicating the wear mechanism at cathodic potential includes abrasive wear, which is induced by the asperities of Si₃N₄ ball or wear debris within the wear track. According to Fig. 6.15b, several microcracks were detected on the worn surface obtained under OCP conditions. The formation of microcracks can provide a diffusion channel for corrosive agents such as chloride and potassium ions, which accelerate the corrosion process inside the wear track, causing the formation of corrosion products in the wear track. This observation is confirmed by EDS results where high percentages of chloride (0.34 to 0.52 wt.%) and potassium (0.02 to 0.10 wt.%) ions were detected on the worn surface. A closer examination of SEM-EDS data performed on the wear track showed that most areas of the wear track were covered by a uniform oxide layer which is rich in oxygen (13.1 to 18.1 wt.%) and iron (73.67 to 79.77 wt.%). Fig. 6.15c depicts that the worn surface at 0.1 V was covered with a broken oxide layer, which can be correlated to the breakdown and repair of the oxide layer during the sliding process at the anodic potential. Many corrosion products, microcracks and ploughs can be observed inside the wear track. The EDS analysis of the determined areas within the wear track at 0.3 V revealed higher weight percentages of oxygen (16.34 to 22.53 wt.%), chloride (0.39 to 0.67 wt.%) and potassium (0.06 to 0.13 wt.%) elements than at other potentials. The formation of broken oxide film at 0.3 V was insufficient in providing steel corrosion protection during tribo-corrosion tests. This observation is consistent with the electrochemical data shown in Fig. 6.11 and 6.12. However, the oxide film generated on the worn surface acted as an intermediate layer

between the steel and Si₃N₄ ball to reduce their contact area, providing the lowest COF values at anodic potentials (Fig. 6.13).

Fig. 6.16 demonstrates the remarkable effect of PEG-6 isotridecyl phosphate on improving the tribo-corrosion resistance of carbon steel at different applied potentials. Under the condition of cathodic polarization (-0.1 V), no corrosion indication can be found on the worn surface (Fig. 6.16a), which was consistent with the recorded negative current density during the whole testing process (Fig 6.11d). EDS data revealed a small percentage of oxygen element (1.85 to 5.53 wt.%) and no signs of corrosive ions inside the wear track of steel immersed in WBE (B3). A smooth surface with much fewer signs of corrosion products was observed at OCP condition, indicating that the corrosion inhibitor provided significant protection against corrosion, as shown in Fig. 6.16b. It is worth noting that sliding wear was identified as the leading cause of material loss in both cathodic and OCP conditions and was recognized as the dominant degradation mechanism. In contrast, at high potential (Fig. 6.16c), more corrosion products scattered over the wear track. At anodic potential, the protective film could be damaged or even removed because of electrochemical reactions occurring on surface of steel, leading to the breakdown of the protective layer. This observation can be confirmed by EDS analysis, which depicted a reduction in the amount of phosphorous (from 0.32 to 0.42 wt.% in the cathodic potential to 0.17 to 0.38 wt.% in anodic potentials). The EDS analysis also showed an increase in the weight percentages of oxygen (5.44 to 17.01 wt.%), chloride (0 to 0.2 wt.%) and potassium (0 to 0.02 wt.%) on the wear track, resulting from the anodic dissolution of metal and the penetration of corrosive ions towards the worn surface at the anodic potential.

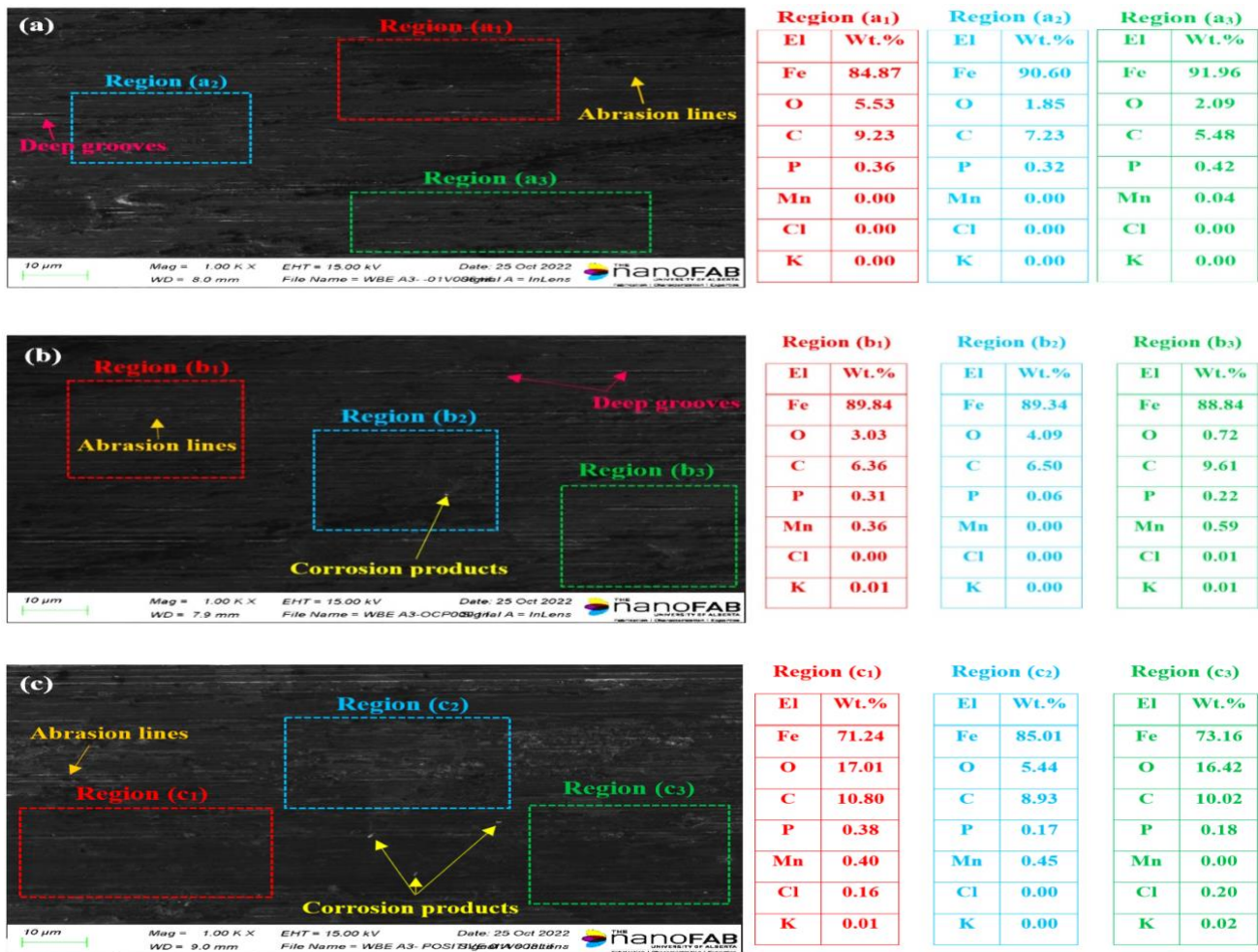
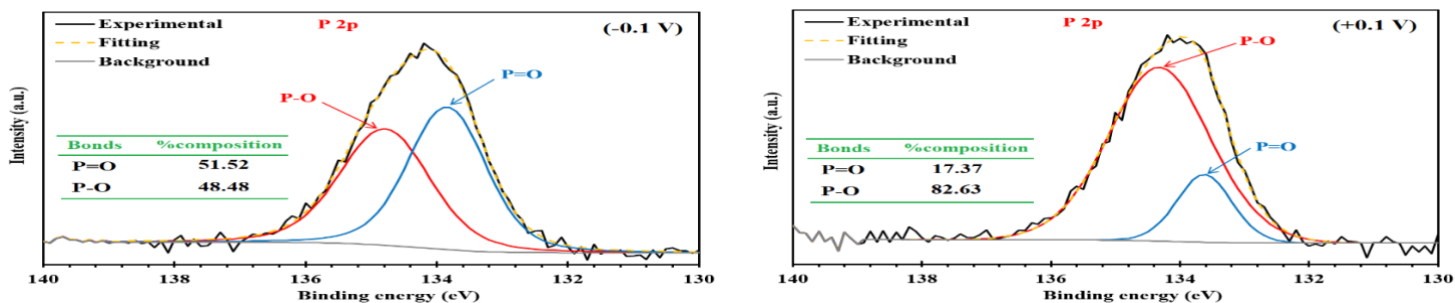


Fig. 6.16 SEM images and EDS data of worn surface experienced test in the WBE (B3) at different applied potentials (a) -0.1 V, (b) 0 (OCP) and (c) +0.1 V.

Fig. 6.17 displays the high-resolution XPS spectra of P 2p, C 1s, O 1s, and Fe 2p recorded from the wear track of carbon steel immersed in WBE (B3) at different potentials.



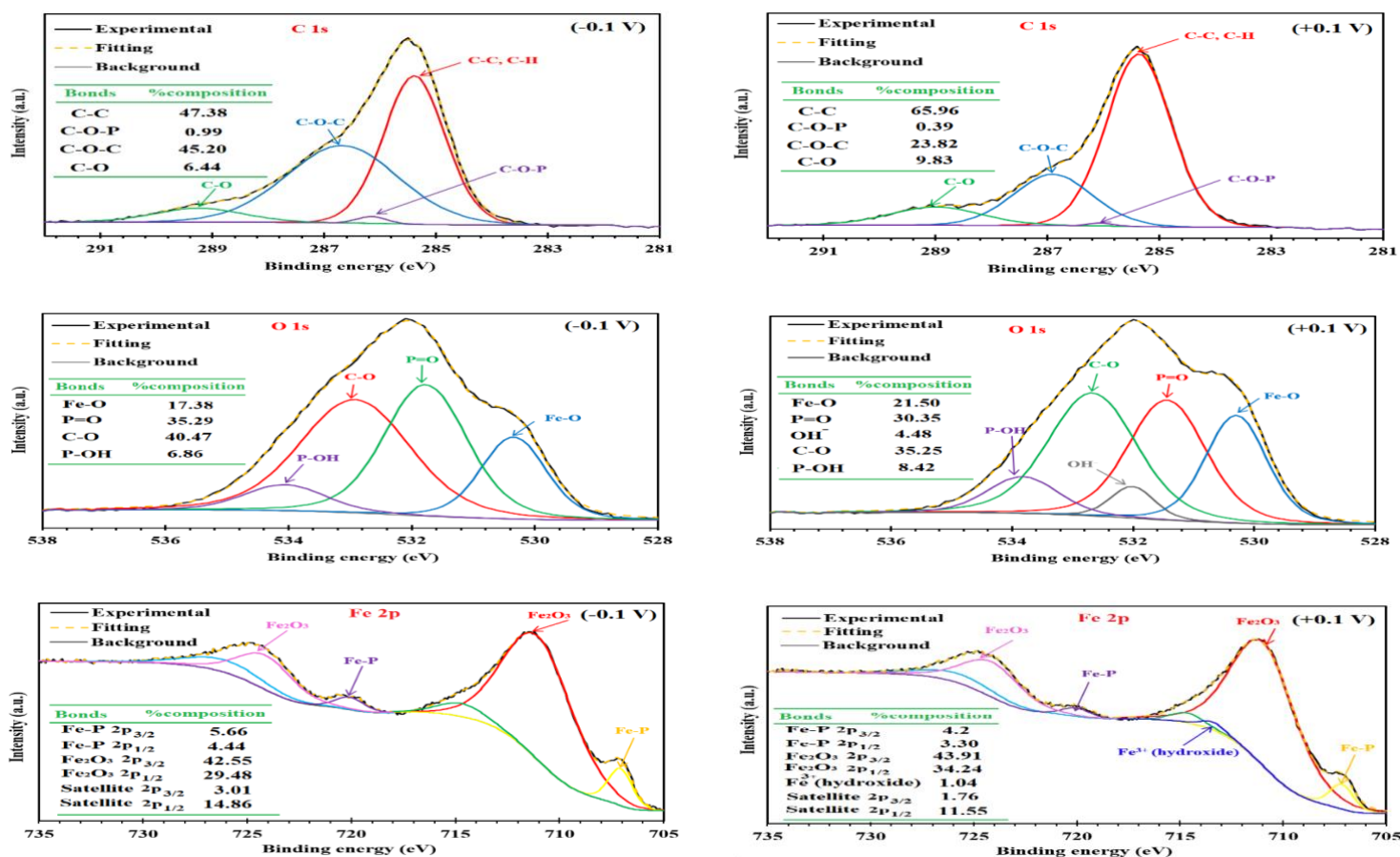


Fig. 6.17 XPS survey spectra of worn surface immersed in WBE (B3) at two different applied potentials (a) -0.1 V and (b) $+0.1$ V.

As shown in Fig. 6.17, P 2p spectra at both applied potentials are composed of two peaks at binding energies of 133.84 eV and 134.79 eV representing P=O and P-O bonds, respectively [236]. This indicates that corrosion inhibitor adsorbed on the worn surface during the tribo-corrosion process at two different applied potentials. The peaks at binding energies of 285.38 eV (C-C), 286.32 eV (C-O-P), 286.67 eV (C-O-C), and 289.23 eV (C-O) in C 1s spectra also confirm the presence of organic compounds existing in the PEG-6 isotridecyl phosphate onto the wear track [237,268]. The O 1s spectra reveal the formation of different bonds within the wear track, including Fe-O (530.34 eV), P=O (531.77 eV), and C-O (532.91 eV) at both applied potentials [240,269]. Fig. 6.17 shows that the composition percentage of Fe-O increased while the composition of P=O and

C-O decreased with increasing potential from cathodic to anodic. This suggests that the protective layer induced by the corrosion inhibitor was damaged by applying anodic potential, leading to an increase in the oxidation of iron. In addition, the OH⁻ bond (532 eV) only appeared under an anodic potential (0.1 V), illustrating the participation of water molecules during the tribo-corrosion process [39, 152]. This involvement causes the generation of hydroxyl radicals which can degrade the protective film, thereby increasing carbon steel's tribo-corrosion rate. After deconvolution analysis of Fe 2p spectra at both cathodic and anodic potentials, the curves were divided into four different peaks ascribed to Fe-P (707.07 and 720.06 eV) and Fe₂O₃ (711 and 724.08 eV) [114,270]. Upon comparing these peaks, a decrease and increase were observed in the composition percentage of Fe-P and Fe₂O₃ with increased applied potential, respectively. A new peak corresponding to Fe³⁺ (713.40 eV) was identified on the wear track under an anodic potential of 0.1 V, suggesting a change in the oxidation state of iron during the tribo-corrosion process [39, 152]. According to XPS data, it can be confirmed that at cathodic potential, tribo-corrosion products are composed of Fe-O and Fe₂O₃, produced through chemical reactions as follows:



However, when the potential applied shifts towards anodic potential, tribo-corrosion products are more diverse, originating from both the above reactions and corrosion electrochemical reactions as mentioned:



Therefore, OH^- and Fe^{3+} peaks were detected in O 1s and Fe 2p spectra with potential increasing, leading to accelerating electrochemical reactions and a decrease in tribo-corrosion resistance of steel in tested solutions.

6.3.2.7 Tribo-corrosion mechanism under different potentials

Fig. 6.18 schematically depicts the tribo-corrosion mechanism of 1018 carbon steel in WBE (B3) containing PEG-6 isotridecyl phosphate in three electrochemical states. Under the condition of cathodic polarization, the anodic reaction's driving force declined, limiting carbon steel's dissolution rate. As a result, the reduction reaction of dissolved oxygen (reaction (4)) is known as the dominant reaction, leading to a reduction in the corrosion rate of steel specimens in aggressive media. At cathodic potential, an inhibitive barrier film formed on the metal surface through physisorption, or chemisorption of PEG-6 isotridecyl phosphate, impeding the access of corrosive agents such as chloride ions to the surface of carbon steel. In addition, oxidation reactions which could damage the inhibitive barrier layer are less likely to occur. Thus, the protective layer generated on the steel surface could provide significant protection against corrosion, consistent with potentiostatic and EIS measurements (Fig. 6.11 and 6.12). XPS and SEM-EDS studies confirmed the presence of PEG-6 isotridecyl phosphate on the worn surface at cathodic potential through the formation of various chemical bonds such as P=O, P-O, and Fe-P. Therefore, when steel is cathodically polarized in WBE (B3), corrosion is restrained, and the tribo-corrosion process is dominated by mechanical wear with no synergistic effect between wear and corrosion (Fig. 6.18a).

As depicted in Fig. 6.18b, in OCP condition, where the rate of anodic and cathodic reactions is equal, the steel specimen experienced some degree of corrosion. Nevertheless, the protective layer induced by the corrosion inhibitor still offered high corrosion resistance, as evident in Fig. 6.11

and 6.12. However, during the tribo-corrosion process, some corrosion products appeared on the worn surface due to anodic reactions, reducing the effectiveness of the protective layer.

At anodic potential, as shown in Fig. 6.18c, the dominant reaction is the oxidation of iron (reaction (3)), leading to an accelerated dissolution of iron. This can damage the protective layer, as supported by a decrease in the amount of phosphorous element detected in EDS analysis (Fig. 6.16). As the applied potential increases, corrosive chloride ions can penetrate the carbon steel surface, reducing its corrosion resistance. Indeed, aggressive chloride ions can react with the protective layer formed on the steel surface, breaking its protective performance, and promoting further corrosion. Moreover, the penetration of these ions leads to the generation of complex ions, such as FeCl_4^- , which can be more aggressive on the steel surface, further decreasing its corrosion resistance. The change in the steel surface impedance and the electrochemical response of the system with increasing the applied potential is confirmed by EIS results (Fig. 6.12). It is worth mentioning that when the applied potential exceeds OCP, the hydroxyl ions (OH^-) are generated through reaction (4), and then migrate towards the anode site. In reaction (5), hydroxyl ions react with ferrous ion (Fe^{2+}) to form ferrous hydroxide ($\text{Fe}(\text{OH})_2$), which is unstable and undergoes further oxidation to generate ferric hydroxide ($\text{Fe}(\text{OH})_3$), as presented in reaction (6). XPS data confirms the presence of this new layer of ferric hydroxide (Fig. 6.17). Although this new oxide layer cannot provide sufficient protection against corrosion, it decreased the COF of carbon steel at anodic potentials by preventing direct contact between carbon steel and Si_3N_4 ball (Fig. 6.13).

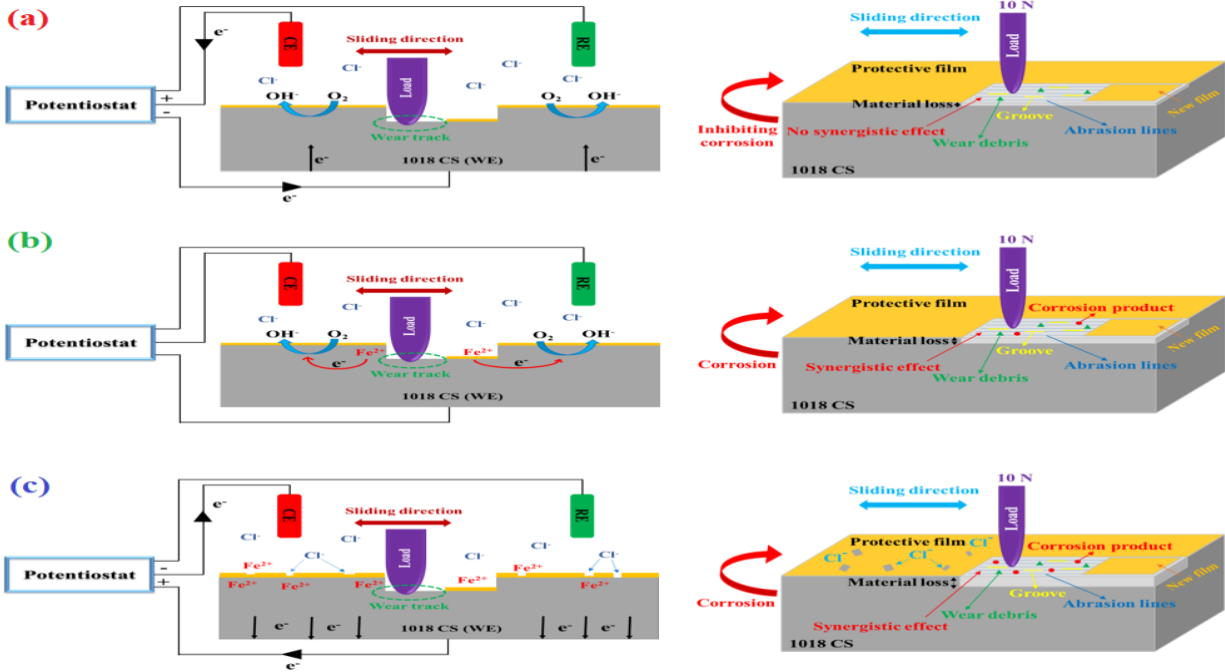


Fig. 6.18 Schematic diagram of the tribo-corrosion mechanism of 1018 carbon steel immersed in WBE (B3) at (a) cathodic potential, (b) OCP, and (c) anodic potential.

6.4 Conclusions

In the study reported, the tribo-corrosion performance of 1018 carbon steel immersed under different sliding forces and electrochemically applied potentials was investigated in brine solution and WBEs containing corrosion inhibitors by in-situ electrochemical methods, tribological, SEM-EDS, and XPS tests. Based on the results obtained in the present paper, the following conclusion can be made:

1. The corrosion resistance of carbon steel tested in different solutions decreased at higher contact forces and potentials. It is attributed to higher contact pressure between the surfaces in contact and higher Cl^- penetration through the protective film, weakening its protectiveness and increasing electrochemical activity on the worn surface.

2. The total material loss during the tribo-corrosion process increased with applied forces and potential, in which pure mechanical wear and corrosion-accelerated wear were determined as the dominant damage mechanism.
3. With the increased applied force and potential, the average COF value reduced and reached the lowest values at 10 N and +0.3 V vs OCP. This reduction in COF with force was ascribed to increased contact points between the steel surface and the ball, leading to a larger contact area and increased interactions between the two surfaces. The reduction in COF with potential can be correlated to the formation of a new oxide layer ($\text{Fe}(\text{OH})_3$) and defects such as ploughs, which reduce the contact area between steel and ball.
4. Three corrosion inhibitors, especially PEG-6 isotridecyl phosphate, in WBEs, enhanced the tribo-corrosion behavior of steel at different applied forces and potential.
5. SEM-EDS and XPS results showed that the corrosion inhibitors were successfully adsorbed on the surface of carbon steel; however, their effectiveness was reduced with increases in force and potential.

Chapter 7 Conclusion and Recommendations

7.1 Conclusions

This study is conducted to comprehensively investigate the stability of emulsion-based drilling fluids containing various concentrations of mineral oil, surfactant, and corrosion inhibitors to make highly stable WBEs that can significantly improve drilling fluid's performance. The effect of various green corrosion inhibitors on carbon steel's corrosion, tribological and tribo-corrosion behavior in different solutions was investigated under various conditions. The main findings are summarized as follows:

- 1- Emulsion-based drilling fluids with lower surfactant concentrations and higher concentration of green corrosion inhibitors enhanced the stability of drilling fluids with a remarkable decrease in interfacial tension between droplets and the aqueous phase. This work identified the combination of (65% mineral oil + 3-5% surfactant + 30-32% corrosion inhibitor) as an emulsion-based drilling fluid with remarkable stability.
- 2- Corrosion inhibitors in WBEs effectively mitigated CO₂ corrosion of carbon steel by forming protective films through adsorption interactions with the steel's surface. PEG-6 isotridecyl phosphate and PEG-2 oleamide demonstrated superior anti-corrosion performance.
- 3- The presence of corrosion inhibitors, particularly PEG-6 isotridecyl phosphate, substantially improved carbon steel's resistance to tribo-corrosion. This was evident in reduced corrosion rate, wear rate, and friction coefficient. These results unequivocally affirm that our study has effectively met the objectives we set forth in our thesis, demonstrating the significant advancements made in enhancing the resistance of carbon steel to tribo-corrosion through the application of corrosion inhibitors.

- 4- Sliding speed exerted a significant influence on the kinetic response of carbon steel to corrosion and tribo-corrosion behavior. Electrochemical parameters and friction coefficients decreased with increasing sliding speed, primarily due to increased adsorption of corrosion inhibitors. However, volume loss increased with higher sliding speeds.
- 5- A decrease in contact force led to a increase in carbon steel's tribo-corrosion performance against a Si_3N_4 ball, as observed in increased R_{ct} and R_t values. The wear resistance of samples was declined by lower applied forces, resulting in lower volume loss and wear rates. Conversely, friction coefficients increased with decreasing contact forces.
- 6- The tribo-corrosion resistance of carbon steel samples immersed in drilling fluids exhibited a notable improvement as the electrochemical potential transitioned from anodic to cathodic conditions. This improvement is evidenced by a significant reduction in both the corrosion rate and wear rates. Intriguingly, it's worth noting that the lowest coefficients of friction (COF) were achieved under anodic potentials.
- 7- The presence of green corrosion inhibitors, notably PEG-6 isotridecyl phosphate added to Water-Based Emulsions (WBEs), exerted a more pronounced influence in mitigating the wear-corrosion synergy compared to other solutions. This heightened effectiveness can be attributed to its remarkable corrosion reduction capabilities.
- 8- Analysis through SEM-EDS, XPS, and Gibbs free energy calculations confirmed the physical and chemical adsorption of corrosion inhibitors on the steel surface. The quantity of inhibitor molecules adsorbed increased with sliding speed but decreased with higher contact force and potential.

In summary, adding corrosion inhibitors to WBEs significantly increased the resistance to corrosion, wear, and tribo-corrosion for 1018 carbon steel immersed in drilling fluids. Besides,

increasing speed and decreasing contact force and electrochemical potential in the ranges under study further improved the performance of the steel samples during tribo-corrosion tests in the tested solutions. These results effectively align with the core objectives we set out to achieve in our study, which aimed at enhancing the tribo-corrosion resistance of carbon steel in drilling fluid following the incorporation of green corrosion inhibitors under a variety of controlled conditions.

7.2 Recommendations for Future Studies

This study comprehensively investigated the the tribo-corrosion behavior of carbon steel in emulsion-based drilling fluids containing green corrosion inhibitors. These investigations were carried out under controlled laboratory conditions, which allowed us to isolate and study the fundamental aspects of tribo-corrosion. Future research endeavors should focus on conducting experiments that closely mimic the actual working conditions of drilling equipment. Thus, the following studies are suggested for possible near future work:

1. Future research could be conducted to search for more green corrosion inhibitors, which may have higher capability to improve the performance of the drilling fluids in protecting steel from wear, corrosion, and tribo-corrosion under more realistic conditions.
2. Extend the ranges of various factors, e.g., the sliding speed, contact force, and temperature on the tribo-corrosion performance of the modified drilling fluids under field-like consitions, enabling us how drilling equipment change in the real world.
3. Conduct a comprehensive examination of the damage and re-growth of the inhibitor-induced protective film on steel surfaces during tribo-corrosion, particularly in the context of the actual operating conditions encountered in the drilling industry. This investigation will help us identify the critical factors that influence the performance of green corrosion

inhibitors and develop strategies to either modify existing inhibitors or identify new green inhibitors that can be effectively applied in the challenging real-world conditions of drilling operations. Understanding how these protective films evolve and interact under realistic drilling conditions is vital for enhancing the long-term durability and corrosion resistance of drilling equipment

References

- [1] J. Xu, Zh. Qiu, X. Zhao, T. Mou, H. Zhong and W. Huang, A polymer microsphere emulsion as a high- performance shale stabilizer for water-based drilling fluids, *RSC Advances*, 8 (2018) 20852.
- [2] M. Ali, H. Jarni, A. Aftab, A. Razak Ismail, N. M. Cata Saady, M. Faraz Sahito, A. Keshavarz, S. Iglauer and M. Sarmadivaleh, Nanomaterial-Based Drilling Fluids for Exploitation of Unconventional Reservoirs: A Review, *Energies*, 13 (2020) 3417.
- [3] M. Abdelsattar, A. El-Fattah M. Badawi, S. Ibrahim, A. F. Wasfy, A. H. Tantawy, and M. M. Dardir, Corrosion Control of Carbon Steel in Water-Based Mud by Nanosized Metallo-Cationic Surfactant Complexes During Drilling Operations, *ACS Omega*, 5 (2020) 30881–30897.
- [4] B. Borah, B. Mech Das, A review on applications of bio-products employed in drilling fluids to minimize environmental footprint, *Environmental Challenges* 6 (2022) 100411.
- [5] P. K. Jha, V. Mahto, V. K. Saxena, Emulsion Based Drilling Fluids: An Overview, *International Journal of ChemTech Research*, 6 (2014) 2306-2315.
- [6] S. Ghaderi, S. Arash Haddadi, Sh. Davoodi, M. Arjmand, Application of sustainable saffron purple petals as an eco-friendly green additive for drilling fluids: A rheological, filtration, morphological, and corrosion inhibition study, *Journal of Molecular Liquids*, 315 (2020) 113707, <https://doi.org/10.1016/j.molliq.2020.113707>.
- [7] B. Paswan, V. Mahto, Development of environment-friendly oil-in-water emulsion-based drilling fluid for shale gas formation using sunflower oil. *Journal of Petroleum Science and Engineering*, 191 (2020) 107129, <https://doi.org/10.1016/j.petrol.2020.107129>.
- [8] D. Li, J. Jin, D. Zhang, F. Li, X. Wang and L. Liu, pH-Responsive Drilling Fluid With High-Temperature and High-Density Performance, *Frontiers in Earth Science*, 10 (2022) 851097.
- [9] S. Ghaderi, A. Ramazani S.A., S. Arash Haddadi, Applications of highly salt and highly temperature resistance terpolymer of acrylamide/styrene/maleic anhydride monomers as a

rheological modifier: Rheological and corrosion protection properties studies, *Journal of Molecular Liquids* 294 (2019) 111635.

[10] A. Iyasara, J.E.O Ovri, Corrosion behavior and effects of drilling mud, *International Journal of Scientific Research Engineering & Technology*, 4 (2015) 917-923.

[11] Zh. Wang, D. Yin, Y. Luo, H. Liang, L. Yang, H. Lu, Corrosion and Its Inhibition in Water-Based Drilling Fluid Used in Onshore Oilfield, *Natural Resources*, 4 (2013) 456-459.

[12] F. S. Kadhim, Investigation of Carbon Steel Corrosion in Water Base Drilling Mud, *Modern Applied Science*, 5 (2011) 224-229.

[13] T. Nagalakshmi, A. Sivasakthi, Corrosion Control, Prevention and Mitigation in Oil & Gas Industry, *International Journal of Innovative Technology and Exploring Engineering*, 9 (2019) 1568-1572.

[14] L. Popoola, A. Shehu Grema, G. Kayode Latinwo, B. Gutti and A. Saheed Balogun, Corrosion problems during oil and gas production and its mitigation, *International Journal of Industrial Chemistry*, 4 (2013), <https://doi.org/10.1186/2228-5547-4-35>.

[15] O. Osman, N. Merah, M. Abdul Samad, M. Murtuza A. Baig, R. Samuel, M. Alshalan and A. Alshaarawi, Casing Wear and Wear Factors: New Experimental Study and Analysis, *Materials*, 15 (2022) 6544, <https://doi.org/10.3390/ma15196544>.

[16] J.M. Gonzalez, F. Quintero, L.R. Marquez, S.D. Rosales, G. Quercia, *Surfactants in tribology*, 2. CRC Press Taylor & Francis Group; (2010) 241–265.

[17] M.T. Albdiry, M.F. Almensory, Failure analysis of drillstring in petroleum industry: A review, *Engineering Failure Analysis* 65 (2016) 74–85.

[18] Sh. Liu, H. Zheng and X. Zhu, Drill string failure analysis and erosion wear study at key point for gas drilling, *Energy Exploration & Exploitation*, 32 (2014) 553-568.

- [19] A. López-Ortega, J. L. Arana, R. Bayón, On the comparison of the tribocorrosion behavior of passive and non-passivating materials and assessment of the influence of agitation. *Wear*, 456-457 (2020) 203388, <https://doi.org/10.1016/j.wear.2020.203388>.
- [20] X. Wang, Y. Wang, Zh. Huang, Q. Zhou, and H. Wang, Tribocorrosion Behavior of CoCrNi Medium Entropy Alloy in Simulated Seawater, *Metals*, 12 (2022) 401, <https://doi.org/10.3390/met12030401>.
- [21] A. López-Ortega, J. L. Arana, and R. Bayón, Tribocorrosion of Passive Materials: A Review on Test Procedures and Standards, *International Journal of Corrosion*, (2018) 7345346, <https://doi.org/10.1155/2018/7345346>.
- [22] Zh. Li, H. Yu, D. Sun, The tribocorrosion mechanism of aluminum alloy 7075-T6 in the deep ocean, *Corrosion Science* 183 (2021) 109306.
- [23] M. Stemp, S. Mischler, D. Landolt, The effect of mechanical and electrochemical parameters on the tribocorrosion rate of stainless steel in sulphuric acid, *Wear* 255 (2003) 466–475.
- [24] A. K. Kasar, A. Siddaiah, R. Ramachandran, P. L. Menezes, Tribocorrosion Performance of Tool Steel for Rock Drilling Process, *Journal of Bio- and Tribo-Corrosion* (2019) 5:44 <https://doi.org/10.1007/s40735-019-0238-4>.
- [25] S. Soltanahmadi, A. Morina, M. C.P. van Eijk, I. Nedelcu, A. Neville, Tribochemical study of micropitting in tribocorrosive lubricated contacts: The influence of water and relative humidity, *Tribology International* 107 (2017) 184–198.
- [26] Y. Zhang, X. Yin, Y. Yan, J. Wang, and F. Yan, Tribocorrosion behaviors of 304SS: effect of solution pH, *RSC Advances*, 5 (2015) 17676.
- [27] E. Martin, M. Azzi, G.A. Salishchev, J. Szpunar, Influence of microstructure and texture on the corrosion and tribocorrosion behavior of Ti–6Al–4V, *Tribology International* 43 (2010) 918–924.

- [28] D. Niu, C. Zhang, X. Sui, X. Lu, X. Zhang, C. Wang, J. Hao, Zh. Shi, Microstructure, mechanical properties, and tribo-corrosion mechanism of $(\text{CrNbTiAlVMo})_x\text{N}_{1-x}$ coated 316 L stainless steel in 3.5 wt% NaCl solution, *Tribology International* 173 (2022) 107638.
- [29] A. Hammood, L. Thair, H. Diab Altawaly, N. Parvin, Tribocorrosion Behaviour of Ti–6Al–4V Alloy in Biomedical Implants: Effects of Applied Load and Surface Roughness on Material Degradation, *Journal of Bio- and Tribo-Corrosion* (2019) 5:85, <https://doi.org/10.1007/s40735-019-0277-x>.
- [30] J. N. Panda, E. Y. Orquera, A. A. Mohanty, Ph, Egberts, Tribo-corrosion inhibition of AISI 4715 steel pipe carrying hydraulic fracturing fluid, *Tribology International* 161 (2021) 107066, <https://doi.org/10.1016/j.triboint.2021.107066>.
- [31] R. C. Silva, R. P. Nogueira, I. N. Bastos, Tribocorrosion of UNS S32750 in chloride medium: Effect of the load level, *Electrochimica Acta* 56 (2011) 8839–8845.
- [32] J. Chen, J. Wang, F. Yan, Q. Zhang, Q. Li, Effect of applied potential on the tribocorrosion behaviors of Monel K500 alloy in artificial seawater, *Tribology International* 81 (2015) 1–8.
- [33] Q. J. Wang, Chung Y W. *Encyclopedia of tribology*, Springer, (2013) 1903-2158, <https://doi.org/10.1007/978-0-387-92897-5>.
- [34] M. A. Chowdhury, M. K. Khalil, D. M. Nuruzzaman, M. L. Rahaman, The Effect of sliding speed and normal load on friction and wear property of aluminum. *International Journal of Mechanical & Mechatronics Engineering* 11 (2011) 45-49.
- [35] J. Sun, X. Mao, X. Zhou, X. Zhao, D. Li, Effect of loads on wear behavior of carbon steel surface with gradient microstructure at high temperature, *Materials Letters* 261 (2020) 126999.
- [36] R. Jamshidi, O. Bayat, A. Heidarpour, Tribological and corrosion behavior of flame sprayed Al–10 wt% Ti_3SiC_2 composite coating on carbon steel, *Surface & Coatings Technology* 358 (2019) 1–10.
- [37] M. Wendler, M.R. Kaizer, R. Belli, U. Lohbauer, Y. Zhang, Sliding contact wear and subsurface damage of CAD/CAM materials against zirconia, *Dental Materials*, 36 (2020) 387-401.

- [38] Ch. Liu, Z. G. Neale, and G. Cao, Understanding electrochemical potentials of cathode materials in rechargeable batteries, *Materials Today*, 19 (2016) 109-123.
- [39] B. B. Zhang, J-Z. Wang, Y. Zhang, G. F. Han and F. Y. Yan, Tribocorrosion behavior of 410SS in artificial seawater: effect of applied potential, *Materials and Corrosion*, 68 (2016), <http://dx.doi.org/10.1002/maco.201609119>.
- [40] A. Munoz, L. Casabán Julián, Influence of electrochemical potential on the tribocorrosion behaviour of high carbon CoCrMo biomedical alloy in simulated body fluids by electrochemical impedance spectroscopy, *Electrochimica Acta* 55 (2010) 5428–5439.
- [41] C. M. Fernandes, Th. da S. Ferreira Fagundes, N. Escarpini dos Santos, T. Shewry de M. Rocha, R. Garrett, R. Moreira Borges, G. Muricy, Alessandra Leda Valverde, Eduardo Ariel Ponzio, *Ircinia strobilina* crude extract as corrosion inhibitor for mild steel in acid medium, *Electrochimica Acta* 312 (2019) 137-148.
- [42] M. Motta, M. Zanocco, A. Rondinella, V. Iodice, A. Sin, L. Fedrizzi, F. Andreatta, Inhibitive effect of 8-hydroxyquinoline on corrosion of gray cast iron in automotive braking systems, *Electrochimica Acta* 449 (2023) 142221.
- [43] Y. Yao, B. Pan, W. Wang, S. Tan, Effects of benzotriazole and imidazoline on the tribocorrosion behaviors of a WC-based material in saline silica slurries, *Int. J. Refract. Met. Hard Mater.* 97 (2021) 105523.
- [44] E. McCafferty, *Introduction to Corrosion Science*, Chapter 12, 2009, 357-400.
- [45] M. Finšgar, J. Jackson, Application of corrosion inhibitors for steels in acidic media for the oil and gas industry: A review, *Corrosion Science* 86 (2014) 17–41.
- [46] R. Haldhar, D. Prasad, D. Kamboj, S. Kaya, O. Dagdag, L. Guo, Corrosion inhibition, surface adsorption and computational studies of *Momordica charantia* extract: a sustainable and green approach, *SN Applied Sciences*, 3 (2021), <https://doi.org/10.1007/s42452-020-04079-x>.

- [47] D. S. Chauhan, Chandrabhan Verma, M.A. Quraishi, Molecular structural aspects of organic corrosion inhibitors: Experimental and computational insights, *Journal of Molecular Structure*, 1227 (2021) 129374.
- [48] L. Mao, M. Cai, Q. Liu, G. Wang, Influence of oil-water ratio on the wear of Cr13 casing lubricated with drilling fluid, *Materials Today Communications* 25 (2020) 101341.
- [49] Y. Yao, B. Pan, W. Wang, S. Tan, Effects of benzotriazole and imidazoline on the tribo-corrosion behaviors of a WC-based material in saline silica slurries, *International Journal of Refractory Metals and Hard Materials*, 97 (2021) 105523, <https://doi.org/10.1016/j.ijrmhm.2021.105523>.
- [50] M. Ouknin, J. Costa, L. Majidi L, Tribo-corrosion and electrochemical behavior of AISI 304L stainless steel in acid medium and Thymus will denowii Boiss & Reut essential oil effect, *Chemical Data Collection*, 28 (2020) 100389, <https://doi.org/10.1016/j.cdc.2020.100389>.
- [51] N.P. Brandon and R.J.K. Wood, The influence of interfacial potential on friction and wear in an aqueous drilling mud, *Wear*, 170 (1993) 33-38.
- [52] O. Osman, N. Merah, M. Abdul Samad, M. Murtuza A. Baig, R. Samuel, M. Alshalan and A. Alshaarawi, Casing Wear and Wear Factors: New Experimental Study and Analysis, *Materials*, 15 (2022) 6544, <https://doi.org/10.3390/ma15196544>.
- [53] L. Mao, M. Cai, G. Wang, Effect of rotation speed on the abrasive–erosive–corrosive wear of steel pipes against steel casings used in drilling for petroleum, *Wear* 410–411 (2018) 1–10.
- [54] L. Mao, M. Cai, Q. Liu, Y. He, Effects of sliding speed on the tribological behavior of AA 7075 petroleum casing in simulated drilling environment. *Tribology International* 145 (2020) 106194, <https://doi.org/10.1016/j.triboint.2020.106194>.
- [55] A. M. Salem Ragab and A. Noah, Reduction of Formation Damage and Fluid Loss using Nano-sized Silica Drilling Fluids, *Petroleum Technology Development Journal*, 2 (2017) 75-88.

- [56] M. Humooda, M. H. Ghamary, P. Lan, L. L. Iaccino, X. Bao, A. A. Polycarpou, Influence of additives on the friction and wear reduction of oil-based drilling fluid, *Wear* 422–423 (2019) 151-160.
- [57] X. Huang, J. Sun, K. Lv, J. Liu and H. Shen, an alternative method to enhance w/o emulsion stability using modified dimer acid and its application in oil-based drilling fluids, *Royal Society of Chemistry* 8 (2018) 26318-26324.
- [58] S. F. Wong, J. S. Lim, S. S. Dol, Crude oil emulsion: A review on formation, classification and stability of water-in-oil emulsions, *Journal of Petroleum Science and Engineering* 135 (2015) 498-504.
- [59] F. Goodarzi and S. Zendehboudi, A Comprehensive Review on Emulsions and Emulsion Stability in Chemical and Energy Industries, *Canadian Journal of Chemical Engineering* 97 (2019) 281-309
- [60] M. I. Abduo, A. S. Dahab, H. Abuseda, M. AbdulAziz, M. S. Elhossieny, Comparative study of using Water-Based mud containing Multiwall Carbon Nanotubes versus Oil-Based mud in HPHT fields, *Egyptian Journal of Petroleum* 1 (2015), <http://dx.doi.org/10.1016/j.ejpe.2015.10.008>.
- [61] M. Al-Yasiri, M. Al-Khateeb & D. Wen, Examination of drill pipe corrosion in water-based drilling fluids under wellbore Conditions, *Corrosion Engineering, Science and Technology* 53 (2017) 183-187.
- [62] B. Xing, Li Shao-hua, Investigating the Effect of Acid Gas on Drilling Mud Rheological Property in SP11 Block, *Electronic Journal of Geotechnical Engineering* 21 (2016) 6157.
- [63] A. Kahyarian and S. Nestic, A New Narrative for CO₂ Corrosion of Mild Steel, *Journal of Electrochemical Society* 166 (2019) c3048.
- [64] X. Jiang, S. Nestic, F. Huet, B. Kinsella, B. Brown, and D. Young, Selection of Electrode Area for Electrochemical Noise Measurements to Monitor Localized CO₂ Corrosion, *Journal of Electrochemical Society* 159 (2012) c283.

- [65] A. Shamsa, R. Barker, Y. Hua, E. Barmatov, T. L. Hughes and A. Neville, Impact of corrosion products on performance of imidazoline corrosion inhibitor on X65 carbon steel in CO₂ environments, *Corrosion Science* 185 (2021) 109423.
- [66] B.Yu, D.Y. Li, Amélie Grondin, Effects of the dissolved oxygen and slurry velocity on erosion–corrosion of carbon steel in aqueous slurries with carbon dioxide and silica sand, *Wear*, 302 (2013) 1609-1614.
- [67] S. Yin, D.Y. Li, Effects of prior cold work on corrosion and corrosive wear of copper in HNO₃ and NaCl solutions, *Material Science Engineering A* 394 (2005) 266-276.
- [68] H. Cen, J. Cao, Zh. Chen, X. Guo, 2-Mercaptobenzothiazole as a corrosion inhibitor for carbon steel in supercritical CO₂-H₂O condition, *Applied Surface Science* 476, (2019) 422-434.
- [69] W. Zhang, Ch. Li, W. Wang, B. Li, X. Liu, Y. Liu, H. Guo, Sh. Chen, Y. Feng, Laminarin and sodium molybdate as efficient sustainable inhibitor for Q235 steel in sodium chloride solution, *Colloids Surf. A: Physicochem. Eng. Asp.* 637 (2022) 128199.
- [70] W. Zhang, B. Nie, M. Wang, Sh. Shi, L. Gong, W. Gong, H. Pang, X. Liu, B. Li, Y. Feng, Y. Wu, chemically modified resveratrol as green corrosion inhibitor for Q235 steel: Electrochemical, SEM, UV and DFT studies, *Journal of Molecular Liquid* 343 (2021) 117672.
- [71] L. Feng, Sh. Zhang, Y. Qiang, Sh. Xu, B. Tan, Sh. Chen, The synergistic corrosion inhibition study of different chain lengths ionic liquids as green inhibitors for X70 steel in acidic medium, *Material Chemistry Physics* 215 (2018) 229-241.
- [72] M. Chafiq, A. Chaouiki, R. Salghi, H. Tachallait, Kh. Bougrin, I. H. Ali, M. Siaj, Adsorption mechanism of 3-(1,4-disubstituted-1,2,3-triazolyl) uridine nucleosides against the corrosion of mild steel in HCl, *Material Chemistry Physics* 268 (2021) 124742.
- [73] R. Gupta, M. Malviya, K.R. Ansari, H. Lgaz, D.S. Chauhan, M.A. Quraishi, Functionalized graphene oxide as a new generation corrosion inhibitor for industrial pickling process: DFT and experimental approach, *Material Chemistry Physics* 236 (2019) 121727.

- [74] E. A. Badr, M.A. Bedair, Samy M. Shaban, Adsorption and performance assessment of some imine derivatives as mild steel corrosion inhibitors in 1.0 M HCl solution by chemical, electrochemical and computational methods, *Material Chemistry Physics* 219 (2018) 444-460.
- [75] I. Abdulazeez, A. Zeino, Ch. Kee, A. A. Al-Saadi, M. Khaled, M. Wong, A. A. Al-Sunaidi, Mechanistic studies of the influence of halogen substituents on the corrosion inhibitive efficiency of selected imidazole molecules: A synergistic computational and experimental approach, *Applied Surface Science* 471 (2019) 494-505.
- [76] A. Miralrio and A. E. Vázquez, Plant Extracts as Green Corrosion Inhibitors for Different Metal Surfaces and Corrosive Media: A Review, *Process*, 8 (2020) <https://doi.org/10.3390/pr8080942>.
- [77] M. J. Palimi, E. Alibakhshi, G. Bahlakeh, B. Ramezanzadeh and M. Mahdavian, Electrochemical Investigations of the Corrosion Protection Properties of an Epoxy-Ester Coating Filled with Cerium Acetyl Acetonate Anticorrosive Pigment, *Journal of Electrochemical Society* 164 (2017) 709-716.
- [78] P. N. Swathi, K. Rasheeda, S. Samshuddin, D.P. Alva, Fatty acids and its derivatives as corrosion inhibitors for mild steel- An overview. *Journal of Asian Scientific Research* 78 (2017) 301.
- [79] K. Tamalmani and H. Husin, Review on Corrosion Inhibitors for Oil and Gas Corrosion Issues, *Appl. Sci.* 10 (2020) 3389.
- [80] S. H. Alrefae, K. Y. Rhee, Ch. Verma, M.A. Quraishi, E. Ebenso, Challenges and advantages of using plant extract as inhibitors in modern corrosion inhibition systems: Recent advancements,” *Journal of Molecular Liquid* 321 (2021), <https://doi.org/10.1016/j.molliq.2020.114666>.
- [81] Ch. Verma, E. Ebenso, I. Bahadur, M.A. Quraishi, An overview on plant extracts as environmental sustainable and green corrosion inhibitors for metals and alloys in aggressive corrosive media, *Journal of Molecular Liquid* 266 (2018) 577-590.

- [82] S. Varvara, R. Bostan, O. Bobis, L. Gaina, F. Popa, V. Mena, R. M. Souto, Propolis as a green corrosion inhibitor for bronze in weakly acidic solution, *Applied Surface Science* 426 (2017) 1100-1112.
- [83] H. Akhavan, M. Izadi, I. Mohammadi, T. Shahrabi, and B. Ramezanzadeh, The Synergistic Effect of BTA-Co System on the Corrosion Inhibition of Mild Steel in 3.5 wt. % NaCl Solution, *Journal of Electrochemical Society* 165 (2018) c670.
- [84] A. Sehmi, H. B. Ouici, A. Guendouzi, M. Ferhat, O. Benali, and F. Boud, Corrosion Inhibition of Mild Steel by newly Synthesized Pyrazole Carboxamide Derivatives in HCl Acid Medium: Experimental and Theoretical Studies, *Journal of Electrochemical Society* 167 (2020).
- [85] I.B. Onyechu, I. B. Obot, A. A. Sorour, M. I. Abdul-Rashid, Green corrosion inhibitor for oilfield application I: Electrochemical assessment of 2-(2-pyridyl) benzimidazole for API X60 steel under sweet environment in NACE brine ID196, *Corrosion Science* 150 (2019)183-193.
- [86] Zh. Xionghu, S. B. Egwu, D. Jingen, and M. Liujie, Application of Benzotriazole Corrosion Inhibitor in Synthetic-Based Drilling Fluid and its Overall Impact in Improving Drilling Fluid Functionality, SPE International Oilfield Corrosion Conference and Exhibition, June 2021. doi: <https://doi.org/10.2118/205055-MS>
- [87] S. Ghareba and S. Omanovic, Interaction of 12-aminododecanoic acid with a carbon steel surface: towards the development of “green” corrosion inhibitors, *Corrosion Science* 52 (2010) 2104-2111.
- [88] G. Palumbo, M. Gorny, and J. Banas, Corrosion Inhibition of Pipeline Carbon Steel (N80) in CO₂-Saturated Chloride (0.5 M of KCl) Solution Using Gum Arabic as a Possible Environmentally Friendly Corrosion Inhibitor for Shale Gas Industry, *Journal of Materials Engineering and Performance* 28 (2019) 6458-6470.
- [89] Q.H. Zhang, B.S. Hou, N. Xu, H.F. Liu, G.A. Zhang, two novel thiadiazole derivatives as highly efficient inhibitors for the corrosion of mild steel in the CO₂ -saturated oilfield produced water, *Journal of the Taiwan Institute of Chemical Engineers* 96 (2019) 588–598.

- [90] Y. Wu, F. Zhang, H. Liu, Corrosion inhibition performance of lauric acid and thiourea for carbon steel in a CO₂-saturated and SRB-containing artificial sewage, *Corros. Sci. Prot. Technol.* 27(2015) 219-225.
- [91] W. F. Hameed, Kh. H. Rashid, A. A. Khadom, Investigation of Tetraazaadamantane as Corrosion Inhibitor for Mild Steel in Oilfield Produced Water Under Sweet Corrosive Environment, *Journal of Bio and Tribo-corrosion* 8:27 (2022), <https://doi.org/10.1007/s40735-021-00626-0>.
- [92] H. Liu, T. Gu, G. Zhang, W. Wang, Sh. Dong, Y. Cheng, H. Liu, Corrosion inhibition of carbon steel in CO₂-containing oilfield produced water in the presence of iron-oxidizing bacteria and inhibitors, *Corrosion Science* 105 (2016) 149–160.
- [93] Q.H. Zhang a, B.S. Hou a, Y.Y. Li a, Y. Lei a, X. Wang a, H.F. Liu a,b, G.A. Zhang, Two amino acid derivatives as high efficient green inhibitors for the corrosion of carbon steel in CO₂-saturated formation water, *Corrosion Science* 189 (2021) 109596.
- [94] M. A. Deyab, M. M. Osman, A. E. Elkholy and F. El-Taib Heakal, Green approach towards corrosion inhibition of carbon steel in produced oilfield water using lemongrass extract, *RSC Adv.* 7 (2017) 45241–45251.
- [95] M. Naeimavi, F. Khazali, M. Abdideh & Z. Saadati, Potassium sorbate as substitute for KCl to shale inhibition in water-base drilling fluids, Potassium sorbate as substitute for KCl to shale inhibition in water-base drilling fluids. *Energy Sources A: Recovery Util. Environ. Eff.* (2019) 1691-1705.
- [96] Z. M. Wang, G. Song and J. Zhang, Corrosion Control in CO₂ Enhanced Oil Recovery from a Perspective of Multiphase Fluids, *Front. Mater.* 6 (2019), <https://doi:10.3389/fmats.2019.00272>.
- [97] A. Carmona-Hernandez, E. Vazquez-Velez, J. Uruchurtu-Chavarin, J. G. Gonzalez-Rodriguez and L. Martinez-Gomez, Use of an imidazol synthesized from palm oil as a corrosion inhibitor for a supermartensitic stainless steel in H₂S, *Green Chemistry Letters and Reviews* 12 (2019) 89-99.

- [98] Y. El-Shattory, G. A. Abdo-Elwafa, S. M. Aly and El-Shahat H. A. Nashy, Production of ethoxylated fatty acids derived from jatropa non-edible oil as a non-ionic fat-liquoring agent, *Journal of Oleo Science* 6 (2012) 255-266.
- [99] R.T. Loto, Anti-corrosion performance of the synergistic properties of benzenecarbonitrile and 5-bromovanillin on 1018 carbon steel in HCl environment, *Scientific Reports* 7 (2017), <https://doi.org/10.1038/s41598-017-17867-0>.
- [100] J. Wynn, Lipids, Fatty Acids, *Comprehensive Biotechnology* (Third Edition), Pergamon, (2011) 39-50, <https://doi.org/10.1016/B978-0-444-64046-8.00005-7>.
- [101] Ma. Bonto, A. A. Eftekhari and H. M. Nick, An overview of the oil-brine interfacial behavior and a new surface complexation model, *Scientific Reports* 9 (2019), <https://doi.org/10.1038/s41598-019-42505-2>.
- [102] J. Zhang, D. Ge, X. Wang, W. Wang, D. Cui, G. Yuan, K. Wang, and W. Zhang, Influence of Surfactant and Weak-Alkali Concentrations on the Stability of O/W Emulsion in an Alkali-Surfactant–Polymer Compound System, *ACS Omega*, 6 (2021) 5001-5008.
- [103] W. Zheng, X. Wu, Y. Huang, Impact of polymer addition, electrolyte, clay and antioxidant on rheological properties of polymer fluid at high temperature and high pressure, *Journal of Petroleum Expolaration and Production Technology* 10 (2020) 663-671.
- [104] J. Liu, Zh. Dai, K. Xu, Y. Yang, K. Lv, X. Huang, J. Sun, Water-Based Drilling Fluid Containing Bentonite/Poly(Sodium 4-Styrenesulfonate) Composite for Ultrahigh-Temperature Ultradeep Drilling and Its Field Performance, *Society of Petroleum Engineers*, 25 (2020) 1193-1203.
- [105] M.J. Palimi, E. Alibakhshi, B. Ramezanzadeh, G. Bahlakeh, M. Mahdavian, Screening the anti-corrosion effect of a hybrid pigment based on zinc acetyl acetate on the corrosion protection performance of an epoxy-ester polymeric coating, *Journal of the Taiwan Institute of Chemical Engineers* 82 (2018) 261-272.

- [106] E. Alibakhshi E. Ghasemi M. Mahdavian B. Ramezanzadeh, A comparative study on corrosion inhibitive effect of nitrate and phosphate intercalated Zn-Al- layered double hydroxides (LDHs) nanocontainers incorporated into a hybrid silane layer and their effect on cathodic delamination of epoxy topcoat, *Corrosion Science* 115 (2017) 159-174.
- [107] M. J. Palimi, M. Rostami, M. Mahdavian, B. Ramezanzadeh, A study on the corrosion inhibition properties of silane-modified Fe₂O₃ nanoparticle on mild steel and its effect on the anticorrosion properties of the polyurethane coating, *Journal of Coating Technology and Research* 12 (2015) 277-292.
- [108] J. Porcayo-Calderon, E.M. Rivera-Muñoz, C. Peza-Ledesma, M. Casales-Diaz, L.M. Martínez dela Escalera, J. Canto and L. Martinez-Gomez, Sustainable Development of Palm Oil: Synthesis and Electrochemical Performance of Corrosion Inhibitors, *Journal of Electrochemical Science and Technology* 8 (2017) 133-145.
- [109] M. Mahdavian, M.M. Attar, Another approach in analysis of paint coatings with EIS measurement: Phase angle at high frequencies, *Corrosion Science* 48 (2006) 4152-4157.
- [110] F. Askari, E. Ghasemi, B. Ramezanzadeh, M. Mahdavian, Potassium Zinc Phosphate Pigment Coupled with Benzotriazole for Enhanced Protection of Carbon Steel, *Corrosion*, 72 (2016) 1526-1538.
- [111] M. Tourabi, K. Nohair, M. Traisnel, C. Jama, F. Bentiss, Electrochemical and XPS studies of the corrosion inhibition of carbon steel in hydrochloric acid pickling solutions by 3,5-bis(2-thienylmethyl)-4-amino-1,2,4-triazole, *Corrosion Science* 75 (2013) 123-133.
- [112] M. J. Palimi, M. Rostami, M. Mahdavian, B. Ramezanzadeh, Surface modification of Fe₂O₃ nanoparticles with 3-aminopropyltrimethoxysilane (APTMS): An attempt to investigate surface treatment on surface chemistry and mechanical properties of polyurethane/ Fe₂O₃ nanocomposites, *Applied Surface Science* 320 (2014) 60-72.
- [113] F. Askari, E. Ghasemi, B. Ramezanzadeh, M. Mahdavian, Mechanistic approach for evaluation of the corrosion inhibition of potassium zinc phosphate pigment on the steel surface:

Application of surface analysis and electrochemical techniques, *Dyes and Pigments* 109 (2014) 189-199.

[114] T. Yamashita, P. Hayes, Analysis of XPS spectra of Fe²⁺ and Fe³⁺ ions in oxide materials, *Applied Surface Science* 254 (2008) 2441-2449.

[115] M. Ghaffari, M. R. Saeb, B. Ramezanzadeh, P. Taheri, Demonstration of epoxy/carbon steel interfacial delamination behavior: Electrochemical impedance and X-ray spectroscopic analyses, *Corrosion Science* 102 (2016) 326-337.

[116] B. Ramezanzadeh, Gh. Bahlakeh, M. Ramezanzadeh, Polyaniline-cerium oxide (PANI-CeO₂) coated graphene oxide for enhancement of epoxy coating corrosion protection performance on mild steel, *Corrosion Science* 137 (2018) 111-126.

[117] M. Finšgar, D. Merl, An electrochemical, long-term immersion, and XPS study of 2-mercaptobenzothiazole as a copper corrosion inhibitor in chloride solution, *Corrosion Science* 83 (2014) 164-175.

[118] M. Damej, M. Benmessaoud, S. Zehra, S. Kaya, Hassane Lgaz, A. Molhi, N. Labjar, S. El Hajjaji, Awad A. Alrashdi, Han-Seung Lee, Experimental and theoretical explorations of S-alkylated mercaptobenzimidazole derivatives for use as corrosion inhibitors for carbon steel in HCl, *Journal of Molecular Liquids* 331 (2021), <https://doi.org/10.1016/j.molliq.2021.115708>.

[119] L. Mao, M. Cai, Q. Liu, Q. Wang, Y. Fan, Y. He, G. Wang. Effects of Nano-SiO₂ Addition in Drilling Fluid on Wear Behavior of 2Cr13 Steel Casing. *Tribology Letters* 2020; 68, <https://doi.org/10.1007/s11249-019-1253-9>.

[120] T. A. Bertness, G. V. Chilingarian, M. Al-Bassam. Chapter 8- Corrosion in Drilling and Producing Operations, *Developments in Petroleum Science*, Elsevier; 1989, p. 283-317.

[121] J. G. Speight. Chapter e1- Corrosion, *Oil and Gas Corrosion Prevention*, Gulf Professional Publishing; 2014, p. e1-e24, <https://doi.org/10.1016/B978-0-12-800346-6.00001-6>.

[122] S. Mischler, A. I. Munoz. Tribocorrosion. *Encyclopedia of Interfacial Chemistry*, Elsevier; 2018, p. 504-514, <https://doi.org/10.1016/B978-0-12-409547-2.13424-9>.

- [123] S. Alkan, M. S. Gök, Effect of sliding wear and electrochemical potential on tribocorrosion behavior of AISI 316 stainless steel in seawater. *Engineering Science and Technology, an International Journal* 2021;24: 524–532.
- [124] Y. Sun, V. Rana. Tribocorrosion behavior of AISI 304 stainless steel in 0.5 M NaCl solution. *Materials Chemistry and PPhysics* 2011; 129: 138– 147.
- [125] A. Siddaiah, A. Kasar, R. Ramachandran, P. L. Menezes. Chapter 1- Introduction to tribocorrosion, Academic Press; 2021, p. 1-16, <https://doi.org/10.1016/B978-0-12-818916-0.00002-X>.
- [126] P. Renner, Y. Chen, Zh. Huang, A. Raut and H. Liang. Tribo-corrosion Influenced Pitting of a Duplex Stainless Steel. *Lubricants* 2021; 9, <https://doi.org/10.3390/lubricants9050052>.
- [127] M. Oukni, Y. Yang, J. Paolini, J. Costa, P. Ponthiaux, L. Majidi, The Effect of Corsican Poplar Leaf Buds (*Populus nigra* var. *italica*) Essential Oil on the Tribo-corrosion Behavior of 304L Stainless Steel in the Sulfuric Medium. *Journal of Bio and Tribo-Corrosion* 2019; 5:83, <https://doi.org/10.1007/s40735-019-0275-z>.
- [128] A. Lopez-ortega, J. L. Arana, R. Bayon, On the comparison of the tribo-corrosion behavior of passive and non-passivating materials and assessment of the influence of agitation. *Wear* 2020; 456-457, <https://doi.org/10.1016/j.wear.2020.203388>.
- [129] Ch. Yan, Q. Zeng, W. He, J. Zhu. Enhanced surface hardness and tribo-corrosion performance of 60NiTi by boron ion implantation and post-annealing. *Tribology International* 2021; 155, <https://doi.org/10.1016/j.triboint.2020.106816>.
- [130] H. Xiao, Sh. Liu, Y. Chen, D. Han, D. Wang. Impacts of polypropylene glycol (PPG) additive and pH on tribological properties of water based drilling mud for steel-steel contact. *Tribology International* 2017; 110:318-325.
- [131] J. Hairui, Zh. Xu, and T. Tianwei. Preparation of a Water-Based Lubricant from Lignocellulosic Biomass and Its Tribological Properties. *Industrial & Engineering Chemistry Research* 2017; 56: 7858–7864.

- [132] P. Lan P, L. Iaccino, X. Bao, A. Polycarpou. The effect of lubricant additives on the tribological performance of oil and gas drilling applications up to 200°C. *Tribology International* 2020; 141, <https://doi.org/10.1016/j.triboint.2019.105896>.
- [133] J. Abdo. Nano-attapulgitite for improved tribological properties of drilling fluids. *Surf Interface Anal* 2014; 46: 882–887.
- [134] P. Lan, A. Polycarpou. Stribeck performance of drilling fluids for oil and gas drilling at elevated temperatures. *Tribology International* 2020; 151, <https://doi.org/10.1016/j.triboint.2020.106502>.
- [135] Y. Chen, R. Wu, J. Zhou, H. Chen, Y. Tan. A novel hyper-cross-linked polymer for high-efficient fluid-loss control in oil-based drilling fluids. *Colloids and Surfaces A: Physicochemical and Engineering Aspects* 2021; 626, <https://doi.org/10.1016/j.colsurfa.2021.127004>.
- [136] M. M. Fayad, D. E. Mohamed, E. A. Soliman, M. El-Fattah, S. Ibrahim, M. M. Dardir. Optimization of invert emulsion oil-based drilling fluids performance through heterocyclic imidazoline-based emulsifiers. *Colloids and Surfaces A: Physicochemical and Engineering Aspects* 2021; 613, <https://doi.org/10.1016/j.colsurfa.2020.126092>.
- [137] M. Ji, Sh. Liu & H. Xiao, Effect of Ionic Liquids as Additives in Water-based Drilling Mud for Steel-steel Friction Pair. *Tribology Transaction* 2020; 63: 453-467.
- [138] J. Ma, J. Xu, Sh. Pang, W. Zhou, B. Xia, and Y. An. Novel Environmentally Friendly Lubricants for Drilling Fluids Applied in Shale Formation. *Energy Fuels* 2021; 35: 8153–8162.
- [139] H. R. Saffari, R. Soltani, M. Alaei, M. Soleymani. Tribological properties of water-based drilling fluids with borate nanoparticles as lubricant additives. *Journal of Petroleum Science and Engineering* 2018; 171: 253-259.
- [140] Y. Jeng, P. Tsai, Ch. Chang and K. Hsu. Tribological Properties of Oil-in-Water Emulsion with Carbon Nanocapsule Additives. *Materials* 2020; 13, <https://doi:10.3390/ma13245762>.

- [141] J. Wang, W. Hu and J. Li. Lubrication and Anti-Rust Properties of Jeffamine-Triazole Derivative as Water-Based Lubricant Additive. *Coatings* 2021; 11, <https://doi.org/10.3390/coatings11060679>.
- [142] L. Guo, J. Tan, S. Kaya, S. Leng, Q. Li, F. Zhang. Multidimensional insights into the corrosion inhibition of 3,3- dithiodipropionic acid on Q235 steel in H₂SO₄ medium: A combined experimental and in silico investigation. *Journal of Colloid and Interface Science* 2020; 570: 116–124.
- [143] S. Marzorati, L. Verotta and S. P. Trasatti. Green Corrosion Inhibitors from Natural Sources and Biomass Wastes. *Molecules* 2019; 24, 48; <https://doi.org/10.3390/molecules24010048>.
- [144] B. Tan, B. Xiang, Sh. Zhang, Y. Qiang, L. Xu, Sh. Chen, He J. Papaya leaves extract as a novel eco-friendly corrosion inhibitor for Cu in H₂SO₄ medium. *Journal of Colloid and Interface Science* 2021;582: 918–931.
- [145] I. A. HadiAlnashia, I. I. Mohamed, M. M. Almelian, M. A. Omran. The Impact of Partial Discharge on the Dielectric Properties of Refined Bleached and Deodorized Palm Oil (RBDPO). *Journal of Telecommunication, Electronic and Computer Engineering* 2018; 10:81-85.
- [146] R. Khan, M. A. Inam, S. Khan, A. N. Jiménez, D. R. Park and I. T. Yeom. The Influence of Ionic and Nonionic Surfactants on the Colloidal Stability and Removal of CuO Nanoparticles from Water by Chemical Coagulation. *International Journal of Environmental Research and Public Health* 2019; 16:1-17.
- [147] Ch. Yuan, W. Pu, X. Wang, L. Sun, Y. Zhang, and Sh. Cheng. The effects of interfacial tension, emulsification and surfactant concentration on oil recovery in surfactant flooding process for high temperature and high salinity reservoirs. *Energy Fuels* 2015; 29: 6165–6176.
- [148] O. Sarheed, M. Dibi and K. Ramesh. Studies on the Effect of Oil and Surfactant on the Formation of Alginate-Based O/W Lidocaine Nanocarriers Using Nanoemulsion Template. *Pharmaceutics* 2020; 12, <http://doi:10.3390/pharmaceutics12121223>.

- [149] L. Moreau, H. Kim, E. A. Decker, and J. McCleme. Production and Characterization of Oil-in-Water Emulsions Containing Droplets Stabilized by β -Lactoglobulin-Pectin Membranes. *Journal of Agricultural and Food Chemistry* 2003; 51: 6612-6617.
- [150] S. Alkan, M. Sabri Gök. Effect of sliding wear and electrochemical potential on tribocorrosion behaviour of AISI 316 stainless steel in seawater. *Engineering Science and Technology, an International Journal* 24 (2021) 524–532. <https://doi.org/10.1016/j.jestch.2020.07.004>.
- [151] A. López-Ortega, J. L. Arana, E. Rodríguez, R. Bayón. Corrosion, wear and tribocorrosion performance of a thermally sprayed aluminum coating modified by plasma electrolytic oxidation technique for offshore submerged components protection. *Corrosion Science* 143 (2018)258–280. <https://doi.org/10.1016/j.corsci.2018.08.001>.
- [152] Y. Zhang, X. Yin, J. Wang, and F. Yan. Influence of potentials on the tribocorrosion behavior of 304SS in artificial seawater. *RSC Advances* 4 (2014) 55752. <https://doi.org/10.1039/C4RA05831C>.
- [153] M. Ouknin, J. Costa, L. Majidi. Tribocorrosion and electrochemical behavior of AISI 304L stainless steel in acid medium and Thymus willdenowii Boiss & Reut essential oil effect. *Chemical Data Collections* 28 (2020) 100389. <https://doi.org/10.1016/j.cdc.2020.100389>.
- [154] J. Villanueva, L. Trino, J. Thomas, D. Bijukumar, D. Royhman, M. M. Stack, M. T. Mathew, Corrosion, tribology, and tribocorrosion research in biomedical implants: progressive trend in the published literature. *Journal of Bio and Tribo-Corrosion* 3 (2017), <https://doi.org/10.1007/s40735-016-0060-1>.
- [155] L. Mao, M. Cai, G. Wang. Effect of rotation speed on the abrasive–erosive–corrosive wear of steel pipes against steel casings used in drilling for petroleum. *Wear* 410–411 (2018) 1–10. <https://doi.org/10.1016/j.wear.2018.06.002>.
- [156] P. Lan, K. Polychronopoulou, L.L. Iaccino, X. Bao, A. A. Polycarpou. Elevated-temperature and -pressure tribology of drilling fluids used in oil and gas extended-reach-drilling applications. *SPE J.* 23 (2018) 2339–2350.

- [157] Q. J. Wang, Y. W. Chung. Encyclopedia of tribology, Springer, (2013) 1903-2158, <https://doi.org/10.1007/978-0-387-92897-5>.
- [158] A. Gad Elshafie, A. M. El-Shamy. Mechanism of corrosion and microbial corrosion of 1,3-dibutyl thiourea using the quantum chemical calculations. Journal of Bio and Tribo. Corrosion 8 (2022) 71, <https://doi.org/10.1007/s40735-022-00669-x>.
- [159] A. M. Abdel-Karim, A. M. El-Shamy, Y. Reda, Corrosion and stress corrosion resistance of Al Zn alloy 7075 by nano-polymeric coatings. Journal of Bio and Tribo. Corrosion 8 (2022) 57, <https://doi.org/10.1007/s40735-022-00656-2>.
- [160] A.M. El-Shamy, Kh. Zakaria, M.A. Abbas, S. Z. El-Abedin, Anti-bacterial and anti-corrosion effects of the ionic liquid 1-butyl-1-methylpyrrolidinium trifluoromethylsulfonate. Journal of Molecular Liquids 211 (2015) 363–369. <https://doi.org/10.1016/j.molliq.2015.07.028>.
- [161] A.M. El-Shamy, M. Abdelbar. Ionic liquid as water soluble and potential inhibitor for corrosion and microbial corrosion for iron artifacts. Egyptian Journal of Chemistry. 64 (2021) 1867-1876. [10.21608/ejchem.2021.43786.2887](https://doi.org/10.21608/ejchem.2021.43786.2887).
- [162] Y. L. Kobzar, K. Fatyeyeva, Ionic liquids as green and sustainable steel corrosion inhibitors: Recent developments. Chemical Engineering Journal 425 (2021) 131480. <https://doi.org/10.1016/j.cej.2021.131480>.
- [163] D. K. Verma, R. Aslam, J. Aslam, M. A. Quraishi, E. E. Ebenso, Ch. Verma, Computational modeling: theoretical predictive tools for designing of potential organic corrosion inhibitors. Journal of Molecular Structure 1236 (2021) 130294. <https://doi.org/10.1016/j.molstruc.2021.130294>.
- [164] D. S. Chauhan, Ch. Verma, M. A. Quraishi. Molecular structural aspects of organic corrosion inhibitors: Experimental and computational insights. Journal of Molecular Structure 1227 (2021) 129374. <https://doi.org/10.1016/j.molstruc.2020.129374>.
- [165] A. M. Abdel-Karim, A.M. El-Shamy, A review on green corrosion inhibitors for protection of archeological metal artifacts. Journal of Bio and Tribo-Corrosion 8 (2022) 35, <https://doi.org/10.1007/s40735-022-00636-6>.

- [166] M. A. Abbas, A. S. Ismail, K. Zakaria, A. M. El-Shamy & S. El-Abedin, Adsorption, thermodynamic, and quantum chemical investigations of an ionic liquid that inhibits corrosion of carbon steel in chloride solutions. *Scientific Reports* 12 (2022) 12536, <https://doi.org/10.1038/s41598-022-16755-6>.
- [167] M. A. Quraishi, D. S. Chauhan, F. A. Ansari, Development of environmentally benign corrosion inhibitors for organic acid environments for oil-gas industry. *Journal of Molecular Liquids* 329 (2021) 115514. <https://doi.org/10.1016/j.molliq.2021.115514>.
- [168] D. K. Verma, M. Kazi, M. S. Alqahtani, R. Syed, Berdimurodov E, Savas Kaya, Salim R, Asatkar A, Haldhar R. N-hydroxybenzothioamide derivatives as green and efficient corrosion inhibitors for mild steel: Experimental, DFT and MC simulation approach. *Journal of Molecular Structure* 1241(2021) 130648. <https://doi.org/10.1016/j.molstruc.2021.130648>.
- [169] S. Paul, I. Koley (2016) Corrosion inhibition of carbon steel in acidic environment by papaya seed as green inhibitor. *Journal of Bio and Tribo-Corrosion* 6, <https://doi.org/10.1007/s40735-016-0035-2>.
- [170] F. El-Hajjaji, R. Salim, M. Messali, B. Hammouti, D. S. Chauhan, S. M. Almutairi, M. A. Quraishi, Electrochemical studies on new pyridinium derivatives as corrosion inhibitors of carbon steel in acidic medium. *Journal of Bio and Tribo-Corrosion* 4 (2019), <https://doi.org/10.1007/s40735-018-0195-3>.
- [171] M. F. Shehata, A. M. El-Shamy, Kh. Zohdy, E. M. Sherif and Sh. El-Abedin, Studies on the antibacterial influence of two ionic liquids and their corrosion inhibition performance. *Applied science* 10 (2020) 1444, <https://doi.org/10.3390/app10041444>.
- [172] M. A. Abbas, Kh. Zakaria, A. M. El-Shamy and Sh. El-Abedin, Utilization of 1 butylpyrrolidinium Chloride Ionic Liquid as an Eco-friendly Corrosion Inhibitor and Biocide for Oilfield Equipment: Combined Weight Loss, Electrochemical and SEM Studies, *Zeitschrift für Physikalische Chemie*. 235 (2019) 377-406, <https://doi.org/10.1515/zpch-2019-1517>.

- [173] X. Liu, Q. Shen, X. Shi, J. Zou, Y. Huang, A. Zhang, Z. Yan, X. Deng, and K. Yang, Effect of applied load and sliding speed on tribological behavior of TiAl-Based self-lubricating composites. *Journal of Materials Engineering and Performance* 27 (2018) 194-201. [10.1007/s11665-017-3106-8](https://doi.org/10.1007/s11665-017-3106-8)
- [174] J. Shen, Ch. Wu & L. Zhang, Effects of sliding speed and lubrication on the tribological behavior of stainless steel. *International Journal of Advanced Manufacturing Technology* 94 (2018) 341–350. <https://doi.org/10.1007/s00170-017-0907-8>.
- [175] H. Zhao, G. C. Barber, J. Liu, Friction and wear in high-speed sliding with and without electrical current. *Wear* 249 (2001) 409–414. [https://doi.org/10.1016/S0043-1648\(01\)00545-2](https://doi.org/10.1016/S0043-1648(01)00545-2).
- [176] Z. Xu, X. Shi, Q. Zhang, W. Zhai, X. Li, J. Yao, L. Chen, Q. Zhu, Y. Xiaov, Effect of sliding speed and applied load on dry sliding tribological performance of TiAl matrix self-lubricating composites. *Tribology Letter* 55 (2014) 393–404. <https://doi.org/10.1007/s11249-014-0367-3>.
- [177] N. Saka, A. M. Eleiche, N. P. Suh, Wear of metals at high sliding speeds. *Wear* 44 (1977) 109-125. [https://doi.org/10.1016/0043-1648\(77\)90089-8](https://doi.org/10.1016/0043-1648(77)90089-8).
- [178] F. A. Essa, A. H. Elsheikh, J. Yu, O. A. Elkady, B. Saleh, Studies on the effect of applied load, sliding speed and temperature on the wear behavior of M50 steel reinforced with Al₂O₃ and / or graphene nanoparticles. *Journal of Materials Research and Technology* 12 (2021) 283-303. <https://doi.org/10.1016/j.jmrt.2021.02.082>.
- [179] M. J. Palimi, Y. Tang, V. Alvarez, E. Kuru, D. Y. Li, Green corrosion inhibitors for drilling operation: New derivatives of fatty acid-based inhibitors in drilling fluids for 1018 carbon steel in CO₂-saturated KCl environments. *Materials Chemistry and Physics*. 288 (2022) 126406. <https://doi.org/10.1016/j.matchemphys.2022.126406>.
- [180] R. Namus, J. Nutter, J. Qi, W. M. Rainforth, Sliding speed influence on the tribo-corrosion behaviour of Ti6Al4V alloy in simulated body fluid. *Tribology International* 160 (2021) 107023. <https://doi.org/10.1016/j.triboint.2021.107023>.
- [181] M. J. Palimi, Y. Tang, M. Wu, V. Alvarez, M. Ghavidel, E. Kuru, Q. Y. Li, W. Li, D. Y. Li, Improve the tribo-corrosion behavior of oil-in-water emulsion-based drilling fluids by new

derivatives of fatty acid-based green inhibitors. *Tribology International* 174 (2022) 107723. <https://doi.org/10.1016/j.triboint.2022.107723>.

[182] Ph. Refait, A. Grolleau, M. Jeannin, C. Remazeilles and Sabot R, Corrosion of carbon steel in marine environments: role of the corrosion product layer. *Corrosion Materials Degradation* 1 (2020) 198-218. <https://doi.org/10.3390/cmd1010010>.

[183] L. Mao, M. Cai, Q. Liu, X. Wang, Y. Fan, Y. He, G. Wang, Effects of Nano-SiO₂ Addition in Drilling Fluid on Wear Behavior of 2Cr13 Steel Casing, *Tribology Letters* 68:10 (2020), <https://doi.org/10.1007/s11249-019-1253-9>.

[184] Y. Wang, J. Zhang, Sh. Zhou, Y. Wang, Ch. Wang, Y. Wang, Y. Sui, J. Lan, Q. Xue, Improvement in the tribocorrosion performance of CrCN coating by multilayered design for marine protective application, *Applied Surface Science* 528 (2020) 147061, <https://doi.org/10.1016/j.apsusc.2020.147061>.

[185] F. Toptan, A. Rego, A.C. Alves, A. Guedes, Corrosion and tribocorrosion behavior of Ti–B4C composite intended for orthopaedic implants, *Journal of the Mechanical Behavior of Biomedical Materials* 61 (2016) 152-163.

[186] P. Ponthiaux, F. Wenger, D. Drees, J.P. Celis, Electrochemical techniques for studying tribocorrosion processes, *Wear* 256 (2004) 459-468.

[187] L. Benea, F. Wenger, P. Ponthiaux, J.P. Celis, Tribocorrosion behaviour of Ni–SiC nanostructured composite coatings obtained by electrodeposition, *Wear* 266 (2009) 398–405.

[188] K. Sadiq, M.M. Stack, R.A. Black, Wear mapping of CoCrMo alloy in simulated bio-tribocorrosion conditions of a hip prosthesis bearing in calf serum solution, *Materials Science and Engineering:C* 49 (2015) 452–462.

[189] R. Priya, C. Mallika, U. K. Mudali, Wear and tribocorrosion behavior of 304L SS, Zr-702, Zircaloy-4 and Ti-grade2, *Wear* 310 (2014) 90–100.

[190] Y.N. Kok, R. Akid, P.Eh. Hovsepian, Tribocorrosion testing of stainless steel (SS) and PVD coated SS using a modified scanning reference electrode technique, *Wear* 259 (2005) 1472–1481.

- [191] D.Y. Li, Corrosive wear failure, in ASM Handbook, Vol.11, Failure Analysis and Prevention, edited by B. Miller, R. Shiplay, R. Parrington, D. Dennies, 2021, Doi: <https://doi.org/10.31399/asm.hb.v11.a0006794>.
- [192] D.Y. Li, Corrosive Wear. In: Wang, Q.J., Chung, YW. (eds) Encyclopedia of Tribology. 2013 Springer, Boston, MA. https://doi.org/10.1007/978-0-387-92897-5_866.
- [193] L. Vilhena, G. Opong, A. Ramalho, Tribocorrosion of different biomaterials under reciprocating sliding conditions in artificial saliva, Lubrication Science (2019)1–17.
- [194] B. Zhang, J. Wang, Y. Zhang, G. Han, and F. Yan, Comparison of tribocorrosion behavior between 304 austenitic and 410 martensitic stainless steels in artificial seawater, RSC Advances 6 (2016) 107933.
- [195] E. Huttunen-Saarivirta, L. Kilpi, T.J. Hakala, L. Carpen, H. Ronkainen, Tribocorrosion study of martensitic and austenitic stainless steels in 0.01 M NaCl solution, Tribology International 95 (2016) 358–371.
- [196] M. Ziomek-Moroz, A. Miller, J. Hawk, K. Cadien, D.Y. Li, An overview of corrosion-wear interaction for planarizing metallic thin films, Wear, 255 (2003) 869-874.
- [197] Q. Bi, W. Liu, J. Ma, J. Yang, Y. Pu, Q. Xue, Tribocorrosion behavior of Ni-17.5Si-29.3Cr alloy in sulfuric acid solution, Tribology International 42 (2009) 1081–1087.
- [198] X. Wang, Y. Wang, Zh. Huang, Q. Zhou, and H. Wang, Tribocorrosion Behavior of CoCrNi Medium Entropy Alloy in Simulated Seawater, Metals 12 (2022) 401, <https://doi.org/10.3390/met12030401>.
- [199] S. Mischler, A. Spiegel, D. Landolt, the role of passive oxide films on the degradation of steel in tribocorrosion systems, Wear 225–229 (1999) 1078–1087.
- [200] M. T. Mathew, P. Srinivasa Pai, R. Pourzal, A. Fischer, and M. A. Wimmer, Significance of Tribocorrosion in Biomedical Applications: Overview and Current Status, Adv. Tribol. (2009) <https://doi.org/10.1155/2009/250986>.

- [201] A. Rostami, H. A. Nasr-El-Din, Review and Evaluation of Corrosion Inhibitors Used in Well Stimulation, SPE International Symposium on Oilfield Chemistry, The Woodlands, Texas, April 2009. <https://doi.org/10.2118/121726-MS>.
- [202] B. Tiu, C. Advincula, Polymeric corrosion inhibitors for the oil and gas industry: Design principles and mechanism, *Reactive and Functional Polymers* 95 (2015) 25–45.
- [203] A. M. Elsharif, I. Abdulazeez , M. A. Almarzooq, Sh. A. Haladu, Synthesis, and experimental evaluation of novel 4-(-3-(2-hydroxyethoxy)-3oxopropenyl)-1,2-phenylene nanohybrid derivatives as potential corrosion inhibitors for mild steel in 1 M HCl, *Journal of Industrial and Engineering Chemistry* 116 (2022) 474-488.
- [204] R. Aslam, M. Mobin, Huda, M. Shoeb, M. Murmu, P. Banerjee, Proline nitrate ionic liquid as high temperature acid corrosion inhibitor for mild steel: Experimental and molecular-level insights, *Journal of Industrial and Engineering Chemistry* 100 (2021) 333-350.
- [205] S. Alareeqi, D. Bahamon, R. P. Nogueira, L. F. Vega, Understanding the relationship between the structural properties of three corrosion inhibitors and their surface protectiveness ability in different environments, *Applied Surface Science* 542 (2021) 148600, <https://doi.org/10.1016/j.apsusc.2020.148600>.
- [206] Q. H. Zhang, Y. Y. Li, Y. Lei, X. Wang, H.F. Liu, G.A. Zhang, Comparison of the synergistic inhibition mechanism of two eco-friendly amino acids combined corrosion inhibitors for carbon steel pipelines in oil and gas production, *Applied Surface Science* 583 (2022) 152559, <https://doi.org/10.1016/j.apsusc.2022.152559>.
- [207] L. Mao, M. Cai, G. Wang, Effect of rotation speed on the abrasive—erosive—corrosive wear of steel pipes against steel casings used in drilling for petroleum, *Wear* 410-411 (2018) 1-10.
- [208] M. Muro, G. Artola, A. Gorriño, and C. Angulo, Wear and Friction Evaluation of Different Tool Steels for Hot Stamping, *Advances in Materials Science and Engineering* (2018), <https://doi.org/10.1155/2018/3296398>.

- [209] Th. Nguyen, S. Chang, B. Condon, R. Slopek, E. Graves, and M. Yoshioka-Tarver, Structural Effect of Phosphoramidate Derivatives on the Thermal and Flame-Retardant Behaviors of Treated Cotton Cellulose, *Industrial & Engineering Chemistry Research* 52 (2013) 4715-4724.
- [210] X. Hu, H. Yang, Y. Jiang, H. He, H. Liu, H. Huang, Ch. Wan, Facile synthesis of a novel transparent hyperbranched phosphorous/nitrogen-containing flame retardant and its application in reducing the fire hazard of epoxy resin, *Journal of Hazardous Materials* 379 (2019) 120793.
- [211] Ch. Jiang, Y. Wang, H. Su, W. Li, W. Lou, X. Wang, Synthesis, and evaluation of a protic ionic liquid as a multifunctional lubricant additive, *Friction* 8 (2020) 568–576.
- [212] M. Krstić, Đ. Medarević, J. Đuriš, S. Ibrić, Chapter 12 - Self-nanoemulsifying drug delivery systems (SNEDDS) and self-microemulsifying drug delivery systems (SMEDDS) as lipid nanocarriers for improving dissolution rate and bioavailability of poorly soluble drugs, *Lipid Nanocarriers for Drug Targeting*, William Andrew Publishing (2018) 473-508.
- [213] B. Wang, H. Tian, and D. Xiang, Stabilizing the Oil-in-Water Emulsions Using the Mixtures of *Dendrobium Officinale* Polysaccharides and Gum Arabic or Propylene Glycol Alginate, *Molecules* 25 (2020) 759; doi:10.3390/molecules25030759.
- [214] E. Rezvani, G. Schleining, A. R. Taherian, Assessment of physical and mechanical properties of orange oil-in-water beverage emulsions using response surface methodology, *LWT - Food Sci. Technol.* 48 (2012) 82-88.
- [215] P. Refait, A. Grolleau, M. Jeannin, C. Remazeilles, R. Sabot, Corrosion of carbon steel in marine environments: role of the corrosion product layer. *Corrosion and Materials Degradation*, 1 (2020) 198–218. <https://doi.org/10.3390/cmd1010010>.
- [216] X. Dong, X. Zhai, Y. Zhang, J. Yang, F. Guan, J. Duan, J. Sun, R. Zhang, B. Hou, Steel rust layers immersed in the South China Sea with a highly corrosive *Desulfovibrio* strain. *npj Materials Degradation*, 91 (2022). <https://doi.org/10.1038/s41529-022-00304-7>.
- [217] Y. Kim and J. Kim, Corrosion Behavior of Pipeline Carbon Steel under Different Iron Oxide Deposits in the District Heating System, *Metals*, 7 (2017), <https://doi.org/10.3390/met7050182>.

- [218] H. Becerra, C. Retamoso, Digby D. Macdonald, The corrosion of carbon steel in oil-in-water emulsions under controlled hydrodynamic conditions, *Corrosion Sciences* 42 (2000) 561-575.
- [219] E. Gulbrandsen and J. Kvarekvål, Effect of Oil-in-Water Emulsions on the Performance of Carbon Dioxide Corrosion Inhibitors, *corrosion*, 63 (2017) 187-196.
- [220] M. Askari, M. Aliofkhaezaei, R. Jafari, P. Hamghalam, A. Hajizadeh, Downhole corrosion inhibitors for oil and gas production – a review, *Applied Surface Science Advances* 6 (2021) 100128. <https://doi.org/10.1016/j.apsadv.2021.100128>.
- [221] B. A. Alink, B. Outlaw, V Jovancicevic, S. Ramachandran and S. Campbell, Mechanism of CO₂ Corrosion Inhibition by Phosphate Esters, *Corrosion* 99, San Antonio, Texas, April 1999.
- [222] D. Zheng, T. Su, Ch. Ju, Influence of ecofriendly protic ionic liquids on the corrosion and lubricating properties of water-glycol, *Tribology International* 165 (2022) 107283.
- [223] M. J. Palimi, M. Rostami, M. Mahdavian, B. Ramezanzadeh, Studying the effects of surface modification of Cr₂O₃ nanoparticles by 3-aminopropyltrimethoxysilane (APTMS) on its corrosion inhibitive performance, *Journal of Sol-Gel Science and Technology* 73 (2014) 141-153.
- [224] Y. Fu, F. Zhou, Q. Wang, M. Zhang, Zh. Zhou, Electrochemical and tribocorrosion performances of CrMoSiCN coating on Ti-6Al-4V titanium alloy in artificial seawater, *Corrosion Science* 165 (2020) 108385.
- [225] P. Fernández-López, S. A. Alves, I. Azpitarte, Jose T. San-Jose, R. Bayon, Corrosion and tribocorrosion protection of novel PEO coatings on a secondary cast Al-Si alloy: Influence of polishing and sol-gel sealing, *Corrosion Science* 207 (2022) 110548.
- [226] R. S. Oguike, O. Oni, A. U. Barambu, D. Balarak, T. Buba, Ch. U. Okeke, L. S. Momoh, Sh. Onimisi, W. J. Nwada, Computational Stimulation and Experimental Study on Corrosion Inhibition Qualities of Emilia sonchifolia Leaf Extract for Copper (CU131729) in Hydrochloric Acid, *Computational Chemistry*, 9 (2021) 18-36.

- [227] T. Dinh Manh, Th. Liem Huynh, B. Viet Thi, S. Lee, J. Yi, and N. Nguyen Dang, Corrosion Inhibition of Mild Steel in Hydrochloric Acid Environments Containing *Sonneratia caseolaris* Leaf Extract, Cite This: ACS Omega 2022, 7, 8874–8886.
- [228] S. Choudhary, K. Ogle, O. Gharbi, S. Thomas, N. Birbilis, Recent insights in corrosion science from atomic spectroelectrochemistry, *Electrochemical Science Advances* (2021) e2100196, <https://doi.org/10.1002/elsa.202100196>.
- [229] Koichi Hashiguchi, Chapter 10 - Subloading-friction model: finite sliding theory, *Nonlinear Continuum Mechanics for Finite Elasticity-Plasticity*, Elsevier, 2020 333-363, <https://doi.org/10.1016/B978-0-12-819428-7.00010-9>.
- [230] P. Ren, H. Meng, Q. Xia, Zh. Zhu, M. He, Influence of seawater depth and electrode potential on the tribocorrosion of Ti6Al4V alloy under the simulated deep-sea environment by in-situ electrochemical technique, *Corrosion Science* 180 (2021) 109185.
- [231] P. Ren, H. Meng, Q. Xia, Zh. Zhu, M. He, Tribocorrosion of 316L stainless steel by in-situ electrochemical methods under deep-sea high hydrostatic pressure environment, *Corrosion Science* 202 (2022) 110315.
- [232] A. M. El-Haddad, A. Bahgat Radwan, Mostafa H. Sliem, Walid M. I. Hassan & A. M. Abdullah, highly efficient eco-friendly corrosion inhibitor for mild steel in 5 M HCl at elevated temperatures: experimental & molecular dynamics study, *Scientific reports* 9 (2019) 6395.
- [233] N. Hashim, El. Anouar, K. Kassim, H. Mohd Zaki, A. Alharthi, Z. Embong, XPS and DFT investigations of corrosion inhibition of substituted benzylidene Schiff bases on mild steel in hydrochloric acid, *Applied Surface Science* 476 (2019) 861-877.
- [234] L. Chen, D. Lu and Y. Zhang, Organic Compounds as Corrosion Inhibitors for Carbon Steel in HCl Solution: A Comprehensive Review, *Materials* 15 (2022) 2023.
- [235] A. Dehghani, Gh. Bahlakeh, B. Ramezanzadeh, Green Eucalyptus leaf extract: A potent source of bio-active corrosion inhibitors for mild steel, *Bioelectrochemistry* 130 (2019) 107339.

- [236] J. Li, W. Xu, D. Zhou, J. Luo, D. Zhang, P. Xu, L. Wei, and D. Yuan, Synthesis of 3D flower-like cobalt nickel phosphate grown on Ni foam as an excellent electrocatalyst for the oxygen evolution reaction, *Journal of Materials Science* 53 (2018) 2077–2086.
- [237] B. Mulik, T. Dhupal, S. Sapner, N. M. A. Rehman, P. Dixit and R. Sathe, Graphene oxide-based electrochemical activation of ethionamide towards enhanced biological activity, *RSC Advances* 9 (2019) 35463–35472.
- [238] T.Q. Phan, T. Nguyen, H. Pham, T. Pham, Vi Vi Do, N. Hoang, N. Nguyen, J. Kim, and D. Hoang, Excellent Fireproof Characteristics and High Thermal Stability of Rice Husk-Filled Polyurethane with Halogen-Free Flame Retardant, *Polymers* 11 (2019) 1587.
- [239] L. Li, P. Ma, S. Hussain, L. Jia, D. Lin, X. Yin, Y. Lin, Z. Cheng, and L. Wang, FeS₂/carbon hybrids on carbon cloth: a highly efficient and stable counter electrode for dye-sensitized solar cell, *Sustain. Energy Fuels*. 3(2019), DOI: [10.1039/C9SE00240E](https://doi.org/10.1039/C9SE00240E).
- [240] E. Hoque, J.A. DeRose, B. Bhushan, K.W. Hipps, Low adhesion, non-wetting phosphonate self-assembled monolayer films formed on copper oxide surfaces, *Ultramicroscopy* 109 (2009) 1015–1022.
- [241] Ch. Wang, X. Qi, Y. Wang, B. Wu, and Y. Tian, Room-Temperature Direct Heterogeneous Bonding of Glass and Polystyrene Substrates, *Journal of Electrochemical Society* 165 (2018) B3091-B3097.
- [242] Y. Yao, N. Mahmood, L. Pan, G. Shen, R. Zhang, R. Gao, Fazal-e Aleem, X. Yuan, X. Zhang, and Ji-Jun Zou, Iron phosphide encapsulated in P-doped graphitic carbon as efficient and stable electrocatalyst for hydrogen and oxygen evolution reactions, *Nanoscale* 10 (2018) DOI: [10.1039/C8NR06752J](https://doi.org/10.1039/C8NR06752J).
- [243] T. Yamashita, P. Hayes, Analysis of XPS spectra of Fe²⁺ and Fe³⁺ ions in oxide materials, *Applied Surface Science* 254 (2008) 2441–2449.
- [244] Ji-Chao Wang, J. Ren, Hong-Chang Yao, L. Zhang, Jian-Sh. Wang, Shuang-Quan Zang, Li-Feng Han, Zhong-Jun Li, Synergistic photocatalysis of Cr (VI) reduction and 4-Chlorophenol

degradation over hydroxylated $\text{-Fe}_2\text{O}_3$ under visible light irradiation, *Journal of Hazardous Materials* 311 (2016) 11–19.

[245] James M. Howe, *Interfaces in Materials – atomic structure, thermodynamics, and kinetics of solid-vapor and solid-liquid interfaces*, John Wiley & Sons, Inc., 1997.

[246] M. J. Palimi, V. Alvarez, E. Kuru, W. G. Chen, D. Y. Li, Effects of Sliding Speed on Corrosion and Tribo-Corrosion of Carbon Steel in Emulsion-Based Drilling Fluids with Green Corrosion Inhibitors, *Journal of Bio- and Tribo-Corrosion* 9 (2023), <https://doi.org/10.1007/s40735-022-00722-9>.

[247] P. Lan, K. Polychronopoulou, L. L. Iaccino, X. Bao, A. A. Polycarpou, Elevated-temperature and—pressure tribology of drilling fluids used in oil and gas extended-reach-drilling applications. *SPE J* 23 (2018) 2339–2350.

[248] S.N. Chen, W.Q. Yan, B. Liao, X.Y. Wu, L. Chen, X. Ouyang, X.P. Ouyang, Effect of temperature on the tribocorrosion and high-temperature tribological behaviour of strong amorphization AlCrNiTiV high entropy alloy film in a multifactor environment, *Ceramics International* 49 (2023) 6880–6890.

[249] M. Keddam, P. Ponthiaux, V. Vivier, Tribo-electrochemical impedance: A new technique for mechanistic study in tribocorrosion, *Electrochimica Acta* 124 (2014) 3–8.

[250] P. Fernandez-Lopez, Sofia A. Alves, I. Azpitarte, Jose T. San-Jose, Raquel Bayon, Corrosion and tribocorrosion protection of novel PEO coatings on a secondary cast Al-Si alloy: Influence of polishing and sol-gel sealing, *Corrosion Science* 207 (2022) 110548.

[251] Zh. Li, H. Yu, D. Sun, The tribocorrosion mechanism of aluminum alloy 7075-T6 in the deep ocean, *Corrosion Science* 183 (2021) 109306.

[252] S. Soltanahmadi, A. Morina, Marcel C.P. van Eijk, I. Nedelcu, A. Neville, Tribochemical study of micropitting in tribocorrosive lubricated contacts: The influence of water and relative humidity, *Tribology International* 107 (2017) 184–198.

- [253] Y. Zhang, X. Yin, Y. Yan, J. Wang, and F. Yan, Tribocorrosion behaviors of 304SS: effect of solution pH, *RSC Advances*, 5 (2015) 17676-17682.
- [254] L. Tan, Zh. Wang, Y. Ma, Y. Yan, and L. Qiao, Tribocorrosion investigation of 316L stainless steel: the synergistic effect between chloride ion and sulfate ion, *Materials Research Express*, 8 (2021) 086501.
- [255] D. Niu, C. Zhang, X. Sui, X. Lu, X. Zhang, C. Wang, J. Hao, Zh. Shi, Microstructure, mechanical properties, and tribo-corrosion mechanism of $(\text{CrNbTiAlVMo})_x\text{N}_{1-x}$ coated 316 L stainless steel in 3.5 wt% NaCl solution, *Tribology International* 173 (2022) 107638.
- [256] M. Stemp, S. Mischler, D. Landolt, The effect of mechanical and electrochemical parameters on the tribocorrosion rate of stainless steel in sulphuric acid, *Wear* 255 (2003) 466–475.
- [257] R. Jamshidi, O. Bayat, A. Heidarpour, Tribological and corrosion behavior of flame sprayed Al–10 wt% Ti_3SiC_2 composite coating on carbon steel, *Surface & Coatings Technology* 358 (2019) 1–10.
- [258] Ch. Liu, Z. G. Neale, and G. Cao, Understanding electrochemical potentials of cathode materials in rechargeable batteries, *Materials Today*, 19 (2016) 109-123.
- [259] A. Igual Muñoz, L. Casabán Julián, Influence of electrochemical potential on the tribocorrosion behaviour of high carbon CoCrMo biomedical alloy in simulated body fluids by electrochemical impedance spectroscopy, *Electrochimica Acta*, 55 (2010) 5428–5439.
- [260] T. Eduardo Schmitzhaus, M. R. Ortega Vega, R. Schroeder, I. Lourdes Muller, S. Mattedi, M. Taryba, J. Carlos Salvador Fernandes, C. Fraga Malfatti, Localized corrosion behavior studies by SVET of 1010 steel in different concentrations of sodium chloride containing [m-2HEA] [OI] ionic liquid as corrosion inhibitor, *Electrochimica Acta*, 419 (2022) 140385.
- [261] E.M. Sherif, Su-Moon Park, Effects of 2-amino-5-ethylthio-1,3,4-thiadiazole on copper corrosion as a corrosion inhibitor in aerated acidic pickling solutions, *Electrochimica Acta*, 51 (2006) 6556–6562.

- [262] C. M. Fernandes, Th. da S. Ferreira Fagundes, N. Escarpini dos Santos, T. Shewry de M. Rocha, R. Garrett, R. Moreira Borges, G. Muricy, A. Leda Valverde, E. Ariel Ponzio, *Ircinia strobilina* crude extract as corrosion inhibitor for mild steel in acid medium, *Electrochimica Acta*, 312 (2019) 137e148.
- [263] M. Muro, G. Artola, A. Gorriño, and C. Angulo, Wear and Friction Evaluation of Different Tool Steels for Hot Stamping, *Advances in Materials Science and Engineering* (2018), <https://doi.org/10.1155/2018/3296398>.
- [264] Q. Bi, W. Liu, J. Ma, J. Yang, Y. Pu, Q. Xue, Tribocorrosion behavior of Ni-17.5Si-29.3Cr alloy in sulfuric acid solution, *Tribology International*, 42 (2009) 1081–1087.
- [265] Z. Wang, Y. Yan, Y. Wu, X. Huang, Y. Zhang, Y. Su, L. Qiao, Corrosion and tribocorrosion behavior of equiatomic refractory medium entropy TiZr(Hf, Ta, Nb) alloys in chloride solutions, *Corrosion Science*, 199 (2022) 110166.
- [266] M.T. Mathew, E. Ariza, L.A. Rocha, A.C. Fernandes, F. Vaz, TiC_xO_y thin films for decorative applications: Tribocorrosion mechanisms and synergism, *Tribology International*, 41 (2008) 603–615.
- [267] Ph. Refait, A. Grolleau, M. Jeannin, C. Rémazeilles and R. Sabot, Corrosion of carbon steel in marine environments: role of the corrosion product layer, corrosion, and materials degradation 1 (2020) 198-218.
- [268] T.Q. Phan, T. Nguyen, H. Pham, T. Pham, Vi Vi Do, N. Hoang, N. Nguyen, J. Kim, and D. Hoang, Excellent Fireproof Characteristics and High Thermal Stability of Rice Husk-Filled Polyurethane with Halogen-Free Flame Retardant, *Polymers*, 11 (2019) 1587.
- [269] L. Li, P. Ma, S. Hussain, L. Jia, D. Lin, X. Yin, Y. Lin, Z. Cheng, and L. Wang, FeS_2 /carbon hybrids on carbon cloth: a highly efficient and stable counter electrode for dye-sensitized solar cell, *Sustainable Energy & Fuels*, 3(2019), DOI: [10.1039/C9SE00240E](https://doi.org/10.1039/C9SE00240E).
- [270] Y. Yao, N. Mahmood, L. Pan, G. Shen, R. Zhang, R. Gao, Fazal-e Aleem, X. Yuan, X. Zhang, and Ji-Jun Zou, Iron phosphide encapsulated in P-doped graphitic carbon as an efficient

and stable electrocatalyst for hydrogen and oxygen evolution reactions, *Nanoscale*, 10 (2018) DOI: [10.1039/C8NR06752J](https://doi.org/10.1039/C8NR06752J).